Dennis Albert

Analysis of Power Transformers under DC/GIC Bias

DOCTORAL THESIS

to achieve the university degree of

Doktor der technischen Wissenschaften

submitted to

Graz University of Technology

Supervisor

Ao. Univ.-Prof. Dipl.-Ing. Dr. techn. Herwig Renner

Institute of Electrical Power Systems

External Reviewer

Prof. Hans Kristian Høidalen, PhD.

Department of Electric Power Engineering

Norwegian University of Science and Technology (NTNU)

Graz/Austria, October 2022

Affidavit

I declare that I have authored this thesis independently, that I have not used other than the declared sources/resources, and that I have explicitly indicated all material which has been quoted either literally or by content from the sources used. The text document uploaded to TUGRAZonline is identical to the present doctoral thesis.

Graz, 10st October 2022

Acknowledgement

This dissertation is submitted for the degree of philosophy doctor at Graz University of Technology (TUG) in Graz/Austria. The research presented herein is conducted in the field of measuring and calculating the effects of geomagnetically induced currents (GICs) on power transformers. The research and this thesis were composed during my employment at the Institute of Electrical Power Systems (IEAN) at Graz University of Technology.

My special thanks go to Ao. Univ. Prof. Dipl.-Ing. Dr. techn. Herwig Renner and Univ.-Prof. DDipl.-Ing. Dr. techn. Robert Schürhuber, who not only gave me the opportunity to conduct my dissertation on this interesting and exciting topic. Moreover, they supported me during this time and helped me with their commitment. The faith they had in me they had placed in me and the scope they had given me for new ideas has contributed significantly to the success of this work. I also like to thank Prof. Hans Kristian Høidalen, PhD. for being the external reviewer and his conscientious review as well as his helpful comments and advice on this dissertation.

This dissertation has been part of the joint research project 'Niederfrequente Sternpunktströme 2' together with Siemens Energy Austria GmbH and Austrian Power Grid AG. I also thank our project partners for their support and helpful discussions during our project. Throughout the project we were also in contact with other companies and authorities who supported our project with information, data and valuable discussions, but whose naming would go beyond the scope of this acknowledgement. Therefore, I thank all these colleagues for their support. Many thanks to Prof. Dr. Sergey E. Zirka from Dnipro National University in Ukraine for the valuable cooperation and long-lasting discussions on transformer modelling. I also like to thank my colleagues, fellow PhD students and friends, who helped me with their creative ideas, discussion and help conducting the laboratory test. In addition, I thank all students who supported and contributed to my work during the bachelor and master thesis or as student assistant with great commitment and great dedication in the context of their work.

Mein Dank geht auch an meine Familie und meine Großeltern, die mich auf meinem bisherigen Lebensweg stets unterstützt und ermutigt und damit diese Arbeit erst ermöglicht haben. Meiner Frau Verena danke ich für ihre Unterstützung und unermesslich aufgebrachte Geduld während meiner Promotion, aber auch während des Verfassens dieser Arbeit. Danke, dass ich mich auf Euch immer verlassen konnte und auch in Zukunft immer kann.

Graz, October 2022
Dennis Albert

Abstract

Power transformers are key components in the interconnected bulk power transmission grid. Moreover, to ensure the reliable and stable operation of the power grid, the interaction of the transformers and the power grid during normal and abnormal operation conditions were studied. To study abnormal operation conditions of power transformers it may be necessary to include the non-linear hysteresis characteristics of the transformer cores in electromagnetic transient studies. The modelling of the hysteresis characteristics of the transformer cores requires detailed information about the transformer core design and material. If this information is not available, it is challenging to establish an adequate electromagnetic transformer model. Especially during deep saturation conditions, typically near two Tesla for gain-oriented steels, an accurate modelling of the hysteresis characteristics can be essential for the calculated phase currents. Such saturation conditions could be caused by geomagnetically induced currents (GICs) or direct current (DC) bias caused e. g. by power electronic devices. This work is a follow-up investigation, motivated by increased transformer sound, which could be traced back to GICs in the high and extra high-voltage transmission grid.

This work presents a measurement based modelling approach to establish electromagnetic topology models of power transformers, including the transformer's core hysteresis characteristics. First the AC saturation test was developed with the idea to saturate the outer two limbs of a three-phase transformer core by two elevated 180° phase-shifted single-phase voltages. The AC saturation test was successfully used to parametrise the hysteresis model of two transformer topology models, using the inductance-reluctance and the capacitance-permeance analogy. Because the AC saturation test requires a sufficiently large power source, it was further developed to the DC hysteresis test. Instead of using a 50/60 Hz sinusoidal voltage, a DC with reversal polarity was used. The DC hysteresis test was also successfully used to parametrise the transformer hysteresis models. The implementation of the DC hysteresis test in a portable transformer test allows to conduct this test in the laboratory and in the field. Together with the principle of variable core gap inductance the transformer topology models of a 50 kVA reveal a high accuracy of the calculated and measured current waveforms during the AC saturation and the standard no-load test, as well as the corresponding power demand.

For the measurement of transformer neutral point currents, including geomagnetically induced currents (GICs), an existing measurement system was further developed to minimise the constraints of the monitoring system on grid operations. The utilisation of a split-core current transducer around the earthing switch, together with a software-supported correction of the offset drift, reveals a low long-term offset drift of the measured transformer neutral point current. In addition to the measurement of the transformer neutral point current, the measurement system was extended to monitor a direct current compensation (DCC) system, installed in several transformers in the transmission grid. The analysis of the DCC measurements, which allows a calculation of the DC per phase, reveals an equal distribution of the DC between the high-voltage phases and the capability of the system to minimise the effects of GICs in transformers.

Kurzfassung

Leistungstransformatoren sind Schlüsselkomponenten des elektrischen Übertragungsnetzes. Um einen zuverlässigen und stabilen Betrieb des Stromnetzes zu gewährleisten, wurde die Wechselwirkung zwischen den Transformatoren und dem Stromnetz unter verschiedenen Betriebsbedingungen untersucht. Um auch ungewöhnliche Betriebsbedingungen von Leistungstransformatoren zu untersuchen, kann es notwendig sein, die nichtlinearen Hystereseeigenschaften der Transformatorkerne in der Modellierung zu berücksichtigen. Die Modellierung der Hystereseeigenschaften von Transformatorkernen erfordert detaillierte Informationen über die Konstruktion und das Material des Transformatorkerns. Wenn diese Informationen nicht verfügbar sind, ist es schwierig, ein geeignetes elektromagnetisches Transformatormodell zu erstellen. Insbesondere bei Sättigung des Transformatorkerns, typischerweise in der Nähe von zwei Tesla für kornorientierte Elektrobleche, kann eine genaue Modellierung der Hystereseeigenschaften für die Berechnung der Phasenströme entscheidend sein. Solche Sättigungsbedingungen können z. B. durch den Einfluss von leistungselektronischen Geräten verursacht werden. Bei dieser Arbeit handelt es sich um eine Folgeuntersuchung, die auf Grund von zunehmenden Transformatorengeräuschen initiiert wurde und auf geomagnetisch induzierte Ströme (engl. GICs) im Übertragungsnetz zurückgeführt werden konnte.

Der in dieser Arbeit vorgestellte Modellierungsansatz basiert auf einer zusätzlichen Messung an den Transformatorklemmen. Mit den Transformatorkenndaten, wie z. B. der Nullimpedanz, und der zusätzlichen Messung wird das Topologiemodell des Transformators samt Hysterecharakteristik des Kernmaterials erstellt. Dazu wurde zunächst der AC Sättigungstest entwickelt, bei dem die beiden äußeren Schenkel eines Dreischenkeltransformators durch zwei erhöhte, um 180° phasenverschobene Einphasenspannungen gesättigt werden. Der AC Sättigungstest wurde erfolgreich zur Parametrierung des Hysteresemodells von zwei Transformator-Topologiemodellen eingesetzt, wobei die Induktions-Reluktanz- und die Kapazitäts-Permeanz-Analogie verwendet wurden. Da der AC Sättigungstest eine Spannungsquelle mit ausreichend großer Leistung erfordert, wurde aus dem AC Sättigungstest der DC Hysteresetest entwickelt. Anstelle einer 50/60 Hz-Sinusspannung wird für die Messung eine Gleichspannung mit wechselnder Polarität verwendet. Der DC Hysteresetest wurde ebenfalls erfolgreich zur Parametrierung der Transformator-Hysteresemodelle im Rahmen des Modellierungsansatzes verwendet. Die Implementierung des DC Hysteresetests in einem tragbaren Transformatorprüfgerät ermöglicht die Durchführung dieser Messung im Labor und im Feld. Zusammen mit dem Prinzip der veränderbaren Luftspaltinduktivtität zeigen die Transformatortopologiemodelle eines 50 kVA eine hohe Genauigkeit des berechneten und gemessenen Stroms während des AC Sättigungs- und des Leerlauftests.

Für die Messung von Transformatorsternpunktströmen, einschließlich GICs, wurde ein bestehendes Messsystem weiterentwickelt, um die Einschränkungen durch das Messsystem auf den Netzbetrieb zu minimieren. Die Verwendung eines teilbaren Stromwandlers um den Erderarm eines Erdungsschalters in Verbindung mit einer softwaregestützten Korrektur des Offsetdrifts, der auf den verbauten Hallsensor im Stromwandler zurückzuführen ist, wird der Langzeit Offsetdrift reduziert. Dadurch kann das Messsystem für Langzeitmessungen verwendet werden. Zusätzlich

zur Messung des Transformatorsternpunktstroms wurde das Messsystem erweitert, um die Ströme eines Gleichstromkompensationssystems (engl. Direct Current Compensation, kurz DCC), das in mehreren Transformatoren im Übertragungsnetz installiert ist, zu messen. Die Analyse der DCC-Messungen, die eine phasenaufgelöste Berechnung des überlagerten Gleichstroms auf den Hochspannungswicklungen ermöglicht, zeigt eine gleichmäßige Verteilung des Gleichstroms zwischen den drei Hochspannungsphasen. Im Vergleich mit dem gemessenen Sternpunktstrom konnte gezeigt werden, dass das System auch während eines Sonnensturms und den damit einhergehenden GICs die Auswirkungen auf den Transformator minimieren kann.

Contents

List of Abbreviations

AC alternating current

AD anna domini

ADC analog digital converter

BCE before common era

B2B back-to-back

CGO conventional grain-oriented

CIM complex-image method

CM common mode

CME coronal mass ejection

CPH capacitance-permeance hysteresis

CT current transducer

DC direct current

DCC direct current compensation

DER distributed energy resources

DHM dynamic hysteresis model

emf electromotive force

EMP electromagnetic impulse

EMTP electromagnetic transient program

FEM finite element method

FFT fast Fourier transformation

FORC first-order reversal curve

FSR full scale range

GIC geomagnetically induced current

GMD geomagnetic disturbance

GO grain-oriented

GSM Global System for Mobile Communication

GSR global solar radiation

GUI graphical user interface

HEMP high-altitude electromagnetic impulse

HGO high grain-oriented

HVAC high-voltage alternating current

HVDC high-voltage direct current

IC integrated circuit

IFFT inverse fast Fourier transformation

IMF interplanetary magnetic field

JA Jiles-Atherton

LFC low-frequency current

LSB least significant bit

mmf magnetomotive force

NEMP nuclear electromagnetic pulse

NMS Nelder-Mead Simplex

NO non-oriented

NOAA National Oceanic and Atmospheric Administration

NPC neutral point current

NS negative-sequence

op amp operation amplifier

PCB printed circuit board

PFC phase-fired control

PMU phasor measurement unit

ppm parts per million

PS positive-sequence

PSO particle swarm optimisation

PWM pulse-width modulation

rms root mean square

SCADA supervisory control and data acquisition

SCW Substorm Current Wedge

SFRA Sweep Frequency Response Analysis

SHM static hysteresis model

SI sudden impulse

SSC sudden storm commencement

SVC static VAR compensator

THD total harmonic distortion

UMTS Universal Mobile Telecommunications System

List of Symbols

Symbol	Unit	Description
A, $\vec{A}$	m^2	area
a	A/m	JA hysteresis model parameter
B, $\vec{B}$	T	magnetic flux density
C	F	electric capacitance
c		JA hysteresis model parameter
D, $\vec{D}$	As/m_2	electric displacement field
Dst	nT	index for ring current strength
E	J	energy
E, $\vec{E}$	V/m	electric field strength
f	Hz	frequency
H, $\vec{H}$	A/m	magnetic field strength
J, $\vec{J}$	A/m_2	electric displacement current density
k	A/m	JA hysteresis model parameter
L	H	electric inductance
l	m	length
N		number of turns in a winding
N	var	non-active power
M_w		moment magnitude for earthquakes
m	am^2	magnetic moment per unit volume
M_s	A/m	JA hysteresis model parameter
P	W	active power
PF		power factor
Q	var	reactive power
q	As, C	electric charge
R	Ω	electric resistance
S	VA	apparent power
T	°C, K	temperature Celsius/Kelvin
t	s	time
V	V	DC voltage
V	m^3	volume
v		susceptibility coefficient
v	m/s	speed
v	V	variable voltage
$\hat{v}$	V	amplitude of voltage
W	J	work, transferred energy
Z	Ω	electric impedance
ü		transmission ratio of transformer
α		JA hysteresis model parameter

Symbol	Unit	Description
Δ	m	equivalent air gap length
δ		directional parameter ± 1
κ	$\Omega \cdot \mathrm{m}$	electric conductivity
λ_e	m	penetration depth
μ_0	$4\pi \cdot 10^{-7}$ Vs/Am	magnetic permeability constant
μ_r		relative magnetic permeability
ρ	kg/m^3	density
$\underline{\varrho}$	As/m^3	charge density
σ	m	skin depth
σ		standard deviation
τ	s	time constant
Φ	$\mathrm{Wb} = \mathrm{Vs}$	magnetic flux
$\dot{\Phi}$	V	flux rate
φ	rad, $^\circ$	angle
χ		magnetic susceptibility
Ψ ($\approx N \cdot \Phi$)	T	linked magnetic flux
ω	rad/s	angular frequency
$\mathcal{F}$	A	magneto motive force
$\mathcal{P}$	H	permeance
$\mathcal{R}$	H^{-1}	reluctance

1 Introduction

1.1 Motivation and Research Questions

An increased transformer sound level initially motivated this research work after the commissioning of a new transformer in a substation where an east-west 380 kV transmission line terminates. Measurements in the transformer neutral revealed an increased low-frequency current (LFC) or quasi-DC level [Hal+14]. Further analysis of the measured transformer neutral point current (NPC) and the magnetic field revealed that GICs are the dominating source of the LFC measured in the transformer neutral. In the Austrian transmission grid one transformer neutral point per voltage level (220 kV and 380 kV) and per substation is solidly grounded. Due to the solidly grounded neutral points, GICs can enter and leave the transmission grid via the transformer neutrals and can cause transformer saturation, which is accompanied by an increased level of harmonics and increased reactive power demand. Long-term measurements, started in 2016, were used to validate GIC calculations in the transmission grid [Hal19], to monitor the GICs and to identify other LFC sources besides GICs. In alternating current (AC) power systems LFCs are undesired, due to the increase of losses and possible saturation effects in transformers and reactors with a magnetic core. Nevertheless, a certain LFC level may be present in any grounded, electrically conductive circuit. One origin of LFCs in AC circuits is a time varying magnetic field penetrating conductive circuits, such as AC power transmission grids.

This PhD work is a follow-up of [Hal19] investigating the effects of LFCs on the power grid and power transformers. The former work focused on the development of a transformer neutral point current measurement and the calculation of GICs based on magnetic field measurements [Hal+14; Hal14; Hal+16; HRA18; Bai+18; Hal19; Alb+19]. Moreover, this work focuses also on power transformer modelling [Alb+20; Pro+20; Alb+21a; Alb+22b; Alb+22a] based on terminal measurements [AMR21] and the development of a transformer NPC measurement system which does not restrict the power grid operation as the previous system. Moreover, the measurement system was extended to monitor a direct current compensation (DCC) system installed in several transformers in the transmission grid [Alb+21b]. The DCC system compensated the undesired DC flux inside the transformer core with an additional compensation winding on the wounded limbs of the transformer. The compensation winding is connected to an external power electric device, providing a phase-cut current which induces a compensating flux in the wounded limbs. In this scope the following research questions are addressed.

Research questions regarding *power transformers*:

1. How can the transformer core hysteresis characteristics be modelled and parametrised from transformer terminal measurements?
2. What is an appropriate modelling technique that reproduce the transformer terminal characteristics during saturation?
3. What is an appropriate transformer terminal measurement for the parametrisation of transformer hysteresis models including moderate saturation conditions?

4. How can five-limb multi-winding power transformers be reliable demagnetised and how can the successful demagnetisation be proofed?

Research questions regarding low frequency *transformer neutral point current measurements*:

1. What are the specifications for a measurement system in order to measure low frequency transformer neutral point currents?
2. What is the measurement accuracy of the developed system?

1.2 Research Methodology and Scope

The research methodology in this thesis is primarily experimental. The measurement data from laboratory tests is used to parametrise a transformer model, which replicates the transformer voltage and current terminal characteristics best, as well as the power demand (abduction). The simulated and measured current waveforms and power demand are compared and used to judge the models accuracy.

1.3 Thesis Outline and Scientific Contribution

Chapter 2 provides the state-of-the-art on the calculation and measurement of GICs in power grids as well as their causes. Subsequently, the effects of LFCs and GICs, especially on power transformers are highlighted. To calculate the transformer terminal behaviour under LFC/GIC bias, transformer grey box topology models are introduced. Furthermore, GIC mitigation techniques and important aspects during the power transformer GIC studies are presented.

GICs are caused by the varying earth magnetic field. Strong earth magnetic fields can be caused by space weather events. Therefore, the interaction processes between the space weather and the earth magnetic field are reviewed in **Section 2.1.1**. The principle of geomagnetically induced electric fields are explained on a simple example, using the Maxwell Equations, in **Section 2.1.2**. In order to derive an induced electric field from geomagnetic field variations, the earth conductivity need to be taken into account. Important aspects related to the earth conductivity modelling in the scope of GIC calculations are presented in **Section 2.1.3**. To derive the GICs in the power grid, a model of the power grid is required. The important grid parameters for the model are explained in **Section 2.1.4**.

LFCs in power grid can be caused by space weather events, but also by other sources. These sources, such as DC powered public transportation systems or nuclear electromagnetic pulses (NEMPs), are presented in **Section 2.2.2** and **Section 2.2.3**.

To validate calculated GICs in power grids, measurements are required. The principle of GIC measurements in power grids and a promising technology, the optical current measurement technique, are presented in **Section 2.3**.

Section 2.4 focuses on the fundamentals of electromagnetic modelling of power transformers in the context of grey box topology models. The inductance-reluctance and capacitance-permeance analogy are presented and used to derive a transformer topology model in **Section 2.4.1**. The transformer grey box model parameter derivation from the transformer factory acceptance test and the effects of these parameters are highlighted in **Section 2.4.2**. Effects of the transformer design in the scope of transformer core saturation and terminal behaviour is reviewed in **Section 2.4.3**. Subsequently, the modelling of the transformer core material hysteresis is presented in **Section 2.4.4**. The transformer susceptibility in the context of GICs and the mitigation of GICs presented in **Section 2.5**. In order to remove a remanent flux in a transformer core before energisation, the demagnetisation techniques of power transformers are reviewed in **Section 2.6**

The technical design aspects for LFC measurements in transformer neutral points are given in **Chapter 3**. The existing measurement system, using a mobile earthing equipment which is feed through a current transducer (CT), was further developed to reduce the restrictions during operation of the transformers. In addition to the NPC measurement, the measurement system was extended to monitor the currents of DC compensation system. The system design and measurement system uncertainty is presented in **Section 3.1** and **Section 3.2**.

In **Chapter 4** a developed measurement based modelling approach is presented with examples of two 50 kVA three-limb transformers. The two grey box models are parametrised based on the data from the factory acceptance test, the transformer core design and the supplemented AC saturation or DC hysteresis test, to provide models also valid for deep transformer core saturation conditions. **Section 4.1** provides and overview of the modelling process. **Section 4.2** presents the laboratory setup and the transformers under test. The model's parameter derivation and the effect of the model parameters on the transformer electrical characteristics are presented in **Section 4.3**. The developed AC saturation and DC hysteresis tests are explained in detail in **Section 4.3.2**. The derived transformer models from the AC saturation and DC hysteresis test are compared to the measurement in **Section 4.4.2** and validated with the standard no-load test in **Section 4.4.3**. Moreover, the modelling approach was successfully applied to calculate inrush currents with the ATPDraw software in [Zir+22b], with the results presented in **Section 4.4.4**. Furthermore, the measurement results of back-to-back (B2B) tests with and without superimposed DC from different DC sources are outlined in **Section 4.4.5**. The effects of different transformer vector groups on the power demand during various superimposed DC levels are examined in **Section 4.5**. Besides the increased power demand of transformer during DC bias, the transformer sound level increases during DC bias. Different aspects related to the transformer sound level measurement are discussed in **Section 4.6**. The DC bias mitigation effect of a delta winding is analysed on a measurement example and new DC mitigation setup is proposed in **Section 4.7**. The effects of long-term GIC on power transformers are discussed in the context of a GIC_{sum} value in **Section 4.8**. Finally, a new procedure to demagnetise five-limb transformer is presented and tested on transformers of different rated power in **Section 4.9**.

The major findings of this thesis and an outlook on further research in the field of power transformer modelling and LFC measurements are given in **Chapter 5**.

The main contribution to science in the field of power transformer grey box modelling are:

- provide a modelling guideline for grey box models of three- and five-limb power transformers, validated by laboratory test,
- provide electromagnetic grey box models of three-limb and five-limb power transformers, compared to tests with transformer saturation and validated by no-load measurements,
- present a developed method to measure the transformer hysteresis up to deep saturation on-site,
- approach to use the measured hysteresis characteristics to model the transformer hysteresis characteristics in transformer topology models
- investigation of power transformer power demand during unbalanced and non-sinusoidal conditions
- proposed and successfully evaluated a new demagnetisation approach for five-limb transformers

The main contribution to science in the field of low frequency current measurements are:

- design specifications for transformer neutral point current measurement systems,
- field experience with transformer neutral point current measurements on a transformer neutral point switch,
- LFC distribution on the three phases are analysed with measurements.

2 State of the Art

2.1 Geomagnetically Induced Current Modelling and Simulation

GICs are caused by space weather events, which affect the earth magnetic field. The varying earth magnetic field induces an electromagnetic field in the transmission lines of the power grid and the earth itself. For the calculation of GICs in the electric power grid, the following data and information are required:

- ground conductivity model,
- power grid model or transformer neutral point current measurements,
- magnetic or electric field data.

Depending on the geographic location of the (power) system under investigation, different approaches for the geoelectric field calculation from magnetic field data can be used. The magnetic-geoelectric field relation can be modelled as plane-wave, with a thin-sheet model or with the complex-image method (CIM). The plane-wave and the thin-sheet model are used in mid-latitude countries, because the ring current[1] is assumed as dominating source of the magnetic field variations. At higher latitudes, the CIM is an adequate method for the geoelectric field calculation, which allows taking into account the more complex polar current systems. A detailed mathematical analysis of the plane-wave method, assuming an infinite horizontal current sheet and assuming an infinitely long harmonically oscillating straight line current as primary source, is given in [Pir82]. An explanation and example of the thin-sheet model can be found in [HL93]. The CIM approach is explained in detail in [BP98].

Another aspect, which is related to geographic location, is the earth conductivity in the region of interest. Depending on the complexity of the earth conductivity structure, a 1D, 2D or 3D earth conductivity model should be selected for GIC calculations.

2.1.1 Space Weather

The interference of the space weather with the earth magnetic field causes earth magnetic field changes ($\mathrm{d}H/\mathrm{d}t$), inducing an electromotive force (emf) in the earth, described in **Section 2.1.2**. The magnetosphere contains various current systems, which contribute to the overall earth magnetic field. Therefore, it is crucial to study the structure of the earth magnetosphere in order to understand magnetic field variations on earth. The magnetosphere around the earth is dominated by the earth magnetic field and less affected by the interplanetary space. It is the boundary between the earth magnetic field and the solar wind. The shape of the earth's magnetosphere is mainly affected by the solar wind, which is a flow of plasma, and is therefore in constant motion. The solar wind compresses the sunward side of the magnetosphere to a distance of about six to ten times the radius

[1] The ring current is part of the earth magnetospheric current system. The ring current ranges from approx. three to eight earth radius toroidally around the earth in the equatorial plane [Dag+99]. The main charge carriers are positive ions with energies in the range of 1 - 200 keV. The charge carriers are trapped in the geomagnetic field and undergo different motion types [PB04].

of the earth. A supersonic shock wave is created sunward, called the bow shock. Most of the solar wind particles are heated and slowed down at the bow shock and detour around the earth in the turbulent magnetosheath. Below the magnetosheath, the magnetopause is located with a thickness of less than 100 km. It is the outer boundary of the earth magnetosphere, where the dynamic pressure (left side of (2.1)) of the solar wind and the magnetic pressure (right side of (2.1)) of the geomagnetic field just cancel each other out.

$$\frac{\rho v^2}{2} = \frac{B^2}{2\mu_0} \tag{2.1}$$

with the density ρ and the speed v. **Figure H.2** depicts the primary areas of the magnetosphere. The solar wind drags out the night-side magnetosphere to possibly 1,000 times earth's radius (moon orbit is approx. 60 earth radius away from earth), its exact length is unknown. This extension of the magnetosphere is known as the magnetotail. The earth's magnetosphere is a highly dynamic structure that responds to solar variations. The interaction between the solar wind and earth's magnetic field, and the influence of the underlying atmosphere and ionosphere, creates various regions of fields, plasma, and currents inside the magnetosphere, such as the plasmasphere, the ring current, and the radiation belts [PB04].

A complex current system inside the magnetosphere is created and influenced by the solar wind and the coupled geodynamo. This system preserves the earth's magnetic field and protects the earth from high radiation levels. The equatorial ring current (**Figure 2.1b**) is flowing in east-west direction in the equatorial sphere in a distance to earth of four to six earth radius.

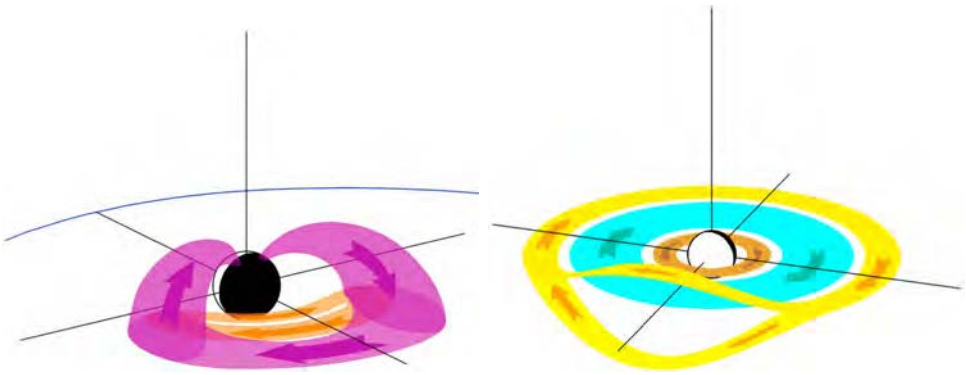

(a) Region 2 field-aligned current and partial ring current.

(b) Ring current.

Figure 2.1: Magnetospheric current systems [GLD18].

The resulting magnetic field is opposite to the earth's magnetic field. Thus, solar storms can cause a major reduction of the overall magnetic field at low latitude areas. The magnetic fields of the ring current are measured using the Dst index. If the Dst value drops below $-50\,\mathrm{nT}$, then the event is classed as a magnetic storm, whereas a negative Dst value indicates a weakened earth magnetic field. For comparison: during the Halloween Storm in October 2003 the Dst reached almost -450 nT. The

index is derived from four magnetic observatories (Hermanus, Kakioka, Honolulu, and San Juan) aligned along the earth equator. Further information on the Dst value can be found in [SK91].

The effects caused by space weather interaction with the earth magnetic field also depend on the magnetic field in the region of interest, because the earth magnetic field is not homogenous across the earth, as depicted in **Figure 2.2**.

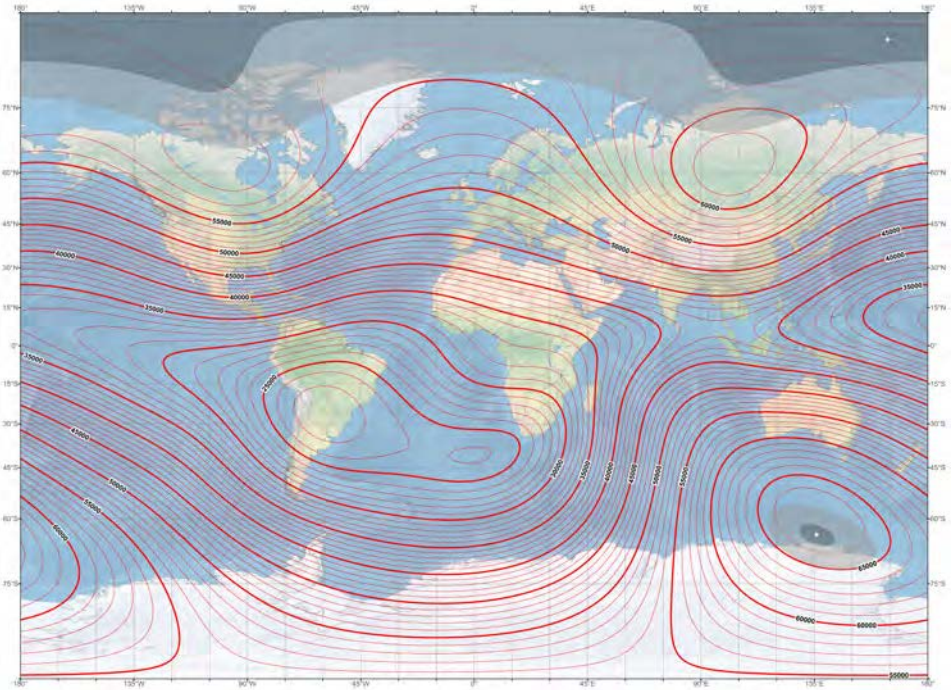

Figure 2.2: US/UK world magnetic model - Epoch2020.0; main field total intensity B_F (red) adopted from [NN20].

Although the cities Québec/Canada and Vienna/Austria are approximately located at the same geographic latitude, both are exposed to different earth magnetic field strength B_{F}, as it can be seen in **Figure 2.2**. Therefore, also the magnetic latitude on earth affects the GICs. Countries at higher geomagnetic latitude, such as the Scandinavian countries, usually experience higher GICs. This is due to the complex current systems in the Northern Hemisphere (see **Figure H.2a**) and the lower distance between ground and the magnetospheric current systems at higher latitudes. Whereas magnetic field variations in mid-latitude countries, such as Austria, are dominated by distant magnetospheric currents and spatially smooth mid-latitude ionospheric currents [GLD18].

Space Weather Indices

For the measurement of geomagnetic disturbances (GMDs), mainly the global K_{p} index and Dst value are used. The K_{p} index is a measure of the natural magnetic field disturbances. It is calculated in several steps from the disturbance index K of the two horizontal magnetic field components at 13 selected observatories outside the auroral zone. The K_{p} index ranges from 0 to 9 with 28

steps and is calculated for a 3 h period [Mat+21c; Mat+21b]. The global K_{p} is calculated in Potsdam/Germany [Mat+21c]. The National Oceanic and Atmospheric Administration (NOAA) in Boulder/USA [NOA20] calculates a pseudo K_{p} index for real-time use. This pseudo K_{p} index is based on a limited number of stations and is therefore only an approximation of the global K_{p} index calculated in Potsdam/Germany. The K_{p} index can be used to identify disturbed periods, but short-time duration disturbances can be hidden by the averaging effect of the 3 h-value.

The Dst value in nano Tesla (nT) is dominated by the magnitude of the ring current, which produces an axially symmetric disturbance field. The Dst value is based on the measurement of the horizontal magnetic field component H at four measurement station located at low latitudes in the equatorial region [SK91; Nos+15]. During periods with low geomagnetic disturbances the Dst value is above -50 nT. In [EGT11] storms with Dst values below -50 nT from 1957 to 2008 are analysed. During the Carrington event, which is known as the largest documented geomagnetic disturbance, a Dst between -850 nT and -1760 nT was estimated [Lan01; Tsu03].

GMDs can be characterised in several phases. The largest GICs at higher latitudes are usually caused by magnetic substorms. Sudden storm commencements (SSCs) have a high latitude enhancement during larger space weather events. This increases the risk factor for power systems [FBG14].

2.1.2 Geomagnetically Induced Electric Field

The time varying magnetic field induces an electric field, according to Faraday's law of induction. An example for slow magnetic field variations is the regular daily geomagnetic field variation, also referred to as solar quit, or Sq, day variation [YM17]. The geomagnetic field usually varies within several tens of nano Tesla per day [Bai18]. These slow magnetic field changes induce a slow varying electric field in electrically conductive materials. The induced electric field depends on the material conductivity and the local magnetic field change. Considering now that the electric power transmission grid spans hundreds of kilometres across the land. Integrating the induced electric field along a loop, results in an emf unequal to zero. This emf drives a current in the loop formed by e. g. an overhead line, two grounded transformer neutral points at both ends and the earth. Such a setup is depicted in **Figure 2.3**.

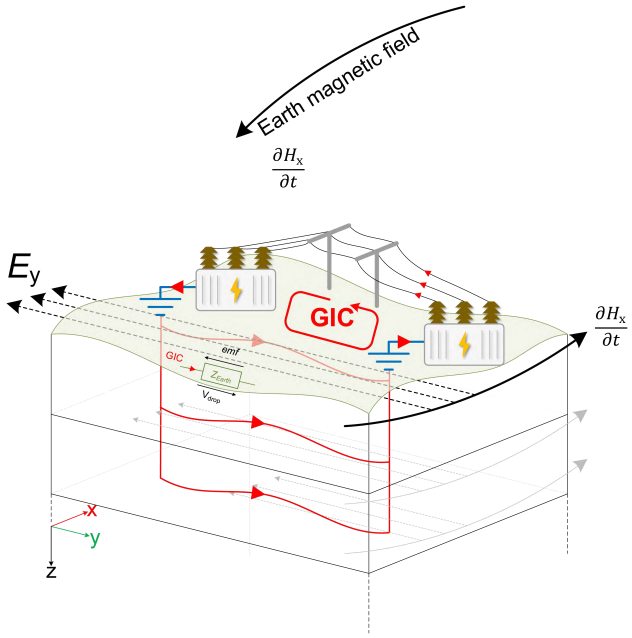

Figure 2.3: The time varying earth magnetic causing geomagnetically induced currents in electric power systems.

The emf amplitude is equal to the voltage drop (V_{drop}) across the earth impedance but has the opposite sign. Thus, the voltage drop across the earth impedance and the emf vanishes. Otherwise, a potential difference on earth would be caused, which is not the case [BP17]. The current is also referred to as GIC or quasi-DC, because of frequencies below 1 Hz, which is well below the nominal power system frequency of 50/60 Hz.

Taking a closer look at the emf induced in the earth and assuming a rectangular electrical conductor with the conductivity σ, a relative permeability μ_{r}, a length of L in x-direction and a height of H in z-direction [Sim71]. The conductor has an *infinitesimal thickness* and is located in free space, as depicted in **Figure 2.4**.

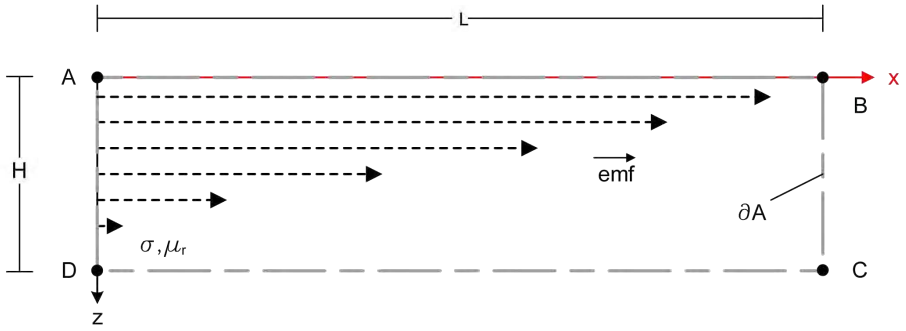

Figure 2.4: Electric field in a conductor with infinitesimal thickness.

The conductor in free space is penetrated by a xy-planer magnetic field $\vec{H}$ propagating in z-direction. Because the source field horizontal extension is greater than the skin depth, the change in x- and

y-direction can be neglected in comparison to the change in z-direction ($\partial/\partial y = \partial/\partial x = 0$). Therefore, the disturbance field $\vec{H}$ can be approximated as a plane wave propagating vertical down. Further, the magnetic field $\vec{H}$ varies with a frequency well below 1 Hz, therefore, magneto-quasi static conditions can be assumed. This is valid if, $\partial\vec{D}(\vec{r},t)/\partial t$ can be neglect with respect to $\kappa\vec{E}(\vec{r},t)$, which is the case when:

$$\max_{r\in\mathcal{R}^3}\left|\frac{\partial\vec{D}}{\partial t}\right| \ll \max_{r\in\mathcal{R}^3}\left|\kappa\vec{E}\right|, \tag{2.2}$$

applies, where κ is the electric conductivity. The Maxwell equations in differential form are:

$$\mathrm{rot}\underline{\vec{E}} = -\mathrm{j}\omega\underline{\vec{B}}, \tag{2.3}$$

$$\mathrm{rot}\underline{\vec{H}} = \underline{\vec{J}}_l + \underline{\vec{J}}_e, \tag{2.4}$$

$$\mathrm{div}\underline{\vec{D}} = \underline{\varrho}, \tag{2.5}$$

$$\mathrm{div}\underline{\vec{B}} = 0, \tag{2.6}$$

with the consideration of a plane-wave magnetic field ($\partial/\partial y = \partial/\partial x = 0$), the Maxwell equations from (2.3) and (2.4) resolved in:

$$\mathrm{rot}\underline{\vec{E}} = \begin{vmatrix} \vec{e}_\mathrm{x} & \vec{e}_\mathrm{x} & \vec{e}_\mathrm{z} \\ 0 & 0 & \partial/\partial z \\ \underline{E}_\mathrm{x} & \underline{E}_\mathrm{y} & \underline{E}_\mathrm{z} \end{vmatrix} = -\frac{\partial\underline{E}_\mathrm{y}}{\partial z}\vec{e}_\mathrm{x} + \frac{\partial\underline{E}_\mathrm{x}}{\partial z}\vec{e}_\mathrm{y} + 0\,\vec{e}_\mathrm{z}$$
$$\stackrel{!}{=} -\mathrm{j}\omega\mu\left(\underline{H}_\mathrm{x}\vec{e}_\mathrm{x} + \underline{H}_\mathrm{y}\vec{e}_\mathrm{y} + \underline{H}_\mathrm{z}\vec{e}_\mathrm{z}\right), \tag{2.7}$$

$$\mathrm{rot}\underline{\vec{H}} = \begin{vmatrix} \vec{e}_\mathrm{x} & \vec{e}_\mathrm{x} & \vec{e}_\mathrm{z} \\ 0 & 0 & \partial/\partial z \\ \underline{H}_\mathrm{x} & \underline{H}_\mathrm{y} & \underline{H}_\mathrm{z} \end{vmatrix} = -\frac{\partial\underline{H}_\mathrm{y}}{\partial z}\vec{e}_\mathrm{x} + \frac{\partial\underline{H}_\mathrm{x}}{\partial z}\vec{e}_\mathrm{y} + 0\,\vec{e}_z$$
$$\stackrel{!}{=} \kappa\left(\underline{E}_\mathrm{x}\vec{e}_\mathrm{x} + \underline{E}_\mathrm{y}\vec{e}_\mathrm{y} + \underline{E}_\mathrm{z}\vec{e}_\mathrm{z}\right), \tag{2.8}$$

with the coefficient comparison follows $\underline{E}_z = 0$. The link between the individual magnetic field components and the electric field components are given in (2.9) - (2.12).

$$-\frac{\partial \underline{E}_{\mathrm{y}}}{\partial z} = \mathrm{j}\omega\mu\underline{H}_{\mathrm{x}}, \tag{2.9}$$

$$\frac{\partial \underline{E}_{\mathrm{x}}}{\partial z} = -\mathrm{j}\omega\mu\underline{H}_{\mathrm{y}}, \tag{2.10}$$

$$\frac{\partial \underline{H}_{\mathrm{y}}}{\partial z} = -\kappa\underline{E}_{\mathrm{x}}, \tag{2.11}$$

$$\frac{\partial \underline{H}_{\mathrm{x}}}{\partial z} = \kappa\underline{E}_{\mathrm{y}}, \tag{2.12}$$

where $\mu = \mu_0\mu_{\mathrm{r}}$ with the magnetic permeability constant μ_{r} and μ_0 the vacuum magnetic permeability constant. Differentiating (2.9) and (2.10) again and substituting (2.11) and (2.12) respectively, results in the following equations:

$$\frac{\partial^2 \underline{E}_{\mathrm{x}}}{\partial z^2} = -\mathrm{j}\omega\mu\frac{\underline{H}_{\mathrm{y}}}{\partial z} = \mathrm{j}\omega\mu\kappa\underline{E}_{\mathrm{x}}, \tag{2.13}$$

$$\frac{\partial^2 \underline{E}_{\mathrm{y}}}{\partial z^2} = \mathrm{j}\omega\mu\frac{\underline{H}_{\mathrm{x}}}{\partial z} = -\mathrm{j}\omega\mu\kappa\underline{E}_{\mathrm{y}}. \tag{2.14}$$

Introducing the relations:

$$\underline{p}^2 = \mathrm{j}\omega\mu\kappa, \tag{2.15}$$

$$\underline{p} = (1+\mathrm{j})k, \tag{2.16}$$

$$k = \sqrt{\frac{\omega\mu\kappa}{2}}, \tag{2.17}$$

results in the following homogeneous, differential equations second order:

$$\frac{\mathrm{d}^2 \underline{E}_{\mathrm{x}}}{\mathrm{d}z^2} = \underline{p}^2\underline{E}_{\mathrm{x}}, \tag{2.18}$$

$$\frac{\mathrm{d}^2 \underline{E}_{\mathrm{y}}}{\mathrm{d}z^2} = -\underline{p}^2\underline{E}_{\mathrm{y}}. \tag{2.19}$$

The general solution for (2.18) and (2.19) is of type:

$$\underline{E} = \underline{A}e^{\underline{p}z} + \underline{B}e^{-\underline{p}z}. \tag{2.20}$$

The complex constants $\underline{A}$ and $\underline{B}$ are determined by the boundary conditions. The first boundary condition requires that the field inside a conductor, for $z \to \infty$, reduces to zero, because inside the medium power is converted to Joule heating. If the earth model is assumed as half-space with uniform conductivity, the second boundary condition requires the defined electric field on the conductor surface. Therefore, the complex constants are:

$$\underline{A} = 0,$$
$$\underline{B} = \underline{E}_0.$$

The electric field in x- and y-direction can therefore be written as:

$$\underline{E}_{\mathrm{x}} = \underline{E}_0 e^{-kz} e^{-\mathrm{j}kz} = \underline{E}_0 e^{-kz(1+\mathrm{j})}, \tag{2.21}$$

$$\underline{E}_{\mathrm{y}} = -\underline{E}_0 e^{-kz} e^{-\mathrm{j}kz} = -\underline{E}_0 e^{-kz(1+\mathrm{j})}. \tag{2.22}$$

The induced electric field in **Figure 2.4** fall off exponentially from the edge $\overrightarrow{AB}$ to the edge $\overrightarrow{CD}$, according to (2.21) and (2.22). Following Faraday's law of induction, the induced electric field $\vec{E}(\vec{r}, t)$ drives a current in the same direction as the emf. The induced voltage V_{ind} between the edges $\overrightarrow{BC}$ and $\overrightarrow{DA}$ can be calculated with (2.23).

The sections $\overrightarrow{AB}$, $\overrightarrow{BC}$, $\overrightarrow{CD}$ and $\overrightarrow{DA}$ are the edge ∂A of the surface A. The voltage of $\partial\mathrm{A}$ can be split up in the section-wise electric potential, as derived in (2.23).

$$V_{\mathrm{ind}}(t) = \int_{\overrightarrow{AB}+\overrightarrow{CD}} \vec{\underline{E}}(t)\mathrm{d}\vec{s} \tag{2.23}$$

Integrating the electric field along $\overrightarrow{BC}$ and $\overrightarrow{DA}$ results in 0 V, because the electric field is orthogonal to the integration path.

For GIC calculations in mid-latitude countries, such as Austria, GIC studies can be performed with the plane-wave or thin-sheet method, which is acceptable if no spatial dependence of the magnetic/electric field in the area under investigation is considered and no conductivity anomalies appear in the area under investigation [Cag53; McK03; Bai+17; Bai+18; Hal19; Tho+05; Ngw+09; Pul+12].

Under geomagnetically disturbed conditions the magnetic field strength measured by the Conrad Observatory (WIC[2]), as part of the INTERMAGNET observatory network [Int18], is in the range of 200 - 400 nT. The magnetic field variations during geomagnetic quiet conditions are in the range of 0.4-2.0 nT/min [Leo+20]. During a geomagnetic storm on May, 12th 2021 a maximum magnetic field change of 100 nT/min was measured. **Figure 2.5** depicts the measured absolute magnetic field and magnetic field change from May, 12th 2021. The event on May, 12th 2021 was triggered by a coronal mass ejection (CME) on May 9th 2021 on the sun. Further information on the May 2021 event can be found in **Section 3.5.2**.

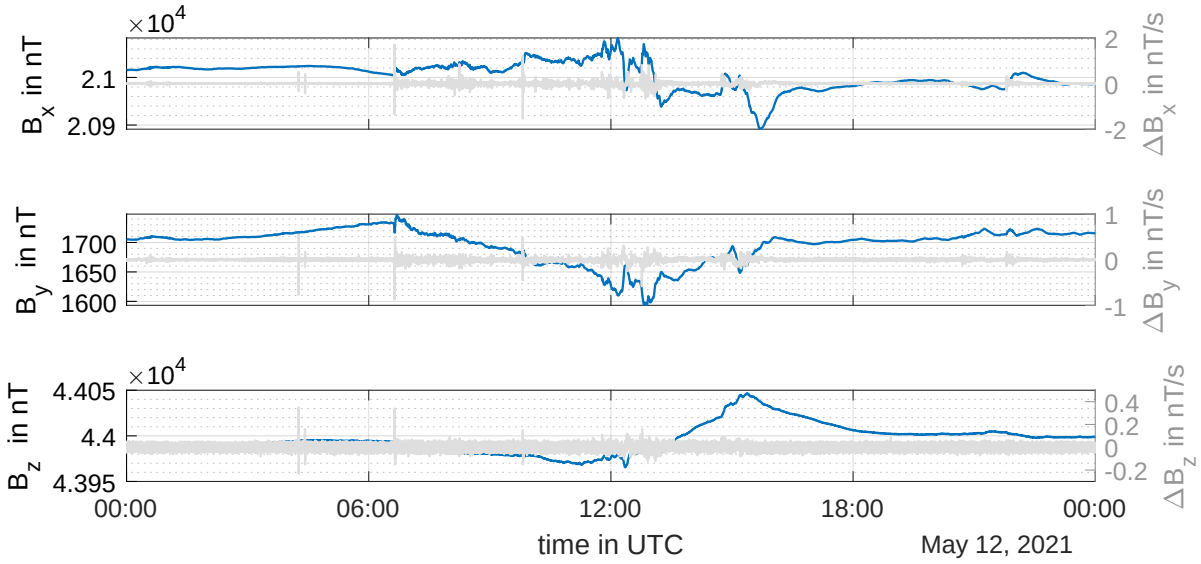

Figure 2.5: Measured magnetic field and magnetic field change of in west-east (x), north-south (y) and vertically down (z) components from WIC.

2.1.3 Earth Conductivity Model

The geomagnetic induction depends on the frequency of the source field. In this context, the skin effect need to be considered. The skin effect describes the field density near the surface of a conductor, which is not uniform across the cross-section. The density is higher near the conductor surface and decreases exponentially with increasing distance to the surface. The distance, where the density reaches 37 %, or $1/e$, is referred to as skin depth. This provides an indicator for the depth of penetration of the disturbance field.

In order to calculate the depth of penetration, the skin depth is defined as follows:

$$\sigma = \frac{1}{k} = \sqrt{\frac{2}{\omega\mu\kappa}}. \tag{2.24}$$

The penetration depth λ_e is defined with:

[2]WIC is the INTERMAGNET code for the Conrad Observatory.

$$\lambda_e := 2\pi\sigma. \tag{2.25}$$

Considering the geomagnetic induction in the earth, it can be seen from **Figure 2.4** and **Figure 2.6**, that modelling the earth up to a certain deep is essential for calculating the driving emf. **Figure 2.6a** depicts the magnetic and electric field as function of depth from above the earth into the earth ground, whereas the earth ground is separated into two sections with different conductivity. The red and blue marked areas indicate the time varying magnetic and electric field. The thick blue and red line indicate the electric and magnetic field at one time instant. In **Figure 2.6b** the magnetic field from above ground into the earth is depicted for different frequencies. It can be seen that the penetration depth of the time-varying magnetic and corresponding electric field depends on the ground conductivity and the frequency.

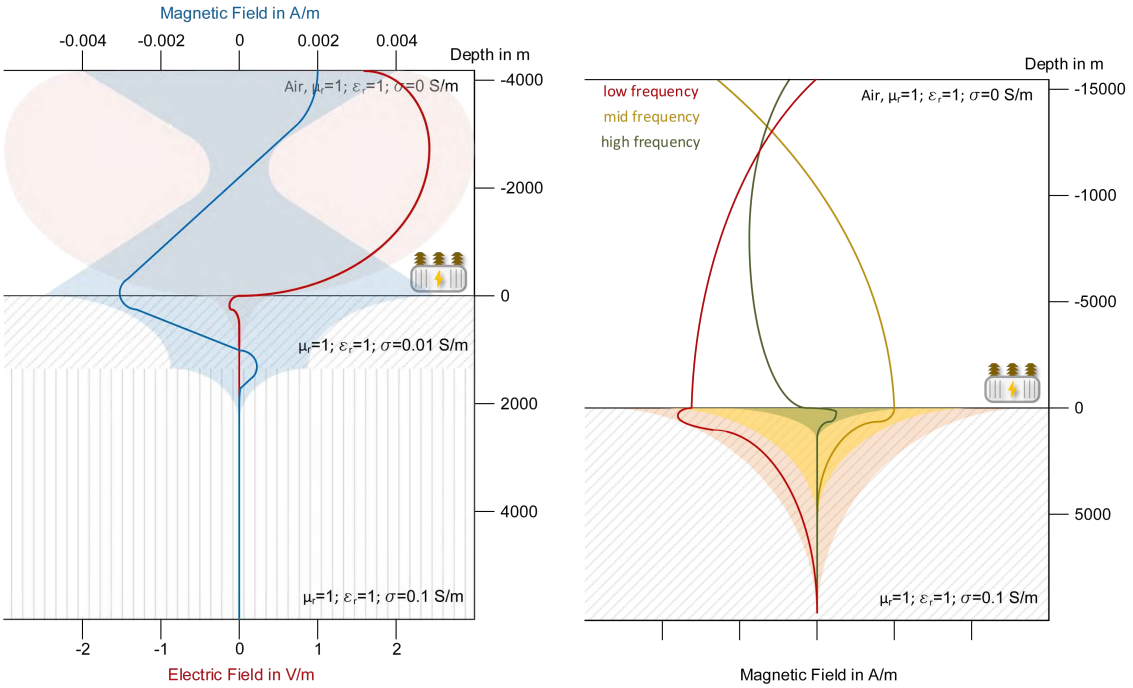

(a) Geomagnetically induction.

(b) Geomagnetic field of different frequencies.

Figure 2.6: Schematic representation of geomagnetic and geoelectric field from above ground into ground.

Evaluating the electric field at $z = \lambda_e$ reveals, that the electric field amplitude is reduced below 0.2 % of its value on the (conductor) surface. For $z > \lambda_e$ the penetrating field practically disappears.

To get an idea of the penetration depth magnitude, assuming a field with an alternating frequency of 10 mHz, $\mu_r = 1$ and $\kappa = 1/1000\,(\Omega \cdot \mathrm{m})^{-1}$, the penetration depth is calculated to be 159.15 km, according to (2.25) and (2.24). Because the penetration depth is in the range of at least several hundred kilometres and more, GICs require an earth conductivity model down to those depths. If only a loop, formed by the transmission line and the earth surface, is taken into account, the

induced voltage is miscalculated. The loop needs to be extended into the earth to calculate the correct driving emf. In GIC studies the height of the transmission line above the earth surface is usually neglected, because the average height is in the range of several ten meters. Compared to the penetration depth of several hundred kilometres and more into earth, the distance above ground can be neglected. A review of GIC modelling methods is presented in [BP17].

The induced emf in the conductor of the overhead transmission line and the earth have the same direction. The induced current in the earth and the associated voltage drop is distributed equally across any chosen length. The induced emf across this length exactly matches the voltage drop. Thus, no potential difference across the considered length arises. The current is driven purely by the induced emf, without any potential gradients in the earth. Due to the previously derived induced emf and explanation, GICs in power system calculations should be implemented as voltage source located in the high-voltage transmission line [BP17].

The earth conductivity can be modelled as 1D-, 2D- or 3D-models [Tho+05; Fer12; AKP15; LLK18; KL20]. In 1D-layered models, the earth conductivity varies only in z-direction (vertically down into the earth). 2D models also contain varying earth conductivity in one horizontal direction. 3D models contain varying earth conductivity in the two horizontal directions and vertically down [Hon+18]. The 1D-layered models can be used for homogeneous earth conductivity areas. The 2D models are more likely used if the earth conductivity changes abrupt in one horizontal direction, which is e. g. the case at a coastline between the land and the sea (coastal effect [Bot94; Iva+18]). 3D models usually require on-site magnetotelluric soundings[3] [Al-13] and are computationally intensive. For Austria, the comparison of a 1D-layered and a 2D earth conductivity model indicated a slightly higher accuracy of the GIC calculation with a 2D earth conductivity model, at the expense of a significantly increased modelling effort [Bai+18]. Besides the earth conductivity, the substation grounding resistance affects the GIC amplitude. Available data on substation grounding resistance in Austria indicate an overestimation of the substation grounding resistance for Austria with standard values in range of $0.2\,\Omega$ to $1\,\Omega$, recommended in [Hor+12; Kel+17; RH19]. More realistic values for substations in Austria are $0.1\,\Omega$ and below. In case of missing earth impedance models, the earth impedance can be calculated using transformer neutral point current measurements [SAR21b].

1D-layered earth conductivity models are available for Europe, e. g. from EURISGIC WP2 project [ÁPW12]. Data for 1D-layered models is commonly available in fairly good resolution, regarding the number of layers and the spanned area. The equivalent surface earth impedance from a 1D-layered earth conductivity model can be derived with recursive convolution, as presented in [MRB14]. The multi-layered earth conductivity model is reduced to a single surface layer by recursive convolution[4], using the analogy between transmission line theory and electromagnetic-

[3] Magnetotelluric soundings are used to explore the earth conductivity. The electric field is linked to the primary magnetic field via the impedance. In order to determine the earth impedance in practice, the horizontal and vertical magnetic in combination with the horizontal electric field components are measured at the earth surface. The electric field is measured via non-polarising electrodes, which are placed in the ground. The magnetic field is measured with fluxgate magnetometers [Sim05].

[4] Assuming the impulse response is being causal and also a minimum phase-shift function. A transfer function is said to be minimum-phase if the transfer function and its inverse are causal and stable. This is the case if all poles and zeroes of the transfer function are in the left half of the complex plane.

wave reflections. The electric field intensities can be expressed as an incident and reflected-wave intensity or, as field-intensity components at the surface of a discontinuity [Bro44]. A 1D-layered earth conductivity model is also used in the simulation tool 'LFC Simulator' (`https://github.com/P-Schachinger/LFC_simulator`) [SAW22].

The thin-sheet approximation, originally developed in [VW77] and based on [PRI49], holds true if, (1) the electric field within the layer is roughly constant, (2) the thickness of the surface layer must be small in comparison with the skin depth of the underlying medium, (3) the cell spacing between the thin-sheet model not exceed a third of the skin depth of the underlying medium and (4) the side length of the thin-sheet model grid may not be less than the skin depth of the underlying medium [HL93].

2.1.4 Power Grid Modelling for GIC studies

To identify transformers and other assets at risk from GICs, a model of the power system is required. But not all voltage levels and assets need to be modelled. Three important aspects, regarding GIC calculations are (1) the transformer neutral point treatment (solidly grounded, resonance grounded[5], low-resistance grounded, or isolated), (2) the distance between two grounded transformer neutrals and (3) the power grid resistances. All three aspects are related to the voltage level. In Austria the 220 kV and 380 kV transmission levels are operated solidly grounded, with one grounded transformer neutral per substation and voltage level. Typically, with increasing voltage level, the distance (length of transmission lines) between the grounded transformer neutrals increases. Thus, higher GIC amplitudes are more likely to occur in higher transmission voltage levels. The 110 kV voltage level in Austria is operated with resonance grounded transformer neutrals. Thus, the winding resistance of a Petersen coil need to be added between the transformer neutral and the substation grounding. In addition to the resonance grounded transformer neutrals, the distance between the resonance grounded transformer neutrals is shorter, as the distance between the grounded transformer neutrals in the 220 kV and 380 kV transmission levels. With decreasing voltage of the transmission level, usually the power grid resistance increases, offering an increased resistance to GICs in comparison to transmission levels with higher operating voltage. Therefore, only the solidly grounded voltage levels are considered during GIC simulations in the power grids. The main components which need to be included in the power grid model are the substation grounding resistance R_{G}, the transformer winding resistances R_{w}, and the transmission line resistance R_{L}.

The resistance of the transmission line R_{L} is divided by three, because of the three parallel conductors/phases. The shield wires are commonly neglected, based on the assumption that their resistance is always much larger than those of the transmission lines. If the measured substation grounding resistance is used instead of standard values, the resistance of the shield wires and transmission line towers are considered by the standardised grounding resistance measurements

[5] In case of a line-to-ground fault a capacitive current via the transformer neutral flow via the earth capacitance from between the line and ground. If an inductance of an appropriate value is connected in parallel with the capacitance of the system, the fault current flowing through the inductance will be in phase opposition to the capacitive current. This is known as resonant grounding.

[IEC01b; IEE15]. The effect of shield wires on GIC amplitudes is discussed in detail in [LBP20]. **Figure 2.7** depicts the aforementioned power grid components. In black e. g. the 380 kV and in grey the 220 kV voltage level. The impedance Z represents the earth impedance calculated with the plane-wave method, described in **Section 2.1.3**.

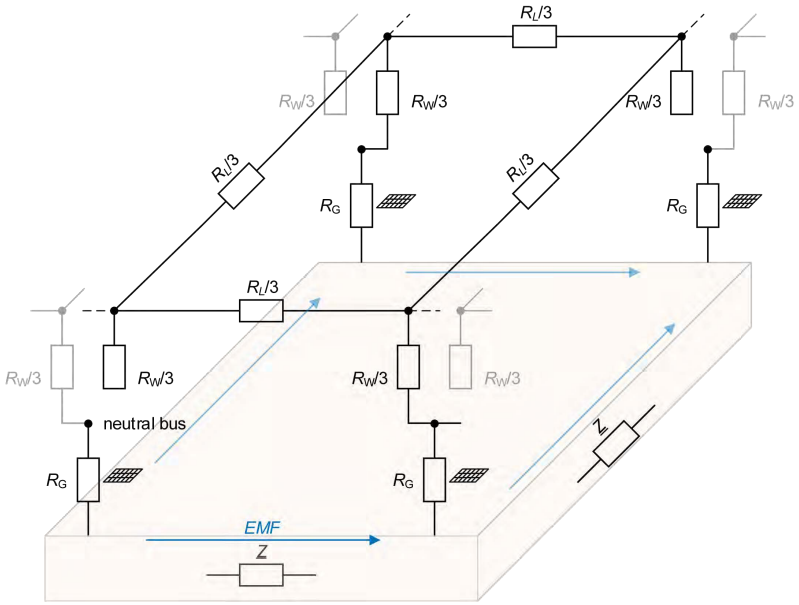

Figure 2.7: Components of the power grid for GIC studies.

For the GIC calculation the stand-alone LFC-Simulator was developed, based on MATLAB, with a graphical user interface (GUI) (**Figure 2.8**) [SAW22]. The GICs are calculated with the nodal analysis from a predefined electric field or from a measured geomagnetic field. The driving voltage sources are placed between the substation ground resistances R_0, which results in the same GICs as they were located in series to the resistances $R_L/3$ of the high-voltage transmission lines [SAW22]. The power system data can be loaded via an Excel spreadsheet. The GUI is depicted in **Figure 2.8**.

Figure 2.8: GUI of LFC-Simulator [SAW22].

For the GIC calculation, the electric field is calculated in the frequency domain by recalculating the measured magnetic field to an emf with the 1D earth impedance model. The calculated electric field in the frequency domain is transformed back into the time domain with an inverse fast Fourier transformation (IFFT). With the power grid data and the nodal voltage, the GICs in each transmission line and transformer are calculated, using the nodal analysis. The calculated GICs in the different transformer neutrals are verified with nine transformer NPC measurements, installed in the transmission grid. For a further power grid risk analysis, the transformer models and used to calculate e. g. the reactive power demand. The described process is depicted in **Figure 2.9**.

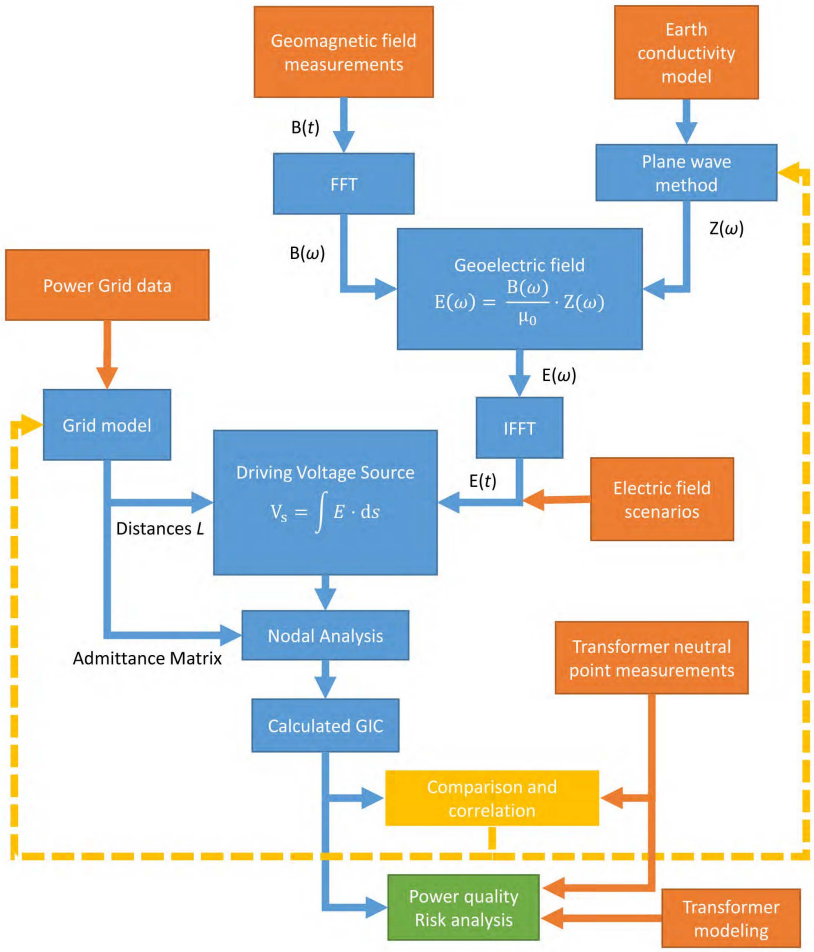

Figure 2.9: GIC calculation work flow [ASB21].

2.2 Sources of Low Frequency Currents in Transformer Neutrals

Transformer NPCs can have different origins. NPCs can be caused by space weather events, as described in **Section 2.1.1**, then the NPCs are referred to as GICs. Besides space weather effects, technical systems can cause LFCs in the electric power transmission grid, highlighted in **Section 2.2.2**. The NPC can be further analysed using a frequency analysis, to identify further sources of contribution to the overall measured NPC [Alb+20]. Thus, mitigation or counter measures can be planned (**Section 2.5.2**) to prevent the interference with the power grid and to increasing the grid reliability.

2.2.1 Space Weather

The earth magnetic field is affected by the space weather, as outlined in **Section 2.1.1**. The earth magnetic field is constantly varying, causing an induced emf, which drives currents in electrically conductive infrastructures, such as pipelines or electrical power grids. Even the day/night cycle of the earth can be measured in the power grid [Kel+21; Alb+21b]. Besides the daily cycle the solar cycle with an approximately 11-year cycle causes increased GICs, which also caused power grid

disturbances [Lun06; Bol02]. The current solar cycle 25 began in December 2019. The next solar maximum with the highest solar activity is expected for 2025 [McI+20].

2.2.2 Power Electronics and DC Infrastructure

Power Electronic Converters

Power electronic devices and converters connected to the AC grid can inject a certain DC in AC power grids [GKS05; IEE03]. The DC can appear in common mode (CM), which can have an impact on the power loss of transformers [WNM21].

Semiconductor switches are subject to a certain scattering regarding unmatched turn-on/off times, forward voltage drop (forward on resistance), gate driving signal delays, insufficient pulse-width modulation (PWM) resolution, or pulsating loads [OMe83; Xu+94; Ort+14; Rah+19; Ngn+12]. E. g. in [Xu+94] a voltage drop deviation of $\pm 70\,\mathrm{mV}$ across each thyristor of a static VAR compensator (SVC) is reported. Power converters with a high current or voltage rating are built with arrangements of multiple semiconductor switches in parallel and/or in series. The component tolerances in combination with a serial and/or parallel structure of the converts can result in a positive or negative volt-second value, which results in a DC magnetic flux component in the transformer core. As an example, consider a three-phase AC/DC converter connected to the low-voltage terminals of the transformer T3Sa (**Appendix C.1**), as depicted in **Figure 2.10**.

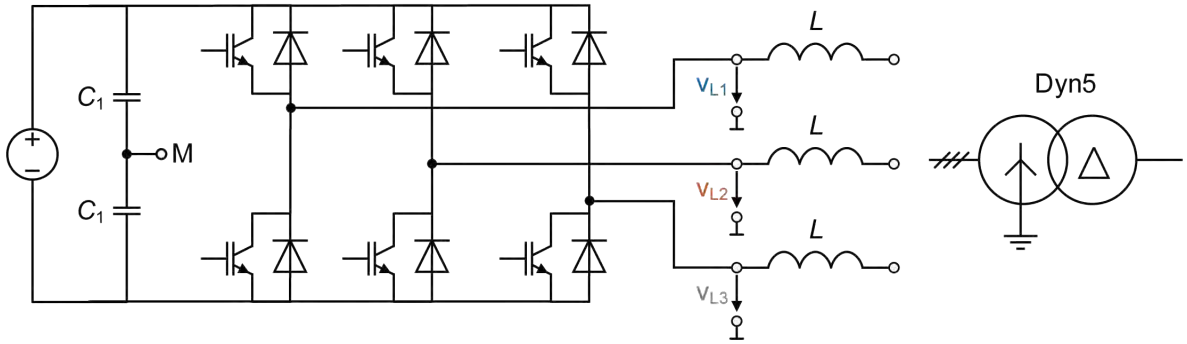

Figure 2.10: Schematic of AC/DC converter connected to the transformer T3Sa.

The converter output voltages at the terminals and the three-phase sinusoidal voltages as well as the control signal are depicted in **Figure 2.11**. For a better visualisation the control signal frequency in **Figure 2.11** is set to 1 kHz.

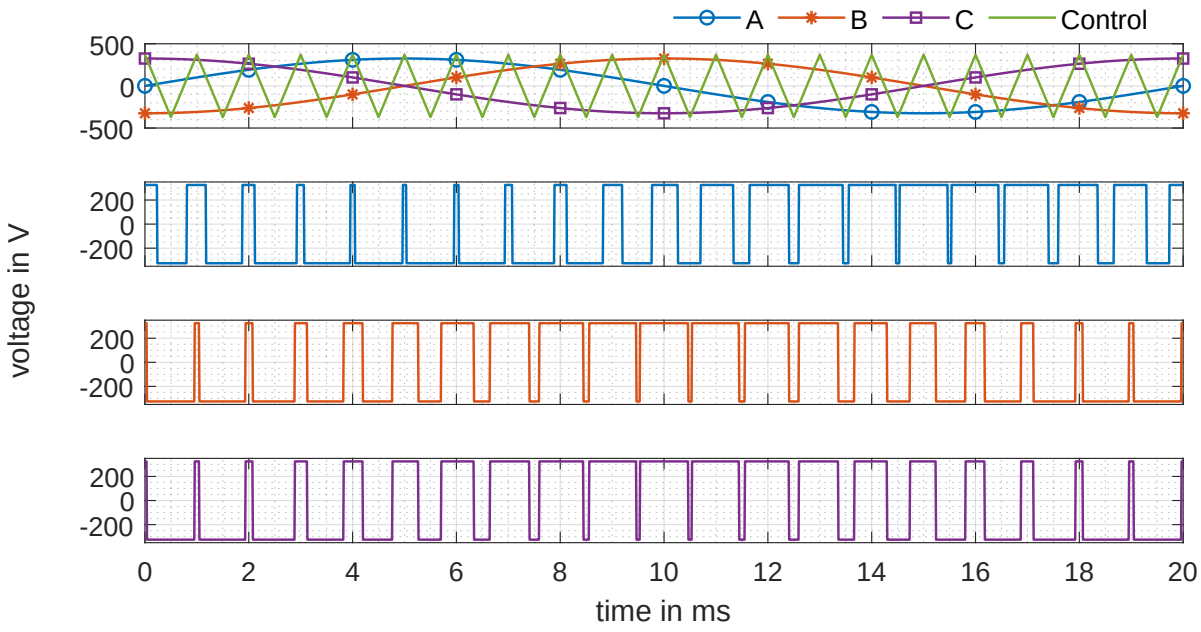

Figure 2.11: Three-phase sinus-PWM output voltage of converter.

Assuming ideal steady state conditions, the turn-on and turn-off times of the power electronic switches are equal. Thus, no DC flux offset is present in the transformer core. Assuming a relative difference between 0.02 % in the duration of the positive and negative semi-cycles at a switching frequency of 20 kHz, a switching time error of 5 ns arises. The equivalent DC voltage component can be derived from (2.26).

$$V_{\mathrm{DC}} = 0.02\,\% \cdot |V_{\mathrm{max}}|, \tag{2.26}$$

where $|V_{\mathrm{max}}|$ is the peak of the AC voltage. The corresponding DC flux density offset per limb is calculated as follows:

$$B_{\mathrm{dc}} = \frac{V_{\mathrm{DC}}}{R_{\mathrm{p}}} \cdot \frac{N_{\mathrm{p}}}{l_{\mathrm{m}}} \cdot \mu_0 \bar{\mu}_{\mathrm{r}}, \tag{2.27}$$

where V_{DC} is the DC voltage in the primary circuit, R_{p} the average winding resistance of a low-voltage winding, N the number of turns per winding, μ_0 the vacuum permeability, $\bar{\mu}_{\mathrm{r}}$ the relative mean permeability in the linear region of the transformer core material and l_{m} the mean magnetic path length of the transformer core. With $V_{\mathrm{DC}} = 32.5\,\mathrm{mV}$, $N = 102$, $l = 1.91\,\mathrm{m}$, $\bar{\mu}_{\mathrm{r}} = 15,000$ (assumption based on **Appendix C.1 Figure C.2**) and $R_{\mathrm{p}} = 81.32\,\mathrm{m\Omega}$, the DC flux density offset is 0.37 T. For the transformer T3Sa this flux offset of 0.37 T corresponds to 21.2 % of the minimum saturation inductance (1.746 T **Appendix C.1**). This flux offset corresponds to an AC root mean square (rms) voltage increase of 56.51 V for the transformer T3Sa, which corresponds to 17.38 % of the nominal peak voltage per phase.

A maximum allowed DC value can be calculated using the $B-H$ characteristic of the core material, assuming a constant μ_{r}, and defining the minimum saturation flux density B_{S}, the corresponding magnetic field strength H_{S}, the coercive force H_0, the remanent magnetisation B_{R}, and the nominal operation point B_1, H_1.

$$I_{\mathrm{DC}} < \frac{\Delta H}{l \cdot N}, \tag{2.28}$$

where $\Delta H = H_{\mathrm{S}} - H_0$, l is the mean magnetic path and N the number of turns per winding penetrated by the DC. Appling (2.28) to the aforementioned setup with the AC/DC converter and the transformer T3Sa, with $H(B_{\mathrm{S}} = 1.746\,\mathrm{T}) \equiv 300\,\mathrm{A/m}$ and $H_1(B_1 = 1.5\,\mathrm{T}) \equiv 40\,\mathrm{A/m}$ the maximum allowed DC is 1.33 A (1.84 % of the rated current) without causing transformer saturation. Taking into account the mean winding resistance of the transformer T3Sa of 88.31 mΩ, these currents correspond to a DC voltage of 117 mV per phase.

HVDC and HVAC Systems

In order to increase the transmission capacity of bulk power systems, it is planned to convert existing high-voltage alternating current (HVAC) overhead lines into high-voltage direct current (HVDC) lines. If one HVAC system on a multi-system tower is converted to a HVDC system, this is referred to as hybrid HVAC/DC transmission. This will result in an ionic coupling of the different systems installed on one transmission line tower. DC ion currents in the adjacent AC system can cause transformer saturation. On the other side, a current ripple is caused by an induced AC voltage in the DC system, causing also transformer saturation, which affects the system performance [LWB89; UYM98; Ngn+12]. Depending on weather conditions, conductor surface and distance between the different systems, DC ion currents in the range 15 mA/km [PHF18] can be caused in parallel hybrid HVDC/AC systems. In a field test 2012 one out of four 420 kV AC systems, along a distance of 2.4 km, were supplied with DC in bipolar, monopolar and hybrid configuration. The maximum ion current amplitude of 10 mA/km were measured in one conductor [Rus+13]. Besides the ionic coupling of HVDC and HVAC systems, the monopole operation of HVDC systems could increase the DC stray currents in AC systems [DDY05]. Moreover, asymmetries between the phases can cause asymmetric currents, which are usually below 1-2 % of the rated current [Fuc+14], which also contribute to transformer saturation.

DC Leakage Currents by Public Transportation Systems

Leakage currents of public transportation systems in transformer neutral point current measurements were first described by [Hal19]. Comparing the operating hours of the Vienna subway system and analysing the frequency spectrum of several transformer neutral point current measurement in Austria, revealed that during the operating hours of the Vienna subway system the leakage currents contribute roughly 0.2 A to the measured transformer neutral point current [Alb+21b]. Further

analysis of transformer NPC measurements during the COVID-19 pandemic further support the aforementioned influence of the Vienna subway system [SAR21a; Sch+22].

2.2.3 Physical Phenomena

Electrochemical/Galvanic Effect

As a possible cause of long-term fluctuations or continuous offsets in the transformer neutral point current, electrochemical/galvanic effects in the earth should be investigated. Different metallic materials have different electric potentials (galvanic series [Lid96]). The different occupied electron levels of two metals attached to each other cause a diffusion of electrons from the metal with the lowest work function to the other metal. During the diffusion, a voltage between the two metals arises, which causes electrons to move in the opposite direction. If this voltage is equal to the Fermi energy difference between the metals, the electron transition stops. Another voltage difference can be caused by the thermoelectric effect [Mes15]. Depending on the geological structure and the power grid configuration (grounded transformer neutrals and transmission line corridors), the galvanic and thermoelectric effect could drive a current via the transmission grid. This is part of ongoing research and need to be further analysed. In order to (optically) measure small voltage deviations over a long time, the Lippmann electrometer could be used, which also serves as a null measurement instrument [Mes15].

Photovoltaic Effect

A daily offset in all transformer neutral point current measurements were recognised [Hal19]. Therefore, the electric potential between the substations changed in a daily cycle. One hypothesis, causing the daily fluctuations, is the photoelectric effect. The photoelectric effect describes the mechanism of electron emission during the impingement of energetic photons on matter [Mes15]. To prove this hypothesis measurements during low (cloudy/night) and high (sunny/day) global solar radiation (GSR) from the measurement station "Wien Hohe Warte" [ZAM19] were taken into account. No correlation between the GSR and the transformer neutral point current could be detected during the observation interval of three months in 2017 [Hal19] and 2018 [Alb+20].

Lithospheric Sources

The earth lithosphere is the outermost shell of the earth. The lithosphere is composed out of the crust and part of the upper mantle up to depth of about 80 km - 100 km [Cla16]. During earthquakes, anomalous electromagnetic signals are detected [Zha+21]. The mechanism causing the anomalous electromagnetic signals is not fully understood, but different physical mechanisms are used to model the anomalous signals [SPS18; Zha+21]. The measured electric fields during earthquakes reached amplitudes in the region of 15 mV/km (Qingchuan earthquake $\mathrm{M_w} = 6.1$)

[Zha+21]. Therefore, the effect of electric dipoles, formed in the lithosphere before an earthquake, and their effects on power system infrastructure close to the epicentre was evaluated in [VGK20].

Nuclear Electromagnetic Pulse

NEMP can be caused by nuclear explosions at altitudes of 30 km above ground, they are referred to as electromagnetic impulse (EMP) and/or high-altitude electromagnetic impulse (HEMP) [IEC21]. The impulse duration ranges from sub-nanoseconds to several hundred seconds. They can cause electric fields up to several tens of V/km [VU88; Gil+10; Hor+19]. Nuclear burst at high-altitude (30 km above ground) produce three types of electromagnetic pulses, which can be observed on the earth's surface:

(1) E1 early-time HEMP (fast),
(2) E2 intermediate-time HEMP (medium),
(3) E3 late-time HEMP (slow),

whereas the E2 and E3 class HEMPs are important regarding the power gird susceptibility, due to their period range of 1 ns - 1 s (E2) and above 1 s (E3) [PS18]. E3 HEMPs is often compared to GMDs, but the duration of E3 EMPs is much shorter than server GMDs, which can last several days [Hor17; Hor+19].

The EMP is caused by the motion of ionised particles and atmosphere relative to the geomagnetic field of the earth. The electromagnetic field is caused by two different physical mechanisms. During the first 10 s time period is referred to as 'Blast Wave', which is caused by the compression of the geomagnetic field by the expansion of the burst. The debris are accelerated along the magnetic field lines heating and ionising the atmosphere, causing an expansion and rise in altitude of the heated conductive atmosphere. The conductive and rising atmosphere crosses the compressed magnetic field, causing a current induction which is accompanied by a magnetic field. This process is also referred to as 'Heave' in the time range of 10 s - 300 s after the detonation [GD77; Gil+10]. Further information on the nature and coupling of HEMPs and power grids can be found in [LAT85].

In an example for a 500 kV transmission line in North America a peak electric field of 40 V/km would result in a peak GIC of 1,630 A, approximated as a uniform pulse with a pulse width and rise time of 20 ms [IEC21]. Another example in [LAT85], with a 170 km long three-phase 161 kV overhead transmission line, reveals a current amplitude in the transformer neutral of 286.5 A, caused by a time varying electric field with an amplitude of 20 V/km. In [Hor+19] a blackout of several regions due to a E3 HEMP, is expected to be possible, but widespread transformer outages due to half-cycle saturation and the associate hotspot heating is not expected. But it may be prudent to evaluate the number of transformer spare (parts) to ensure a replacement in case of damage in an adequate time [Hor+19]. Further studies on effects of a HEMP on the power transmission grid can be found e. g. in [Rab87; Min+17; Mat+21a; Ove+22]. Further information on HEMP and their comparison to lightning can be found in [Nan+88; UMK82; Rus87; LC89].

Devices mitigating induced currents in power grids due to EMP E3 pulses are commercially available [emp22]. Other mitigation techniques are comparable to those during GMDs [Hor+19].

2.3 Measurement of Geomagnetically Induced Currents

GIC measurements are an important tool to validate GIC calculations, whereas GIC calculations usually do not take into account other LFC sources (**Section 2.2**). Therefore, GIC or LFC measurements should be used to validate GIC models for the power grid vulnerability to GICs and to determine the level of other LFC sources. This information can also be used for the tendering of new power transformers to specify certain DC levels in the transformer neutrals. This information can affect the design process of a transformer, in order to guarantee e. g. a certain maximum transformer sound level during a specified DC bias.

Also, indirect methods measuring the electric or magnetic field [But+17; LGK18] or using phasor measurement unit (PMU) data [Kaz+15; Nar16] are proposed in literature to measure GICs.

Section 2.3.1 discusses design aspects of transformer NPC measurement systems. Besides NPC measurements, which give the sum of the DC/LFC in all three phases without any information about the distribution across the three phases, DC/LFC measurement on the phase could give information about the distribution, which is usually assumed to be symmetrical. The challenge is the measurement of comparable small DC/LFC to the nominal phase AC. A promising sensor is the optical current transformer, discussed in **Section 2.3.2**.

Besides technical challenges, cybersecurity issues need to be addressed, before the integration of a NPC measurement systems in the power grid's supervisory control and data acquisition (SCADA) system. Therefore, often a Global System for Mobile Communication (GSM) based communication between the measurement system and operator of the measurement system is used, which makes integration of the measurement system into the company's own SCADA system obsolete.

2.3.1 Low Frequency Transformer Neutral Point Current Measurements

GIC/LFC measurements in power transformer neutrals are carried out at different latitudes around the world [Pir89; Tho+05; Cho+15; Bar+15; But+17; Bai+18; Alb+19; Div+20; Rod+20; VCK20; EUR21; Alb+21b; Hug+22]. The current probe of the measurement system is located between the transformer neutral point and the substation grounding. As current probe, a magnetic ring core with a Hall effect sensor or only Hall effect sensors are used [Rad+19; Alb+21b]. For the further signal processing, two options are available:

(1) analogue filtering and sampling with a comparable low frequency,
(2) sampling with a high frequency and digital filtering.

Using (1), the measurement signal is filtered with a low-pass filter with 3 dB cut-off frequency up to several Hertz [Dyn18; Hal19]. The low-pass filter is used, e. g. to suppress the 50 Hz signal from the power system or 16.7 Hz signal from railway systems. A sampling frequency of 5 Hz and below

is accepted in order to capture GIC events in power grids [Cli+20]. The comparatively low sampling rate allows using a low-cost analog digital converter (ADC) and secondary processing electronic, which reduces the overall costs of the measurement system.

In addition to the filtering, the installed CT is required to withstand short-circuit currents and to compensate/prevent remanence flux, caused by short-circuit currents. Besides the over-current capability, the CT and measurement system offset drift, related to the temperature, should be in the range of ppm/month. Also, the linearity error of the measurement system should be in the range of parts per million (ppm).

In order to measure the correct amplitude of the GIC, the measurement system should have a low offset in the range of several milliamps. Especially Hall sensor based current transducers could suffer from a comparable high offset and a temperature related offset drift. Therefore, a periodic offset control/zeroing should be considered, when using current transducers with Hall sensors for GIC measurements.

Employing option (2), higher computational power can be required for the digital signal processing, which increases the overall costs of the measurement system. Using digital filtering instead of analogue filtering, mitigates the effects of tolerance fluctuations of the analogue filter components and allows adopting the sample rate during operation of the measurement system.

Up to the date of writing, no commercially available transformer NPC measurement system exists [WNE21]. Only CTs with a built-in filter but without data logging or data processing unit are commercially available [Dyn18].

2.3.2 Optical Current Transformer

Another option to measure GICs/LFCs is the measurement of the phase GIC/LFC. This is not possible with existing CTs without any modifications. In [RDS13] a conventional CT is converted to a fluxgate CT, which is successfully used to measure DC in transformer neutrals (**Section 2.3.1**). This conversion was tested on a 500 A/5 A 5 VA CT with an accuracy of 10 % for DC and 1.5 % for AC, whereas it is not stated for which AC and DC range these accuracies apply. The weak points of the proposed approach are the possibly reduced accuracy of the CT for 50 Hz current sensing, the dependency of the DC sensing accuracy on the power grid impedance, which can change over time, and the injection of AC into the primary current circuit [RDS13].

Besides conventional current sensing, optical current transformers can be used to measure a DC. Commercial optical current transformers are available from different manufacturers [ABB11; Art16; GE 16; Tre21] and are already used in a test facility [Sme+20] and power grids [Cha18; Hei+20]. The optical current transformer uses the Faraday effect to measure the current. The Faraday effects describes the rotation of polarised light while passing through a magneto-optical medium, which is penetrated by a magnetic field. Research has been carried out on the accuracy of the overall measurement system, which is sensitive to vibration and temperature [WB02; MB02; Boh+05; Len+20; Mad+19]. The advantages of optical current transformers are the reduced weight and

size and the extended frequency operation range [Cha18]. Nevertheless, very little information about the DC accuracy for DC below 1 A are available. Therefore, a dedicated research project was established with the goal to develop an optical current transformer with high accuracy for small DCs [Man+21]. An overview of the technique of optical current transformers can be found in [Sim01; Sil+12; Ria18].

2.4 Power Transformer Modelling for Low Frequency Transients

Transformer topology models usually do not require as much computational power as finite element methods and can accurately reproduce the transformer terminal characteristics.

For modelling the transformer behaviour under deep saturation, the transformer behaviour is dominated by the transformer core properties. Therefore, only phenomena well below the first resonance frequency (usually below 1 kHz) of the transformer are considered. With this restriction some simplifications can be made, e. g. neglecting the transformer winding capacitance, as done in [Cha+03; Mor+07]. For the modelling of low frequency transients in power transformers, the core remanence needs to be considered. Neglecting the transformer core hysteresis effects causes e. g. an underestimation of the remanence flux after a disconnecting event of the transformer from the power grid [Cha+03] or in case of a fault in the power grid.

This work focuses on transformer grey box models, as the transformer models should be derived based on the physical design of the transformer and measured data. The challenge during the modelling process is the implementation of the transformer core's hysteresis characteristics, if the core material is unknown and only supplement measurements via the transformer terminals are possible. In literature, different terminal measurements [DW81; FY02] are proposed to measure the transformer core hysteresis characteristics. But very little information about the model accuracy is available. An overview of available transformer models for low- and mid-frequency studies can be found in [MM05]. Another important aspect is the transformer model validation with laboratory and/or field measurements. Especially, the transformer model validation during saturation requires a sufficiently large short-circuit capacity of the power source and a suitable test setup. The B2B test setup with superimposed DC between the high-voltage neutral points is commonly employed during transformer GIC studies. The B2B test requires two transformers with at least similar core characteristics. The advantage of the B2B tests is that superposition of DC on ground potential. The superimposed DC saturates the transformer core and causes half-cycle saturation. So far, very few large scale B2B tests have been reported in literature [LE02; RA14; Zir+18a].

2.4.1 Grey-Box Transformer Models

Power transformer models for low frequency transients are e. g. used to analyse dielectric failures and study the electrical behaviour under GIC/DC bias. For this purpose, white and black box transformer models were used. *White box* models are based on the physical structure of the transformers and do not depend on measurement data. The white box model parameters are derived with physical laws. *Black box* models, in contrast, are a mathematical representation of the transformers, which

matches the input and output data of the actual transformers. The black box model parameters may have no physical meaning. The model structure is based on a well-known set of models. *Grey box* models are bridging the gap between white and black box models, using the physical structure of the transformer in combination with measurement data (e. g. terminal voltage and current waveforms during no-load and high-voltage winding capacitance) for the parametrisation of the model parameters [Cig14; HR21].

Transformer grey box models are topology models derived from limited design data and measurements. The grey box models take into account the transformer mechanical and electrical design. The models can be fitted to measurement data. The unknown design parameters act as variables during the fitting process. The parameter fitting is done based on empirical knowledge or with optimisation logarithms. Due to the phase-to-phase magnetic coupling, the topology models can reproduce the operation conditions in the yoke and limbs over a wide operation range. Especially for the investigation during transformer core saturation, grey box models offer the advantage to model the different magnetic flux paths with different levels of detail. At the same time, the parametrisation of the model is based on open circuit and short circuit test data [Zir+17]. Different models neglecting [FYR99; FY02] and including the transformer core hysteresis characteristics have been proposed.

Inductance - Reluctance Analogy

In topology models, each section of the core and each flux path can be represented separately. This allows reproducing different flux density levels in the limbs and yokes [Lur08], as it arise when the core approaches saturation. Also, the different off-core (leakage) flux paths can be included in the models [LHC16]. To derive a topology model, the inductance-reluctance analogy, also known as principle of duality between electric and magnetic circuits [Che49], can be used. According to the principle of duality, this requires that:

(1) to each element in the electric network, a counterpart in the magnetic network exists and vice versa;
(2) the current through an element in one network is proportional to the voltage across the counterpart in the other network.

These requirements lead to the analogies given in **Table 2.1**. The inductance-reluctance analogy is limited to planar networks. A counterexample is a transformer possessing four windings per limb with leakage coupling or a transformer core which has a 90° angle between the yoke of the outer two limbs and the middle limb (**Figure 2.12**) [Ham93].

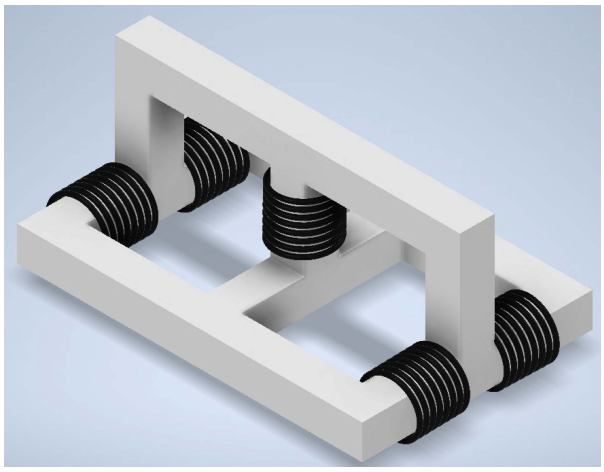

Figure 2.12: Example of non-planar magnetic circuit.

In that case of the aforementioned examples, no physical feasible electric circuit exists, except by the use of five special artifices, summarised and applied in different examples in [Blo46]. For the further course of this work, the transformers under investigation can be considered as planar networks.

Another limitation of the inductance-reluctance analogy is the requirement of equal number of turns for the different windings. This requirement is inconvenient for the modelling of power transformers, but it can be overcome with the implementation, of ideal transformers instead of current sources, whereas the ideal transformer a treated as part of an external load [Che49]. For the practical implementation it is convenient to use two ideal transformers, one with a turn ratio of 1:1 and one with the turn ratio $N_{\mathrm{LV}} : N_{\mathrm{HV}}$. The usage of the two ideal transformers allows using directly the characteristic transformer parameters, such as the zero-sequence impedance from the measurements during the factory acceptance test, without referring these values to the low- or high voltage side with the transmission ratio.

Table 2.1: Analogies between electric and magnetic circuits.

Magnetic Circuit			**Electric Circuit**		
mmf	$\mathcal{F} = \int H \cdot \mathrm{d}l$	A	Voltage	$V = \int E \cdot \mathrm{d}l$	V
Flux rate	$\dot{\Phi}$	V	Current	i	A
Reluctance	$\mathcal{R}$	H^{-1}	Inductance	L	H
Permeance	$\mathcal{P} = 1/\mathcal{R}$	H	Capacitance	C	F
Flux	$\Phi = \int \dot{\Phi} \mathrm{d}t$	Wb	Charge	$q = \int i \mathrm{d}t$	C
Permeability	$\mu = \mu_0 \mu_\mathrm{r}$	H/m	Permittivity	$e = e_0 e_\mathrm{r}$	F/m
Power	$P = F\dot{\Phi}$	W	Power	$P = vi$	W
Energy	$E = \int F \mathrm{d}\Phi$	J	Energy	$E = \int v \mathrm{d}q$	J

The electric equivalent circuit of a transformer with the inductance-reluctance analogy is derived in three steps:

(1) sketch physical design of transformer (**Figure 2.13**),

(2) mark magnetic flux paths, which should be considered in the model (**Figure 2.13**),
(3) sketch magnetic circuit with elements according to **Table 2.1** (**Figure 2.14a**),
(4) place a dot in every closed loop/circuit and mark one reference point outside the circuit, (**Figure 2.14a**)
(5) connect neighbouring dots with line through the circuit elements, whereas these lines crossing the magnetic elements represent the branches of the electric circuit with their equivalent electric component according to **Table 2.1** (**Figure 2.14a**), and
(6) derive electric circuit based on (5), whereas nodes/loops of the magnetic circuit transformed into loops/nodes in the electric circuit (**Figure 2.14b**).

To demonstrate the usage of the principle of duality, according to [Che49], the analogy is applied to one wounded limb of a three-limb three-winding transformer core to derive the equivalent circuit of the first wounded limb step by step in **Figure 2.13** to **Figure 2.14**. The full models of a three-limb and five-limb three-winding three-phase transformer are presented in **Figure 2.15** and **Figure 2.16**.

Figure 2.13 depicts a three-limb three-winding transformer core and its different magnetic flux paths on the example of the first limb. R_{Limb} and R_{Yoke} represent the magnetic reluctance of the limb and yoke, respectively. R_0 is the off-core magnetic flux between the two yoke sections, which is represented by a single flux path, but the off-core flux actually distributed along the length of the yoke [ZMA21]. R_{01} is the reluctance of the flux path between the limb and the innermost winding. R_{12} is the reluctance of the path between the innermost and second innermost winding. R_{23} is the reluctance path between the middle winding and the outer winding.

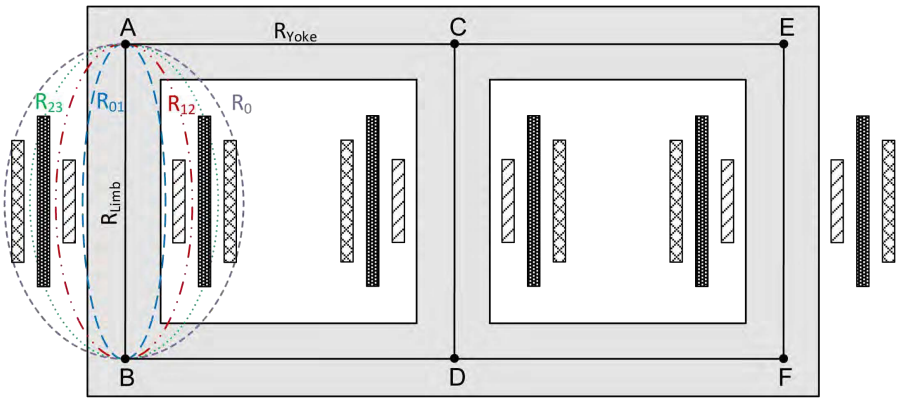

Figure 2.13: Step 1 and 2: for a three-limb three-winding transformer core and different flux paths.

The equivalent magnetic circuit of the first limb is depicted in **Figure 2.14a**. The three windings cause a flux inside the transformer limb, therefore all magnetomotive force (mmf) sources (Φ_{LV}, Φ_{MV}, Φ_{HV}) are in series. The hysteretical transformer limb is represented by the reluctance R_{Limb}, whereas R_{01} is shunting R_{Limb}. The reluctance of the stray path between the inner and middle and between the middle and outer winding is represented by the reluctance R_{12} and R_{23}, respectively. R_0 shunts R_{01}, R_{12} and R_{23}. By reconfiguring the loops from **Figure 2.14a** into nodes and substituting the magnetic elements into their electric equivalent **Figure 2.14b** is derived.

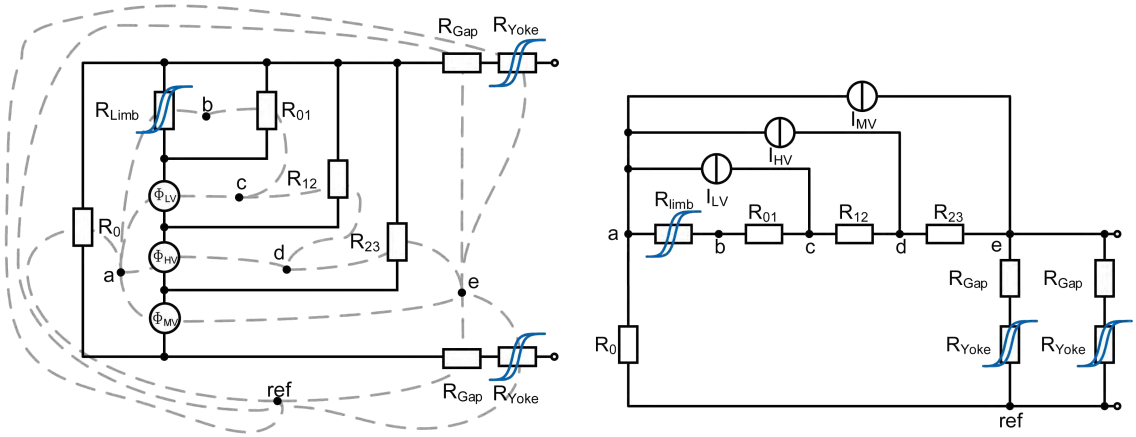

(a) Step 3 and 4: magnetic circuit of first transformer limb with 3 windings.

(b) Step 5 and 6: equivalent circuit of first transformer limb with 3 windings after transformation.

Figure 2.14: Magnetic and electric equivalent circuits applying the inductance-reluctance analogy.

Repeating the aforementioned steps for all limbs of the three-limb transformer, replacing the current sources by ideal transformers and combining the parallel R_{Gap} and R_{Yoke} elements into one element for each part, **Figure 2.15** is derived. The vector group is realised by the electric connection of the ideal transformer terminals.

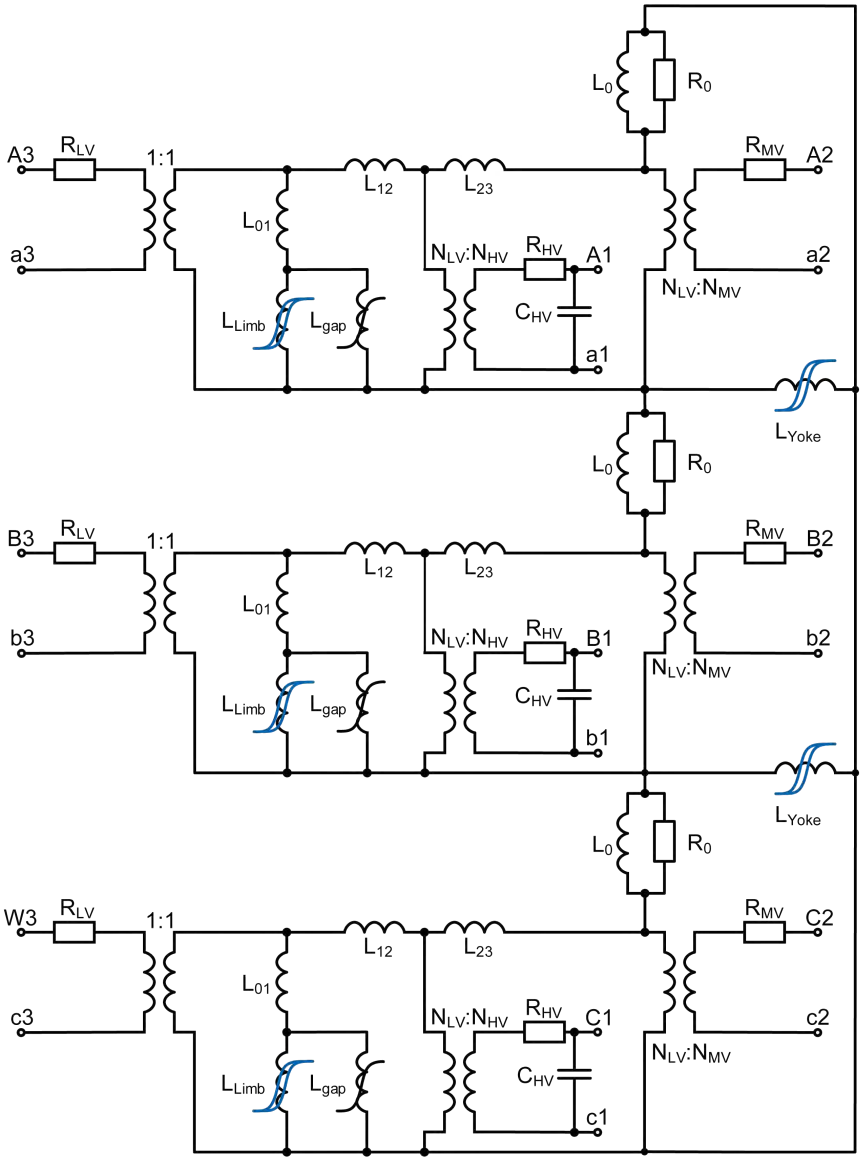

Figure 2.15: three-phase three-winding three-limb transformer grey box topology model.

The topology model of a five-limb three-winding transformer is depicted in **Figure 2.16**. In contrast to the three-limb transformer model, the two unwounded return limbs need to be included considered the model. These unwounded return limbs offer a low reluctance flux path to zero-sequence currents and are therefore in series with the zero-sequence impedance.

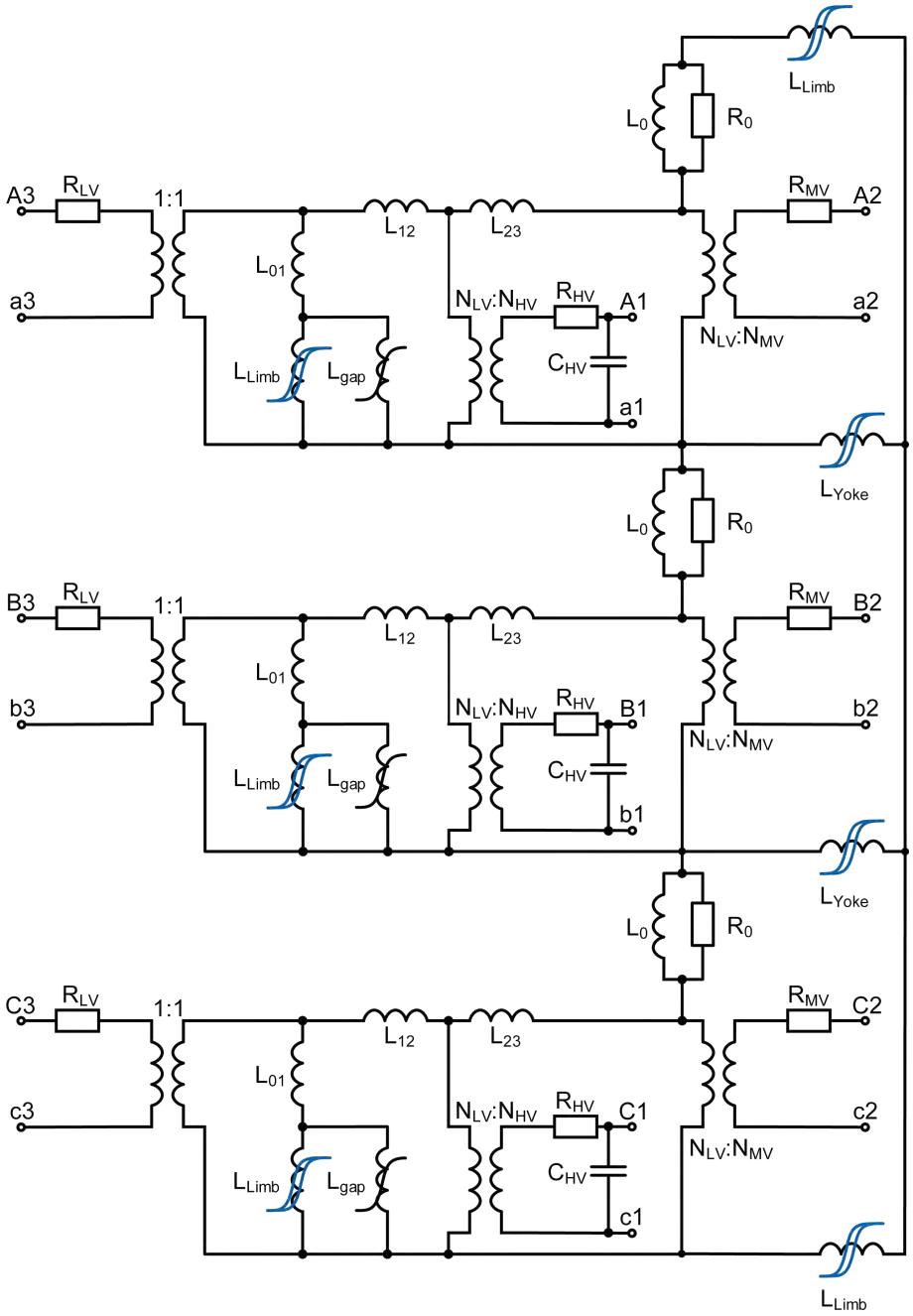

Figure 2.16: three-phase three-winding five-limb transformer grey box topology model.

The blue hysteresis sign in **Figure 2.15** and **Figure 2.16** indicates that this circuit components contains eddy current, hysteresis and excess losses. Detailed information about the underlying structure of this element can be found in **Section 2.4.4** and **Chapter B**.

Capacitance - Permeance Analogy

The capacitance-permeance analogy, also names gyrator-capacitor approach in literature [Ham94; You+16; SZK21; Sze+21] is based on [Bun68; Bun69] and was further applied in [Ham93; Ham94].

The capacitance-permeance analogy links the magnetic and electric domain with a gyrator. The gyrator fulfils the function of an ideal transformer in the inductance-reluctance analogy (see section before). In quasi-static conditions, the magnetic reluctance is represented by a capacitor in an electric circuit, using the modelling technique described in [Ham93].

The gyrator is, physically speaking, a coil on a magnetic core. The gyrator represents the coupling of an electric and magnetic circuit using only electrical elements. With the gyrator, an equivalent electric circuit of a coupled electric and magnetic circuit is derived.

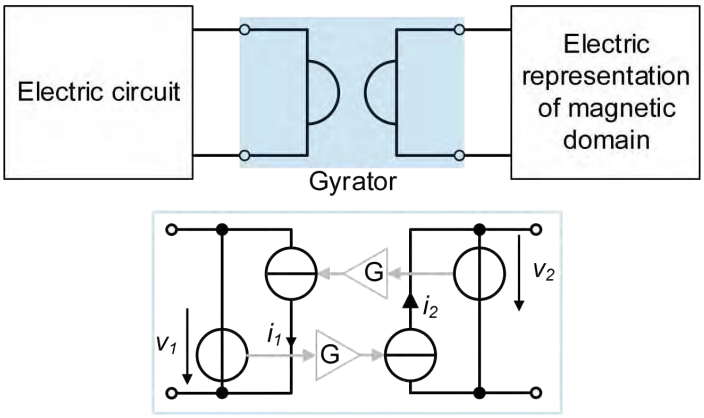

Figure 2.17: Gyrator interfacing an electric circuit and an electric representation of a magnetic circuit.

The gyrator principle, depicted in **Figure 2.17**, uses two voltage controlled current sources, governed by the following equations:

$$v_1 = R_\mathrm{G} \cdot i_2, \tag{2.29a}$$

$$i_2 = \frac{1}{R_\mathrm{G}} \cdot v_1, \tag{2.29b}$$

$$v_2 = R_\mathrm{G} \cdot i_1, \tag{2.30a}$$

$$i_1 = \frac{1}{R_\mathrm{G}} \cdot v_2, \tag{2.30b}$$

whereas the voltage v_1 on the primary (index 1) terminal controls the current i_2 on the secondary (index 2) terminal and the voltage from the secondary terminal v_2 controls the current on the primary current i_1. The currents and voltage are linked via the resistance $R_\mathrm{G} \equiv N$, which corresponds to the number of turns N of the coil coupling the electric and magnetic circuit.

According to **Table 2.2** the electric voltage v is equivalent to the magneto motive force (mmf) $\mathcal{F}$ and the electric current is equivalent to the magnetic flux Φ or the magnetic flux rate $\dot{\phi}$, depending on whether the gyrator is implemented in *integral* or *differential* representation, respectively.

Table 2.2: Capacitance-permeance analogy between electric and magnetic circuits.

Magnetic Circuit			**Electric Circuit**		
magneto motive force	$\mathcal{F}$	A	Voltage/emf	v	V
Flux rate	$\dot{\Phi}$	V	Current	i	A
Reluctance	$\mathcal{R}$	1/H	Resistance	R	Ω
Permeance	$\mathcal{P} = 1/\mathcal{R}$	H	Capacitance	C	F
Flux	$\Phi = \int \dot{\Phi} \mathrm{d}t$	Wb	Charge	$q = \int i \mathrm{d}t$	C
Power	$P = F\dot{\Phi}$	W	Power	$P = vi$	W

For the further analysis the *differential* representation of the gyrator is used, because it mitigates to numerically evaluate integrals, which yields a better convergence behaviour in the calculations than the integral representation of the gyrator. By using the differential representation, the integration of the voltage for each time step becomes obsolete. Besides the improved convergence behaviour with the differential representation of the gyrator, losses in the equivalent circuit also have the unit Watt ($\dot{\Phi} \cdot \mathcal{F} = P$, with $[P] = \mathrm{W}$), as in electric circuits.

Using Faraday's law, the relationship between the electric and magnetic domain are expressed, enabling the usage of the gyrator to couple electric and magnetic circuits.

$$\int_{\partial A} \vec{E}(\vec{r}, t) \cdot \mathrm{d}\vec{s} = \int_{A} \frac{\partial \vec{B}(\vec{r}, t)}{\partial t} \cdot \mathrm{d}\vec{A}. \tag{2.31}$$

This leads to (2.32) assuming a homogeneous field

$$v = -\frac{\mathrm{d}}{\mathrm{d}t}\Phi = -\dot{\Phi}. \tag{2.32}$$

Including the number of turns N of a coil, (2.32) becomes $v = -N\dot{\Phi}$. Recall (2.29), the following analogies ($\rightleftharpoons$) apply:

$$i_2 = \frac{1}{R_\mathrm{G}} \cdot v_1 \rightleftharpoons \dot{\Phi} = \frac{1}{R_\mathrm{G}} v, \tag{2.33}$$

$$i_1 = \frac{1}{R_\mathrm{G}} \cdot v_2 \rightleftharpoons i_1 = \frac{1}{R_\mathrm{G}} \mathcal{F}. \tag{2.34}$$

Taking a closer look at the magnetic domain and the linkage of the magnetic flux rate $\dot{\Phi}_\mathrm{c}$ and the mmf $\mathcal{F}_\mathrm{c}$. Recalling the relation between the current i_c and the voltage v_c across a capacity C:

$$i_{\mathrm{c}} = C \cdot \frac{\mathrm{d}v_{\mathrm{c}}}{\mathrm{d}t} = C \cdot \dot{v}_{\mathrm{c}}. \tag{2.35}$$

Replacing i_{c} and v_{c} in (2.35) with their derived analogies, according to **Table 2.2**, (2.35) yields:

$$\dot{\Phi}_{\mathrm{c}} = C \cdot \frac{\mathrm{d}\mathcal{F}_{\mathrm{c}}}{\mathrm{d}t}. \tag{2.36}$$

Integrating (2.36) and solving for the mmf $\mathcal{F}_{\mathrm{c}}$ yields:

$$\mathcal{F}_{\mathrm{c}} = \frac{1}{C} \cdot \Phi_{\mathrm{c}}. \tag{2.37}$$

(2.37) imply the magnetic reluctance $\mathcal{R}$ can be represented as $1/C$ in its equivalent electric circuit. Thus, C can be interpreted as permeance $\mathcal{P}$ which is equal to $1/\mathcal{R}$. Therefore, the used analogy is also called *reluctance-permeance analogy* or '*ReCap*' [Eat94].

For the modelling of losses in the electric equivalent circuit, the relationship between the mmf $\mathcal{F}$ and the magnetic flux Φ is given by Hopkinson's law, analogue to Ohm's law:

$$\mathcal{F} = R_{\mathrm{m}} \cdot \Phi, \tag{2.38}$$

where R_{m} is the magnetic reluctance with the unit 1/H.

Considering the ohmic loss representation in the equivalent circuit using the reluctance-permeance analogy, they can be expressed as follows [AHS12]:

$$P_{\mathrm{loss}} = \dot{\Phi}^2 \cdot R_{\mathrm{m}}. \tag{2.39}$$

In order to derive the transformer model parameters, such as the different leakage paths, depicted in **Figure 2.18** and **Figure 2.19** the following conversion applies:

$$C = \frac{L}{N^2}, \tag{2.40}$$

where L is the inductance of the specific path in Henry and N is the number of turns of the inductor of the corresponding element/path. The inductance of the stray flux paths are converted to Farad with $N = 1$ according to [Ham94].

The following analogies in words are derived by using the differential gyrator formulations.

The capacitance-permeance analogy offers the following advantages [AHS12; You+16], regarding power transformer modelling:

Table 2.3: Electric and magnetic analogies derived with the differential gyrator equations.

Electric Circuit	**Magnetic Circuit**
resistance	dissipative losses
capacitance	permeance
current	magnetic flux rate
voltage	magnetic voltage

(1) to model dissipating losses electrical resistance are used, which is intuitive,
(2) magnetic fields store energy, this means the magnetic path elements of the circuit should be able to do so, which is true for capacitors. Therefore, the energy relationship is preserved/energy invariant,
(3) the circuit model topology is similar to the physical magnetic component.

The capacitance-permeance analogy was successfully applied in electrical (power) engineering to electromagnetic coupled devices, such as power electronic converters [Eat94; Che+09], a Fluxgate magnetometer [Eat94], a ferroresonant regulator [Eat94], a continuously variable series reactor [You+16; HD21] and power transformers [Alb+21a; Alb+22a].

The ReCap models of a three-limb and five-limb three-winding transformer are depicted in **Figure 2.18** and **Figure 2.19**, respectively. The gyrators on each wounded limb represent the mmf source of each winding (primary (1), secondary (2) and tertiary (3)). The indices of the leakage flux paths, represented as shunting elements of the limb, referred to the corresponding windings, starting with the innermost winding next to the limb (1) and go radial towards the outermost winding (3). The vector group of the transformer is realised by connecting the gyrators to each other via their outer terminals.

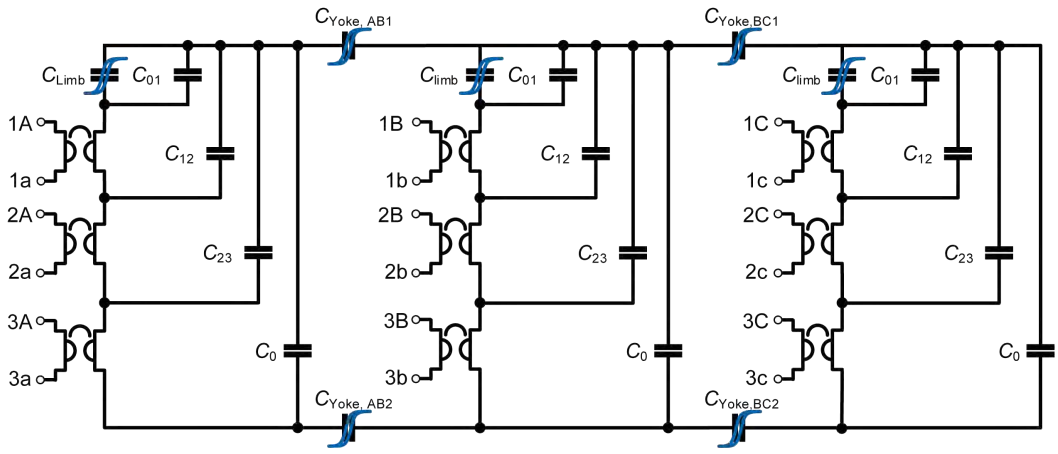

Figure 2.18: three-phase three-winding three-limb transformer grey box ReCap model.

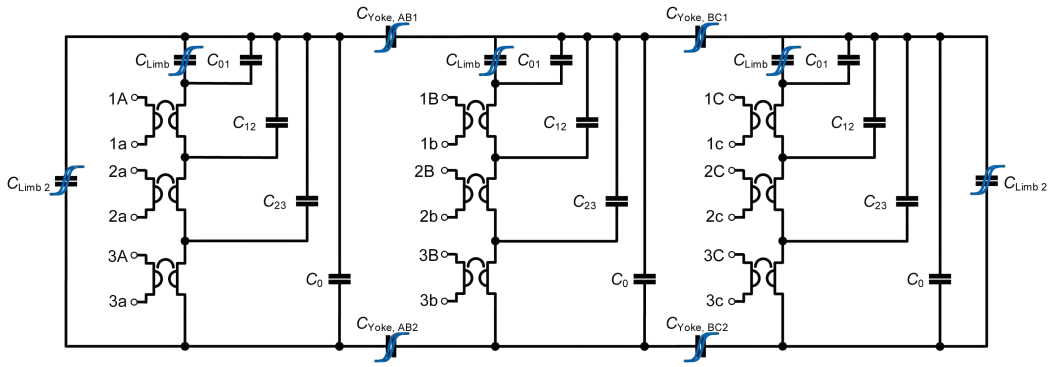

Figure 2.19: three-phase three-winding five-limb transformer grey box ReCap model.

2.4.2 Transformer Grey Box Model Parameters

Depending on the available transformer data and their quality, it can be necessary to approximate transformer parameters. The following section gives an overview of the most important transformer parameters and their calculation or approximation for low-frequency transient models. The formulas represent the values in the equivalent electric parameters, applying the inductance-reluctance analogy. Further information on the representation of network elements for transient studies can be found in [Cig90].

Winding Resistance

The transformer windings resistance R_{w} is measured for each winding with DC. With the resistance measurement the temperature should be recorded or noted, in order to make a temperature correction possible [IEC12a]. The winding resistance measurement is usually performed with a mobile transformer test device and the winding resistance is recorded, if the deviation in Ohm between two measurement points is below a certain limit. Usually, the winding resistance is given for the measured temperature and for 20° C and/or 85° C.

Turns per Winding

The number of turns per winding is usually not listed in the factory acceptance test protocol. This additional information needs to be evaluated from the transformer manufacturer. If the number of turns per winding is unknown, it can be estimated from the transmission ration and the rated winding voltage. Whereas the number of turns on the low-voltage winding is typical in the range of 100 turns. If the transformer core dimensions are known, the number of turns can also be estimated from the transformer core window height and the rated current of the winding. The current density per winding is typical in the range of 2.5-4 $\mathrm{A/mm^2}$. Together with the aforementioned current density and the winding resistance measurement from the factory acceptance test, the number of turns can be approximately determined. For the different vector groups the transmission ratios are calculated as follows:

$$\underline{\ddot{u}}_{\mathrm{Yy}} = \frac{w_{\mathrm{HV}}}{w_{\mathrm{LV}}} = \frac{V_{\mathrm{HV}}}{V_{\mathrm{LV}}}, \tag{2.41}$$

$$\underline{\ddot{u}}_{\mathrm{Yd5}} = \sqrt{3} \cdot \frac{w_{\mathrm{HV}}}{w_{\mathrm{LV}}} \cdot e^{\mathrm{j}\varphi^{\circ}} = \frac{V_{\mathrm{HV}}}{V_{\mathrm{LV}}}, \tag{2.42}$$

$$\underline{\ddot{u}}_{\mathrm{Yz5}} = \frac{2}{\sqrt{3}} \cdot \frac{w_{\mathrm{HV}}}{w_{\mathrm{LV}}} \cdot e^{\mathrm{j}\varphi^{\circ}} = \frac{V_{\mathrm{HV}}}{V_{\mathrm{LV}}}, \tag{2.43}$$

where φ is the angle related to the phase-shift between the windings, w_{HV} and w_{LV} are the number of turns of the high-voltage (index HV) and low-voltage (index LV) windings, respectively.

Transformer Core Cross-Section Area

The transformer cross-section area directly scales the flux density in the transformer core. For three-limb transformer cores, the cross-section area of the yoke and the limb sections are usually the same. For five-limb transformer cores, the cross-section area of the yoke is usually 55-60 % of the limb cross-section area. The cross-section of the unwounded outer two return limbs is typical 88-90 % of the main yoke cross-section area.

Regarding the cross-section area, it is important to note whether the filling factor is already included in the stated cross-section area or not. The filling factor is the ration of the effective transformer core cross-section area to the physical cross-section area. The filling factor is typical in the range of 0.955-0.965 (see **Appendix C**). The transformer is manufactured from stacked laminated steel sheets. The lamination is usually a varnish or an insulating coating to reduce eddy current losses in the transformer core. This lamination thickness is typical in the range of 1.5 - 3 μm on each side of the steel sheet. The lamination reduces the effective cross-section area available for the magnetic flux. Due to the non-linear hysteresis characteristics of the transformer core materials, small changes in the transformer core cross-section area, and thus in the magnetic flux density, can cause significant deviations in the magnetising current.

Mean Magnetic Path Length

The mean magnetic path length of the transformer core can be calculated from the transformer core design data and is used to scale the current in the hysteretic yoke and limb sections of the transformer topology model. If the transformer core design is unknown, it can be estimated from the outer transformer dimensions.

Iron Core Resistance

The iron core resistance R_{fe} represents the eddy current losses in the transformer core. R_{fe} is derived from the three-phase no-load test, subtracting the winding resistance losses ($I_0^2 \cdot R_{\mathrm{w}}$). The resistance R_{fe} is calculated from the no-load voltage and current, whereas the current I_{fe} is calculated as follows:

$$I_{\mathrm{fe}} = \frac{P_{\mathrm{NL}} - 3 \cdot I_0^2 \cdot R_{\mathrm{w}}}{V_{\mathrm{NL}} - V_{\mathrm{w}}}, \tag{2.44}$$

with the three-phase measured no-load losses P_{NL}, the average voltage applied during the no-load test to the three phases V_{NL}, the average voltage drop per phase across the winding resistance V_{w} and the average winding resistance per phase R_{w}.

$$R_{\mathrm{fe}} = \frac{V_{\mathrm{NL}}}{I_{\mathrm{fe}}}. \tag{2.45}$$

Typical the no-load currents per phase vary from phase to phase, as well as the losses per phase [Esc+07]. Therefore, the calculation should be done separately for each phase and then summed up the phase parameters to avoid inaccuracies during the calculation process.

Zero-Sequence Impedance

The method of symmetrical components is used in electrical power engineering, typically on a system-level basis, to analyse the three-phase power systems, which are operated symmetrically during normal operation. The phase symmetry, with respect to the amplitude, is used to simplify the mathematical description of the power system with its different components. The method of symmetrical components uses the modal transformation to decouple the three-phases into equations for the three-phase system, by a change of base. This result in a representation of the power system in three components: positive-sequence (PS), negative-sequence (NS) and zero-sequence component. In the context of power transformers, a distinction is made between two types of zero-sequence impedances, the open-circuit zero-sequence impedance and the short-circuit zero-sequence impedance. The zero-sequence impedance in power transformers also depends on the transformer vector group, the physical winding position and core design and can vary for different test setups [IEC12a]. In transformer grey box models, the zero-sequence path represents a magnetic shunt path of the wounded transformer limbs for a zero-sequence flux, resulting from a zero-sequence current in the windings. This zero-sequence current depends on the neutral point treatment and on the winding connection. In a star-connected winding with grounded neutral the zero-sequence current can only return via ground. In star-connected windings without grounded neutral, no zero-sequence can be formed. In delta-connected windings a zero-sequence current can circulate in the windings, reducing the effective zero-sequence impedance. YNyn-connected transformer without tertiary delta winding has a higher zero-sequence impedance as transformers with a tertiary delta winding [IEC97; ABB10]. If a delta winding is present, providing balancing ampere-turns through the circulating current, the zero-sequence impedance will be approximately equals the short-circuit impedance of the pair of windings (star and delta) [ABB10]. In transformers with zigzag windings, the zero-sequence current component on each limb cancels out, because each limb carries part windings from two phases with opposite winding direction [IEC97]. The effects of a tertiary delta winding on the zero-sequence impedance are discussed in detail in [IEC97; Car+03; SS08; Ros05; SB12; Ram+13; Kam+16; RB17a; RB17b]. In case of a five-limb transformer core, a zero-sequence flux can re-close via the outer unwounded return limbs, offering a low reluctance path for a zero-sequence flux. In case of a three-limb transformer core, a zero-sequence flux between the yokes can only re-close via off-core flux paths. The off-core flux paths can include the transformer tank and/or transformer shields and the oil/air gap between the transformer core and tank. During balanced operation of

the transformer, the zero-sequence impedance and therefore transformer tank has a low influence on the transformer behaviour [FY02]. Typical values for zero-sequence impedances for transformers with different core design and winding connections are given in [IEC97] Tab. 1.

The zero-sequence impedance can be measured by connecting the line terminals in parallel and attaching a single-phase voltage source between the line terminals of a star- or zigzag-connected vector group and the neutral terminal. The test current should not exceed the current-carrying capability of the neutral conductor. If a tertiary delta-connected winding is present, the test current shall be such, that the current in the delta-connected windings is not excessive [IEC12a].

The zero-sequence impedance, represented by a parallel connection of R_0 and L_0 in transformer topology models using the inductance-reluctance analogy, calculates as follows:

$$Z_0 = \frac{3 \cdot V_{\mathrm{rms}}}{I_{\mathrm{rms}}}, \tag{2.46}$$

and is expressed in ohms per phase. The test current per phase $I/3$ should be stated with the zero-sequence impedance. If the phase angle between voltage and current is assessed during the zero-sequence test, the impedance can be split up into a parallel connection of a resistive and reactive part R_0 and X_0, according to the following equations:

$$R_0 = \frac{3 \cdot V_{\mathrm{rms}}^2}{P_{\mathrm{Z0,test}}}, \tag{2.47}$$

$$X_0 = \frac{3 \cdot V_{\mathrm{rms}}^2}{Q_{\mathrm{Z0,test}}}. \tag{2.48}$$

Note that the values for R_0 and X_0 can vary, depending on the calculation method of the reactive power (see **Section 4.4.1**). The measurement method implies an equal distribution of the zero-sequence impedance between the phases/limbs. The zero-sequence path is of interest, especially in case of three-phase three-limb transformer cores. In case of a zero-sequence flux in the transformer core, the zero-sequence flux can only close via the free-space or the transformer tank. The transformer tanks are usually manufactured out of a different steel than the transformer core [AHH95]. Thus, considering the tank with its own hysteretic characteristics could improve the model accuracy. In case of a three-phase five-limb transformer core, the effect of the tank is reduced, due to the outer unwounded limbs, which offer a low magnetic resistance return path for a zero-sequence flux. Three-phase three-limb 300 kVA transformer studies in [Abb20], revealed that the transformer tank can be neglected, if the ratio of core-cover distance and core-wall distance is above 2.5.

The zero-sequence path is important, especially during an increased flux density in the transformer core. E. g. during over excitation of the transformer core, an increased zero-sequence impedance causes a reduction in current amplitude, an increase in active power loss, a reduced non-active power demand and a reduced magnetic flux density in the transformer yoke. These effects are related to the saturated core material.

Inter Winding Leakage Inductance

When studying the transformer under saturation conditions, special attention should be paid to the representation of the leakage inductance [Mah12]. Neglecting the stray path between two opposite yoke sections, will result in an underestimation of inrush currents [Zir+12a]. The inter-winding leakage inductance L_{xy} represents the stray flux paths between winding x and winding y. Usually the windings are numbered starting with 1, which is the innermost windings, next to the transformer core. The leakage inductances are derived from short-circuit tests, whereas the first mentioned winding is the excited winding, and the second mentioned winding is the short-circuited winding. For three-winding transformers usually the three short-circuit impedances are measured, Z_{12} (HV/LV), Z_{13} (HV/TV) and Z_{23} (LV/TV) with HV: high-voltage winding, TV: tertiary-voltage winding, and LV: low-voltage winding. L_{yy} represents the flux path between two opposite yokes via air/oil. This path comes into place during saturation of the yokes and controls the current peak, e. g. during the inrush.

The leakage inductance can be calculated from the short-circuit measurements in different ways, depending on the available data. All methods are presented herein.

Calculation with the angel $\cos(\varphi)$ between voltage and current:

$$L_{\mathrm{xy}} = \frac{X_{\mathrm{xy}}}{2\pi \cdot f_{\mathrm{r}}}, \tag{2.49}$$

where the short-circuit impedance is calculated with (2.50).

$$X_{\mathrm{xy}} = \frac{\bar{V}_{\mathrm{SC}}}{\bar{I}_{\mathrm{SC}}} \cdot \sin(\varphi), \tag{2.50}$$

with the mean short-circuit voltage $\bar{V}_{\mathrm{SC}}$ and the mean short-circuit current $\bar{I}_{\mathrm{SC}}$. The calculation with $\cos(\varphi)$ is only defined for pure sinusoidal voltage and current waveforms. Therefore, distorted current and/or voltage waveforms introduce an error in this calculation method. Some measurement software offers the calculation of a $\cos(\varphi)$ value for each individual harmonic [DEW19].

Calculation with power factor (PF):

$$X_{\mathrm{xy}} = \frac{\bar{V}_{\mathrm{SC}}}{\bar{I}_{\mathrm{SC}}} \cdot (1 - PF), \tag{2.51}$$

whereas in case of non-sinusoidal current $PF \neq \cos(\varphi)$ (see also **Section G.3.1**).

Calculation with relative short-circuit impedance u_{k}:

$$X_{12} = \sqrt{v_{\mathrm{k}}^2 - v_{\mathrm{r}}^2} \cdot \frac{\bar{V}_{\mathrm{SC}}}{\bar{I}_{\mathrm{SC}}}, \tag{2.52}$$

where v_{k} is usually given for the short-circuit test, v_{r} can be found on the transformer nameplate or the factory acceptance test and $\bar{V}_{\mathrm{SC}}$ and $\bar{I}_{\mathrm{SC}}$ is the mean value of the short-circuit voltages and currents per phase. Usually the same leakage inductance is used for all phases, which introduces a model uncertainty [Esc+07].

Core-Inner Winding Leakage Inductance

The leakage inductance between the core and the inner winding next to the core is referred to as L_{01}. If the winding design data is unknown, L_{01} can be approximated according to (2.53) [Mor+07].

$$L_{01} = k_{01} \cdot L_{12}, \tag{2.53}$$

where k_{01} is derived from insulation clearance of the channel between winding 1 (index W1) and 2 (index W2) with (2.54).

$$k_{01} = \frac{V_{W1}}{V_{W2} - V_{W1}}. \tag{2.54}$$

If detailed information on the winding design are available, (2.55) can be used to calculate the leakage inductance between the windings. (2.55) is based on the 'reactive kVA method' proposed in [BLU+38], and is rewritten as follows:

$$L_{\mathrm{HL}} = \frac{\mu_0 N^2}{h} \cdot \left(\frac{l_{\mathrm{mw,H}} \cdot b_{\mathrm{H}}}{3} + \frac{l_{\mathrm{mw,L}} \cdot b_{\mathrm{L}}}{3} + l_{\mathrm{mw,H}} \cdot a_H \right), \tag{2.55}$$

where μ_0 is the vacuum permeability, N is the number of turns of the winding 1 or 2, depending on which voltage level the leakage inductance is referred to, h is the height of the winding, $l_{\mathrm{mw}} = 2\pi r_{\mathrm{mw}}$ is the mean winding length of the circular coil (assumed coil design), with r_{mw} the radius from the middle centre of the core limb to the mean of the corresponding winding, a is the thickness of the (insulation) channel between the conductors of the two windings and b is the coil thickness. Further information on the leakage inductance calculation, based on winding design data, can be found in [BLU+38].

An acceptable approximation for k is 0.5 [CH09; Høi+09; Ave+18; MGI05]. This applies if the gap volume between the primary and secondary winding is equal and the axial and radial dimension of both windings match. In case of a zigzag winding, additional inductance is added by the wiring between the windings on the different limbs [Zha+20].

Limb-Yoke Equivalent Joint Air Gap

Transformer cores are usually manufactured out of multiple sheets stacked together. The limbs and the yokes are commonly produced separately and jointed together during the manufacturing process. Therefore, a small air gap is introduced in the joints between the limbs and yokes. The air gap in power transformer cores is undesired, because they increase the reluctance of the magnetic path, and linearise/rotates the magnetisation characteristics of the transformer core. Thus, a higher

magnetisation current is required to cause the same magnetic flux density in the transformer core, as in a transformer core without an air gap [Zir+12a]. Constructive measures, such as step-lap core design and mitered joints with angles between 30° and 60° are used to reduce the air gap length. Increasing the equivalent air gap inductance L_{gap} in the transformer model results in a counter-clockwise rotation of the hysteresis characteristics.

Figure 2.20 depicts the sheet arrangement in a mitered core joint and the flux. The fringing flux around the gap also increases the losses. The calculation of the loss increase due to the gap is difficult, because the gap size depends on the deviation during the manufacturing process. Taking a closer look at the flux distribution around core joint area for low and high flux density levels, the flux has two ways to pass from one sheet to another in longitudinal and traversal direction.

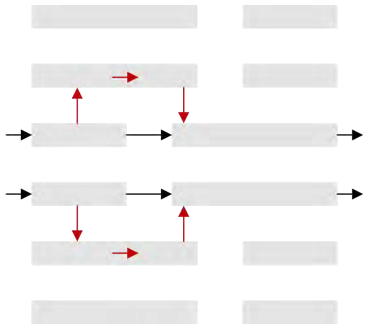

Figure 2.20: Top view of mitered core joint and flux paths at normal flux levels (black dart) and increased flux levels (black and red darts).

During low flux density level (red darts), the flux avoids the longitudinal air gaps and passes to the neighbouring sheet via the overlap (traversal) region. During high flux density levels, the flux is forced also to pass through the longitudinal air gap. Therefore, the equivalent air gap value L_{gap} changes as a function of the flux density inside the core. This change can be reproduced by a varying equivalent air gap length [EP97]. This approach is also used for saturated AC machines [ML92]. Therefore, a transformer topology model with the capability to reproduce the measured transformer characteristics under various flux density levels, should include a variable air gap component [EP98]. Moreover, the air gap between the sheets is a linear reluctance, whereas the path inside the sheets is a non-linear reluctance.

The introduced joint air gap causes the $B-H$ characteristic to flatten around the knee point. In [GM01] Fig. 12 the $B-H$ characteristic shows the flattening effect, if a joint air gap with different effective lengths in introduced in non-oriented (NO) steel. Thus, neglecting the air gap in the transformer model, can be a reason for the discrepancy between calculated and measured hysteresis characteristics in the area of the knee point. The joint air gap inductance is calculated according to (2.56).

$$L_{\mathrm{gap}} = \frac{N^2}{R_{\mathrm{gap}}} = \frac{\mu_0 A_{\mathrm{limb}} N^2}{\Delta}, \tag{2.56}$$

where N is the number of turns, which could be used to refer the air gap to a dedicated side of the transformer, A_{limb} and Δ is the joint air gap cross-section and equivalent joint air gap length, respectively.

It was shown in [CBG18], that the correlation of a finite element method (FEM) model of a single-phase four limb 4.4 kVA laboratory transformer could be improved by incooperating the transformer core joints with the concept of 'equivalent air gap'. Taking into account a DC bias on the transformer, the measured leakage flux exceeded the leakage flux calculated in the FEM studies with solid joints (without air gaps).

Winding Capacitance to Ground

The transformer winding capacitance to ground should be included in the transformer model together with the parameter L_{gap}. Increasing L_{gap} rotates the hysteresis loop counter-clockwise, whereas decreasing the winding capacitance C rotates the hysteresis loop clockwise. The winding capacitance can vary from phase/limb to phase/limb around or below 1 %. The order of magnitude scales is in the range of several nano Farad up to several ten nano Farad, depending on the transformer size/rated power and winding design. In the factory acceptance test, usually the mean capacitance of the corresponding windings is stated. The winding capacitance is measured via the bushings. Therefore, the winding capacitance C also includes the bushing capacitance to ground. A cobra-shaped $\Phi - i$ loops with negative slopes around their waits can be an indication for the effect of the winding capacitance [Zir+22b]. **Figure 2.21** depicts the different transformer winding capacities. C_{HL} is the capacitance between the high- and low-voltage winding, C_{ML} is the capacitance between the low- and medium voltage winding, C_{HM} is the capacitance between the medium- and high-voltage winding and C_{L}, C_{M} and C_{H} is the capacitance between the low-, medium and high-voltage winding to the tanks/ground.

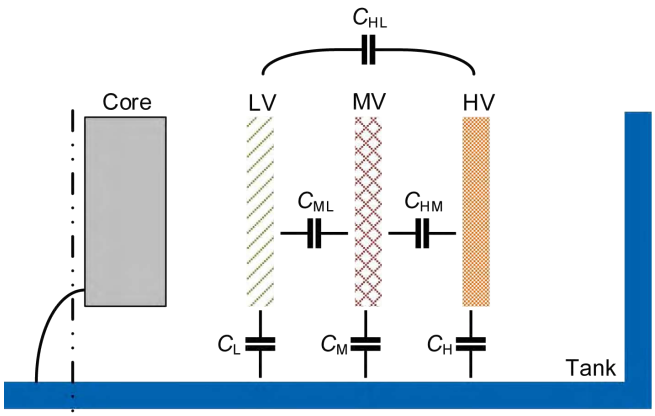

Figure 2.21: Different capacities in transformers during transformer winding capacity measurement.

The transformer winding capacities are usually measured at 10 $\mathrm{kV_{rms}}$ at the rated frequency together with the loss factor $\tan(\delta)$ [IEE13].

2.4.3 Transformer Design - Effects on Behaviour

Due to the transformer design, the hysteresis characteristic of the transformer core material can't be derived from three-phase terminal measurements, as outlined in the following section. Furthermore, the vector group of the transformer can have a positive effect on the transformer saturation, e. g. if delta windings are present that delay the saturation of the transformer during an GIC event, as described below. A remanence in the transformer core, caused by GICs or DC winding resistance measurements, should be considered before conducting diagnostic measurements on the transformer.

Effect of Transformer Magnetic Core Design

The zero-sequence flux can only leave the core in the yoke sections, because the wounded limbs act as a magnetic flux 'tube'. Under ideal conditions, no flux from the core can leave the wounded limb section. Therefore, it should be considered that the flux density in the wounded transformer limb can reach values of the order of 3 T or higher [ZMA21], whereas the magnetic flux density in the yoke will remain moderate during the same time. This difference in flux density is possible due to the shunting effect of the zero-sequence impedance Z_0 and the leakage flux path between the yoke and windings (see **Figure 2.15**, **Figure 2.16**, **Figure 2.18** and **Figure 2.19**).

The tube-like behaviour can be proven by evaluation of the Biot-Savart law (2.57) for a linear current excitation (2.58). The assumed setup is depicted in **Figure 2.22**.

$$\vec{H}(\vec{r}_{\mathrm{p}}) = \frac{I}{4\pi} \int_C \frac{\mathrm{d}\vec{s} \times \vec{r}_{\mathrm{d}}}{r_d^3} \mathrm{d}V, \tag{2.57}$$

$$\vec{H}(\vec{r}_{\mathrm{p}}) = \frac{I}{4\pi} \int_V \frac{\vec{J}(\vec{r}) \times \vec{r}_{\mathrm{d}}}{r_d^3} \mathrm{d}V, \tag{2.58}$$

where the point P is located on the infinitesimal small winding together with point Q. Thus, $\vec{r}_{\mathrm{d}}$ becomes zero and $\vec{r}_{\mathrm{p}} = \vec{r}_{\mathrm{q}}$. With $\vec{s}$ along the conductor (in (2.57)) is only in the current direction x the vector product of $\mathrm{d}\vec{s} \times \vec{r}_{\mathrm{d}}$ becomes zero, and therefore also the magnetic $\vec{H}(\vec{r}_{\mathrm{d}})$ is zero (at the conductor plane).

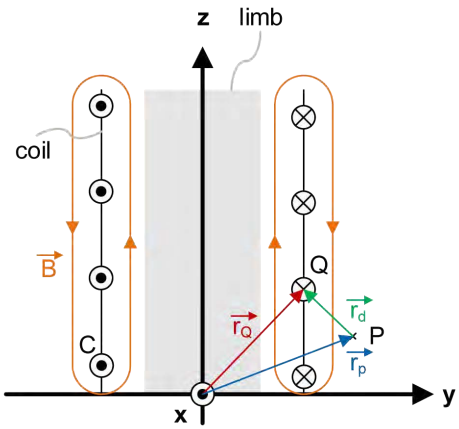

Figure 2.22: Schematic cross-section view of wounded limb and applied Biot-Savart law for line currents.

Taking a closer look on the symmetry of the transformer core and the magnetic path lengths in three-limb transformers, it is noticeable, that the middle limb is magnetically shorter, than the outer two limbs. This results in a zero-sequence current i'_0 (2.63), as derived in the following equations. Amusing a conventional three-limb transformer core with three windings with the same number of turns N connected in star and without a dedicated neutral conductor, as depicted in **Figure 2.23**. The three windings are connected to a balanced three-phase sinusoidal voltage source. The magnetic flux linkages Ψ_U, Ψ_V and Ψ_W are therefore also balanced and sinusoidal. The magnetic paths of the three limbs start at point X and end at point Y. It is obvious that the length of the magnetic path of the middle limb is shorter, than the path of the outer two limbs. The instantaneous mmf Ni' in each limb, causing the flux linkage Ψ. The phase currents i differs from the instantaneous current i', required to produce the mmf Ni', because the phase currents i_A,i_B and i_C depend on the magnetic flux density of all limbs and not just the one limb under consideration. The same holds true for the active and non-active power measured at the transformer terminals [Wal57; KK13].

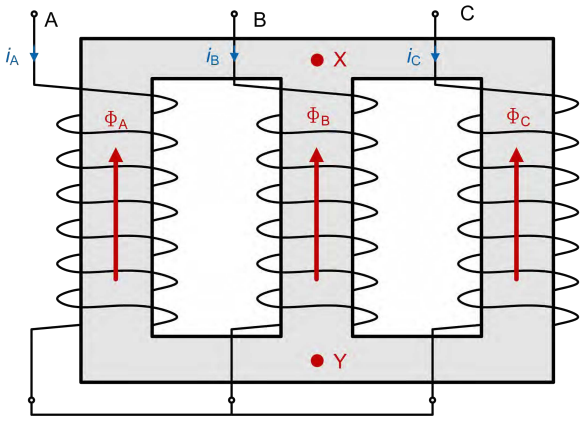

Figure 2.23: Conventional three-limb transformer core with three windings in star connection without dedicated neutral conductor and indicated individual magnetic paths.

The required mmfs and actual mmfs derived from the phase currents are related as follows:

$$Ni_{\mathrm{A}} - Ni_{\mathrm{B}} = Ni'_{\mathrm{A}} Ni'_{\mathrm{B}}, \tag{2.59a}$$

$$Ni_{\mathrm{B}} - Ni_{\mathrm{C}} = Ni'_{\mathrm{B}} Ni'_{\mathrm{C}}, \tag{2.59b}$$

$$Ni_{\mathrm{C}} - Ni_{\mathrm{A}} = Ni'_{\mathrm{C}} Ni'_{\mathrm{A}}. \tag{2.59c}$$

The division of (2.59a) to (2.59c) by the number of turns N leads to:

$$i_{\mathrm{A}} - i_{\mathrm{B}} = i'_{\mathrm{A}} i'_{\mathrm{B}}, \tag{2.60a}$$

$$i_{\mathrm{B}} - i_{\mathrm{C}} = i'_{\mathrm{B}} i'_{\mathrm{C}}, \tag{2.60b}$$

$$i_{\mathrm{W}} - i_{\mathrm{U}} = i'_{\mathrm{W}} i'_{\mathrm{U}}. \tag{2.60c}$$

Due to the star connection of the transformer windings, the following holds true according to Kirchhoff's law:

$$i_{\mathrm{A}} + i_{\mathrm{B}} + i_{\mathrm{C}} = 0. \tag{2.61}$$

Combining (2.61) with (2.60a), (2.60b) and (2.60c) results in the following expressions for the phase currents:

$$i_{\mathrm{A}} = i'_{\mathrm{A}} - \frac{1}{3}\left(i'_{\mathrm{A}} + i'_{\mathrm{B}} + i'_{\mathrm{C}}\right), \tag{2.62a}$$

$$i_{\mathrm{B}} = i'_{\mathrm{B}} - \frac{1}{3}\left(i'_{\mathrm{A}} + i'_{\mathrm{B}} + i'_{\mathrm{C}}\right), \tag{2.62b}$$

$$i_{\mathrm{C}} = i'_{\mathrm{C}} - \frac{1}{3}\left(i'_{\mathrm{A}} + i'_{\mathrm{B}} + i'_{\mathrm{C}}\right). \tag{2.62c}$$

(2.62a) to (2.62c) containing the zero-sequence current component i'_0:

$$i'_0 = \frac{1}{3}\left(i'_{\mathrm{A}} + i'_{\mathrm{B}} + i'_{\mathrm{C}}\right). \tag{2.63}$$

The zero-sequence current i'_0 causes a mmf Ni'_0, also during balanced conditions. The produced zero-sequence flux linkage Ψ_0 is forced to leave the transformer core at point A and return into the core via point B to re-close. In consequence, this means that the magnetisation characteristics of the transformer can't be derived from terminal current and voltage measurements from a balanced three-phase excitation of a three-limb three-winding transformer. This can easily be proven by comparing the $\Psi - i$ characteristics of phase A and C measured in positive sequence (A-B-C) and measured in negative sequence (C-B-A).

Remanence in Transformer Cores

Transformer cores can acquire a remanence flux up to several ten percent of the nominal flux density [Cig96]. Remanence flux can be caused e. g. by DC winding resistance measurements or by transient phenomena, such as inrush. The remanence in the transformer core can be reduced by driving the transformer core into deep saturation and reduce the AC voltage of the supply continuously towards zero volts, decreasing the size of the hysteresis characteristics. The flux density in a transformer core has a finite maximum flux density. This value cannot be exceeded, even not with a remanence flux. Therefore, heavily saturating the transformer force the core to operate on the major hysteresis loop. By reducing the AC supply voltage, the hysteresis loop is decreased in size and the remanence can be reduced to a minimum. The transformer core can be either saturated at rated frequency by over-excitation or by decreasing the excitation frequency, which allows also to reduce the excitation voltage ($\Psi = \hat{u}/f$). The latter approach is used with portable transformer test devices.

Harmonics

Current and voltage harmonics at three-phase transformer terminals arises during balanced and imbalanced operation conditions. Regardless of the operation condition, the transformer characteristics are governed by the history-depended BH-characteristics of the core material, Ampère's law ($I = \oint_S \vec{H} \cdot \mathrm{d}\vec{s}$) and by Kirchhoff's law, which requires the sum of the phase currents to be zero. In order to fulfil all these requirements, the transformer draws a compensating current in the neutral conductor, if the neutral is connected to ground. With or without a dedicated neutral conductor, the requirements are meet by taking into account three effects:

(1) varying flux path $S \rightarrow$ Ampère's law is fulfilled, also with varying current,
(2) varying magnetising voltage $\rightarrow$ flux density is varied in a way that the phase currents sum up to zero,
(3) leakage flux paths $\rightarrow$ leakage H field and core H field sums up to zero, whereas the H filed inside the core corresponds to the BH-characteristics of the magnetic core material.

The dominating effects are the leakage flux paths. The varying of the magnetic flux path inside the core is governed by the reluctance of the paths. In case of an ungrounded star connection, the phase voltages can vary with respect to the voltage of the neutral conductor to ground. The phase voltage variations are usually not very pronounced, because the impedance of the connected grid is very low. The phase voltage is therefore close to a sinusoidal voltage wave form.

In addition to the afore mentioned effects, the magnetic asymmetry of the transformer core introduces a zero-sequence current, as explained before. Further information on triplen harmonics and their effects on symmetric components can be found in [CPT11].

Effect of the Winding Connection

Taking a closer look on transformers with delta windings, such as those found in transmission grid transformers, as tertiary winding. Assuming a transformer with a YNd vector group, which is excited via the star-windings. Any phase current imbalance in the star-connected windings causes an induced current in the delta windings. Especially for tripled harmonics (3^{rd}, 9^{th}, 15^{th},...) the delta windings offer a low-impedance path. With a grounded neutral, the tripled harmonics amplitude can be even higher in comparison to a transformer with an isolated neutral point. Current harmonics circulating in the delta windings are limited by the winding resistance of the delta windings. Thus, the delta windings offer a low-impedance path for zero-sequence currents. If the delta winding would be the innermost winding next to the core and the zero-sequence impedance would be close to zero, nearly DC flux would be present in the core, due to the mmf caused by the circulating current in the delta windings. This would force the DC flux to re-close through paths outside the core. An equilibrium could be reached between the ohmic voltage drop across the low winding resistance in the delta windings and the induced LFC in the delta windings. At that instant, the DC flux does not change over time, causing the circulating current in the delta winding to decrease. This is the commencement of the transformer core saturation. The time constant or time delay of transformer core saturation caused by the delta winding is a function (2.64) of the delta winding resistance R_Δ and the inductance L.

$$\tau = \frac{L}{R_\Delta}, \tag{2.64}$$

whereas L in the range of several Henry and R_Δ in the range of several milliohms, resulting in time constant in the range of several minutes. Regarding the mitigation of GICs this means no further mitigation would be required, e. g. if the polarity of the GIC changes within the time constant. This change of GIC polarity is a common characteristic (**Section 3.5**) for GICs, which is related to the compression and relaxation of the earth magnetic field in the solar wind. The polarity change of the GICs usually do not occur in the timescale of minutes, rather in the timescale of hours. A recent GIC measured at a 380 kV neutral point is depicted in **Figure 2.24**, where the polarity change is pronounced around 5:00 UTC.

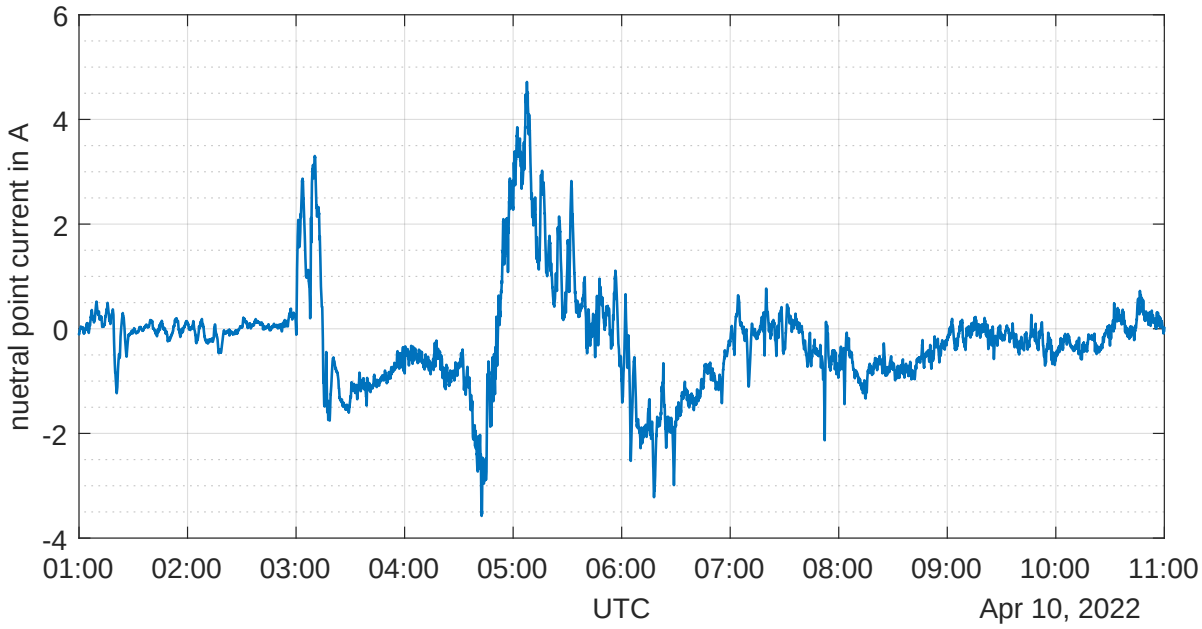

Figure 2.24: Measured GIC at client #05 during April 10th 2022 with pronounced polarity reversal around 5:00 UTC.

2.4.4 Transformer Hysteresis Modelling

A typical hysteresis characteristic with characteristic points used to describe the hysteresis is depicted in **Figure 2.25**. The orange line marks the virgin characteristic for the first time of magnetisation of the material. If the external field is reduced, the flux density B follows the blue characteristic. If the external field is zero, a remanence flux B_r is still present in the material. In order to reduce the magnetisation in the material to zero, a coercive magnetic field H_c is required. During the magnetic field amplitude is further increased with opposite polarity, the magnetic material approaches the negative saturation region. Decreasing the magnetic field again to zero, a remanent magnetisation is present in the material. With increasing positive amplitude of the magnetic field, the material approaches the positive coercive field strength H_c on the red curve. If the magnetic field strength is further increased, the material approaches the positive saturation region again.

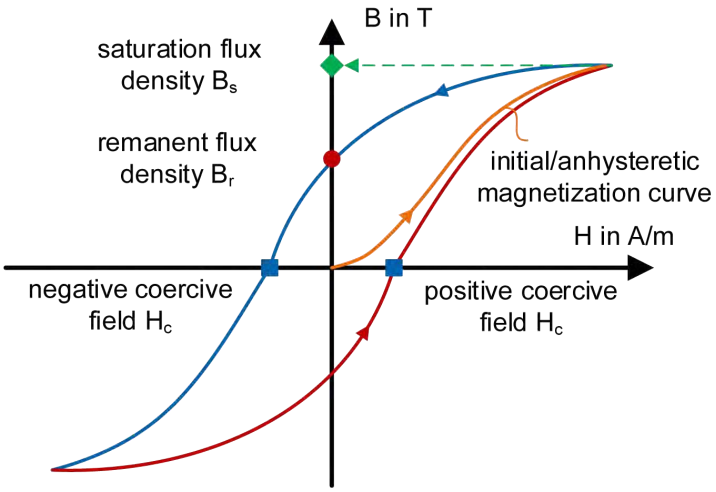

Figure 2.25: Characteristic points on hysteresis characteristic.

For the modelling of transformer transients, the hysteretic properties of the transformer core and the eddy current effect in the laminated core material should be reproduced in the model for accurate simulation results for low and moderate saturation conditions (up to 2.0 T). Whereas the hysteretic properties are often referred to as static and the eddy current effects are referred to as dynamic effects. Especially during transformer energising, reenergising, short-circuit events, generator transformer under synchronisation, voltage switching, ferroresonance phenomena [RI10] and GIC effects on transformers, the ability to reproduce the hysteretic and dynamic behaviour of the model is required. Also for the modelling of current transducer transformers the hysteretic and dynamic properties should be reproduced by the model, because they are closely linked [Ann+00; Dup+01].

The challenge is to accurately model the eddy currents induced in electrical steel e. g. grain-oriented (GO) or NO silicon steel sheets. In case of power transformer cores, the induced eddy current calculation is reduced to 1D diffusion equation (2.65). It should be noted, that (2.65) assumes a homogenous magnetic material without any magnetic domains or grains. Thus, the loss calculation based on (2.65) results in an underestimation of the losses, even using an accurate static hysteresis model (SHM) [Gra82; Bis85; Ber88]. Because the grain and domain size of GO steel, used in stacked transformer cores (thickness usually 0.27 mm or 0.3 mm), is in the range of the steel sheet, additional effort for 2D or 3D models based on (2.65) will not increase the model accuracy, regarding losses.

$$\frac{\partial B}{\partial t} = \rho \frac{\partial^2 H}{\partial x^2} \tag{2.65}$$

Even at rated power frequency the deviation between measured and simulated losses can reach 40 % or more for GO steel, commonly used in power transformers, if (2.65) is perished for the calculation Fig. 6 in [FWD82]. By the time of writing, no reliable physical model has been proposed to model the dynamic behaviour of GO steel sheets. Therefore, the most promising phenomenological approach is

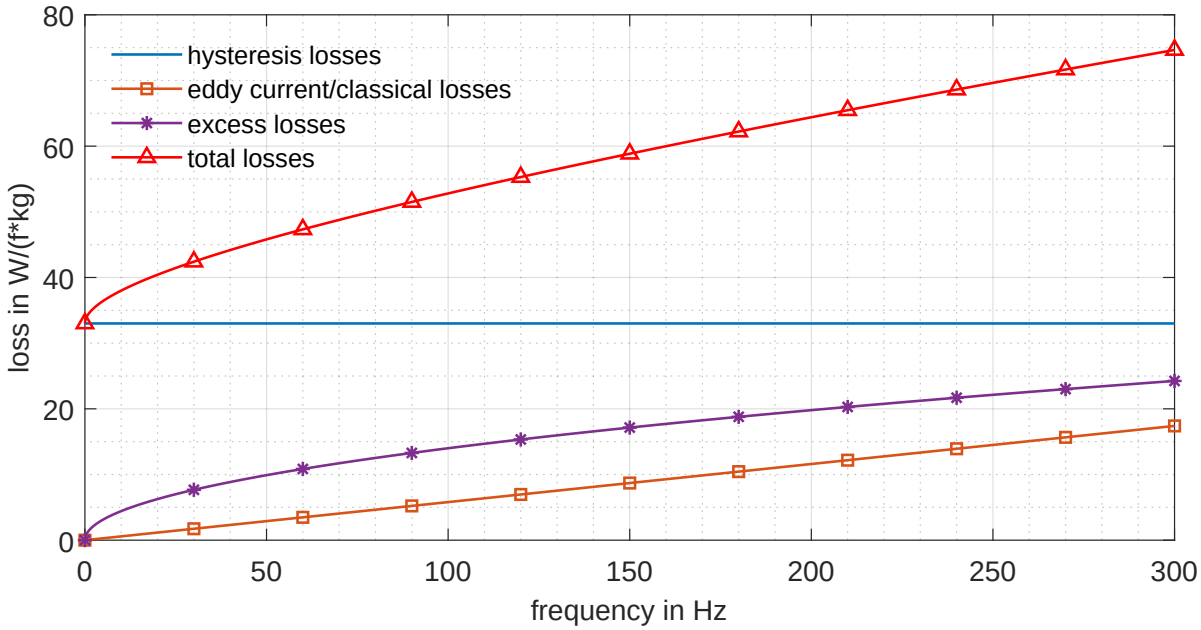

Figure 2.26: Loss components for NO Si-Fe lamination over frequency adopted from [Ber08] Fig. 1.12

based on the loss separation principle, according to (2.66) (see also **Figure 2.26**) [Ber08]. Indeed, up to the time of writing, all proposed hysteresis models are phenomenological models.

$$P_{\mathrm{tot}} = P_{\mathrm{hys}} + P_{\mathrm{eddy}} + P_{\mathrm{exc}}, \tag{2.66}$$

where P_{hys} are the hysteresis or static losses, P_{eddy} the eddy current losses, and P_{exc} the excess losses. Common loss separation values for GO 0.27 mm steel are in the range of 42 % : 21 % : 37 % [Zir+11].

Figure 2.26 depicts the different loss components and the total loss of NO Si-Fe lamination with 0.21 mm thickness at a sinusoidal peak induction of 1.5 T, adopted from [Ber08]. The loss components are calculated according to (2.67).

$$P_{\mathrm{total}} = C_0 + C_1 \cdot f + C_3 \cdot \sqrt{f}, \tag{2.67}$$

with $C_0 = 33$, $C_1 = 0.058$, $C_3 = 1.4$ and the frequency f.

The equivalent of (2.66) is the field separation [Ber08] at the steel sheet surface, whereas the magnetic field strength is the sum of the hysteresis, eddy current and excess field (2.68).

$$H(t) = H_{\mathrm{hys}} + H_{\mathrm{eddy}} + H_{\mathrm{exc}}, \tag{2.68}$$

(2.68) can reformulate into (2.69):

$$H(t) = H_{\mathrm{h}}(B) + \frac{d^2}{12\rho}\frac{\mathrm{d}B}{\mathrm{d}t} + g(B)\delta\left|\frac{\mathrm{d}B}{\mathrm{d}t}\right|^{1/2}, \tag{2.69}$$

where $H_{\mathrm{h}}(B)$ is the field calculated by the SHM, the second term accounts for H_{eddy}, which are also referred to as classical losses [Ber08], with the steel resistivity ρ, which is the magnetic field H calculated from (2.65), $g(B)$ is a scaling factor, which can be constant [Cha+04] or depend on B [Zir+06; Zir+08], δ is the directional parameter ± 1 for the ascending ($\mathrm{d}B/\mathrm{d}t > 0$) and descending ($\mathrm{d}B/\mathrm{d}t < 0$) hysteresis branches. (2.69) should be understood as phenomenological rather than physical [Zir+08].

From (2.69) the following relations can be concluded:

$$W_{\mathrm{eddy}} \propto f, \tag{2.70a}$$

$$W_{\mathrm{exc}} \propto f^{1/2}. \tag{2.70b}$$

An introduction and comparison of different classical hysteresis models can be found in [LPA00; Lot+16]. In the following sections, the used JA and the capacitance-permeance hysteresis (CPH) model are explained in detail. Besides the aforementioned hysteresis models, the Preisach hysteresis model, the dynamic hysteresis model (DHM) and a recent proposed empirical hysteresis model are presented.

Jiles-Atherton Hysteresis Model

The JA hysteresis model was proposed by Jiles and Atherton in 1984 [JA84] and is an analytical SHM for ferromagnetic materials. It is based on the idea of domain wall motion and rotation, but in fact the JA model do not correctly represents the physical behaviour [Zir+12b]. A similar approach to [JA84], taking into account the energy required for the domain wall motion and rotation to align the magnetic moments with the external field, can be found in [SH99]. The JA usually requires no extensive measurements, but more effort during the parameter fitting [PDM95], in comparison to the Preisach model (**Section 2.4.4**). Whereas the deviation between the measured and modelled current is lower for the Preisach model, but still in the same [PDM95; BCP03] range of magnitude. Further information on the JA model can be found in **Appendix B**. For the further usage in this thesis, the inverse JA model is used. The inverse JA model uses the magnetic flux density B as input, instead of the magnetic field H. The implemented inverse JA model with (B.19) is derived in detail in **Appendix B.4**. The JA model uses the five parameters α, a, M_{s}, k and c to change the shape of the hysteresis characteristics. Their effects on the hysteresis characteristics shape are listed in **Table 2.4**.

Table 2.4: JA parameters, their effect on the hysteresis characteristics.

Paramater	Units	Description
α		inter-domain coupling
a	A/m	twists anhysteretic characteristic
M_s	A/m	changes the maximum magnetisation
k	A/m	accounts for hysteresis losses by widen the hysteresis characteristic
c		accounts for the reversibility

The five JA model parameters can be determined by means of an optimisation problem, by trial-and-error method or analytically. For further information on the analytical derivation of the JA parameters, see **Appendix B.3**. However, the analytical method does not always converge. Deriving the JA parameters in the context of an optimisation problem, the least square fit method, using the measured voltage and current waveform together with the corresponding waveforms of the model is a suitable method [Led+99; Alb+21a]. Other optimisation methods, e. g. with a genetic algorithm was proposed and applied in [WRB01]. The JA parameters for comparison or start values can be found in literature [JTD92; Ann+00; Kis06; Cha+06; Ami+20].

Capacitance-Permeance Analogy Hysteresis Models

When using the capacitance-permeance analogy, the reluctance of the transformer core is represented with a capacitance. To reproduce the hysteresis characteristics with eddy current, hysteresis and excess losses, further components are needed. For that purpose, an RLC circuit is proposed in [GE18]. A second hysteresis model [Che+09], using the capacitance-permeance analogy, implements the hysteretical characteristics of the magnetic core material by a series and parallel connection of a capacitor, resistors with a series-controlled voltage and a parallel controlled current source, as depicted in **Figure 2.27**. The capacitance-permeance hysteresis model was successfully implemented in MATALB/Simulink for the simulation of a three-phase three-limb two-winding 50 kVA power transformer in [Alb+21a; Dom22].

The model is parametrised with six model parameters C_s, R_h, a, b, n and m. The individual components are explained below.

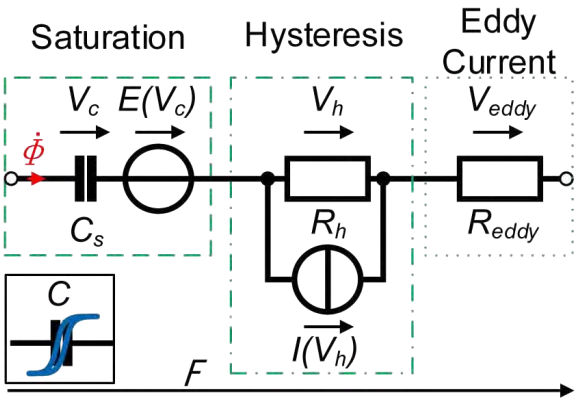

Figure 2.27: Hysteretical transformer core element.

The transformer core non-linear saturation characteristics are model as non-linear capacitance, implemented as voltage-controlled voltage source in series with a linear capacitor. The output voltage of the voltage source is given by:

$$E(V_\mathrm{c}) = (aV_\mathrm{c})^n, \tag{2.71}$$

where E is the output voltage, V_c is the voltage across the capacitor C_s, a and n are positive model parameters. An increased voltage V_c across the capacitor C_0 causes an increased output voltage of the voltage source. The effective capacitance C_eff, representing the series connection of the capacitor C_s and the voltage source E, is given by:

$$C_\mathrm{eff} = \frac{C_\mathrm{s}}{1 + \frac{\mathrm{d}E}{\mathrm{d}V_\mathrm{c}}} = \frac{C_\mathrm{s}}{1 + a^n n V_\mathrm{c}^{n-1}}. \tag{2.72}$$

The excess losses are introduced by inserting the resistor R_h in series to the capacitor C_s and voltage the source E with a parallel voltage controlled current source, since the excess losses are frequency and voltage amplitude dependent. The current source is controlled according to:

$$I(V_\mathrm{h}) = (bV_\mathrm{h})^m, \tag{2.73}$$

where I is the output current, V_h the voltage across the resistor R_h, b and m are positive model parameters. With increasing voltage drop across the resistor R_h, a high current flows in the parallel branch of the current source, representing the saturated behaviour of the core material.

The eddy current losses are implemented by placing a resistor R_eddy in series to the aforementioned components. The parameter R_eddy is used to adjust the losses to the measured losses. Thus, the reluctance of the yokes and the limbs of a transformer core are modelled as a series circuit of capacitance and resistance.

The six model parameters (C_s, R_h, a, b, n and m) are obtained by means of an optimisation problem. The model parameters do not have any physical relation to measured parameters. The aforementioned capacitance-permeance analogy-based hysteresis model is herein referred to as CPH model.

Preisach Hysteresis Model

The Preisach model of hysteresis was first proposed in 1935 in [Pre35] by Ferenc Preisach. The Preisach model is a phenomenological approach based on the parallel connection of independent relay operators, also referred to as Preisach hysteron, to describe the rate-dependent hysteresis phenomena. With increasing number of parallel Preisach hysterons, the accuracy improves [May03]. The Preisach model usually provides a higher accuracy than the JA model at the price of higher demand for computing power [BCP03]. Special attention needs to be paid during the measurements, because the Preisach model is sensitive to errors in the experimental data [Zir+14].

Dynamic Hysteresis Model

The phenomenological DHM proposed in [Zir+14] uses the major hysteresis loop, e. g. from the manufacturer's data sheet or measured, as basis. It uses the magnetic flux density B as input and the magnetic field H as output. A distinguishing feature of the DHM is its 'horizontal' organisation that is a monotonic decrease of the distance ΔH between the ascending (for definiteness) reversal curve and the outer (envelope) loop constructed during the previous process. This keeps any hysteresis trajectory inside the outer loop and guarantees the absence of non-physical negative slopes ($\mathrm{d}B/\mathrm{d}H$) in any constructed trajectory. The model principle was first verified when construction first-order reversal curves (FORCs) [Zir+04]. Further information on the FORCs can be found in [DS13]. Due to the absence of FORCs in steel data sheets and the challenges during the measurement of FORCs, the currently employed DHM was fitted to symmetrical hysteresis loops given in the steel catalogues [Zir+17]. Typical, static $B-H$ loops provided in the catalogues reach 1.7 - 1.8 T. Therefore, they are supplemented with singe-valued saturation curves, which reach (depending on the material) the level of 1.96 - 2.06 T. Two versions of the DHM are presented in [Zir+14], namely a history-dependent (HDHM) and a history-independent model (HIDHM). The dynamic components, namely the last two terms of (2.69) with the parameters $g(B)$ and $\delta = \pm 1$, incorporate the dynamic losses in the hysteresis model and make the SHM to a DHM. The DHM has been successfully applied to many applications, especially in the field of power transformer modelling, e. g. in [Zir+11; ZMA14; Zir+15; Zir+17; ZMR17; Zir+21].

Empirical Hysteresis Models

In [MN21] a semi-empirical hysteresis model is proposed for the loss calculation under non-sinusoidal flux conditions in electrical machines. The model is based on the shift of the anhysteretic characteristic

of the material, which is realised with a time-dependent model parameter. This parameter depends on the last maximum flux density value, the knee point, and the difference between the maximum allowed time shift and the current value. Four additional parameters are used to fit the model to the measured material properties. Epstein frame measurement were used to fit the model parameters and to assess the model performance at different flux density levels and superimposed frequencies at 5 Hz/1.8 T and 5 Hz/80 Hz, with a deviation between simulated and measured loss below 5 % for the measured loss of 0.264 W/kg at 5 Hz/1.8 T. Further measurement and simulation up to 2 kHz revealed a deviation in losses below 10 %. The tests were carried out with electrical steel of the type M400-50A.

Transformer Core Characterisation

The transformer core manufacturer usually provide Epstein frame measurements according to [IEC09]. If the Epstein frame characteristics are not available and the core material is unknown, transformer terminal measurements can be useful to obtain relevant information. From the terminal measurement, the flux linkage versus current hysteresis loops ($\Psi - i$) can be derived. Due to the electromagnetic coupling of all phase windings, the $\Psi - i$ characteristic derived from the terminal measurements cannot be used directly for the subsequent transformer or hysteresis modelling. The $\Psi - i$ characteristic for the three phases differ in their width and shape. For that reason, different single-phase measurement techniques were described to mitigate the interphase coupling [FY02; AMR21], whereas the method described in [FY02] do not distinguish processes in the limbs and yokes, which makes the derived transformer model not topological [Zir+22b].

2.4.5 Heuristic Optimisation Algorithms for Hysteresis Parameter Identification

Heuristic optimisation algorithms are computational processes iteratively trying to improve a possible solution with respect to the pre-defined quality measure. Heuristic optimisation algorithms make few or no assumptions about the given problem to be optimised. They can search large spaces of possible (near-) solutions at reasonable computational cost, without guarantee either their feasibility, optimality or deviation between the obtained and optimal solution [Dub+13]. For the parameter estimation of the JA and the CPH model, the Nelder-Mead Simplex (NMS) algorithm and the particle swarm optimisation (PSO) are used. The NMS algorithm and the PSO algorithm were selected due to their simple implementation, the expected short runtime and no limitation on the number of parameters to be optimised. The PSO were first and only used for the JA hysteresis model, because it turned out during the optimisation that the NMS algorithm computational speed is significantly faster than the PSO algorithm on the same hardware. The same starting points for both optimisations yield similar results, whereas the NMS required several ten minutes and the PSO required several hours. The implementation in MATLAB of both logarithms can be found in **Appendix J**.

Nelder-Mead Simplex Algorithm

The NMS algorithm was introduced in [NM65] in 1965 and is used for unconstrained optimisation. The NMS attempts to minimise a non-linear function of n real variables using the function value without any derivative information and is therefore assigned to the class of direct search methods. The method uses the concept of simplex, which is a polytope of $n+1$ vertices in n dimension. Therefore, a 2-simplex can be illustrated by a triangle in the xy-plane (two dimensions, see **Figure 2.28**). The NMS searches a local optimum of a given function with n variables. Each value in the solution space is weighted, according to is solution quality. This can be done by an objective function, e. g. with the usage of measurement data. The algorithm can be described as follows:

(1) choose $n+1$ starting points x_{n} which build the n-simplex,
(2) sort the starting points in descending order according to their quality,
(3) calculate the mean value m out of all starting points x_{n} neglecting the last/most inaccurate point,
(4) reflect the most inaccurate point on the centre: $r = m + \alpha(m - x_{\mathrm{N}})$,
(5) if the function value of r is more accurate than the one for x_0, determine the expansion point $e = m + \gamma(m - x_{\mathrm{N}})$; replace x_{N} by the more accurate point e or r and start over with step (2),
(6) if the function value of r is more accurate than the second most inaccurate point $x_{\mathrm{N}-1}$, replace x_{N} by r and go back to step (2),
(7) let h be the more accurate function value of the two points x_{N} and r, determine the contracting point $c = h + \beta(m - h)$,
(8) if c results in a more accurate function value than x_{N}, replace x_{N} by c and return to step (2),
(10) compress the simplex for every point x_{i} and replace x_{i} by $x_{\mathrm{i}} + \sigma(x_0 - x_{\mathrm{i}})$.

The iteration of these steps is carried out until the convergence criteria are fulfilled. The simplex usually moves towards a local optimum and decreases its volume/area around the local optimum. Typical values for the parameters α, γ, β, σ are 1 (reflection), 2 (expansion), 1/2 (contraction), and 1/2 (compression), respectively. Whereas the following constrains apply: $0 < \alpha < \gamma$ and $\beta, \sigma \in]0, 1[$. The NMS depend on the starting values and number of iterations. Therefore, suitable starting values combined with a low number of iterations can reduce the computational time. The starting values for the JA and ReCap model were chosen based on trial-and-error method.

Particle Swarm Optimisation

The PSO was proposed by [KE27] in 1995 for the optimisation of non-linear functions. Kennedy and Eberhart were interested in the models proposed by [HG90], where bird flocks flying around in flocks with no particular destination, trying to find a roosting area. The roosting area to Kennedy and Eberhart was the local optimum solution of a function. The following terminology is used in context of the PSO:

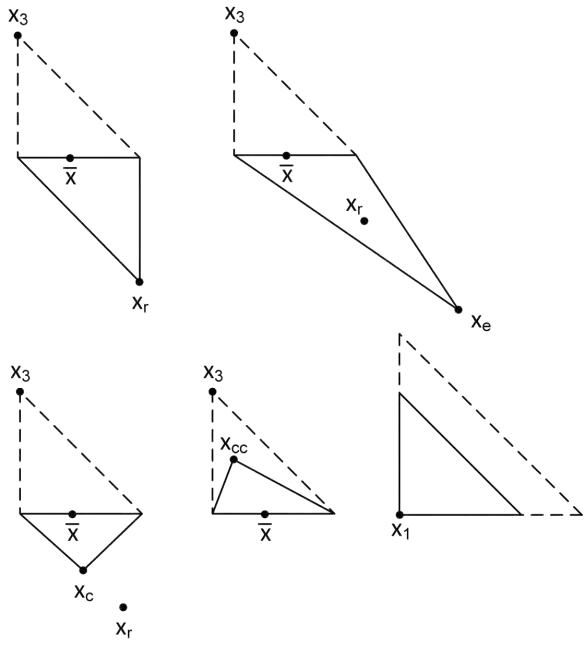

Figure 2.28: NMS operations on the example of 2-simplex with $2+1$ vertices; original simplex is indicated by dashed lines.

- particle: individual point in the solution space which can move/fly,
- swarm: population of particles; multiple swarms exist, attempt to find an accurate solution,
- cycle: change of position of each particle,
- velocity: distance per cycle which can be covered by a particle,
- inertia weight: controls the impact of the previous velocity on the current velocity of the particles,
- pbest: personal best position for each particle found so far,
- gbest: global best position found by swarm so far,
- cognition weight: attraction of particle towards its personal best position,

Assuming a function depending on N parameters x_{N}, on which the PSO algorithm is applied. At the beginning of the PSO algorithm a number I of random initial parameter sets, each consists out of N parameters, are initialised. In order to reduce the computational time, the area for the initialisation of each parameter can be pre-defined. Each parameter is also initialised with a random speed and direction in the N-dimensional space, and the range of speed can be pre-defined. Now, I sets/swarms of N parameters are initialised. After each calculation step, the position, direction and speed is updated, and the function is evaluation with the values of the parameter set/swarm. In the context of hysteresis parameter estimation, the deviation between the measured and the calculated current waveform is taken as a quality measure of the optimisation. The deviation between the measurement and the function value for each parameter set/swarm is stored in the variable *pbest*, and the deviation of all sets/swarm is stored in the variable *gbest*. The speed and direction of the particles is updated in a way that the deviation between the measurement and calculation is reduced to a (pre-defined) minimum. Thus, the PSO can be carried out simultaneously for each

parameter set/swarm to reduce the computational time. This was not done during this work, due to the additional programming effort.

2.5 Susceptibility of Power Transformers to Low Frequency Currents and Mitigation

The transformer core design and vector group is crucial for the transformer response to LFC [WNM21]. The typical transformer fleet of a utility is not homogenous in design and type of transformers, due to the transformer lifetime of several ten years up to 100 years [Cig15]. Therefore, a first transformer fleet scans, taking into account the core design (number of wounded and unwounded limbs), grounding type of each transformer and the transformer geographical location is important. Important for the decision, whether operational or hardware mitigation techniques are required, is also the thermal assessment of the transformer fleet. Short-duration GICs in the range of several ten minutes, will probably not cause half-cycle saturation, whereas long-duration GICs could cause overheating of the transformer or, at least, require a load-reduction, in order to maintain their service. The following two sections highlight the frequency range, which can be harmful to power transformers and possible mitigation techniques.

2.5.1 Susceptibility of Power Transformers to Low Frequency Currents

Besides LFC bias, other low frequency transient phenomena such as inrush current events [LFJ12], ferroresonance operation [Zir+21] and out-of-phase synchronisation of generator transformers [Art91] can cause transformer core saturation. A transformer susceptibility measure is based on the per-unit area of the transformer core available for zero-sequence return flux (**Table 2.5**) [McN90].

Table 2.5: Transformer susceptibility to DC for different core types [McN90].

# Phases & limbs	Core Type	Core return area for DC flux
Single-phase	Core/Shell	1
Three-Phase, seven-limb	Shell	0.67
Three-phase	Shell	0.5
Three-phase, five-limb	Core	0.24 - 0.33
Three-phase, three-limb	Core	0

Regarding the susceptibility of power transformers and the power grid to GICs, not only high GIC/DC amplitudes should be considered [FS08; FS10; Gau14]. Still questionable is the long-term effect of (small) GICs or DC bias on power transformers [Pul+17], because of the significant amount of time can pass between an initial damaging event in a power transformer and its actual failure.

Another aspect regarding the susceptibility is the symmetry of the LFC/DC between the phases. Experiments with three-limb transformers between 2.3 kVA and 45 kVA exposed to unbalanced DC revealed a higher reactive power demand due to the imbalanced mmf in each limb, resulting in a DC flux inside the core [YFB94; You+96].

2.5.2 Mitigation of Low Frequency Currents in the Power Grid

In order to mitigate LFCs or the negative effects of LFCs in the power grid, additional active and passive electrical components can be added to the power grid or operational strategies can implement in the power grid operation procedures.

Besides the installation of additional components in the power grid to mitigate LFCs, operational countermeasures such as load reduction of key power transformer, line switching, restore out-of-service transmission lines and transformers and discontinue planned maintenance work [Bol02; Mol02; KZO18] can be initiated.

Two types of DC suppression devices, which are installed in the transformer neutral points, are standardised in [IEC01d]. The first device uses a resistor as current limiting element in combination with a protection spark gap and a bypass switch.

The second device blocks the DC in the transformer neutral via a capacitor. During a fault in the power grid the capacitor is bypassed with a high-speed bypass switch and with a mechanical bypass switch. A similar device was tested in the Hydro-Québec power system [Bol02] and the Wisconsin ATC power grid [Fax+17]. The effect of a capacitor based neutral blocking device was investigated with an electromagnetic transient program in [Khu+22].

In [DDY05] a DC injection system is proposed and tested in several on-site experiments. The system can inject up to 10 A DC per transformer neutral. The compensating system uses a rectifier bridge, controlled by transformer neutral point current measurements. In [FFM94] an externally excited DC motor connected between the transformer neutral point and ground is proposed to compensate GICs. A similar approach is experimentally investigated in [FFM94] using an externally excited DC motor connected between the transformer neutral point and substation ground.

In [AL07] an active compensation system is proposed, which uses an additional winding on the transformer for compensation. The DC in each phase is separated by a filter from the line current and is supplied into the compensation winding in the opposite direction. Thus, the DC flux inside the core is compensated. This method requires additional filter components, which increases the transformer footprint and volume with increasing rated voltage of the transformer.

Direct Flux Compensation

Another method to mitigate negative effects of LFCs in the power transformer is the compensation of the low-frequency or direct flux inside the transformer core [YFB94; Her+18]. The mmf compensation inside the transformer can be realised with an axillary transformer in the tertiary winding, as proposed in [YFB94]. Whereas the challenge is to build a large linear inductor and maintain a small resistance [YFB94]. Another approach uses an additional winding on the wounded transformer limbs [Ham16]. The system presented in [Ham16] is further referred to as DCC. The method does not block a transformer neutral point current. The current can still flow through the transformer neutral, but the corresponding direct flux inside the transformer core, which causes half-cycle saturation, is compensated. This approach has the advantage, that the transformer

protection is not affected and no adoption in the power system/transformer protection need to consider [Ach22]. The direct flux compensation uses a zero-point control to reduce the direct flux inside the wounded limbs. The input signal for the control is the second harmonic of the induced voltage, measured via two magnetic shunt paths on the top yoke of a power transformer (see **Figure 2.29**) between the limbs A-B and B-C [HL14; Ham+17] or measured inside the limb with a sensor in a transformer limb cooling channel. The second harmonic in the measured voltage increases with increasing direct flux inside the transformer core. The increased direct flux increases the off-core flux and thus increases the voltage induced in the measurement windings on the two magnetic shunt paths. From the two measurements, the relative flux level can be calculated in each wounded limb, according to (2.74) and (2.75).

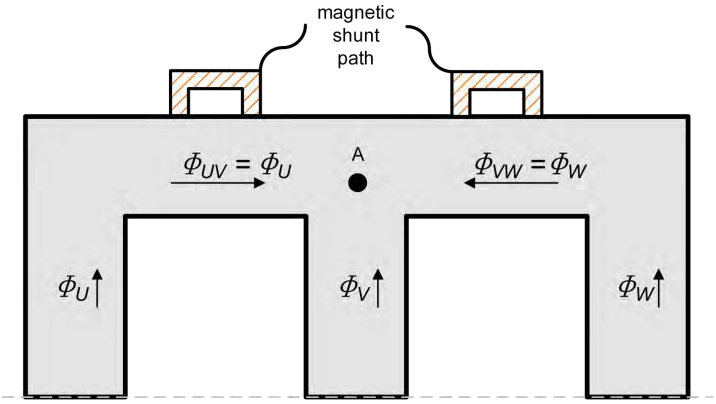

Figure 2.29: Half-section schematic of three-limb transformer core with magnetic shunt path on top yokes.

$$A : 0 = \Phi_{AB} + \Phi_B + \Phi_{BC}, \tag{2.74}$$

where Φ_{UAB} and Φ_{BC} is measured and Φ_B is unknown. Then the unknown flux inside limb V Φ_B is calculated to:

$$\Phi_B = -(\Phi_{AB} + \Phi_{BC}), \tag{2.75}$$

where $\Phi_{AB} = \Phi_A$ and $\Phi_{BC} = \Phi_C$ in case of a three-limb transformer. In case of five-limb transformer core (**Figure 2.30**), the flux inside limb A and C can be calculated with the knowledge of the reluctance of the adjacent limb (A') and the wounded limb (A).

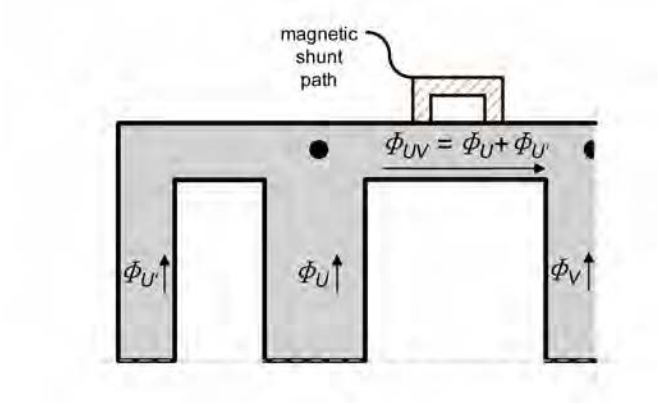

Figure 2.30: Quarter-section schematic of five-limb transformer core with magnetic shunt path on top yoke.

The maximum DC per phase, which can be compensated by the system depends on the number of turns and the current injected in the fourth winding, according to (2.76).

$$I_{\mathrm{DC}} = I_{\mathrm{DC,CW}} \cdot \frac{N_{\mathrm{CW}}}{N}, \tag{2.76}$$

where I_{DC} is the DC per phase which can be compensated by the system, $I_{\mathrm{DC,CW}}$ is the injected rms value of the current in the compensation winding (CW), N_{CW} is the number of turns of the compensation winding per limb and N is the number of turns of the winding where the DC to be compensated is passing through (e. g. the high-voltage winding of the transformer). N can change during the transformer operation, if a tap changer is used in the transformer. Assuming $N_{\mathrm{CW}} = 2$, $N = 846$ and $I_{\mathrm{DC,CW}} = 300\,\mathrm{A}$ a DC of $709\,\mathrm{mA/phase}$ can be compensated by the DCC system. **Figure 2.31** depicts the opened DCC cabinet at the transformer equipped with a NPC and DCC measurement system (**Chapter 3**).

Figure 2.31: DCC cabinet at 400/110/30 kV 300 MVA transformer.

The zero-point phase-fired controller is used together with thyristors to control the compensating flux inside the transformer core [Her+18]. The power electronics supplying the additional compensation winding on each wounded transformer limb is located outside the active part of the transformer, e. g. in a cabinet at the outside of the transformer tank (see **Figure 2.31**). **Figure 2.32** depicts the simplified DCC system.

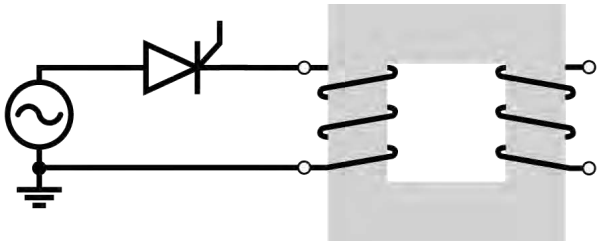

Figure 2.32: Schematic of DCC system.

2.5.3 Damping Effect of the Network Impedance on the Point of Common Coupling

For transformer tests, the network impedance of the supply on the point of common coupling can affect the current and voltage waveform. As reported in [Zir+18b] during a B2B test of two 400 MVA power transformers, it is important ot take into account the positive (Z_1) and zero-sequence (Z_0) impedance of the network at the point of common coupling in the calculation to accurately reproduce the measured current waveform. Especially the 150 Hz third current harmonic in the neutral conductor was pronounced, due to the half-cycle saturation in the three phases of the two B2B transformers under DC bias, resulting in three positive and negative current peaks during one period. Accompanied by the half-cycle saturation, also a voltage drop at the point of common coupling can occur, due to the increased magnetisation currents. Therefore, the excitation voltage (waveform) and amplitude should be monitored for voltage dips during laboratory test with superimposed DC.

2.6 Demagnetisation of Power Transformers

The remanent flux in a transformer core can be some ten percent of the nominal flux density [Cig96]. Remanent flux in transformer cores can be caused by DC like currents in the transformer windings. The remanent flux can negatively affect the transformer diagnosis, such as Sweep Frequency Response Analysis (SFRA) [IEC07a], magnetising current measurements, magnetic balancing tests or transmission ratio measurements. But also re-energising a transformer with remanent flux can cause increased inrush currents [Chi10]. These high inrush currents itself can cause negative effects such as mechanical damage to the windings [SF02], increased transformer audible sound, faulty tripping of protective devices [Kov+11] and increased stress on the insulation. Therefore, it is essential to demagnetise the transformer core and thus reduce the remanent flux to a minimum before energisation. In order to remove any remanent flux in the transformer core, the magnetic flux density in the transformer core needs to be increased above nominal flux density level to force

the transformer on the major hysteresis loop. Lower flux levels will only drive the transformer core on a minor hysteresis loop but will not remove/lower the remanent flux. GO steel materials can be demagnetised by three methods:

(1) increase the material temperature above its Curie temperature (typical, several hundred degrees Celsius),
(3) strong vibration force on the core material,
(3) applying on opposing magnetic field.

The first two methods are not feasible with an assembled and installed transformer. Only the latter method is feasible without damaging the transformer. The last method can be accomplished by applying a varying voltage $U(t)$ and/or a variable frequency f due to the linkage of flux, voltage and frequency $\Psi \propto N \cdot U(t)/f$. Therefore, three electrically demagnetisation options are available [Kov+11]:

(i) variable voltage constant frequency (CVCF),
(ii) constant voltage variable frequency (CVVF),
(iii) decreasing amplitude of DC with polarity reversal,

where (iii) is a variation of (ii). The method from (iii) is a modified version of the method suggested in [IEE13]. The CVCF method has two advantages compared with the CVVF method [Kov+11]:

(a) easier physical realisation as voltage source,
(b) requires less time for reduction of remanent flux.

In commercially available portable transformer test devices, the method (iii) is implemented.

The common procedure for the demagnetisation of a power transformer core is to apply the predefined sequence between the high-voltage terminal of the winding on the middle limb and the high-voltage neutral point, if accessible. If no high-voltage neutral point is accessible via a terminal, e. g. at small distribution power transformers, the windings on the outer two limbs are supplied with an in-phase voltage and the winding on the middle limb is used as current return. Thus, the current via the winding on the middle limb is twice the current in the outer two windings.

SFRA and hysteresis measurement (**Section 4.9**) proofed that demagnetise a three-limb or five-limb transformer core via the middle limb can be insufficient. A sequential demagnetisation of the limbs via their high-voltage windings and the high-voltage neutral also show that the sequential demagnetisation of the limbs is not able to reduce the remanent flux to a minimum, proofed by SFRA measurements [Eng20]. Depending on the demagnetisation sequence of the phases, e. g. A-B-C or B-A-C, and due to the magnetic asymmetry of the magnetic core, a remanent flux can remain on the transformer core.

In [Leo+15] a demagnetisation method with two voltage sources for three-phase transformers with three-limb and five-limb core was tested with topology models of three-limb and five-limb

transformer cores and with a single-phase transformer in a laboratory scaled test. Tests on large power transformers are pending.

3 On-Site Low Frequency Current Measurements

A self-engineered, stand-alone and remote controllable data acquisition system was first developed in [Hal14] as version v2014 and continuously extended and improved [Woh20; Frö21; Alb+21b]. The measurement system is currently located at nine transformer neutral points in the 220 kV and 380 kV power transmission levels. The systems are distributed across the transmission grid in eight different substations, as depicted in **Figure 3.1**. The measurements are used to validate the developed LFC-Simulator [SAR21b] and to continuous monitor LFCs in the power transmission grid.

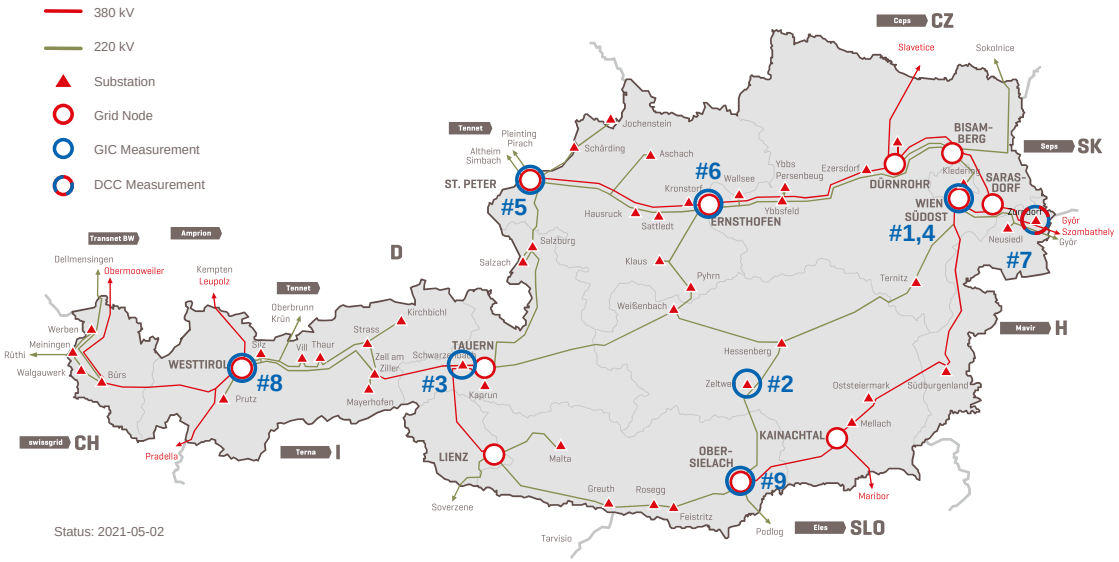

Figure 3.1: Substation in the Austrian transmission grid equipped with measurement system, adopted from [Aus21].

The first version of the measurement system [Hal14], hereafter referred to as v2014, was first installed at measurement point #01, #02, #03, #04 and #05. From 2020 on, the version v2019 was established in #06, #07 and #08. The latest version v2021 was established 2021 in #09. During 2020 and 2021 the installed versions v2014 were updated to v2019. **Table A.2** gives an overview of the versions, runtime and their location.

The measurement systems are build-up with similar building blocks. A CT is used as a current sensor, which delivers an output current proportional to the primary current to be measured. A shunt is used to convert the current signal into a proportional voltage signal. All voltage channels are passed through an active low-pass filter second order Sallen-Key design as unity-gain buffer (amplification $A = 1$) [SK55] with a cut-off frequency of 0.7 Hz. The second order filter has a damping characteristic with a steepness of -20 dB/decade and a magnification factor $Q = 3$. Therefore, the -3 dB damping frequency is 0.7071 Hz. The power system frequency of 50 Hz is damped with -57.5 dB and the 16.7 Hz of the train system is damped with -48.5 dB. The cut-off frequency of 0.7071 Hz allows using a data acquisition system with a comparable low sample rate of

1 Hz. For that purpose, the single board computer Raspberry Pi 4 B is used, which communicates with the ADC via I^2C protocol. In addition to the data acquisition, the single board computer, in combination with a GSM module, provides the remote access to the measurement system.

Version v2014 could measure currents with an amplitude between 3.5 A in one direction and 25 A in the opposite direction. The follow-up version v2019 was designed and tested in [Woh20]. With version v2019 the system is able to measure current amplitudes in the range of ± 25 A. Both versions, v2014 and v2019, operate with the same CT (LEM IT65-S ULTRASTAB) for the NPC measurement. For the measurement of the NPC the earthing switch of the transformer neutral is bypassed with a mobile earthing equipment, which is feed through the CT, as depicted in **Figure 3.2a**.

Besides the extended measurement range of v2019, three additional voltage measurement channels (max. $\pm 5\,\mathrm{V}$) were added to the measurement system. These additional channels are currently used only with client #07 to measure the injected phase currents of a DCC system[1] installed at this transformer.

The latest version v2021 is based on version v2019, but can also be operated with the LEM LA200SD/SP3 CT to measure the transformer NPC. Version v2021 was designed and tested in [Frö21]. This CT requires an additional supply voltage of ± 24 V and an additional burden of $350\,\Omega$. The LEM LA200SD/SP3 CT is a split-core CT, which is installed around the arm of the transformer neutral point switch, as depicted in **Figure 3.2b**. The advantage of version2021 is that the transformer neutral point can be switched from remote, which is not possible with v2019. No additional earthing equipment is required to measure the NPC.

[1] The Direct Current Compensation (DCC) system is part of Siemens Energy Transformers Pretact® concept. The DCC system uses a fourth winding on already wounded limbs which are energised with a phase controlled current. The magnetic flux produced by the DCC systems compensates for a DC flux inside the limbs, e. g. caused by GICs. See also **Section 2.5.2** for detail information on the DCC system.

(a) Installed transformer neutral point current measurement system with open cabinet.

(b) Split-core CT installed on a transformer neutral point switch with the cabinet and temperature sensor.

Figure 3.2: Installed measurement systems.

3.1 Measurement System Design and Characteristic

The measurement systems are built out of three printed circuit boards (PCBs). The supply PCB, the measurement PCB and the DCC PCB. The supply PCB provides the power for the CTs and the rest of the electronics. The measurement PCB contains the signal conditioning of the NPC and DCC channels. The DCC PCB contains the power supply and the active low-pass filter for the three DCC channels. An overview of the different measurement system versions and PCB versions in given in **Table A.1**.

3.1.1 Version v2021

The LFC measurement system v2021 is an extension of v2019 and can be operated either with the LEM IT65-S ULTRASTAB or the LA200SD/SP3 CT. The LEM LA200SD/SP3 CT uses the closed loop hall effect technology to generate an output current proportional to the primary current to be measured. Due to the temperature sensitivity of the Hall sensors used in the CT, the measurement signal is temperature compensated via software. Because the CT has no build-in temperature sensor, an external temperature sensor (DS18S20+ in three-wire configuration) is located in the IP67 rated

enclosure of the CT. The temperature characteristic of the CT and the overall measurement system (CT and secondary electronic) was evaluated in climate chamber tests in the temperature range from -20 °C to +40 °C. The temperature test results and the CTs data sheet [LEM20c] revealed, that only the CT LEM LA200SD/SP3 has a measurable temperature related offset drift. Therefore, the temperature related offset drift was measured in the range of -20 °C to +40 °C in steps of 4 K and 90 min per step. A correction function of fifth order was subsequently fitted to the measurement data. The field test since December 2021 with regular offset check at intervals of 30 days reveals a small offset drift, which is within the measurement accuracy. **Table 3.1** lists the conditions during the offset corrections and the offset. For an almost constant temperature and the period between December 2021 and January 2022 no offset correction was required. Small offset corrections were required from March 2022 on. **Figure 3.3** depicts the electronic layout of v2021. In comparison to v2019 (**Figure A.1**) a non-inverting amplifier is used in block 5 (**Figure 3.3**) to scale input current range of ± 25 A to fit it to a voltage range of 0 V - 4.096 V. The measurement electronic for the DCC monitoring is similar to the neutral point current measurement and is depicted in **Figure 3.4**.

Table 3.1: Offset corrections of client #09.

Date	**relative offset** in mV	**Temperature** in °C	**Remarks**
2021-12-01	-8.31	2.2	
2021-12-21	-1.43	4.9	
2022-01-28	0.0	5.4	no correction; offset within ±4 mA
2022-03-07	-0.08	9.1	offset current: -16.17 mA
2022-04-04	-4.13	13.3	offset current: -14.5 mA
2022-05-04	1.19	10.4	offset current: 63.97 mA

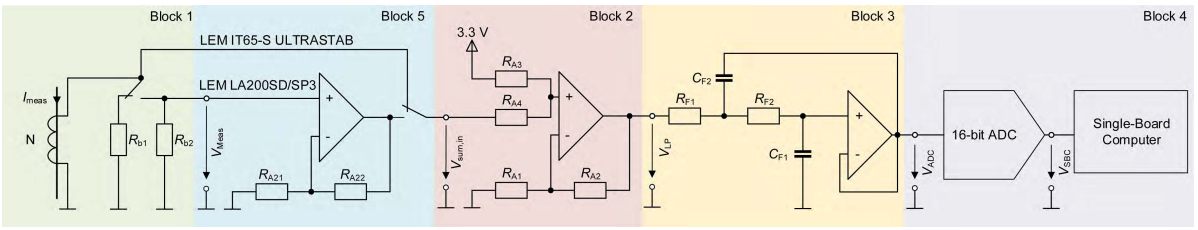

Figure 3.3: NPC measurement electronic layout of v2021.

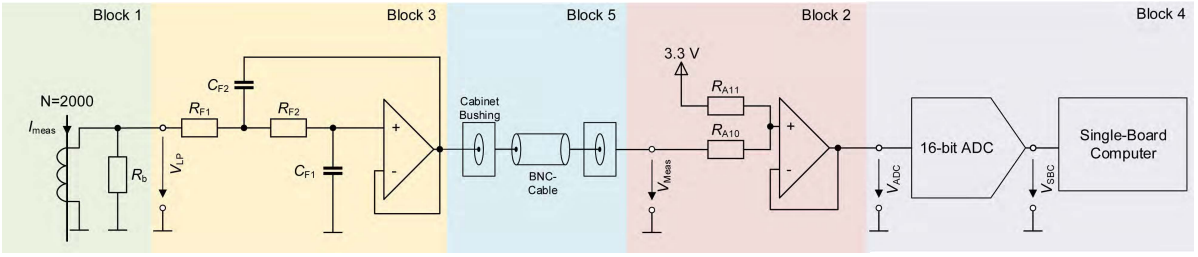

Figure 3.4: DCC current measurement electronic layout.

Figure 3.5 depicts the layout of the extended measurement system, including the DCC measurement in the substation. The *Raspberry Pi* and the *Power Supply* PCB are supplied by an isolating transformer.

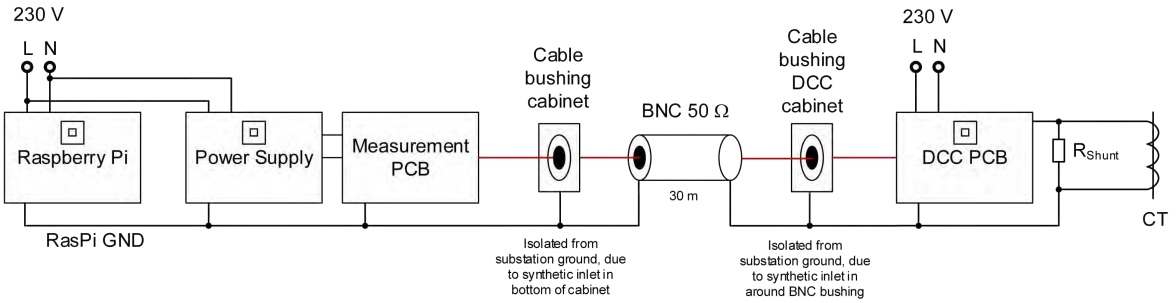

Figure 3.5: Grounding schematic of the measurement system including the DCC measurement.

3.2 Measurement System Uncertainty

The measurement system uncertainty is calculated according to ISO/IEC Guide 98-3 [Joi95]. Detailed information on the measurement systems component tolerances are given in **Appendix A.3**. The overall measurement systems accuracy for the NPC and the DCC channels is given in **Table 3.2**.

Table 3.2: Guaranteed and typical measurement systems accuracy of the versions v2019 and v2021.

Channel	Accuracy		Range
	guaranteed	typical	
NPC	2.0 % ±1 mA	0.5 % ±1 mA	±(1 A_{DC} - 25 A_{DC})
DCC	1.2 % ±10 mA	0.5 % ±10 mA	±(1 A_{DC} - 250 A_{DC})

For the calculation of the measurement uncertainty, the measurement system transfer functions are derived for the different building blocks, depicted in **Figure A.2**, **Figure 3.4** and **Figure 3.3**. The summing amplifier in block 2 of the NPC channel has the following transfer function:

$$V_{\mathrm{LP,NPC}} = \left(V_{\mathrm{meas}} \cdot \frac{R_{\mathrm{A3}}}{R_{\mathrm{A3}} + R_{\mathrm{A4}}} + 3.3\,\mathrm{V} \cdot \frac{R_{\mathrm{A4}}}{R_{\mathrm{A3}} + R_{\mathrm{A4}}} \right) \cdot \left(1 + \frac{R_{\mathrm{A2}}}{R_{\mathrm{A1}}} \right). \tag{3.1}$$

The summing amplifier in block 2 of the DCC channel has the following transfer function:

$$V_{\mathrm{LP,DCC}} = \left(V_{\mathrm{meas}} \cdot \frac{R_{\mathrm{A3}}}{R_{\mathrm{A3}} + R_{\mathrm{A4}}} + 3.3\,\mathrm{V} \cdot \frac{R_{\mathrm{A4}}}{R_{\mathrm{A3}} + R_{\mathrm{A4}}} \right). \tag{3.2}$$

The active low-pass filter second order Sallen-Key design for the NPC and the DCC channels has the following transfer function:

$$G(\mathrm{j}\omega) = \frac{1}{1 + \mathrm{j}\omega C_{\mathrm{F1}}(R_{\mathrm{F1}} + R_{\mathrm{F2}}) + \omega^2 R_{\mathrm{F1}} R_{\mathrm{F2}} C_{\mathrm{F1}} C_{\mathrm{F2}}}. \tag{3.3}$$

The transfer function of the measurement system, as function of the NPC, and the DCC, as function of the primary current, and the system components is given in (3.4a), (3.4b) and (3.4c) respectively. (3.4a), (3.4b) and (3.4c) are the transfer functions of the NPC with the LEM IT65-S ULTRASTAB, the LEM LA200SD/SP3 and the DCC channels with the LEM LF306-S CTs.

$$I_{\text{SBC, NPC LEM IT65}} = \left(1 + \frac{R\text{A2}}{R_{\text{A1}}}\right) \cdot \left(V_{\text{ref}} \cdot \frac{R_{\text{A4}}}{R_{\text{A3}} + R_{\text{A4}}} + \frac{N \cdot V_{\text{meas}}}{R_{\text{b}} \cdot \frac{R_{\text{A3}}}{R_{\text{A3}}+R_{\text{A4}}}}\right) \cdot \left(\frac{1}{1 + \text{j}\omega C_{\text{F1}} \cdot (R_{\text{F1}} + R_{\text{F2}}) + \omega^2 R_{\text{F1}} R_{\text{F2}} C_{\text{F1}} C_{\text{F2}}}\right), \tag{3.4a}$$

$$I_{\text{SBC, NPC LEM LA200SD/SP3}} = \left(V_{\text{ref}} \cdot \frac{R_{\text{A4}}}{R_{\text{A3}} + R_{\text{A4}}} + \frac{N \cdot \left(1 + \frac{R_{\text{A22}}}{R_{\text{A21}}}\right) \cdot V_{\text{meas}}}{R_{\text{b}} \cdot \frac{R_{\text{A3}}}{R_{\text{A3}}+R_{\text{A4}}}}\right) \cdot \left(\frac{1}{1 + \text{j}\omega C_{\text{F1}} \cdot (R_{\text{F1}} + R_{\text{F2}}) + \omega^2 R_{\text{F1}} R_{\text{F2}} C_{\text{F1}} C_{\text{F2}}}\right), \tag{3.4b}$$

$$I_{\text{SBC, NPC LEM LF306-S}} = \left(V_{\text{ref}} \cdot \frac{R_{\text{A4}}}{R_{\text{A3}} + R_{\text{A4}}} + \frac{N \cdot V_{\text{meas}}}{R_{\text{b}} \cdot \frac{R_{\text{A3}}}{R_{\text{A3}}+R_{\text{A4}}}}\right) \cdot \left(\frac{1}{1 + \text{j}\omega C_{\text{F1}} \cdot (R_{\text{F1}} + R_{\text{F2}}) + \omega^2 R_{\text{F1}} R_{\text{F2}} C_{\text{F1}} C_{\text{F2}}}\right), \tag{3.4c}$$

where R_{A1}, R_{A2}, R_{A3}, R_{A4} are the resistor values of the summing amplifier circuit (Block 2); C_{F1}, C_{F2}, R_{F1}, R_{F2} are the low-pass filter components (Block 3); ω is the angular frequency of the measurement signal; V_{ref} is the 3.3 V reference voltage from the single board computer; I_{meas} is the primary current to be measured; R_{b} is the measurement burden; N is the number of turns of the CT.

(3.5) describes the measurement uncertainty u of the measurement system.

$$u(I_{\text{meas}}) = \sqrt{\begin{array}{l}\left(\frac{\partial V_{\text{RasPi}}}{\partial R_{\text{b}}} \cdot u(R_{\text{b}})\right)^2 + \left(\frac{\partial V_{\text{RasPi}}}{\partial R_{\text{F1}}} \cdot u(R_{\text{F1}})\right)^2 + \\ \left(\frac{\partial V_{\text{RasPi}}}{\partial R_{\text{F2}}} \cdot u(R_{\text{F2}})\right)^2 + \left(\frac{\partial V_{\text{RasPi}}}{\partial C_{\text{F1}}} \cdot u(C_{\text{F1}})\right)^2 + \\ \left(\frac{\partial V_{\text{RasPi}}}{\partial C_{\text{F2}}} \cdot u(C_{\text{F2}})\right)^2 + ...,\end{array}} \tag{3.5}$$

where $\frac{\partial X}{\partial y}$ is the deviation of the overall transfer function to each measurement system component, $u(y)$ is the measurement uncertainty for each component. The system component values, and their uncertainty are given in **Appendix A.3**. **Figure 3.6** depict the calculated guaranteed and typical measurement system accuracy for the CTs used for the DCC system and NPC monitoring. For comparison the required accuracy of a class 0.5 CT, according to IEC 61869-2 [IEC12b], is indicated in the figures.

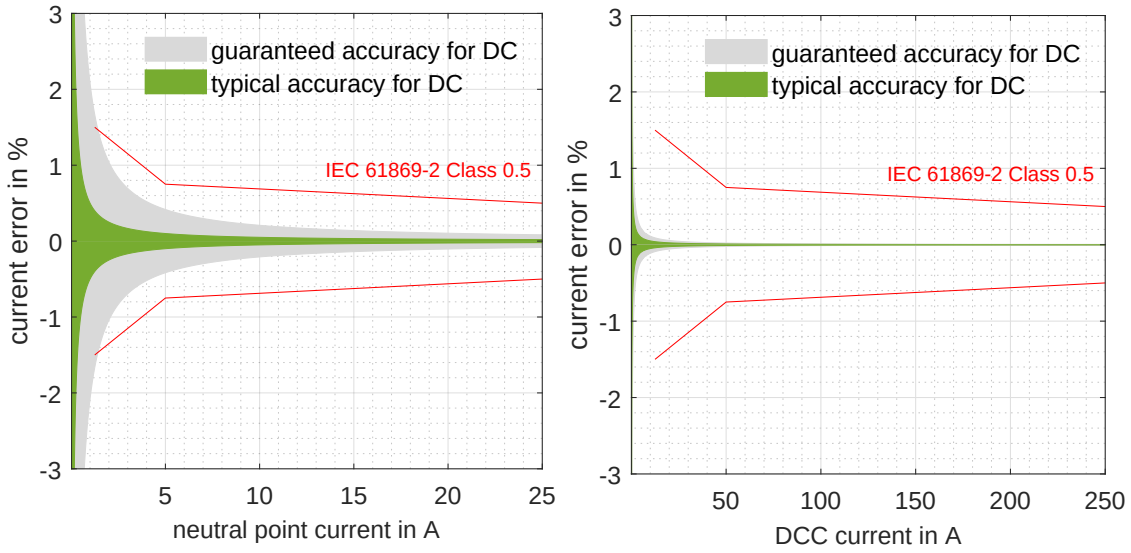

(a) Guaranteed and typical measurement system accuracy for LEM LA200SD/SP3.

(b) Guaranteed and typical DCC measurement system accuracy for LEM LF306-S.

Figure 3.6: Measurement system accuracy for different NPC CTs.

Figure 3.7 presents the Bode diagram and the setup response of the measurement system, which shows the aforementioned characteristics

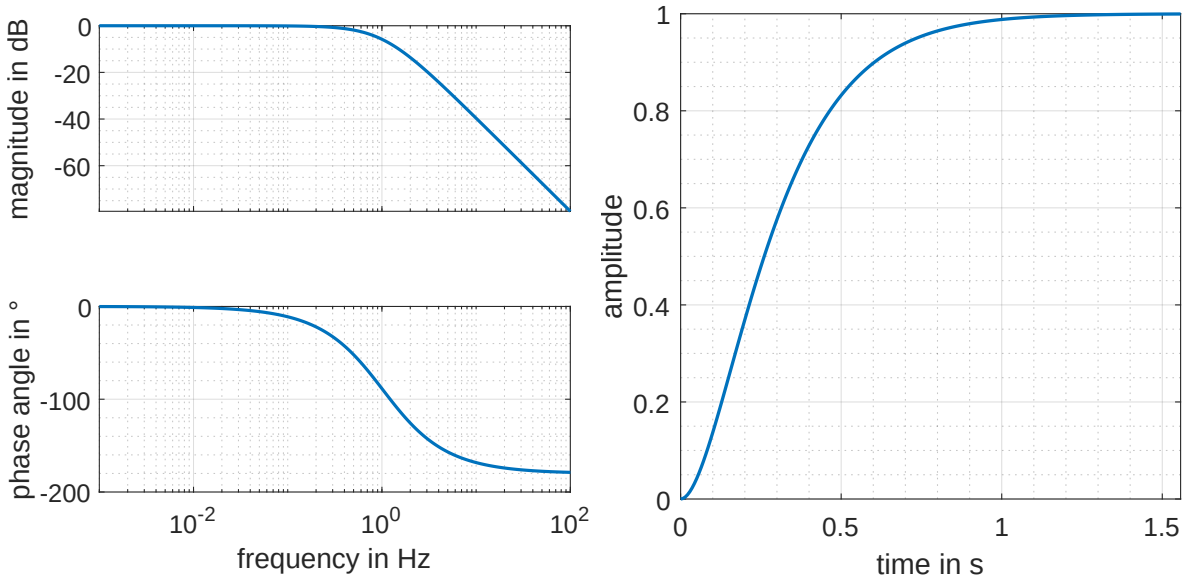

(a) Bode Diagram measurement system.

(b) Step esponse measurement system.

Figure 3.7: measurement system frequency and transient characteristic.

3.3 Calibration of Measurement System

Before the installation of the measurement systems in the substations, the systems offset is calibrated and the measurement accuracy is measured, using a calibrated OMICRON CMC 256-6 (accuracy

0.03 %) as current source.

The offset is corrected running the measurement system for at least 10 min in no-load conditions. From the measurement data the expected value μ from the data between the 0.25-quantile and the 0.75-quantile is derived. The difference between the ideal voltage for 0 V offset and the expected value μ is corrected in the software. Using the data range between the 0.25-quantile and 0.75-quantile, the effects of outlier on the offset correction is reduced.

In order to proof and guarantee the accuracy of the measurement system, a current and frequency sweep between 0 A and 25 $A_{DC/rms}$ and between 0 Hz and 50 Hz, as depicted in **Figure 3.8**, is used. The measurement is automatically processed in MATLAB and exported in an Excel spreadsheet. The data is then compared and guaranteed for accuracy, whereas violations of the calculated accuracy are flagged.

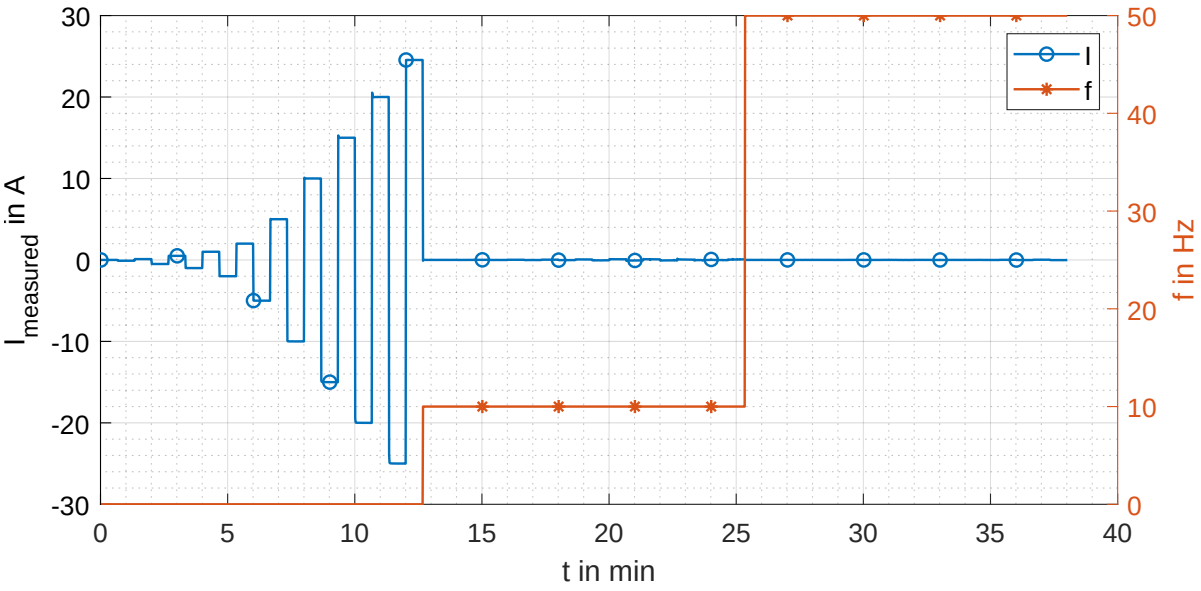

Figure 3.8: Measured current and frequency sweep profile for NPC channel.

As it can be seen from **Figure 3.8** with the first frequency step from 0 Hz to 10 Hz the measured signal/amplitude is sufficiently damped from the low-pass filter.

3.4 Alternative Current Measurement Techniques

This section evaluates other measurement principle for the measurement of transformer NPCs. For the power grid operator and for the mitigation of transformer NPCs it is important that the transformer neutral point can be switched from remote, to reduce the transformer outage time.

3.4.1 Resistive Measurement in Transformer Neutral Point Switch

For a resistive measurement via a shunt, a part of the transformer earthing switch could be replaced by a resistive material. The arm of the switch could be separated into two parts – the lower and

upper arm (yellow and red part in **Figure 3.9**). The diameter of the upper arm is larger than those of the lower arm. The shunt material is clamped between the two parts of the arm (see as an example an earthing switch with rectangular profile **Figure 3.9**).

A possible material could be the alloy MANGANIN®. MANGANIN® is used for example for high-precision resistors, because it has a low temperature coefficient between $+20\,^{\circ}\mathrm{C}$ and $+50\,^{\circ}\mathrm{C}$ with a parabolic $R(T)$ characteristic, a high long-term stability and an extremely low thermal force against copper. The physical properties of MANGANIN® are given in **Table A.4**.

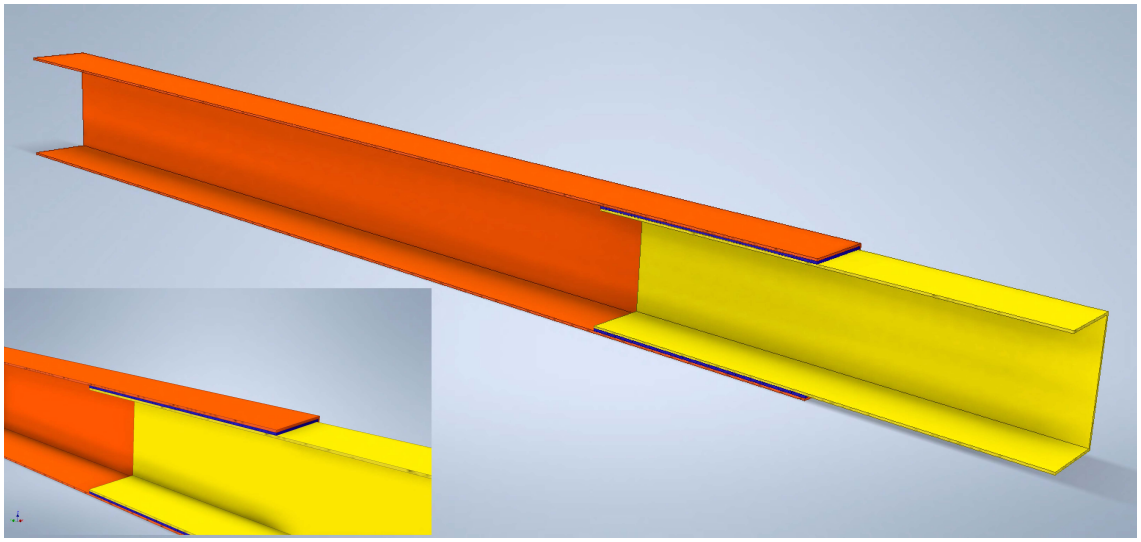

Figure 3.9: Rendered model of transformer earthing switch with upper (red), lower (yellow) and shunt-inlet (blue).

The resistive measurement of NPCs is not feasible due to two limiting effects. The thermoelectric effect limits the minimum shunt resistance and the short-circuit current capability together with the shunt power loss limits the maximum shunt resistance. In addition to the aforementioned limitations, the effort for the implementation of a resistive transformer neutral point current measurement is, compared to the currently used system, not in relation to the extended functionality. The shunt resistance can't be increased up to a level, where the measured voltage signal processing is possible with common effort, due to measurement disturbances. With the low shunt resistance value, electrochemical and thermoelectric effects need to be considered and will increase the measurement error.

3.4.2 Hall Sensors Laboratory Setup

With Hall effect sensors, the current through a conductor can be measured indirect via the magnetic field of the current in the conductor. The advantage of using Hall effect sensors is that the primary current circuit does not need to be opened for the sensor installation. One drawback is the temperature drift of Hall effect sensors. Hall sensors are used in test installation in the United States [Rad+19] for the measurement of the NPC until 2006 in the Forbes substation north of

Duluth, Minnesota [Rad12]. The installation in the Forbes substation was able to measure the transformer NPC with a resolution of approximately 0.1 A [Rad12]. A typical offset drift is 0 mV/° C ± 0.3 mV/° C [Mel13]. Another measurement uncertainty is the earth magnetic field affecting the NPC sensing. Therefore, a pair of two or four Hall sensors should be used and arranged in a 180° or 90° angle to each other around the transformer neutral conductor. For a laboratory setup within the framework of this work one Melxis MLX91205 [Mel13] Hall sensor was used. The schematic of the laboratory setup is depicted in **Figure 3.10**. With a distance of approximately 1 cm (conductor isolation integrated circuit (IC) package) between conductor and Hall sensor, a DC current of ±10 A revealed a differential voltage output of 50 mV. An AC with an amplitude of 10 A and a frequency of 0.5 Hz revealed a peak-to-peak voltage of 63.2 mV.

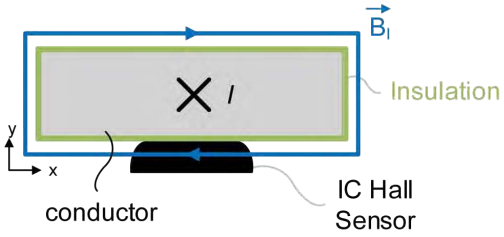

Figure 3.10: Schematic of laboratory setup with rectangular conductor and Hall sensor.

A further improvement using Hall sensors for transformer NPC sensing could be the arrangement of four Hall sensors in a 90° angle to each other, as depicted in **Figure 3.11**. This setup can especially be used around an earthing switch. With this arrangement, the effect of the earth magnetic field could be compensated. The pair of sensors are indicated with A1/2 and B1/2. The sensors A1 and A2 pick up the horizontal component of the earth magnetic field $\vec{B_E}$ with opposite sign, due to the mirrored arrangement. Thus, the horizontal earth magnetic field component vanishes, if the signal of sensor A1 and A2 is summed up and divided by the factor two. The same holds true for the sensor B1 and B2, which pick up the vertical earth magnetic field component.

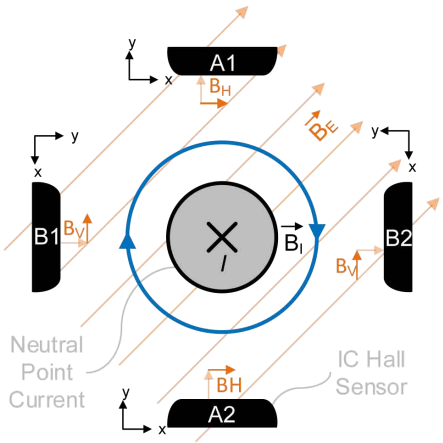

Figure 3.11: Proposed array out of four Hall sensors arrange around the transformer neutral point conductor.

The measured output signal proportional to the magnetic field of the current i of the quadrupole Hall sensor arrangement is:

$$V(i) = \frac{1}{4}(V_{\mathrm{A1}} + V_{\mathrm{A2}} + V_{\mathrm{B1}} + V_{\mathrm{B2}}), \tag{3.6}$$

where V_{Ax} and V_{Bx} is the voltage of the corresponding Hall sensor from **Figure 3.11**.

For a measurement system, using an array of four Hall sensors, the sensor's temperature dependency could be recorded in a climate chamber test in order to compensate the temperature related drift via software. Nevertheless, the long-term offset drift in the field should be monitored and frequently checked.

3.5 Measurement Case Studies

Typical NPC and DCC measurements during high and low geomagnetic activity are analysed in this section, prior to typical waveforms, frequency spectrum and current distribution.

3.5.1 Direct Current Compensation Measurement Analysis for 2021

In addition to the transformer NPC measurement at client #07, a DCC measurement system was installed monitoring the compensating current in the fourths additional winding on each wounded limb of the five-limb 400/110/30 kV 300 MVA transformer. The operating principle of the DCC system is explained in detail in **Section 2.5.2**. The measured compensating phase currents are analysed, regarding phase profile and phase relation with the NPC measurements at the same transformer. Due to improvements in the measurement hardware design, several hardware updates were carried out in 2020. Therefore, only the data from 2021 is analysed. **Table 3.3** lists the data statistics for the DCC measurement data. The total data coverage is 364.31 days which corresponds to a coverage of 99.81 % during 2021. For the further analysis, all measured current value above the maximum acting phase current of 250 A are removed. According to **Section 3.2** the guaranteed/typical DCC measurement accuracy is 1.2 %/0.5 % ±10 mA in the range of 1 A_{DC} - 250 A_{DC}, which corresponds to an error of 3.01 A/1.26 A at 250 A. With (2.76) the DC per phase is calculated from the compensating current measurement. ΔAB/BC/CA indicated the deviation between the compensating current in the dedicated phases. NPC_{DCC} represents the equivalent NPC, calculated from the sum of the DCC currents, according to (2.76). ΔNPC is the deviation between the measured and calculated NPC.

Figure 3.12 depicts the measured primary NPC and DCC currents, measured at client #07 during 2021. The negative offset in the statistics in **Table 3.3** is also visible in **Figure 3.12** in all three DCC phases. According to the CT orientation (see **Table A.2**), the negative offset corresponds to a continuous current flowing from ground into the power grid at client #07. Beginning at the end of October 2021, the operation of the DCC was limited first to positive currents and from December 2021 on it stopped operating. The correct operation of the measurement system was

Table 3.3: DCC data statistics for 2021.

Phase/Characteristic	**Acting Value %** in %	**mean** in A	**median** in A	σ in A
U	-23.11	-57.78	-61.69	29.12
V	-24.49	-61.22	-64.09	29.68
W	-23.10	-57.75	-61.31	26.55
ΔAB		3.43	1.42	21.69
ΔBC		-3.47	-1.63	20.16
ΔCA		-0.034	-0.057	17.58
NPC		-0.473	-0.477	0.156
NPC_{DCC}		-0.422	-0.450	0.213
ΔNPC		-0.051	-0.024	0.155

confirmed on-site. The reason for the inactive DCC system is unknown by the time of this writing. One presumption is that the thyristors of the DCC system are defective.

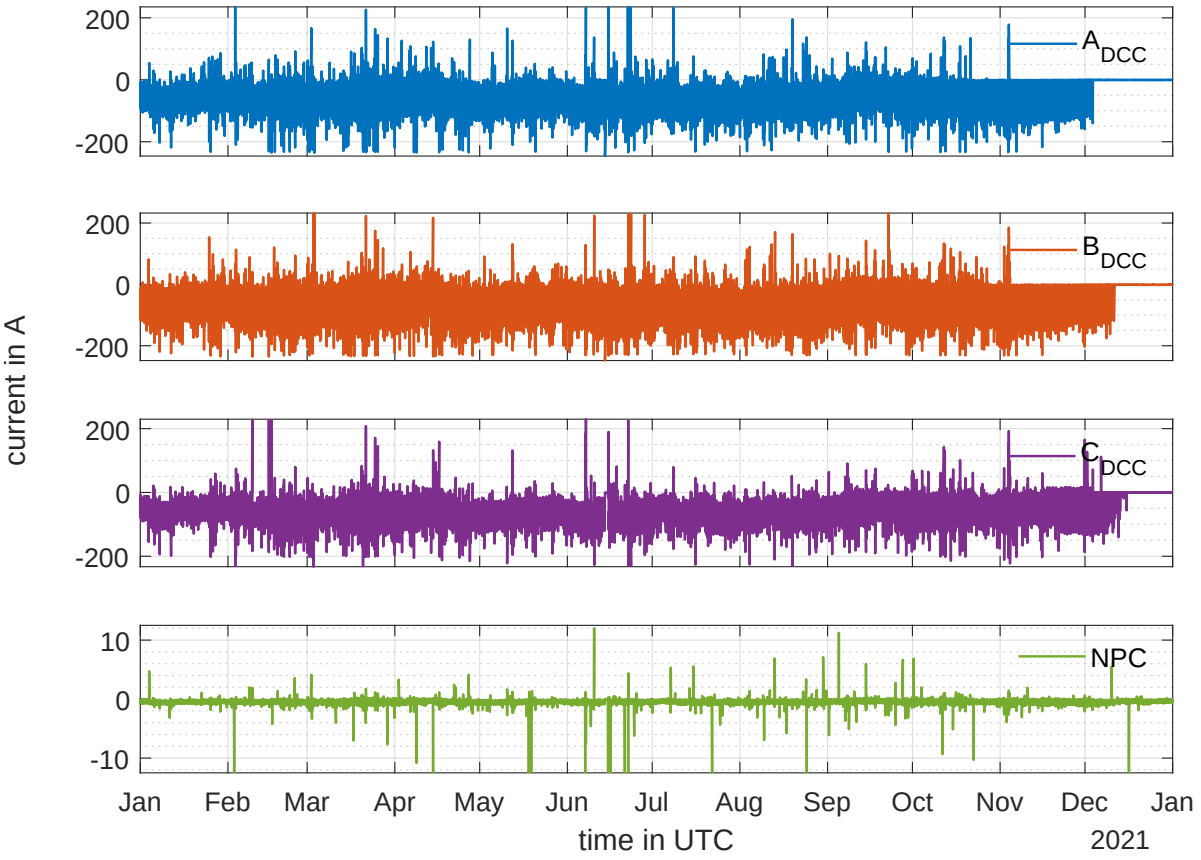

Figure 3.12: Measured DCC and NPC from client #07 during 2021.

Figure 3.13 depicts the weekly mean profile of the DCC and NPC measurements at client #07 based on minutely values. In all four measurement channels, the daily profile is clearly visible, with a minimum current amplitude around midday every day of the week. In comparison with other measurements, the daily profile of the NPC at client #07 is unique. For comparison, see also Fig. 4

in [Alb+21b]. The weekly/daily profile with a minimum current during the night is due to the earth magnetic field expansion into space at the night side of the earth and the compression of the earth magnetic field on the day side. In addition, the influence of the solar wind, man-made LFC sources, such as the Vienna subway system causing an increased current level during their operating hours (also during the weekend nights) [Hal19; Alb+20].

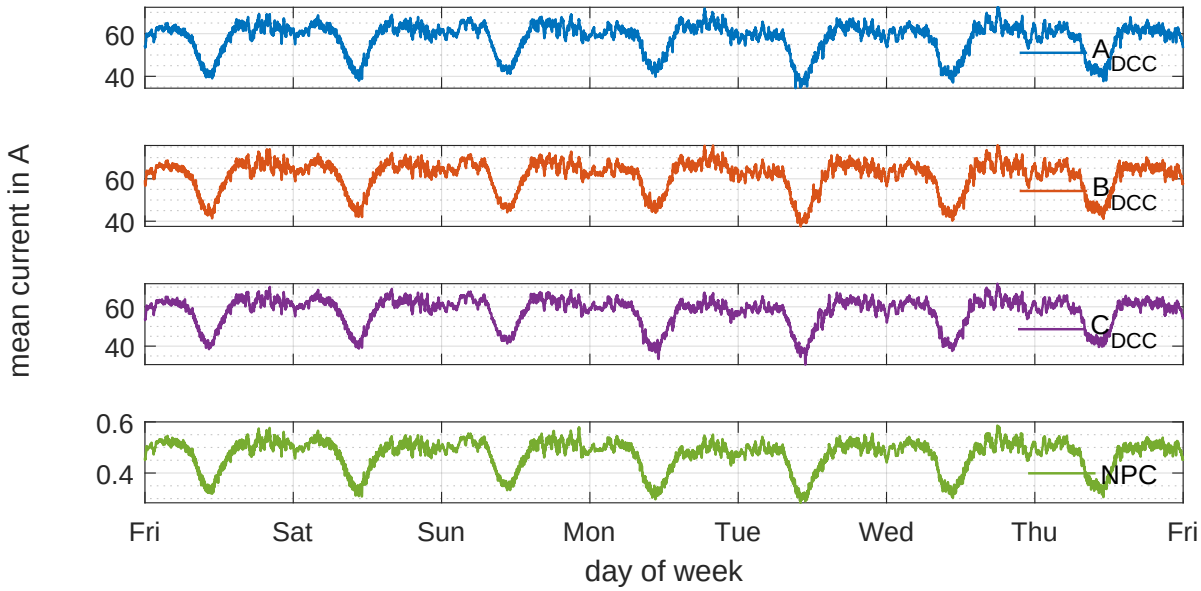

Figure 3.13: Measured weekly profile of NPC and DCC from 2021 based on minutely current values.

Figure 3.14 presents the weekly calculated DC per phase and the comparison of the measured and calculated NPC from the DCC phase measurements. The comparison of the measured and calculated NPC in **Figure 3.15** reveals an underestimation of the calculated NPC from the DCC measurements of maximum 100 mA during 2021. This deviation could partly be related to the measurement accuracy of the DCC measurement system.

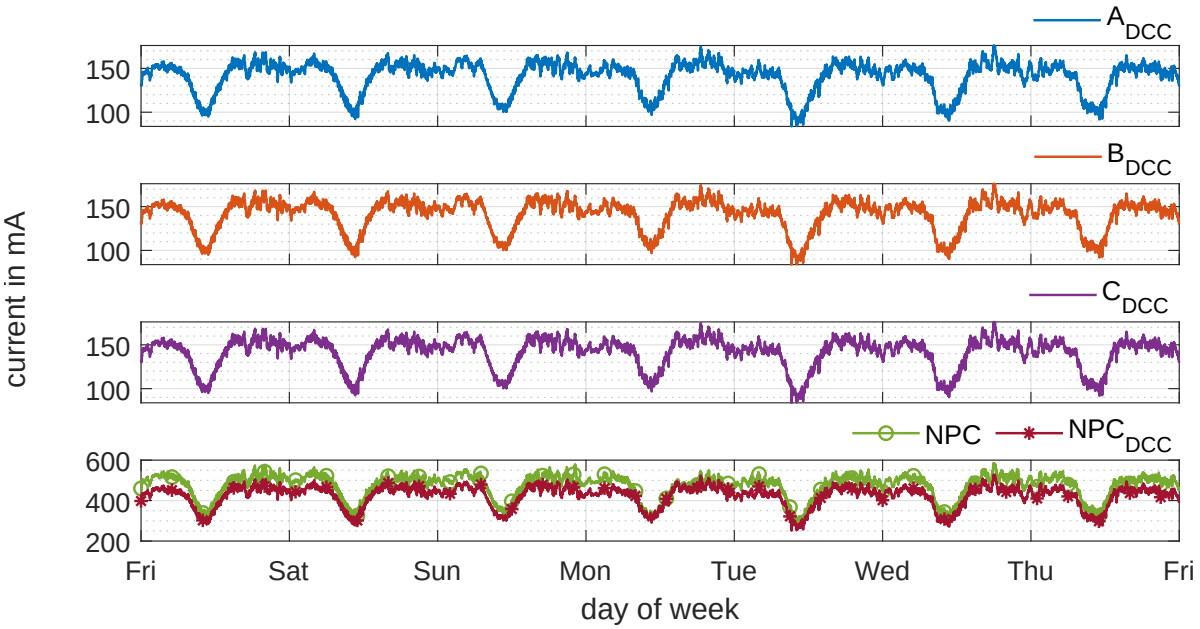

Figure 3.14: Measured weekly profile of NPC, calculated DC_{DCC} and calculated NPC_{DCC} from 2021 based on minutely current values.

In **Figure 3.15** the absolute deviation of the primary injected DCC currents between the phases and the deviation between the measured and calculated NPC from the DCC phase currents is presented. The maximum deviation of the primary injected DCC currents is in all three cases (A-B, B-C, C-A) is in a range of 20 A, which corresponds to a DC deviation between the phases of 47.3 mA, neglecting the measurement uncertainty, according to (2.76). Thus, a symmetrical distribution of the LFC between the high-voltage phases can be assumed. During Mondays an offset change is visible in ΔI_{BC}, ΔI_{CA} and ΔI_{NPC} in **Figure 3.15**. The reason for this characteristic is unknown by the time of writing.

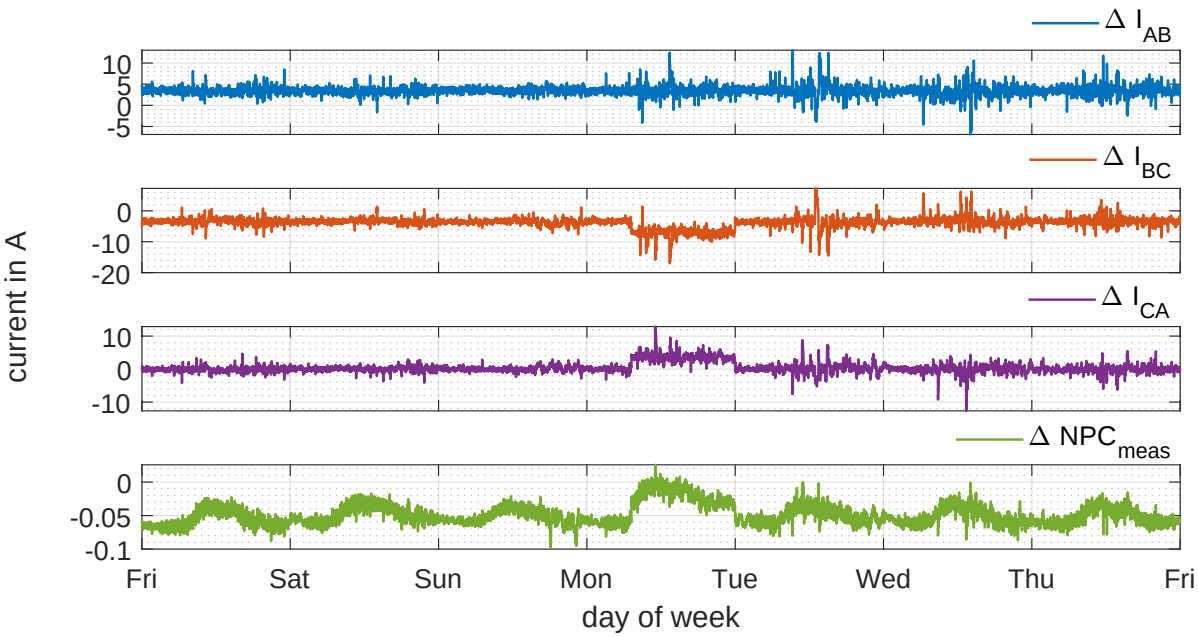

Figure 3.15: DCC phase deviation and deviation of measured and calculated NPC from DCC phase currents.

3.5.2 Geomagnetic Disturbance May 12th 2021

A CME on the May 9th 2021 became geomagnetically effective on earth on May 12th 2021. During this GIC event a maximum NPC of -13.8 A was measured in client #05 (see **Figure 3.17**). **Table 3.4** presents the data statistic for the May 12th event between 6:00 and 18:00 UTC.

Table 3.4: Data statistics for May 12th 2021 GMD. [Zen18]

Client	**Max. NPC** in A	**Min. NPC** in A	**Mean** in A	**Median** in A	σ in A
GIC01	6.34	-8.41	-0.20	-0.15	1.04
GIC02	0.81	-0.70	-0.08	-0.08	0.09
GIC03	2.02	-2.35	-0.24	-0.25	0.38
GIC04	3.55	-4.57	-0.16	-0.13	0.52
GIC05	7.81	-13.8	-0.21	-0.13	1.24
GIC07	1.23	-1.75	-0.51	-0.54	0.24
GIC08	9.31	-6.47	0.32	0.12	1.19

During this GMD the maximum magnetic field change per minute in x- and y-direction was 33.0 and 21.0 nT/min [Zen18], respectively (see **Table 3.5**). The maximum K_p value reached during this GMD was 7o [Deu].

Figure 3.16 depicts the measured relative magnetic field in west-east (x) and north-south (y) direction during the GMD event [Zen18]. The magnetic field change in nt/min is derived from the absolute magnetic field data, measured with a sample rate of 1 S/s. The deviation in nT/min is

Table 3.5: Magnetic field statistics for May 12th 2021 GMD [Zen18].

B-Field	**Max. ΔB** in nT/min	**Min. ΔB** in nT/min	**Mean** μT/min	**Median** in μT/min	σ in nT/min
ΔB_{x}	-52.2	33.0	12.9	5.7	2.2
ΔB_{y}	21.0	-13.8	5.4	0.0	1.3

derived by scaling the deviation in nT/s to nT/min. The largest magnetic field changes occurred in the x-direction.

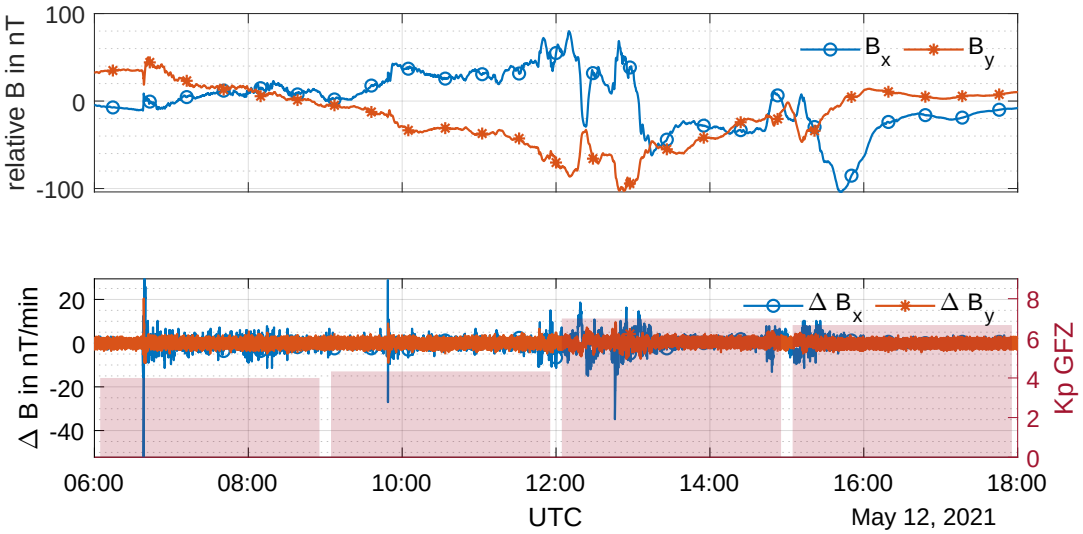

Figure 3.16: WIC relative horizontal magnetic field components and magnetic field change [Zen18] and K_p index [Deu] during the May 2021 GMD.

Figure 3.17 depicts the measured NPCs during the GMD. The large magnetic field changes between 7:00 and 8:00 UTC, before 10:00 UTC, around 12:00 UTC and around 15:00 UTC are visible in almost all NPC measurements. Large currents are more likely measurable in substations with transmission lines perpendicular to direction of the largest magnetic field changes, as it can be seen for client #01, #05 and #08. Besides the transmission line orientation the beginning/end of the line, as it is the case for client #05, can cause an increased current amplitude.

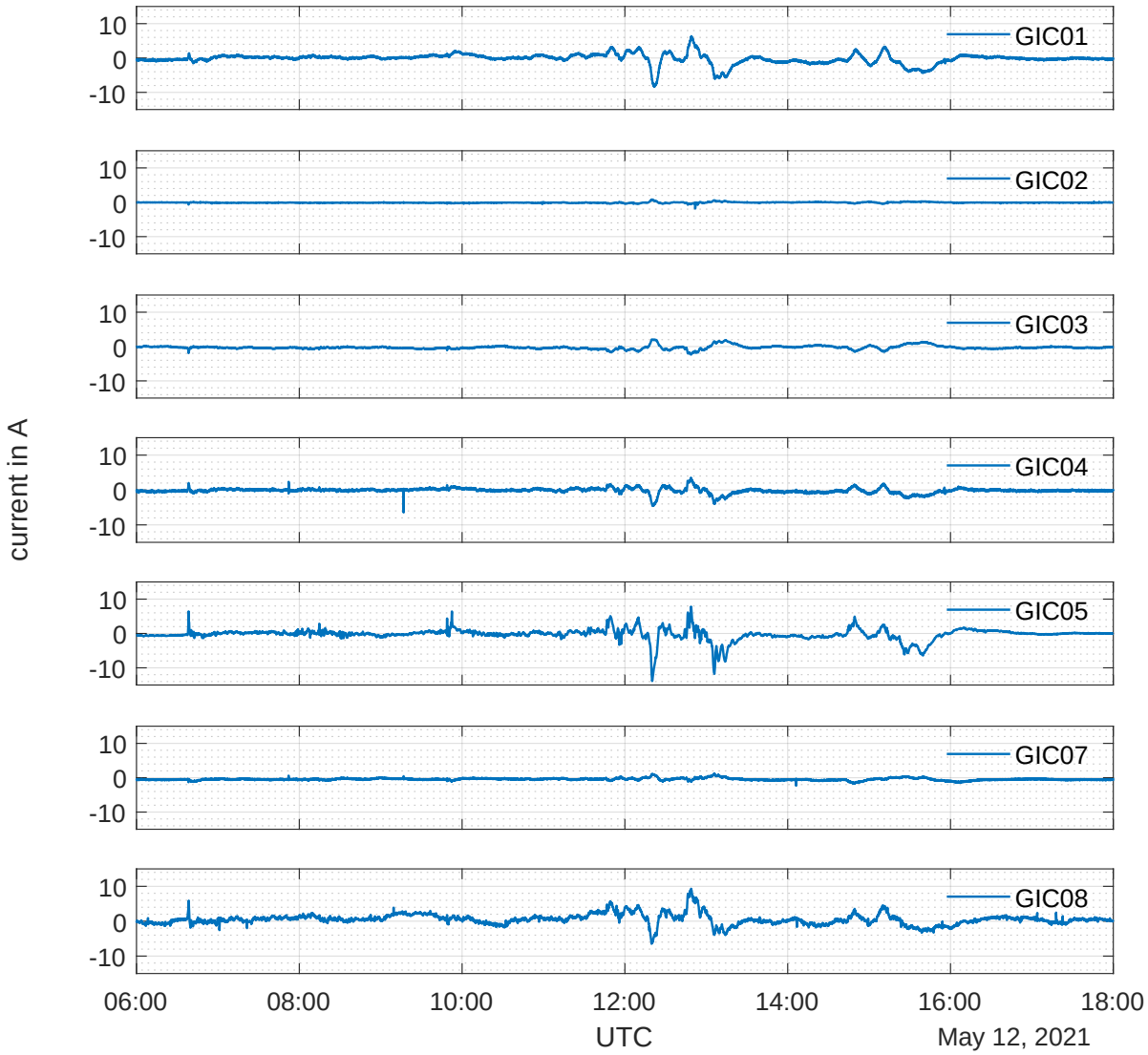

Figure 3.17: Measured NPCs during May 12th 2021 GMD.

Figure 3.18 depicts the single-side amplitude frequency spectrum of the measured NPCs between 6:00 UTC and 18:00 UTC, which show similar frequency patterns with different amplitude.

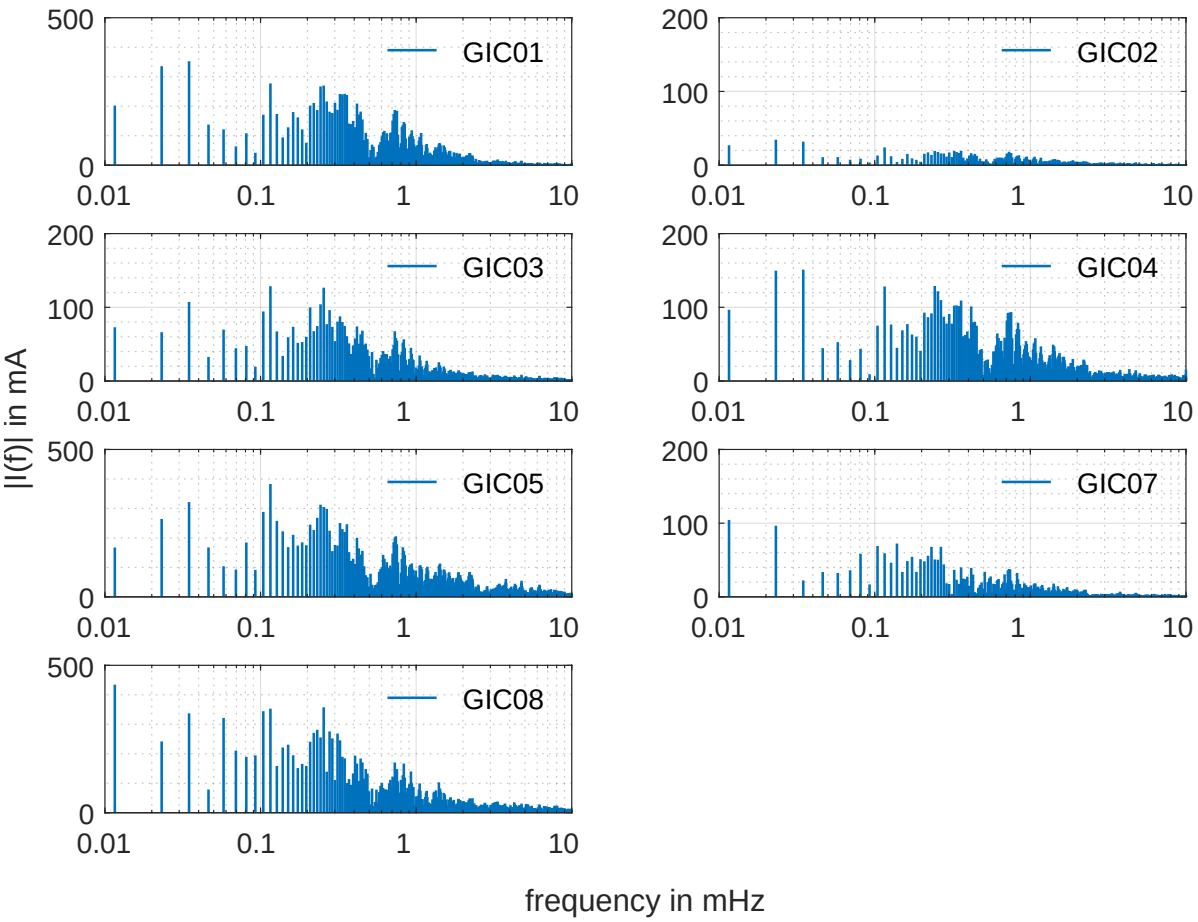

Figure 3.18: Frequency spectrum of measured NPC during May 12th 2021 GMD.

Figure 3.19 depicts the histogram of the measured NPCs with a bin size of 250 mA. Besides client #03 and #07, all other clients show an equal distribution of currents around 0 A. In client #03 and #07 a small negative offset is visible.

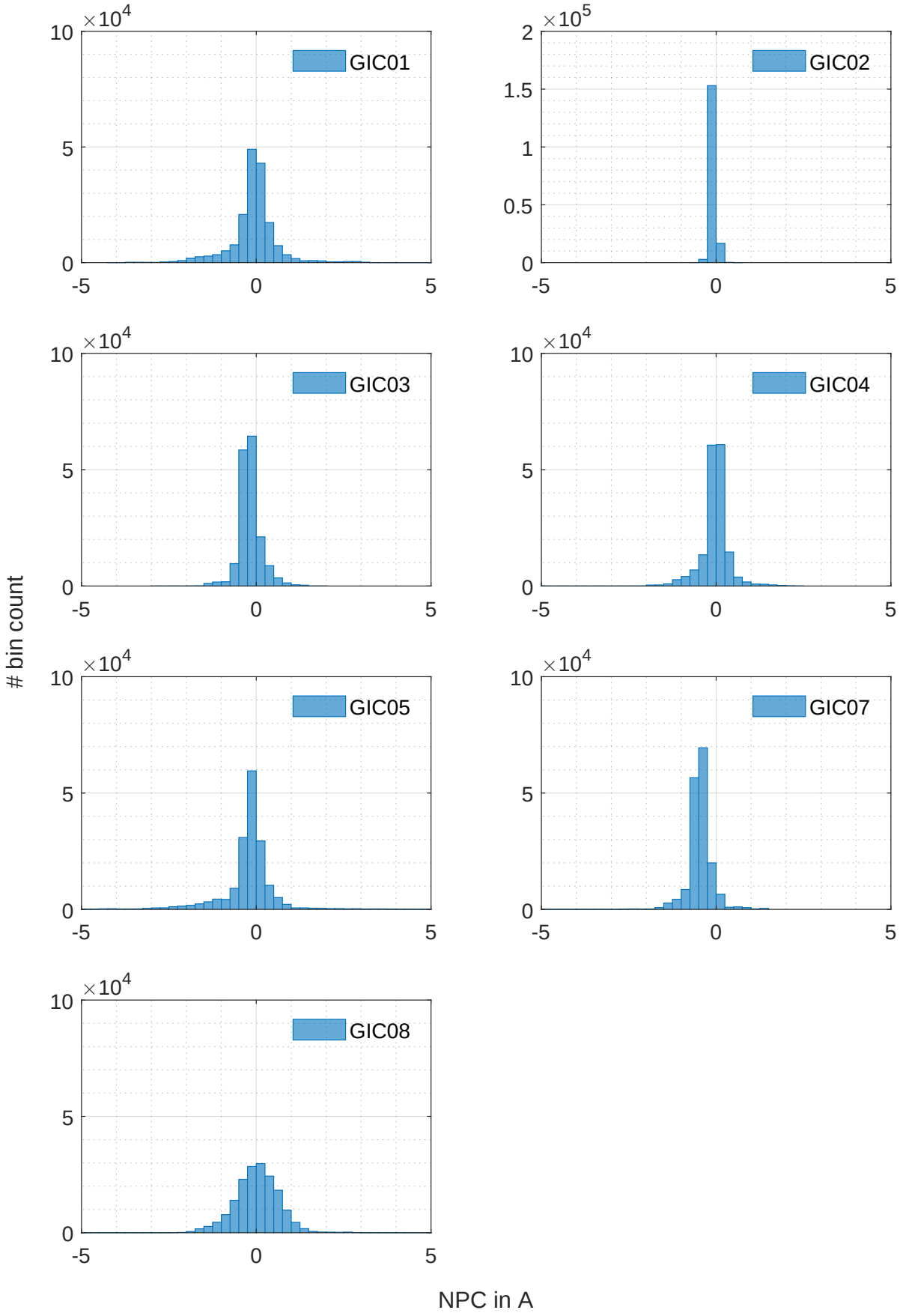

Figure 3.19: Histogram of measured NPC during May 12th 2021 GMD with 250 mA bin size.

3.5.3 Geomagnetic Disturbance November 3rd-4th 2021

On November 1st and 2nd 2021, several CMEs occurred in conjunction with a C1.3 flare of AR 12887 and an M1.6 flare of AR12891, respectively [NOA20]. The GMD became geomagnetically effective on earth on November 3rd and 4th 2021. The solar wind reached a speed up to 809 km/s. The maximum K_p value reached during this event was 8-. **Table 3.6** gives the statistic values for the GMD for all measurement locations in service. The largest current amplitude was measured at client #05 with -9.50 A, as depicted in **Figure 3.21**.

Table 3.6: Data statistics for November 2021 GMD.

Client	**Max. NPC** in A	**Min. NPC** in A	**Mean** in A	**Median** in A	σ in A
GIC01	1.12	-4.01	-0.08	-0.04	0.67
GIC02	0.53	-0.65	-0.08	-0.08	0.07
GIC03	1.86	-2.81	-0.18	-0.21	0.32
GIC04	2.44	-2.44	-0.03	-0.01	0.39
GIC05	9.42	-9.50	-0.21	-0.14	0.86
GIC06	3.33	-9.48	-0.45	-0.48	0.13
GIC07	1.43	-2.47	-0.46	-0.47	0.34
GIC08	2.46	-2.46	0.01	0.3	0.67

The maximum magnetic field changes measured at the Conrad observatory (International Association of Geomagnetism and Aeronomy Code of Conrad observatory: WIC) was 108.0 nT/min and 15 nT/min in x- and y-directions, respectively [Zen18].

Table 3.7: Magnetic field statistics for November 2021 GMD [Zen18].

B-Field	**Max. B** in nT/min	**Min. B** in nT/min	**Mean** in μT/min	**Median** in μT/min	σ in nT/min
ΔB_x	108.0	-54.6	-0.8	-4.3	3.1
ΔB_y	15.0	-13.2	3.7	0.0	1.3

Large magnetic field changes are visible from the graph in **Figure 3.20** between 18:00 UTC on November 3rd and midnight, after midnight and around 9:00 UTC on November 4th 2021.

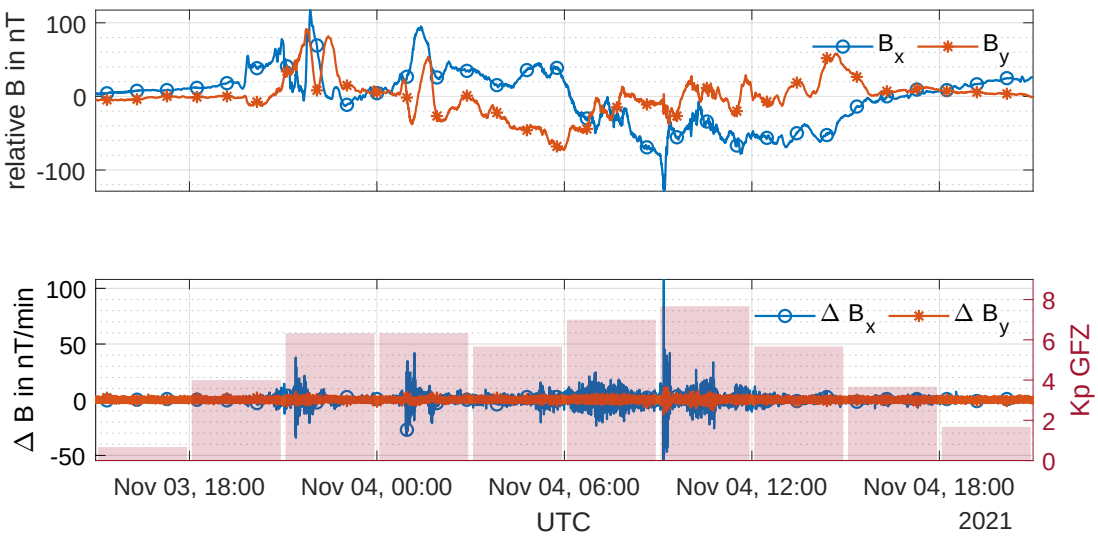

Figure 3.20: WIC relative horizontal magnetic field components and magnetic field change [Zen18] and K_p index [Deu] during the November 2021 GMD.

The large magnetic field changes became especially pronounced in the NPC measurements of client #01, #03, #04, #05 and #07. In the current measurement of client #08 more disturbances are visible, in comparison with the GMD in May 2021 (**Figure 3.17**). Also, visible is the typical current direction reveals of the GIC, e. g. in client #05, related to the compression and expansion of the earth geomagnetic field. Even though the magnetic field changes during the November 2021 GMD were larger than the ones during the May 2021 event, the NPC amplitudes stayed below the measured NPC during the May 2021 event.

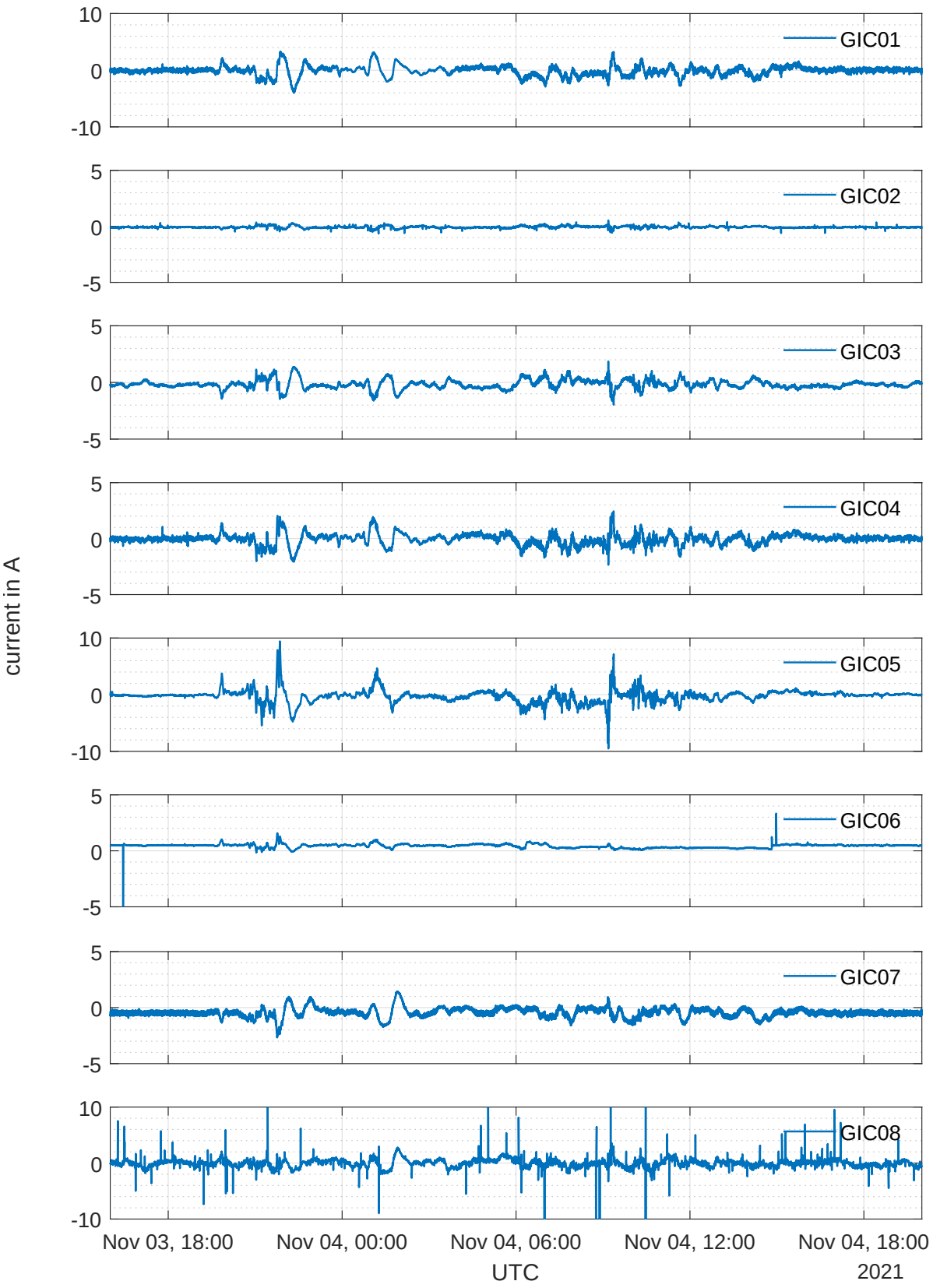

Figure 3.21: Measured NPCs during November 3rd-4th 2021 GMD.

The single-side amplitude spectrum of the measured NPCs has similar characteristics as the spectrum

of the measured NPCs from the May 2021 GMD, whereas the highest amplitudes occur at client #05 and #08.

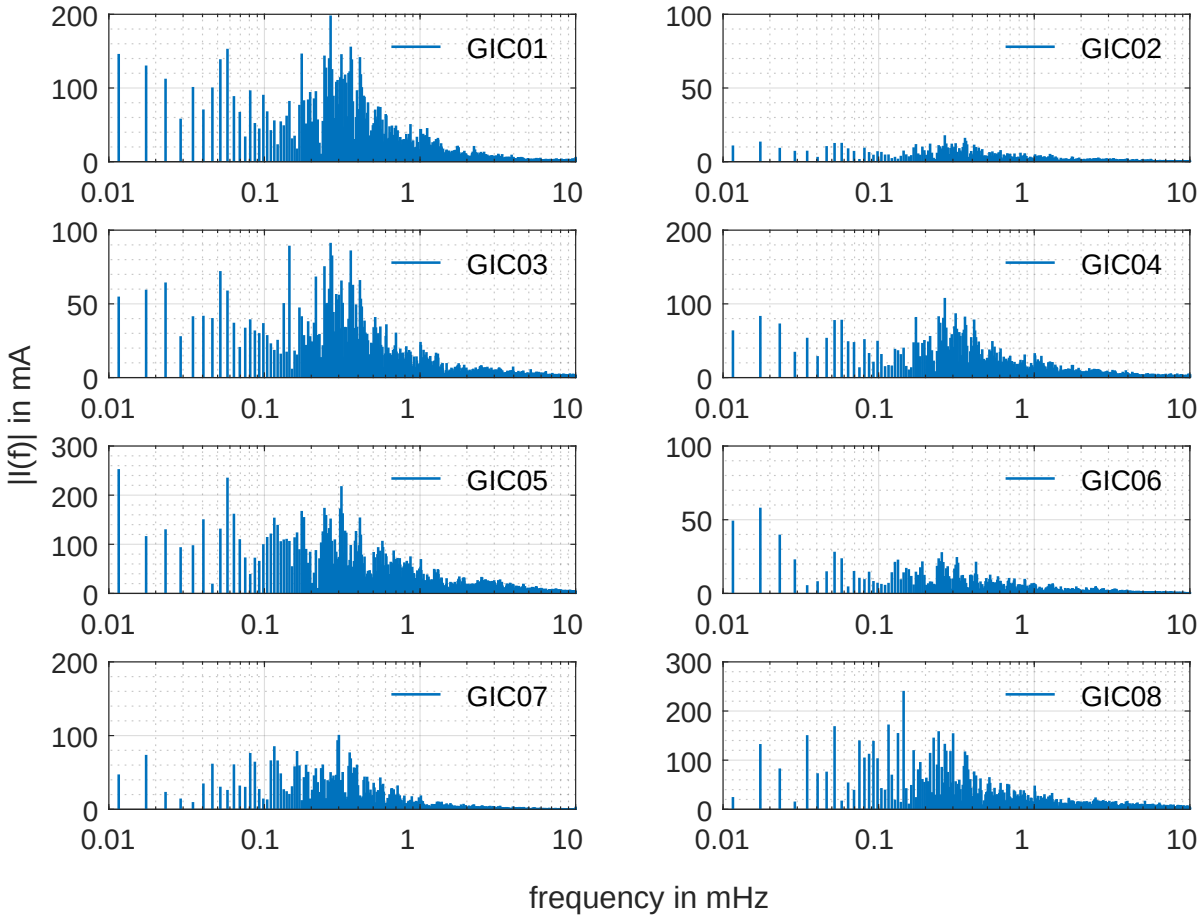

Figure 3.22: Frequency spectrum of measured NPC during November 2021 GMD.

The histogram of the NPCs in **Figure 3.23** shows a symmetrical distribution around 0 A, except for client #03, #06 and #07.

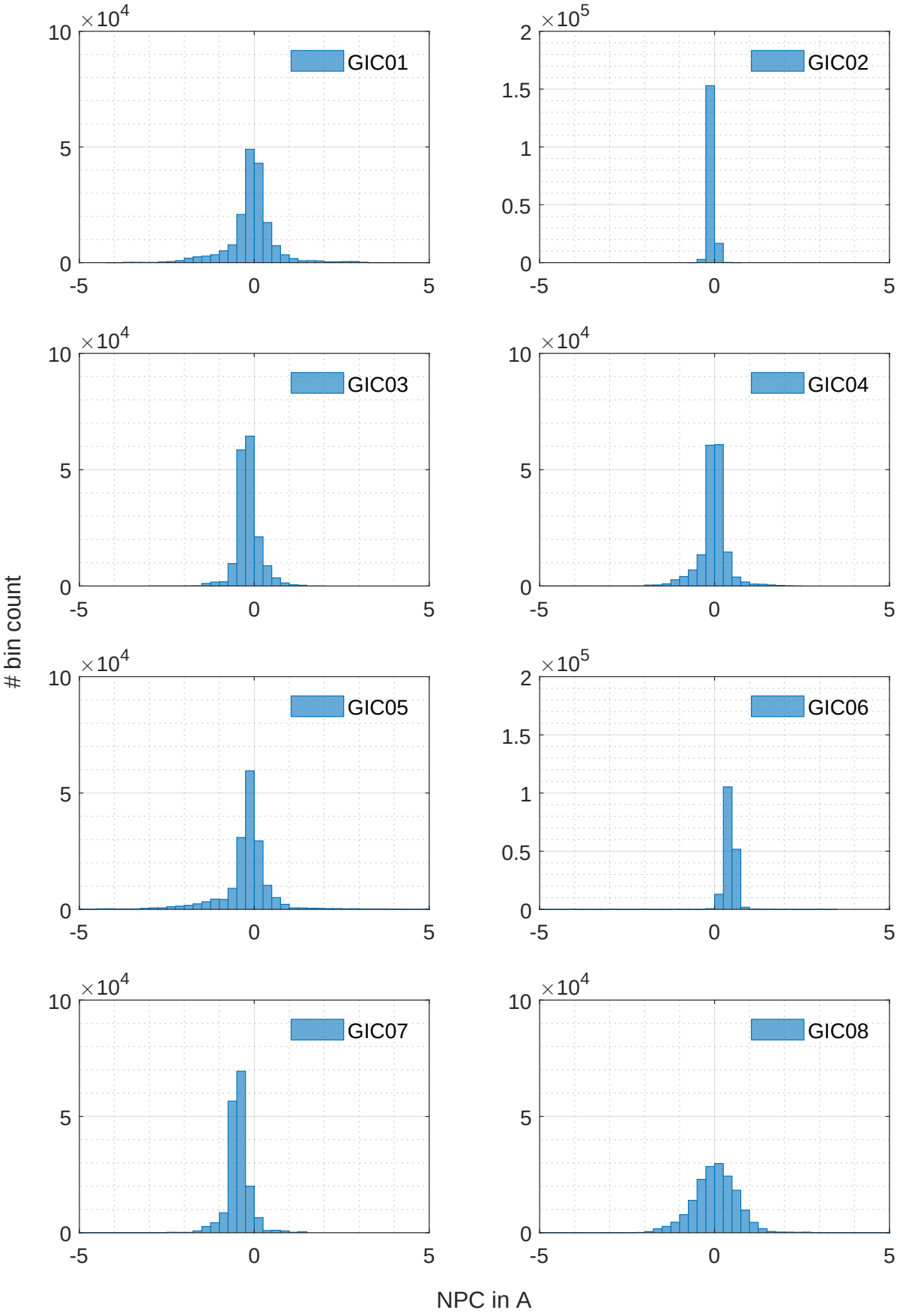

Figure 3.23: Histogram of measured NPC during November 2021 GMD with 250 mA bin size.

3.5.4 Geomagnetic Disturbance September 7th-8th 2017

During the GMD on September 7th - 8th 2017 the minimum K_p value of 4 and the maximum K_p value of 8+ were reached between 12:00 and 15:00 UTC, as depicted in **Figure 3.24**. Between 12:00 and 15:00 UTC the maximum current amplitude of 13.84 A was measured at client #05 (see **Figure 3.25** and **Table 3.8**), which also corresponds to the maximum magnetic field change in west-east direction (B_x) of 46 nT and north-south direction (B_y) -37.2 nT, respectively.

Table 3.8: Data statistics for September 2017 GMD.

Client	**Max. NPC** in A	**Min. NPC** in A	**Mean** in A	**Median** in A	σ in A
GIC01	5.11	-3.58	-0.23	-0.20	0.71
GIC02	1.50	-0.95	0.22	0.22	0.17
GIC03	2.01	-2.42	-0.12	-0.12	0.34
GIC04	3.02	-3.20	-0.20	-0.18	0.37
GIC05	13.84	-3.71	-0.21	-0.19	0.88

Note that for the measurements during 2017, the version v2014 of the measurement system was used, which was limited to 3.5 A in the negative current direction of the CT. Therefore, the plots are scaled from -4 A to 15 A. **Table 3.8** and **Table 3.9** list the NPCs and magnetic field change statistics for the September 2017 GMD.

Table 3.9: Magnetic field statistics for September 2017 GMD [Zen18].

B-Field	**Max. B** in nT/min	**Min. B** in nT/min	**Mean** in μT/min	**Median** in μT/min	σ in nT/min
ΔB_x	45.6	-37.2	4.1	-0.1	2.7
ΔB_y	9.0	-7.2	3.4	0.0	1.1

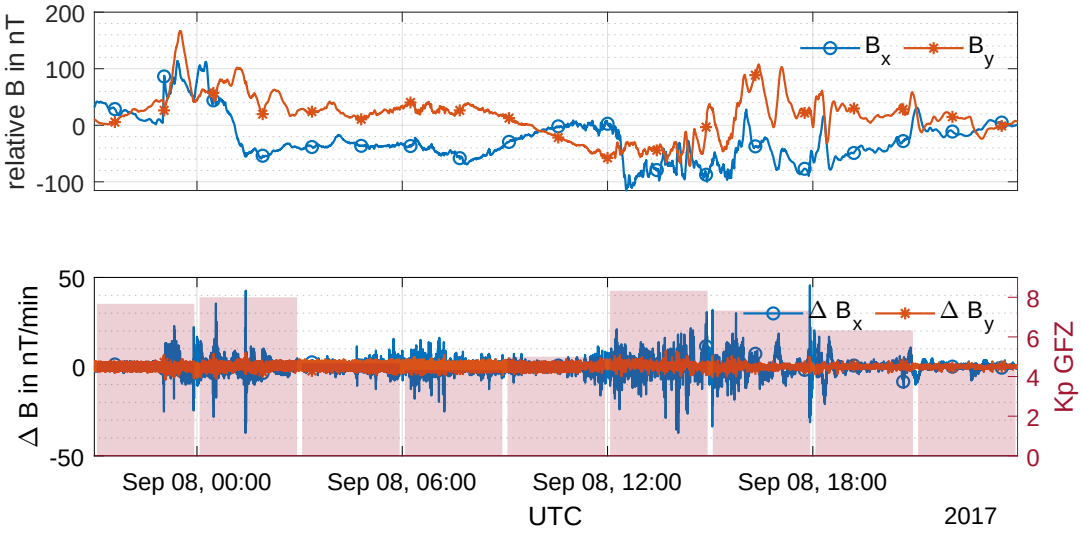

Figure 3.24: WIC relative horizontal magnetic field components and magnetic field change [Zen18] and K_p index [Deu] during the September 2017 GMD.

During the November 2017 GMD five measurement systems were in service.

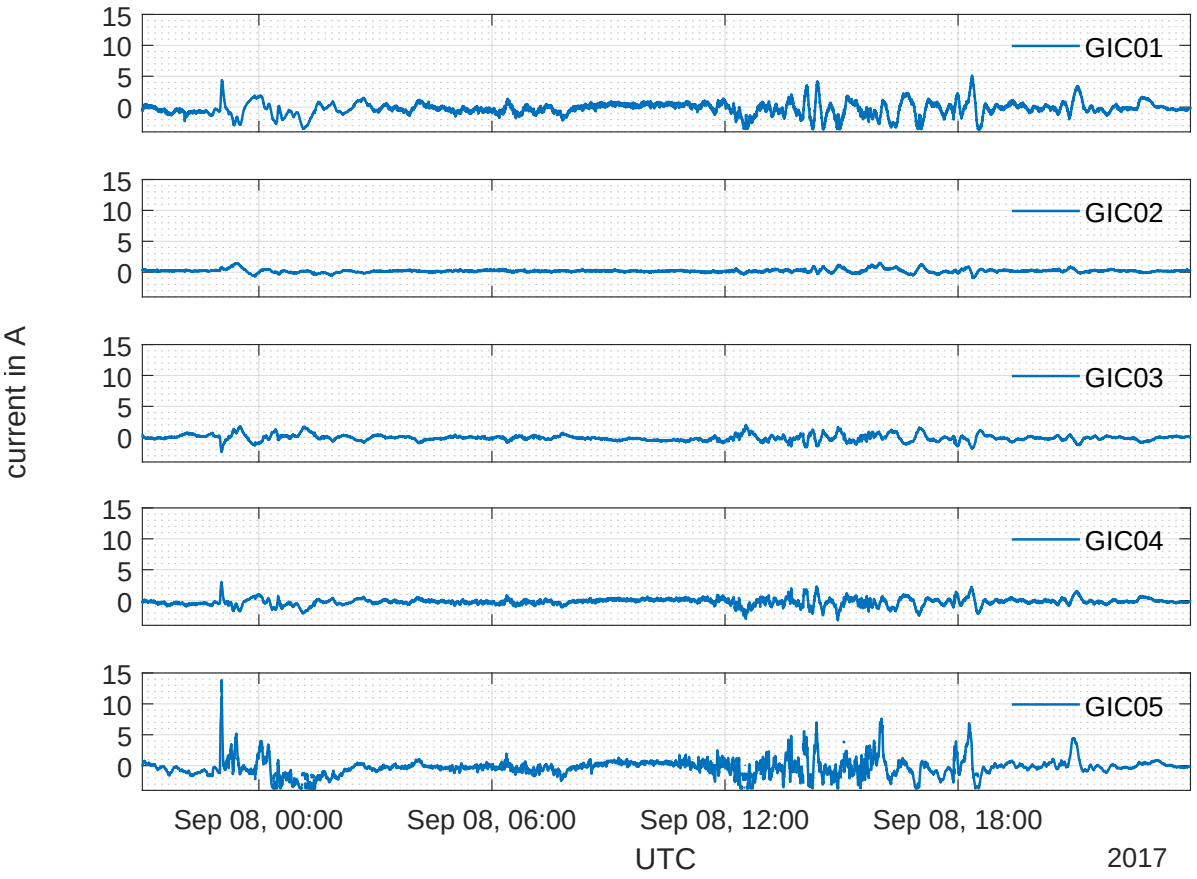

Figure 3.25: Measured NPCs during November 3rd-4th 2021 GMD.

Figure 3.26 depicts the frequency spectrum for the measured NPCs with similar characteristics as the previous GMDs.

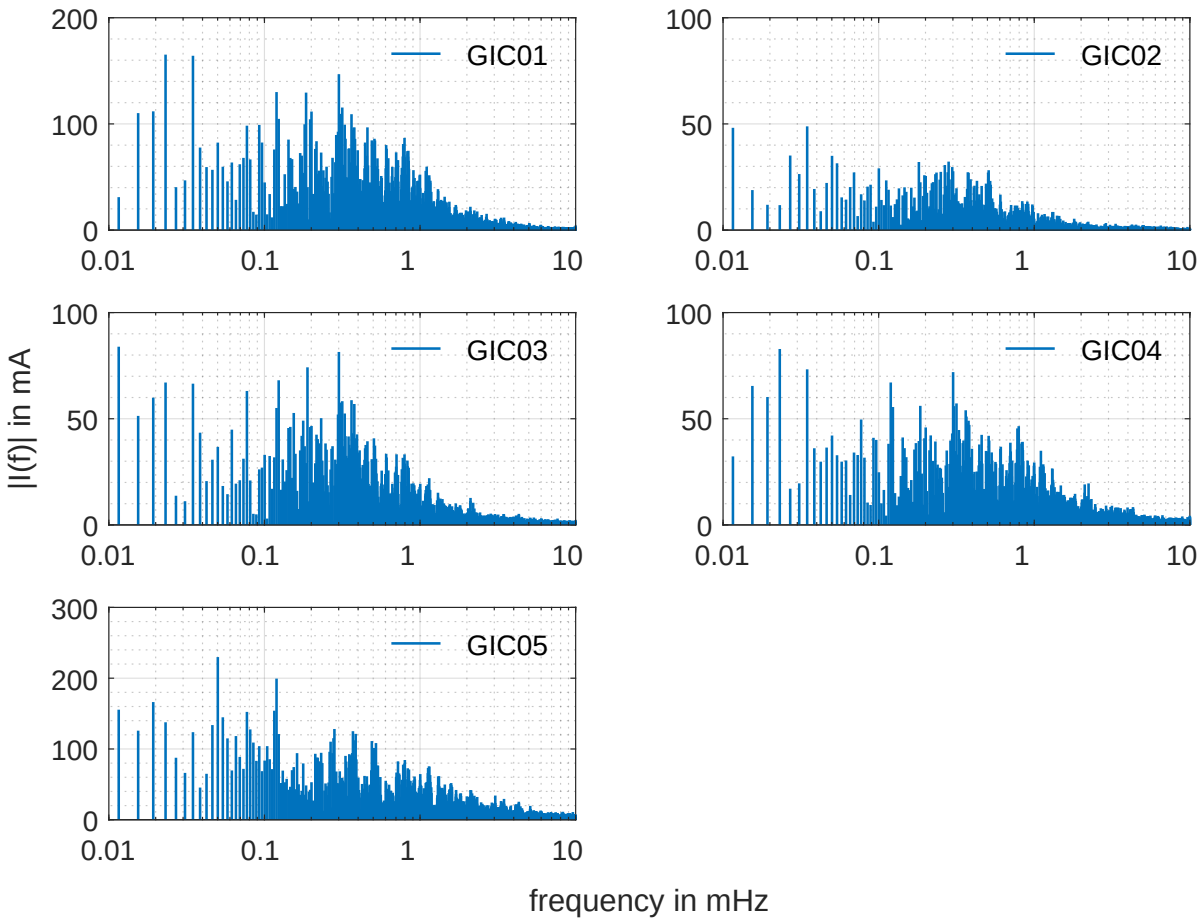

Figure 3.26: Frequency spectrum of measured NPC during September 2017 GMD.

The histogram in **Figure 3.27** with 250 mA bin size, a small negative trend for client #01, #04 and #05.

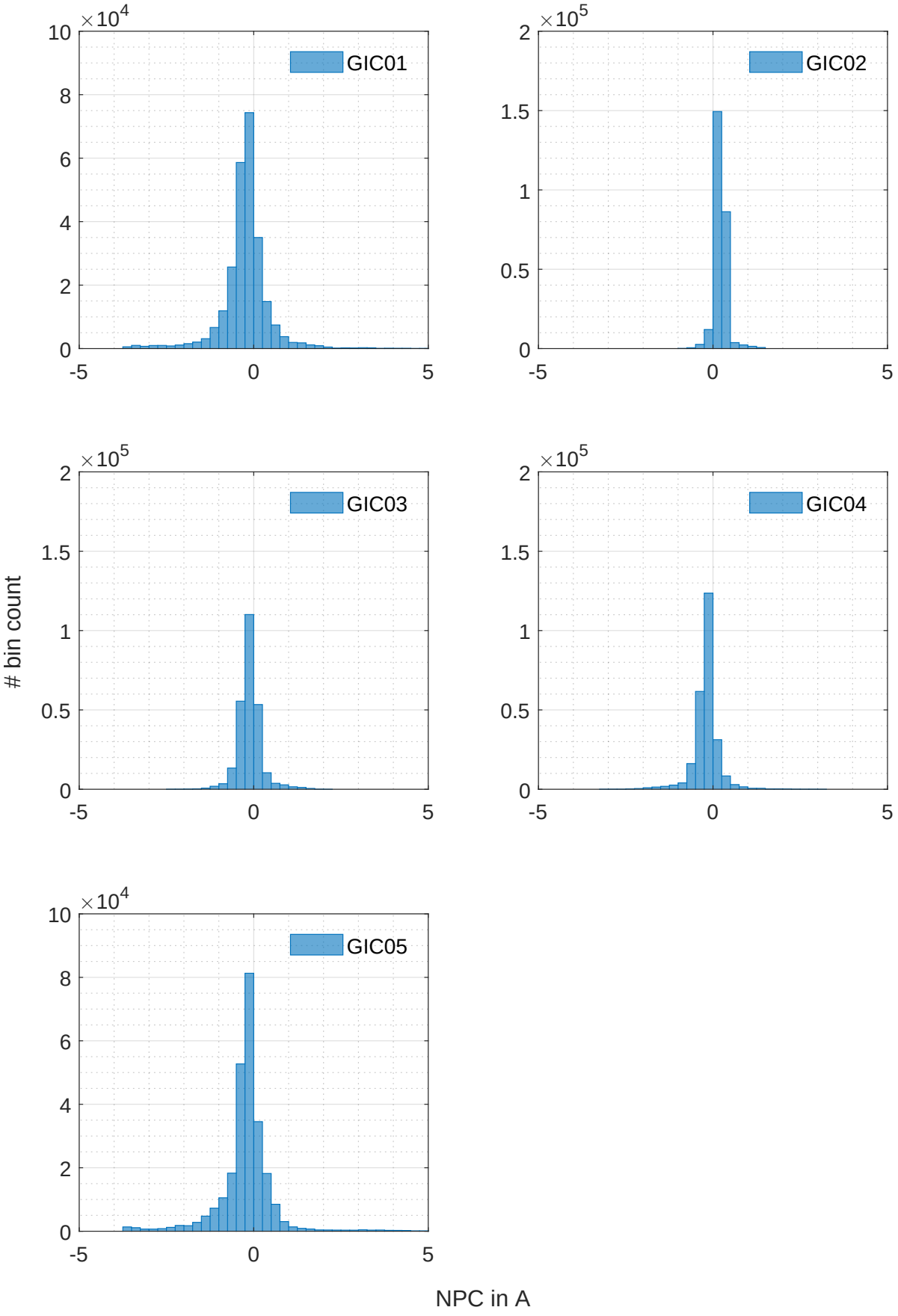

Figure 3.27: Histogram of measured NPC during September 2017 GMD with 250 mA bin size.

3.6 Discussion of On-Site Low Frequency Current Measurements

The first version v2014 of the measurement system could be continuously improved, providing a measurement range of ± 25 A with the closed loop zero-flux CT LEM IT65-S ULTRASTAB and the split-core CT LEM LA200SD/SP3. The guaranteed measurement accuracy of the NPC measurement for both measurement systems of is 2.0 % ± 1 mA for the range of $\pm$ 1-25 A_{DC}. In addition to the measurement range extension with version v2019, three additional current measurement channels were added to the system. These additional channels are currently used only at client #07, where a DC compensation system is installed at the transformer. The DC compensation system (DCC) is compensating the DC flux in the transformer core, with an additional fourth winding on each wounded limb. The primary current of the three additional fourth windings are measured and recorded together with the transformer NPC. This allows to calculate the per phase DC and allows a comparison with the calculated NPC from the DCC measurements per phase and the measured transformer NPC. The analysis of the measurement data during 2021 reveals a maximum deviation between the measured and calculated transformer NPC of 100 mA, which is within in the measurement accuracy of the system. Therefore, the DCC measurements could also be used to monitor the transformer NPC within the maximum compensating range of the DCC system. The split-core CT uses a Hall sensor, therefore the sensor offset drift should be checked frequently. By the time of writing, the maximum relative offset drift was 63.97 mA within 30 days (see **Table 3.1**). Especially the offset drift during the summertime with increased temperature variations should be checked. The temperature correction via software could be improved by longer time steps for each temperature during the reference measurement in the climate chamber. In comparison with the LEM IT65-S ULTRASTAB CT, the split-core CT LEM LA200SD/SP3 allows the remote control of the transformer neutral point earthing switch. Therefore, no grid operator staff is required in the substation, if the transformer needs to be ungrounded for any reason. With the system, using the split-core CT, a frequently remote offset check is also possible.

The unique daily profile of the NPC and the DCC currents at client #07, with a minimum NPC and DCC current around midday (see **Figure 3.13** and **Figure 3.14**), reveals an influence of man-made systems on the measured currents. To the substation of client #07 a large on-shore wind park with several 100 MVA rated power is connected. The hypothesis is that at lower wind speed, usually during nighttime, the DC injection by the distributed energy resources (DER) is higher, because the converter is not operated at its nominal operation point. This raises the question whether the operating point has an influence on the injected DC or not. It should be noted that the injected DC is not totally blocked by the transformer(s) between the converter and the 110/380 kV transformer equipped with the measurement system [GKS05]. After a certain time, determined by the transformer parameters, the DC flux (voltage-seconds) inside the transformer core can cause half-cycle saturation, which causes a DC component in the magnetisation current on both sides of the transformer. A detailed correlation of the wind speed and the measured NPC and DCC currents is pending.

During three analysed geomagnetic disturbances, the largest geomagnetic field change (ΔB) was

always measured in the west-east direction (magnetic field component B_{x}). Thus, the largest electric field is expected in north-south direction. Therefore, substation with long transmission lines in north-south are more likely exposed to elevated GIC amplitudes. Besides the transmission line orientation, beginning and end substations of a transmission line more like are exposed to increased GIC levels.

The histogram representation of storm events shows similar characteristics for each storm event. Due to the short duration of the maximum GIC amplitude the GIC amplitude is not pronounced in the diagram. Therefore, the histogram representation can be used to verify the correct operation of the measurement system.

The frequency spectrum of the measurement during the different GMDs reveal similar frequency patterns. With a cluster between 0.1 mHz and 1 mHz, which indicates the high geomagnetic activity, according to [Alb+20]. The frequency components above 1 mHz are an indicator for man-made LFC sources.

From the presented measurement data, a current measurement range of ± 25 A DC is suitable to measure transformer neutral point currents during moderate GMDs in Austria. An extended measurement range could be required during large GMDs.

4 Power Transformer Modelling and Measurement

Accurate modelling of the electric power grid requires detailed models of the equipment installed in the power grid, in order to reflect the complex dynamics in the grid. E. g. during the evaluation of differential protection settings and parametrisation, inrush current calculations and reactive power demand calculations. Due to inconsistency of data of the individual components, it may be necessary to use measurements for the model parametrisation. Therefore, a measurement-based modelling approach was developed within the scope of this work with the aim of parameterising transformer topology models. For that purpose, two transformer terminal measurement tests were developed and tested namely, the AC saturation test and the DC hysteresis test. Both tests aim to measure the transformer characteristic up to deep saturation. The measurement data is used subsequently to parametrise a saturation or hysteresis model within the transformer topology model. The AC saturation was tested successfully in the laboratory with three 50/60 kVA three-phase three- and five-limb transformers and used to model a three-phase three-limb 50 kVA distribution grid transformer. The DC hysteresis test was also tested successfully in the laboratory with the same transformers and in field with three-phase three- and five-limb transformers with rated power from 50 MVA to 786 MVA. The other model parameters, such as stray inductances between the windings, the high-voltage winding capacitances or the winding resistances can be extracted from the standardised factory acceptance test report. The derived transformer topology model, based on the AC saturation and DC hysteresis test of a three-phase three-limb 50 kVA transformer, including the hysteresis characteristics, reveals a high accuracy between the measured and calculated current waveform and power demand. This chapter presents the modelling approach to setup transformers topology models, based on the data from the factory acceptance test and a supplement DC hysteresis or AC saturation test, which overcomes the challenge of obtaining the transformer core characteristics from three-phase terminal measurements.

The nomenclature for the transformers under test is as follows: T<*number of limbs*><***S**mall/**L**arge rated power*><*small Latin letter for multiple transformers of the same type*>. **Table 4.1** lists the transformer investigated in this work. Further information on the different transformers is given in **Appendix C**.

Table 4.1: Nomenclature for transformers under test.

Abbreviation	Rated Power in kVA	Rated Voltage in kV	Transformer Type
T3Sa	50	0.4/35	distribution
T3Sb	50	0.4/35	distribution
T5S	60	0.4/0.4	laboratory
T3L	50,000	110/10.5/6	transmission
T5La	600,000	345/141.5/13.8	auto
T5Lb	786,000	525/22.8	generator step-up

4.1 Grey Box Topology Transformer Models

For the modelling of power transformers, a grey box model (**Section 2.4.1**) is used. In the model either the saturation characteristic or the hysteresis characteristic of the core material can be implemented. The saturation characteristic is modelled as 1D look-up table with a non-linear inductor. The hysteresis characteristic is modelled as an inverse JA model in the classical inductance-reluctance analogy, which uses the magnetic flux density B as input. When using the capacitance-permeance analogy, the saturation is modelled as non-linear capacitance by a capacitor in series with a voltage-controlled voltage source. The hysteresis is modelled with a resistor in parallel to a voltage controlled current source and the eddy current losses are considered by a resistor in series to the saturation and hysteresis element (**Figure 2.27**). The capacitance-permeance analogy can also be used with a 1D look-up table to model the saturation characteristic. Both models are investigated to determine their advantages and disadvantages, with respect to power transformer modelling. Due to inconsistency of available data on the transformers under investigation, the AC saturation test or DC hysteresis test is used to measure the transformer core characteristics and to identify the model's hysteresis/saturation characteristics. Due to the non-linearity of the transformer models and the multiple unknown hysteresis model parameters, a heuristic optimisation algorithm is used for the hysteresis models parameter identification.

The flow chart in **Figure 4.1** depicts the different steps in the modelling to establish a topology model of power transformers. The structure of the transformer topology model is derived with the capacitance-permeance or the inductance reluctance analogy, according to the steps described in **Section 2.4.1** or **Section 2.4.1**. The level of detail is determined by the number and parametrisation of the considered stray paths and components (e. g. L_{gap}, C). The model parameters are derived from the factory acceptance test, namely the zero-sequence impedance, the DC winding resistance, the high-voltage winding capacitance and the total measured no-load loss. The core dimensions and the number of turns is usually not given in the factory acceptance test. These transformer data need to be acquired from the manufacturer or estimated. For the parametrisation of the hysteresis model parameters (JA model: five parameters; ReCap model: six parameters), the AC saturation test or the DC hysteresis test is simulated. The measured terminal currents from the AC saturation or the DC hysteresis test are used as a reference during the optimisation of the hysteresis model parameters. In the last step, the model is validated in standard no-load condition, with the hysteresis parameters derived in the previous step. To judge the model accuracy, the measured no-load current waveforms and the power demand is used.

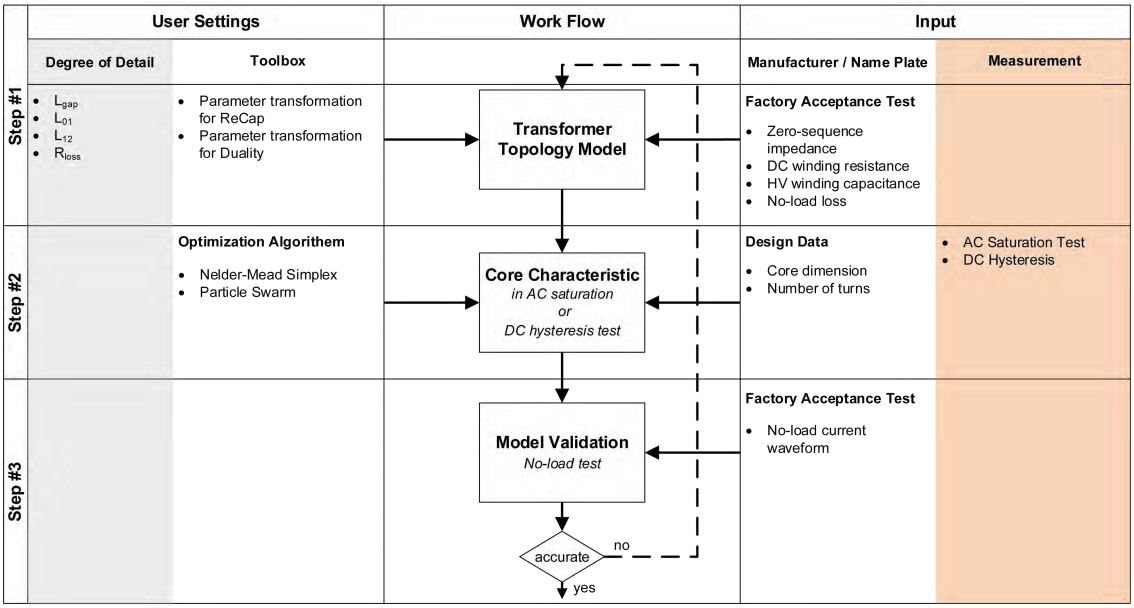

Figure 4.1: Flow chart of the modelling approach.

4.2 Transformers under Test and Laboratory Setup

The data of five power transformers of different rated power and core design were evaluated for modelling procedure. Detailed information on the Transformers under test can be found in **Appendix C**. Some transformers are modified for the tests, which is described in the following section. The overall laboratory setup is described afterwards.

4.2.1 Laboratory Transformers and Test Setup

For the laboratory test two three-limb two-winding 50 kVA distribution transformers (**Figure 4.3**) and one 60 kVA five-limb two-winding transformer (**Figure 4.4**) were used. The distribution transformers were manufactured with the vector group Yzn5. Both 50 kVA transformers (T3Sa and T3Sb) are modified [Tau20], adding an additional bushing for the high-voltage neutral and making all six low-voltage windings of the zigzag windings accessible from outside via a terminal box (see **Figure 4.2**). That enables B2B test with superimposed DC via the high-voltage neutrals and allows to investigate the effects of different vector groups on the transformer behaviour also under DC bias. During the transformer modification the tap changer of T3Sa and T3Sb was fixed at position two.

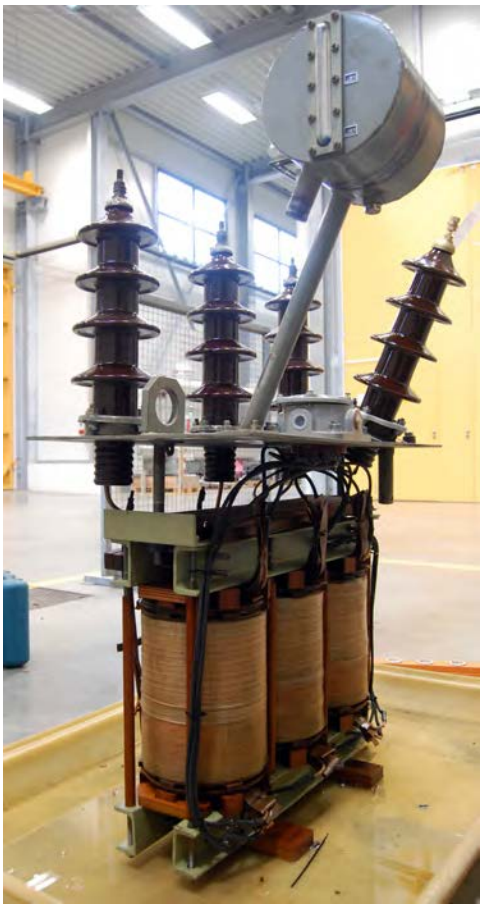

Figure 4.2: Transformer T3Sa active part and bushings during the modifications.

After the modification both transformers were refilled with NYTRO 4000A transformer oil and de-moisture to a value of 8.9 ppm (T3Sa) and 6.3 ppm (T3Sb) over 24 h, according to IEC 60422:2013 [IEC01a], which required a moisture content below 20 ppm. After reassembling, both transformers successfully passed the applied voltage test (AV) and induced voltage withstand test (IVV), according to IEC 60073-3:2013 [IEC07b]. The lightning impulse tests were not performed because the transformers are not used in continuous operation in the public grid and are not exposed to lightning type transient over-voltages.

(a) Transformer T3Sa in the laboratory after the modification.

(b) Transformer T3Sb in the laboratory after the modification.

Figure 4.3: Three-limb two-winding 50 kVA distribution transformers.

The 60 kVA five-limb two-winding transformer is designed and manufactured for laboratory investigations without a tank. Both windings (primary and secondary) are rated for 0.4 $kV_{L\text{-}L}$. The transmission ratio can be changed, using nine winding taps on each winding. The core is manufactured with a rectangular cross-section and with 90° (butt) core joints. **Figure 4.4** depicts the transformer further referred to as T5S.

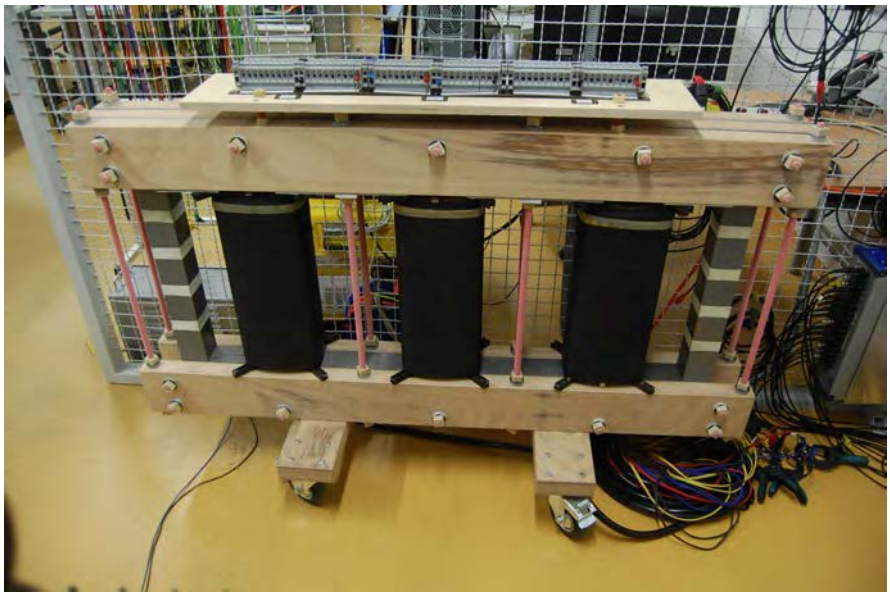

Figure 4.4: Five-limb 60 kVA transformer T5S

As a power source either the public distribution grid (315 kVA Dyn5 9.09/454.4 A; $u_{\mathrm{k}} = 5.8\,\%$) or a power amplifier is used. The 315 kVA distribution transformer is connected to the test cell (**Figure 4.6**) via a 120 m 5x25 mm^2 copper cable. Using the specific resistance for copper at 20°C of 0.0171 Ωmm^2/m, the cable resistance is 82.08 mΩ/phase, neglecting the Skin effect.

Two power amplifiers, with 30 kVA each, can be connected in parallel as controllable voltage source (detailed information can be found in **Appendix D**). **Figure 4.5** depicts the schematic of the laboratory and its possible operation configurations.

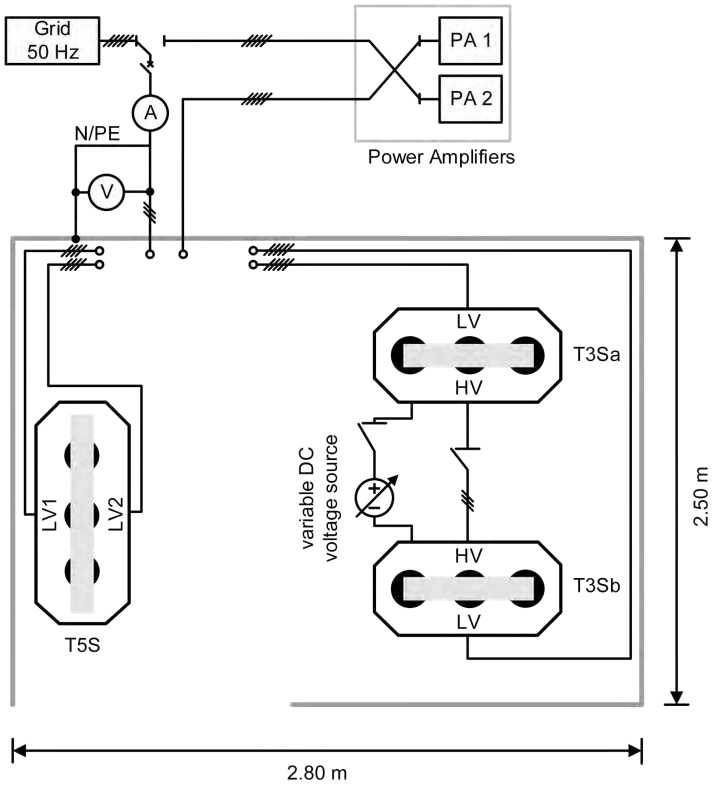

Figure 4.5: Single line diagram and schematic sketch of transformer test cell.

Figure 4.6: Picture of the transformer test cell.

The supply from the power amplifier is mainly used for the short-circuit tests and zero-sequence tests to control the voltage amplitude and frequency. For the B2B test both supplies, from the public grid and the power amplifier, can be used. The comparison of the measurement results from the B2B test with supply from the public grid and the power amplifier reveals a higher harmonic voltage content using the supply from the public grid. The total harmonic distortion (THD) average

of all three phases is 1.5 % and 3.93 % during the supply from the power amplifier and the public grid during no-load conditions, respectively.

The supply network impedance has a damping effect on the measurement setup (see **Section 2.5.3**) To take that into account, the source impedance in symmetrical components of the public low-voltage grid and the power amplifier were determined. This was done by voltage and current measurement in no-load and load condition. Balanced, as well as unbalanced load currents of 45 A (4.9 Ω) were applied to the sources. The symmetrical component values are listed in **Table 4.2**.

Table 4.2: Symmetrical components during the B2B tests with the transformers T3Sa and T3Sb with supply from the public grid and a power amplifier.

	Public Grid	**Power Amplifier**
Z_0 in Ω	0.227	0.243
Z_1 in Ω	0.129	0.056
Z_2 in Ω	0.142	0.051

The symmetrical components are derived from fundamental rms voltage and current components with the power analyser software Oxygen 5.7.

4.2.2 Large Power Transformers and Test Setup

Two large power transformers with a three-limb core (50 MVA) YNd5d5 and five-limb core (786 MVA generator step-up transformer) YNd11 were surveyed during the factory acceptance test at the manufacturers side. The two transformers under test are depicted in **Figure 4.7**. The detailed transformer data is given in **Appendix C**.

(a) Transformer T3L. (b) Transformer T5Lb.

Figure 4.7: Large transformers under test at the manufacturers side.

The DC hysteresis characteristic of the transformers T3L and T5Lb were measured with the portable transformer test device OMICRON Testrano 600 via the high-voltage phases A-C.

4.3 Topology Model Parameter Identification

The parameters required for the power transformer modelling are based on measurements performed during the factory acceptance test (**Section 4.3.1**) and the additional DC hysteresis or AC saturation test (**Section 4.3.2**). Based on the measurements, the parameters, listed in **Table 4.3**, required for the modelling are calculated with the equations in **Section 2.4.2**.

4.3.1 Transformer Design Data and Factory Acceptance Test

For the parametrisation of the models the factory acceptance test, according to IEC 60076-1:2011 [IEC12a], and the transformer design data are used. An overview of the model parameters and the required data/tests for the parameters are given in **Table 4.3**.

Winding Resistance

The winding resistances for the transformers under test were measured with the OMICRON Testrano 600 and stated typically for 20° C in **Table 4.4**. For the T3Sa, T3Sb and T5S all winding resistances

Table 4.3: Test and derived model parameters.

Source	**Model Parameters**
Winding resistance	R_{HV}, R_{LV}
High-voltage winding capacitance	C_{HV}
No-Load test	P_{fe}
Non-linear joint characteristic	L_{gap}
Zero-sequence test	R_0, L_0
Shot-Circuit test	L_{01}, L_{12}, L_{23}
Design Data	N_{LV}, N_{MV},N_{HV}, core cross-sections core section lengths

were measured between the phase and neutral terminal. For the T3L and the T5Lb the winding resistances of the low- and medium-voltage windings were measured between the phase terminals (A-B, B-C, A-C). The tap changer position for the T3L was 11 (available taps: 1-19) and for the T5Lb the tap changer positions was 1 (available taps:1-6).

Table 4.4: Winding resistances for 20° C and 22.5° C for transformer T5La.

	T3Sa	**T3Sb**	**T5S**	**T3L**	**T5Lb**
R_{LV} in Ω	0.08132	0.06374	0.05384	0.02671	0.00755
R_{HV} in Ω	282.00	226.33	0.06853	0.04874	0.25132
R_{MV} in Ω	-	-	-	0.01022	-

Iron Core Resistance

During the transformer no-load test the active, reactive and apparent power is measured with a power analyser (**Appendix G.1**). The no-load loss is used in the model to calculate the resistance R_{fe} which represents the eddy current loss in the JA hysteresis model, according to (4.1).

$$R_{\mathrm{fe}} = k_{\mathrm{loss}} \cdot \left(\frac{U_{\mathrm{n}}}{\sqrt{3}}\right)^2 \cdot \frac{a \cdot l_{\mathrm{limb}} + b \cdot l_{\mathrm{yoke}}}{P_{\mathrm{fe}}}, \tag{4.1}$$

where k_{loss} is a scaling factor determined with trail and error method during the no-load calculation, U_{n} is the nominal rms phase-to-phase voltage of the phases supplied during the test, l_{limb} and l_{yoke} are the sum of the mean length of the limb and yoke sections and P_{fe} are the total no-load losses minus the total ohmic losses in the winding resistances measured during the no-load test at 100 % of the rated voltage and a and b are the numbers of the receptive limb and yoke sections in the transformer core. In each core section in the transformer topology model R_{fe} is multiplied by the corresponding core section length.

Table 4.5 lists the calculated parameter R_{fe} and the determined parameter k_{loss} for the different transformers under test.

Table 4.5: Measured R_{fe}, P_{fe} and k_{loss} for the transformers under test.

	T3Sa	**T3Sb**	**T5S**	**T3L**	**T5Lb**
U_{n} in V	400	400	400	10,500	22,800
R_{fe} in Ω	961.45	990.84	2431.54	30,203.56	31,666.5
P_{fe} in W	178.00	98.61	99.58	13,213	165,600
k_{loss}	1.0	1.0	1.0	1.0	1.0
Vector Group	YNyn0	YNyn0	YNyn0	YNd5d5	YNd11

Leakage Inductances

The leakage inductances are calculated according to (2.51) with the mean short-circuit voltage and current and the power factor from the short-circuit test. The scaling factor k_{01} is calculated using (2.54) for T3Sa and T3Sb. For T5S the value of 0.5 is used, due to the transmission ration of 1:1 (tap position 1-9).

Table 4.6: Leakage inductances and scaling parameter k_{01} for the investigated transformers [(1)] OLTC:10 | [(2)] OLTC:3.

	T3Sa	**T3Sb**	**T5S**	**T3L**	**T5Lb**
L_{01} in mH	0.3673	0.1814	0.2117	2.91	14.78
L_{12} in mH	0.7346	0.3629	0.4234	2.18	325.52 [2)]
L_{23} in mH	-	-	-	271.96 [1)]	-
k_{01}	0.013	0.014	0.5	$4/3$	0.045
Vector Group	YNyn0	YNyn0	YNyn0	YNd5d5	YNd11

Zero-Sequence Impedance

The zero-sequence impedance for the transformers under test and the corresponding vector group are stated in **Table 4.7**. For T3Sb both windings are measured, using the tap position 1-9. The zero-sequence impedances are calculated according to (2.46), (2.47) and (2.48).

Table 4.7: Zero-sequence impedances per phase for the investigated transformers | [(1)] OLTC 10 | [(2)] OLTC 1, Z1N0.

	T3Sa	**T3Sb**	**T5S**	**T3L** [(1)]	**T5Lb** [(2)]
Z_0 in Ω	2.2438	3.3526	9.8006	46.94	61.14
R_0 in Ω	3.7495	7.0707	211.66	1.30	-
L_0 in mH	8.7	11.3	36.7	149.38	-
Vector Group	YNyn0	YNyn0	YNyn0	YNd5d5	YNd11

To justify the assumption of an even distributed zero-sequence impedance between all three limbs of the transformer T3Sa, the phase currents and the applied voltage during the zero-sequence test is measured. The phase currents practically coincide with each other, as depicted in **Figure 4.8**.

Therefore, the zero-sequence impedance can be assumed to be equally distributed between the limbs of the transformer under test.

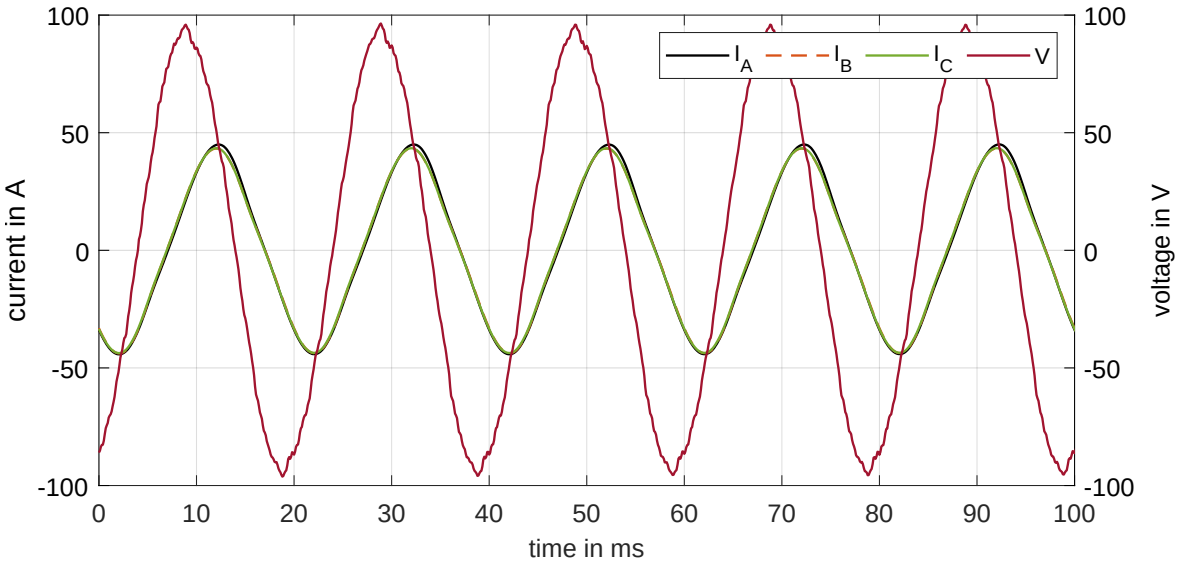

Figure 4.8: Phase currents during zero-sequence test of transformer T3Sa.

Air Gap Inductance

L_{gap} represents the unavoidable gap in the joint between the limb and the yoke. With L_{gap} the residual flux in the transformer limbs is controlled [Zir+17] and therefore also the reactive power demand, as well as the no-load current. In addition to the power demand, L_{gap} rotates the hysteresis characteristic counter-clockwise with the increasing value of L_{gap}. **Figure 4.9** compares a realistic air gap inductance of 80 μH with an unrealistically large value of 2.4 H.

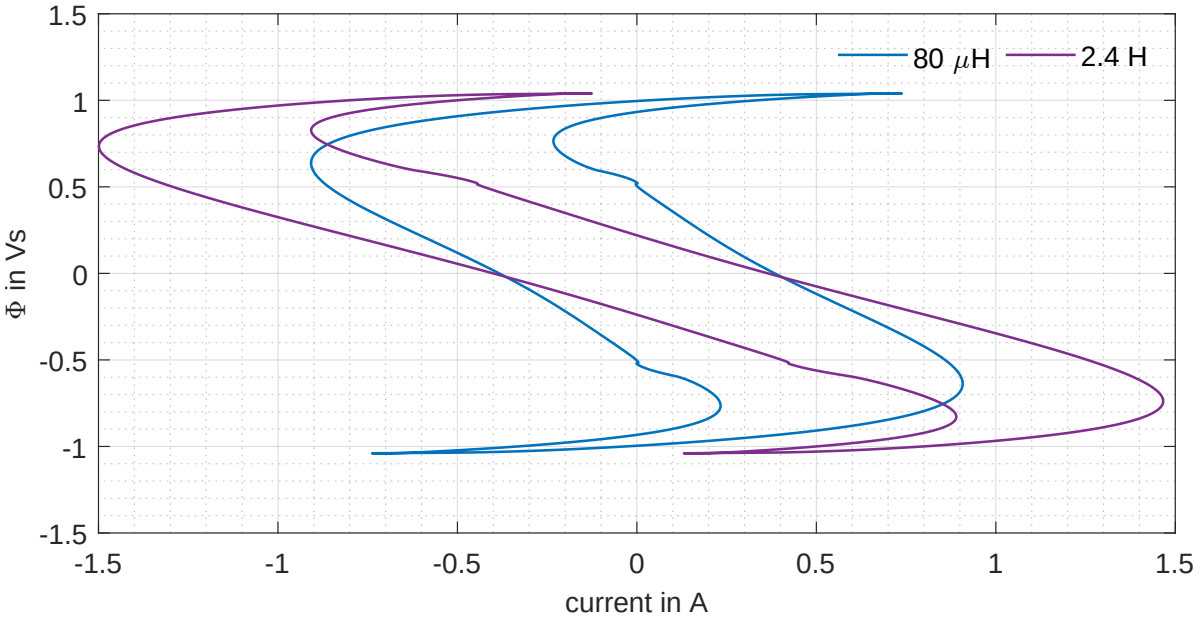

Figure 4.9: Calculated $\Phi - i$ characteristic of T3Sa phase A with $L_{\mathrm{gap}} = 80\,\mu$H and $L_{\mathrm{gap}} = 2.4\,$H.

Moreover, the influence of an air gap between the limbs and yokes is also indicated by the rounded hysteresis loops. **Figure 4.10** compares the $\Phi - i$ DC hysteresis characteristics of the transformers T5S, T3Sa and T3Sb measured with 30 A via the low-voltage terminals A-C with all transformers in YNyn connected windings. The effect of the butt joints (90° angle) of the transformer T5S in the DC hysteresis characteristics is clearly visible, in comparison to the one of the transformers T3Sa and T3Sb with mitered joints.

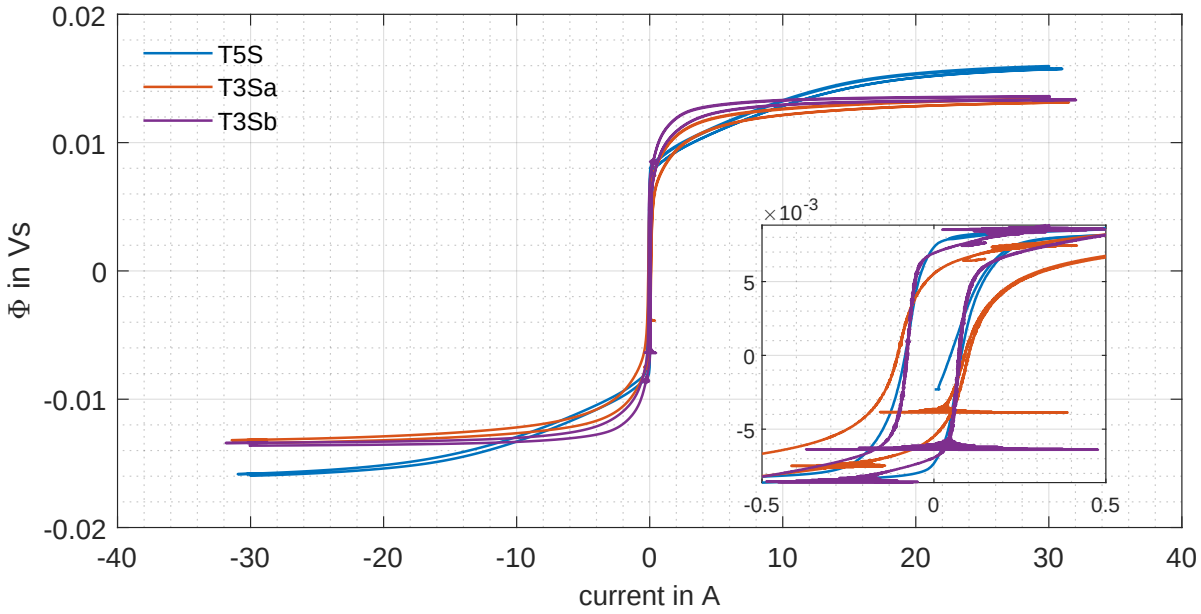

Figure 4.10: Comparison of the measured $\Phi - i$ DC hysteresis characteristics of transformer T5S, T3Sa and T3Sb. The zoomed view also shows the $\Phi - i$ characteristic.

Figure 4.11 depicts the AC and DC hysteresis characteristics of the transformer T3Sa measured with the AC saturation and the DC hysteresis test between the low-voltage terminals A-C. The peak current/flux is nearly the same. The reason for the difference in the hysteresis width is the difference in the excitation frequency. Due to the frequency of 0 Hz during the DC hysteresis test, the curve is narrower than the AC curve, due to the absence of the eddy current and excess losses (see **Section 2.4.4**). Also visible is the cobra shape of the AC hysteresis characteristics, due to the effect of the transformer core joint gap and winding capacity. The 'ringing' in **Figure 4.10** around 0 A in the DC hysteresis test occurs during the current polarity reversals at low currents, where two control parameters of the portable test device work against each other.

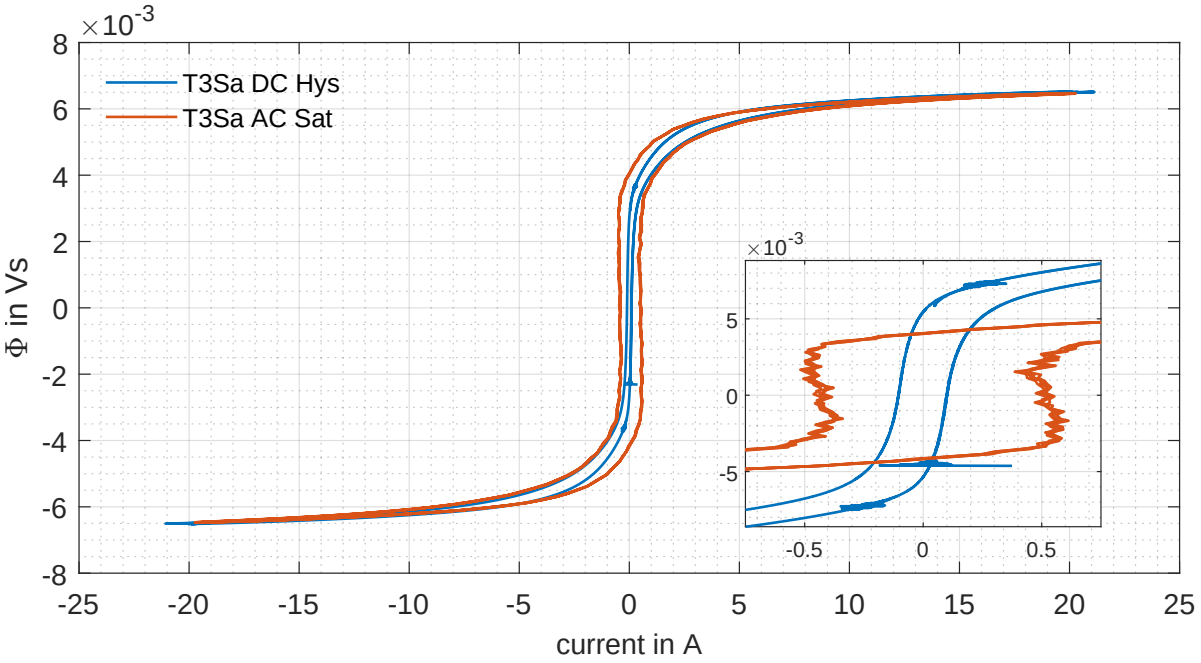

Figure 4.11: Comparison of the $\Phi - i$ DC and AC hysteresis characteristics of transformer T3Sa, measured via the low-voltage terminals A-C.

The equivalent variable air gap inductance L_{gap} is implemented as an inductor with a fixed inductance value or as a non-linear inductor with magnetic flux versus current ($\Phi_{\mathrm{gap}} - i_{\mathrm{gap}}$) characteristic. This characteristic is derived either from the AC saturation or the DC hysteresis test, using the initial magnetisation characteristic up to the knee point. The supporting points beyond the knee point are derived with a linear extrapolation of the last defined segment of the characteristic.

The equivalent gap length Δ is derived for a given point from the ratio Ψ_{gap}/i. Because the equivalent air gap in the joint shares the same flux as the limb, the flux density B inside the gap is calculated as $\Psi_{\mathrm{gap}}/(N \cdot A_{\mathrm{gap}})$, where N is the number of turns of the supply winding, A_{gap} is the cross-section area of the gap, which is assumed to be the same as the cross-section area of the limb A_{limb}, neglecting flux fringing effects. With this information the equivalent air gap length Δ is calculated, as a function of the magnetic flux density B, using (2.56).

Decreasing the equivalent air gap inductance (increasing the equivalent air gap length, see (2.56)) increases the no-load current of the corresponding phase. This effect could be of special interest for the equivalent air gap of phase B, which usually has a lower current amplitude in comparison to phase A and C during the three-phase no-load test. The reason could be the 'T' joint at phase B. If the same equivalent air gap length is assumed for limb B, as for limb A and C, the no-load current of phase B is underestimated. If the equivalent air gap length is increased (increases the equivalent air gap inductance), the no-load current of phase B fits the measured amplitude [Zir+22a]. This could indicate a larger equivalent air gap (length) for phase B, in comparison to phase A and C.

Figure 4.12 to **Figure 4.14** depict the equivalent air gap characteristic for the different transformers under test.

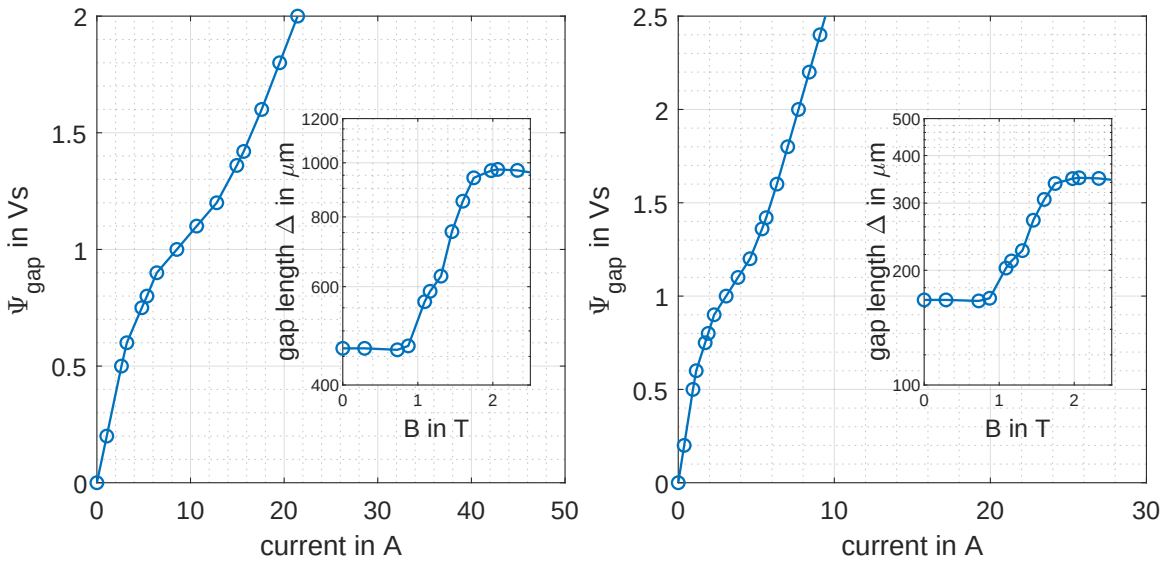

(a) Transformer T3Sa. (b) Transformer T3Sb.

Figure 4.12: $\Phi - i$ characteristic and corresponding equivalent air gap length as function of flux density, derived from DC hysteresis tests.

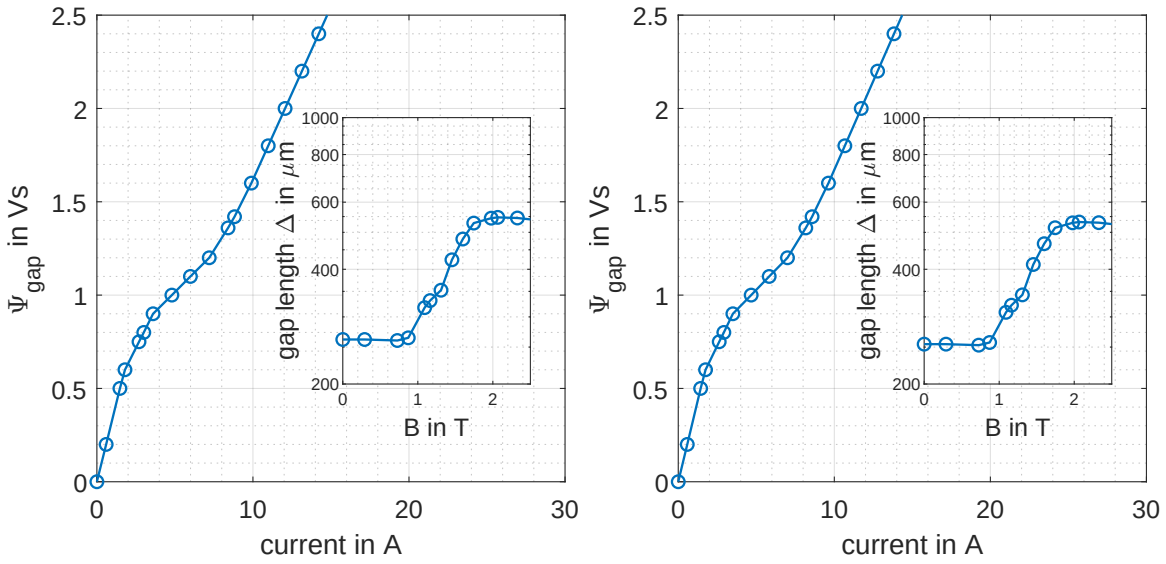

(a) Transformer T5S. (b) Transformer T3L.

Figure 4.13: $\Phi - i$ characteristic and corresponding equivalent air gap length as function of flux density, derived from DC hysteresis tests.

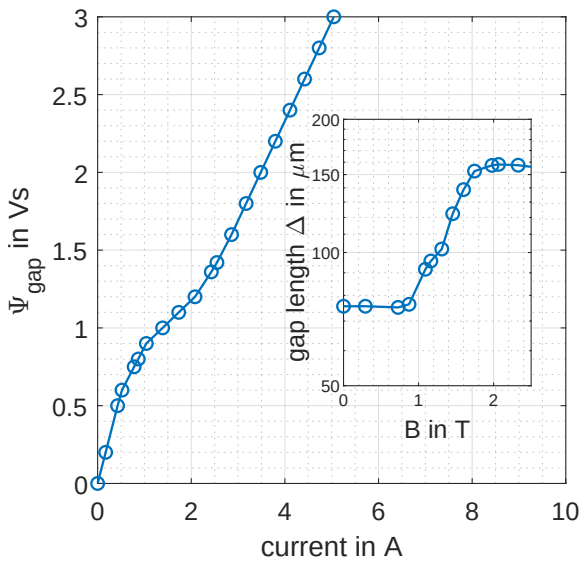

Figure 4.14: Transformer T5Lb $\Phi - i$ characteristic and corresponding equivalent air gap length, as function of flux density derived from the DC hysteresis test.

Winding Capacitance

For the modelling only the winding capacitance between the high-voltage terminals and ground/tank is used and is given in **Table 4.8**. The winding capacities are measured with the OMICRON CPC100 and the Testrano 600, according to **Figure 4.15**.

Table 4.8: Measured high-voltage winding capacitances to tank/ground for the transformers under test | (1) HV to core (no tank).

	T3Sa	**T3Sb**	**T5S**	**T3L**	**T5Lb**
C_{H} in nF	3.0	1.043	0.003457 (1)	3.797	16.1853
Vector Group	YNyn0	YNyn0	YNyn0	YNd5d5	YNd11

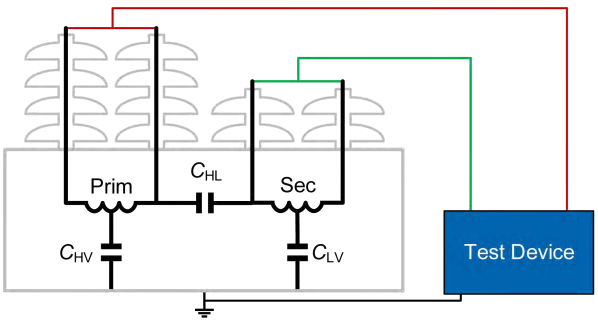

Figure 4.15: Schematic of transformer winding capacitance measurement.

The winding capacitance should be implemented and parametrised before the equivalent air gap inductance because both have an opposite effect on the shape of the hysteresis characteristics [Zir+22b]. Oscillations, measured during the AC saturation test in the ascending and descending

branch of the hysteresis loops, which could occur due to the interaction between the (high-voltage) winding capacitance and the stray inductance L_12, can be used to adopt the winding capacitance to accurately reproduce also the oscillation. The measured winding capacitance is connected to the ideal transformer, in case of the inductance-reluctance analogy model, and to the gyrator, in case of the capacitance-permeance analogy model. To reproduce the oscillation in the calculation a sufficiently small step size is required.

4.3.2 Transformer Saturation and Hysteresis Test Approach

The DC hysteresis and AC saturation test is a setup to measure the transformer core characteristics and mitigate the inter-phase magnetic coupling during the terminal measurements. The inter-phase magnetic coupling is demonstrated in **Figure 4.16** and **Figure 4.17**, where the positive and negative sequence $\Psi - i$ characteristics, deduced from terminal measurement, are depicted.

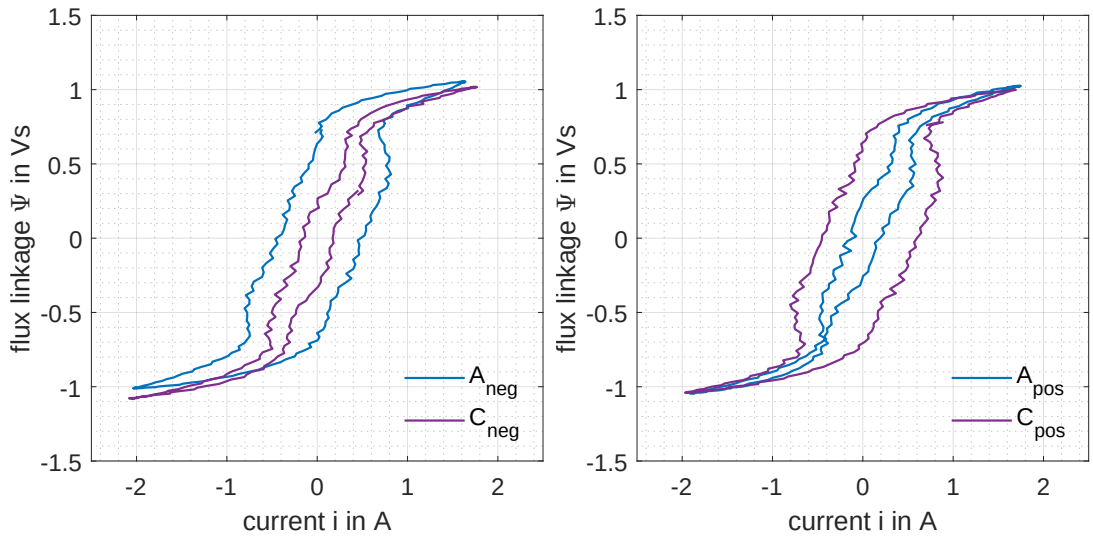

(a) Negative sequence $\Psi - i$ characteristic. (b) Positive sequence $\Psi - i$ characteristic.

Figure 4.16: Measured terminal $\Psi - i$ characteristic of A and C during positive and negative sequence.

Figure 4.17 depicts the $\Psi - i$ characteristic for the T3Sa transformer derived from a three-phase no-load test for 16 periods (50 Hz). The differences in width of the $\Psi - i$ characteristics are clearly visible.

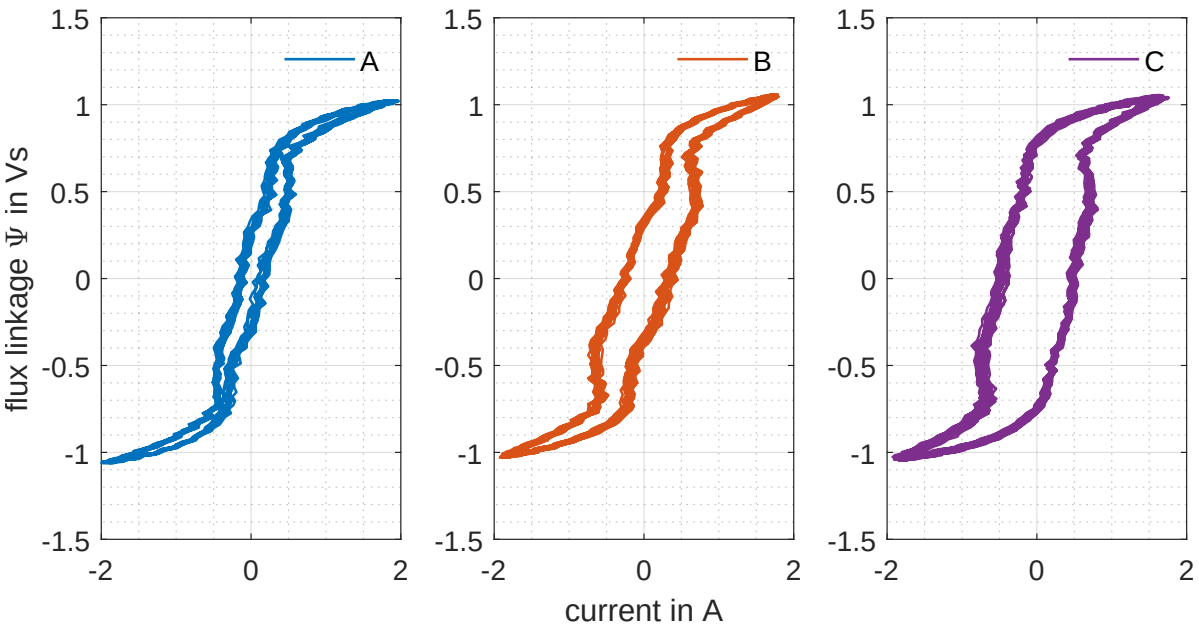

Figure 4.17: $\Psi - I$ characteristic of T3Sa derived from three-phase no-load test.

Both tests, the DC hysteresis and the AC saturation test, can be used for the transformer core parameter identification. The DC hysteresis and AC saturation test setup use the same transformer terminal connections, whereas the hysteresis test is conduct with DC and the saturation test with AC. Therefore, the DC hysteresis measurement does not include eddy current or excess losses, as the AC saturation test. **Figure 4.18** depicts the schematic of the DC hysteresis and AC saturation test on the example of a three-limb transformer core. For both tests, the transformer under test is in no-load conditions. The flux in the middle limbs vanishes under ideal conditions in a three- and five-limb transformer core. Voltage measurement on the primary and secondary windings can be used to verify that the flux in the middle limb vanishes or is significantly reduced (see **Figure 4.19** upper subplot). Therefore, the inter-phase magnetic coupling is mitigated. From the terminal voltage and current measurements, the $\Psi - i$ and/or $\Phi - i$ characteristic can be derived. These characteristics can be used during the hysteresis modelling process. A comparison of an AC saturation test and a DC hysteresis measurement is depicted in **Figure 4.11**.

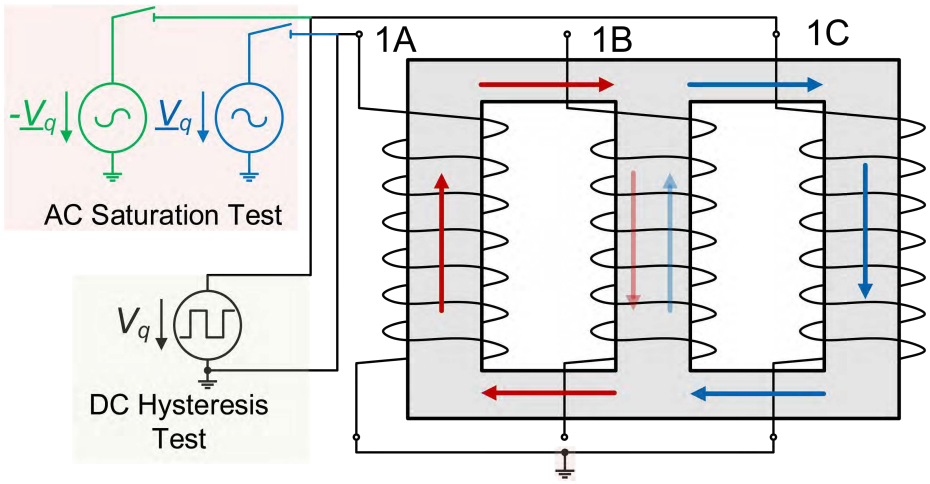

Figure 4.18: Schematic of the AC saturation and the DC hysteresis test setup.

AC Terminal Hysteresis Measurement

The AC saturation test requires a sufficiently large short-circuit capacity of the supply or a power amplifier with sufficiently large rated power. For the AC saturation test the voltage amplitude between the terminals need to be exceed at least twice the rated phase-to-neutral voltage of one phase to cause saturation conditions (up to 2 T) in the transformer core. Usually, a voltage increase of approximately 10 % is sufficient to cause saturation conditions in the core. In the case of the T3Sa a voltage amplitude between the outer terminals of at least twice 376.25 $V_{ph\text{-}n}$ is required. In the laboratory this is fulfilled by applying two single-phase voltages of 415 V_{peak} with 180° phase-shift to the outer terminals ($V_q(t) = -V_q(t)$). Resulting in an effective voltage of 830 $V_{peak\text{-}to\text{-}peak}$ between the terminals of the outer phases. **Figure 4.19** depicts typical voltage and current waveforms during the saturation test, supplied with a power amplifier. The voltage across the low- and high-voltage winding on the middle is below 1 V and below 200 V, receptively. This confirms the assumption that the flux in the middle limb almost vanishes during the AC saturation test.

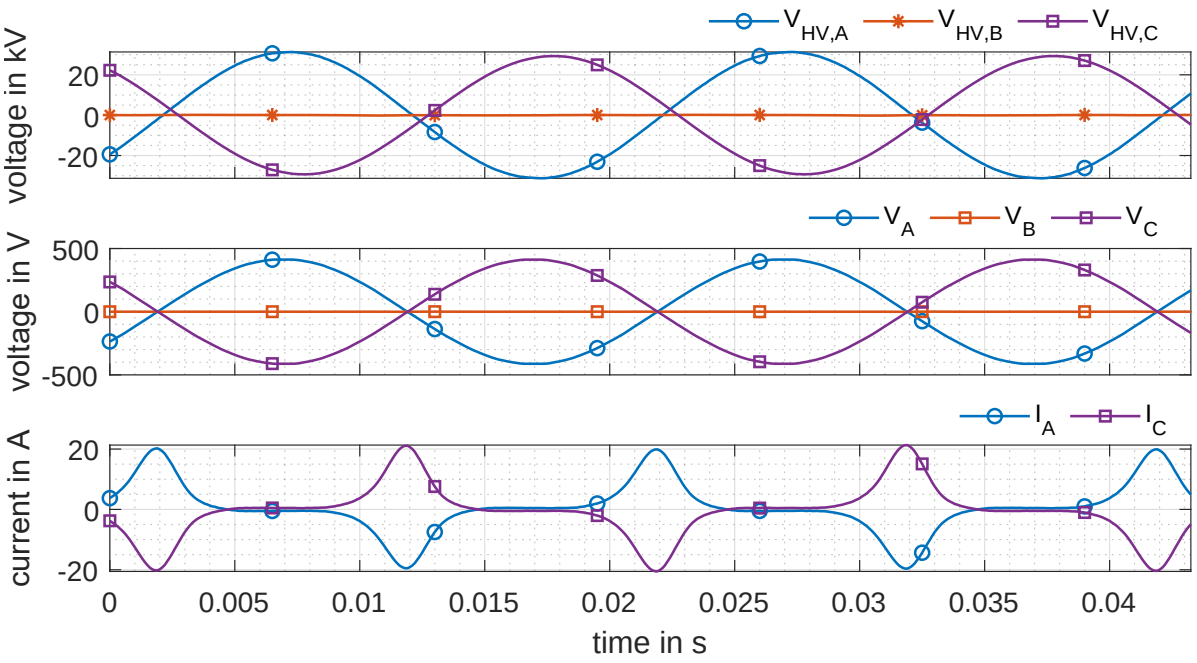

Figure 4.19: Typical measured voltage and current waveforms during the AC saturation test supplied from a power amplifier.

DC Hysteresis Measurement

The DC hysteresis test can also be carried out on transformers installed in substations. Due to the low test voltage and current frequency of 0 Hz/DC, the transformer core can be driven into saturation. Therefore, the hysteresis test can be used, if the AC saturation test (**Section 4.3.2**) can't be carried out. The DC hysteresis test is done in seven sequences, as marked in **Figure 4.20**. The sequences are explained in **Table 4.9**. The oscillation after the polarity reveals appear during tests with comparable small currents (continuous DC of the test device up to 33 A) are caused by two control parameters of the test device, affecting each other.

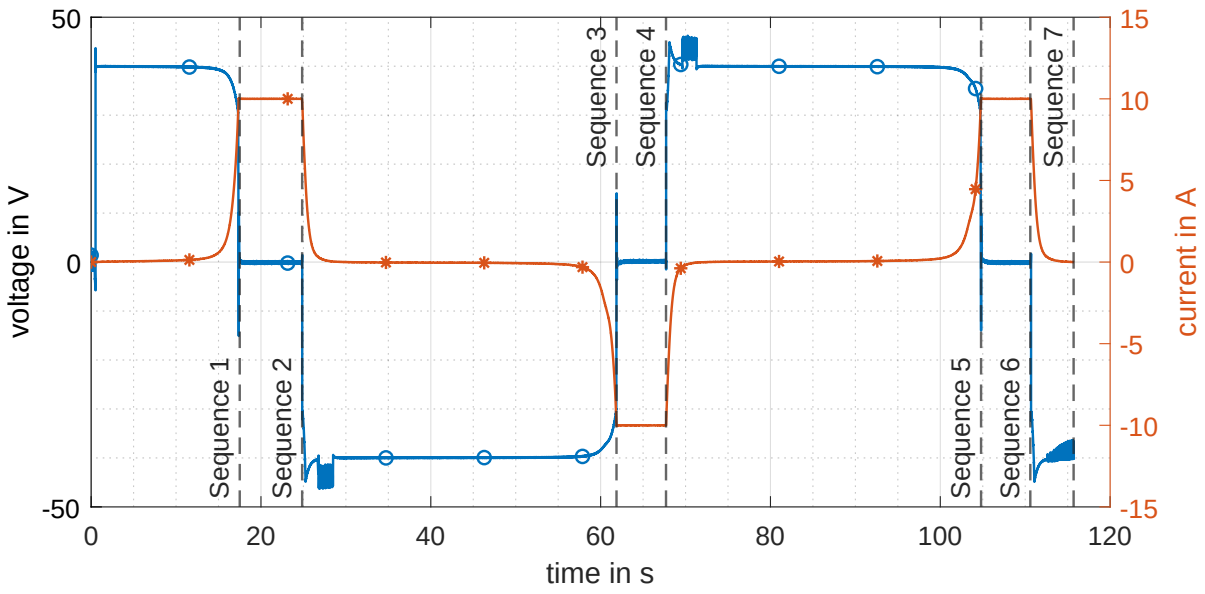

Figure 4.20: Typical measured current and voltage waveform during DC hysteresis test at T3L (**Section C.4**) between high-voltage terminal 1A and 1C.

During the DC saturation test, the hysteresis regions are approach in the following order: positive saturation - negative saturation - positive saturation - possible remanent flux density. If there is any remanent flux present inside the core at the beginning of the measurement, the hysteresis characteristic is shifted along the abscissa.

Table 4.9: Sequences during DC hysteresis test, according to **Figure 4.20**.

Sequence	Voltage	Current	Hysteresis Characteristic Part
1	+DC	$\Delta I > 0$	positive saturation
2	steady state conditions		
3	-DC	$\Delta I < 0$	negative saturation
4	steady state conditions		
5	+DC	$\Delta I > 0$	positive saturation
6	steady state conditions		
7	-DC	$\Delta I < 0$	remanent flux

The corresponding $\Psi - i$ characteristic to the voltage and current waveform measurement in **Figure 4.20** is depicted in **Figure 4.21**. To derive the hysteresis characteristics from the measurement, the measured voltage waveform requires to be processed with the following steps:

1.) subtract voltage drop across winding resistance from measured voltage,
2.) remove data points (current and voltage) where the magnitude of the measured voltage is below the voltage drop across the winding resistance caused by the pre-defined test currents ($< R \cdot I_{\mathrm{pre-defined}}$),
3.) numerical integration of the measured voltage using the trapezoidal method.

The flux linkage over current can be calculated as follows:

$$\Psi = \frac{1}{\Delta t} \cdot \int_{\Delta t} V_{\mathrm{core}}(t) \cdot \mathrm{d}t, \tag{4.2}$$

where Δt is a fixed time step and the reciprocal of the sample rate and $V_{\mathrm{core}}(t)$ is the measured voltage over time minus the ohmic voltage drop across the winding resistance. If further information on the transformer design, such as number of turns per winding or core dimensions are available, the flux per turn over current or even the $B - H$ characteristic can be reproduced from the measurement.

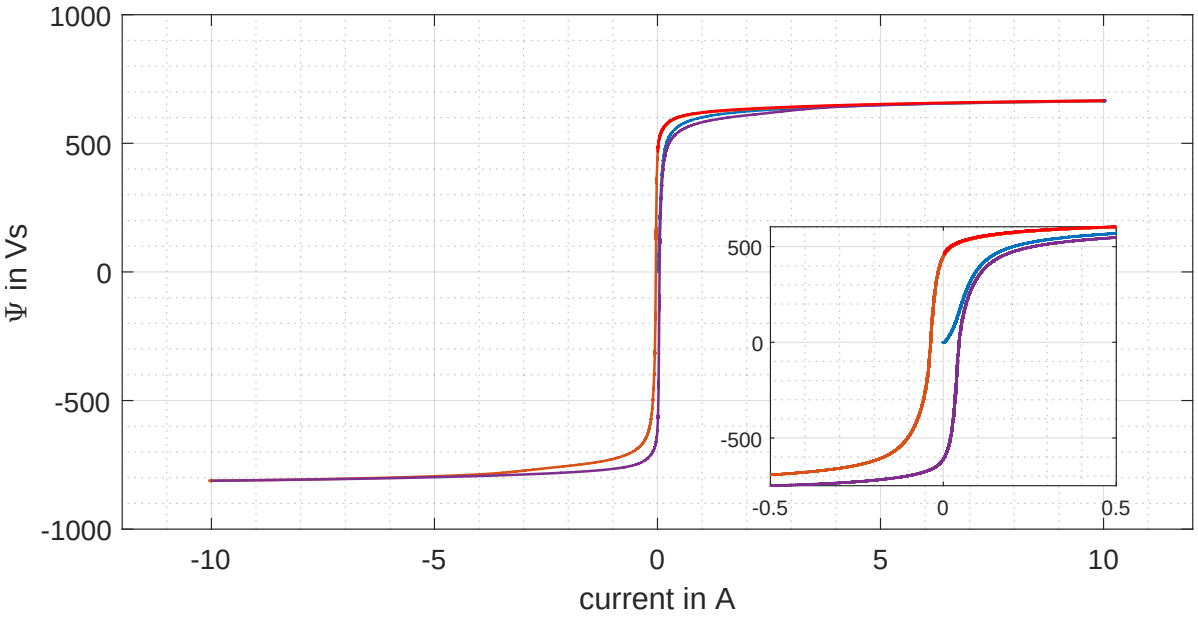

Figure 4.21: Corresponding typical $\Psi - i$ characteristic from DC hysteresis test at T3L (**Appendix C.4**) between high-voltage terminal 1A and 1C; blue: sequence 1; orange: sequence 3; purple: sequence 5; red: sequence 7

Hysteresis Model Parameter Estimation

A first set of JA hysteresis parameters can be determined from measurement data using the following steps, proposed by Jiles et al. in [JTD92] or use parameters reported in literature [JTD92; Ann+00; Kis06; Cha+06; Ami+20].

4.4 Transformer Models and Validation

For the model validation the factory acceptance test protocol data is used to parametrise the topological transformer models (inductance-reluctance, **Section 2.4.1** and capacitance-permeance analogy, **Section 2.4.1**). The AC saturation test or the DC hysteresis test is used during the hysteresis parameter optimisation in Matlab/Simulink. The measured current waveform of the AC saturation test or the DC hysteresis test is used to calculate the error between the measured and calculated current waveforms. During the optimisation process with the NMS algorithm this error

reduced to a minimum, by adjusting the hysteresis model parameters. To validate the models and the corresponding hysteresis model parameters, the standard no-load test is carried out with the derived model and compared to the measured current waveforms from the factory acceptance test.

For the simulation of the inductance-reluctance model with the JA hysteresis model, the step-size during the simulation need to be set to 10 μs, to ensure an acceptable accuracy of the calculation. The capacitance-permeance model can be calculated with a larger step size of 50 μs. Especially the power calculation is sensitive to step size changes.

Attention needs to be paid during the error calculation process to the time-synchronisation of the measured and calculated current waveforms. Besides the comparison of the current waveforms, other data representations such as the fast Fourier transformation (FFT) of the current waveforms and the $B - H$ representation were used and tested to calculate the error between the measured and calculated data. The comparison of the time-dependent current waveform yielded the best qualitative results.

4.4.1 Power Definition and Usage

Different approaches are available to calculate the power drawn by a load in a multi-wire system [FLM01; DIN02; LQC12; Ema07; III10; Wil11; GM12]. The standard IEEE 1459 [III10] is based on the concept of Budeanu. Due to the different power calculation methods, different results for the power demand can arise, while measuring the same the device, for example during DC biased transformers [GM12; KW18].

For the validation of transformer models, not only current and voltage waveforms should be compared, also the power demand should be compared. This allows to better judge the implemented hysteretical behaviour of the transformer core. In the context of transformers exposed to GICs, the symmetrical phase current is biased by the GICs, which shifts the transformer operation point on the hysteresis characteristics of the transformer core material. The shift in operation point can cause transformer half-cycle saturation. As a consequence of the half-cycle saturation, the phase currents get distorted. Thus, the term 'reactive power' is not defined, because it is only defined for the case of pure sinusoidal wave forms [III10].

Therefore, the following definitions of power are used in this thesis for the investigation of non-sinusoidal unbalanced conditions: the term 'active power' is used according to [III10], the term 'reactive power' is used according to (G.22), knowing 'reactive power' is not defined for non-sinusoidal current waveforms. Nevertheless, it is used for the waveforms from the simulation and measurements to make simulation and measurements comparable. The power demand of transformers under GIC bias is also discussed in [KW18].

For the comparison of the transformer models with the measurements the active, fundamental reactive Q_1 and total reactive power Q_t is analysed, according to IEEE Std. 1459:2010 [III10]. Because MATLAB/Simulink does not offer an IEEE Std. 1459:2010 compliant power calculation, the calculation is done with dedicated Simulink blocks, as depicted in **Figure 4.22** and **Figure 4.23**.

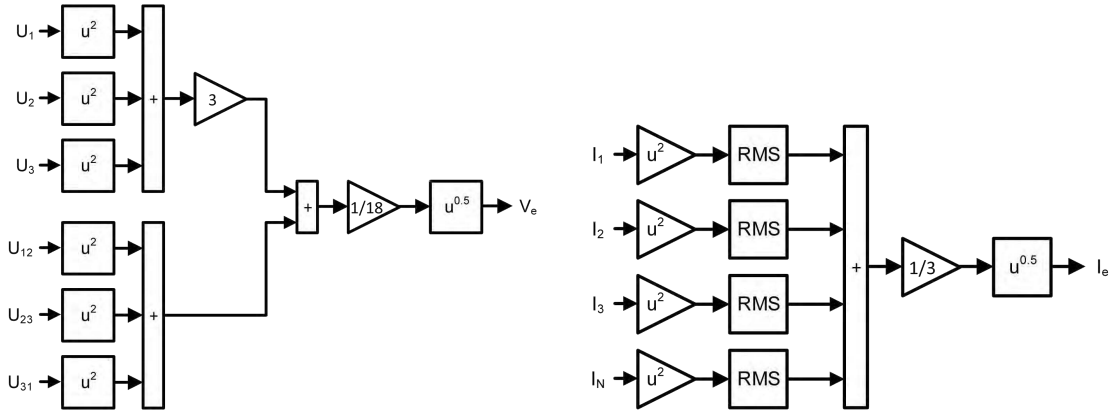

(a) Effective voltage calculation. (b) Effective current calculation.

Figure 4.22: Effective voltage and current calculation according to IEEE Std. 1459:2010 [III10].

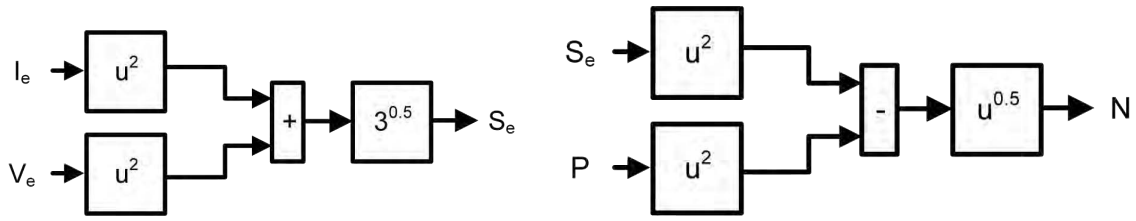

(a) Effective apparent power calculation. (b) active power calculation.

Figure 4.23: Effective apparent power and active power calculation according to IEEE Std. 1459:2010 [III10].

Attention should be paid to the power measurement in the simulation environment, which could be sensitive to simulation step size. Thus, different power values can be derived at different (fixed) step sizes with the same model.

4.4.2 Hysteresis and Saturation Test

In the subsequent sections the measured current and voltage waveforms of the DC hysteresis and AC saturation are used to derive the JA hysteresis parameters during the optimisation of the corresponding test, on the example of the transformer T3Sa and T3Sb. The JA and ReCap hysteresis model parameters derived with the AC saturation test are stated in **Table 4.10**. The model parameters derived with the DC hysteresis test are stated in **Table 4.11**.

DC Hysteresis Test

The transformer T3Sa DC hysteresis characteristic was measured via the high-voltage terminals A and C with a portable transformer test device. The maximum current was set to 0.5 A to stay below the maximum rated current of the high-voltage windings of 0.824 A (**Appendix C.1**). For the

Table 4.10: Hysteresis model parameters derived with the AC saturation test.

Jiles Atherton Hysteresis Parameters						
	M_s	α	k	a	c	
T3Sa	$1.605 \cdot 10^6$	$347.5 \cdot 10^{-6}$	24.87	134.32	0.2199	
T3Sb	$1.863 \cdot 10^6$	$366.8 \cdot 10^{-6}$	24.32	123.03	0.2015	
ReCap Hysteresis Parameters						
	C_s	R_h	a	b	n	m
T3Sa	0.0107	6.9297	1.4953	0.0148	13.0	31.0

Table 4.11: Hysteresis model parameters derived with the DC hysteresis test

Jiles Atherton Hysteresis Parameters						
	M_s	α	k	a	c	
T3Sa	$3.217 \cdot 10^6$	$171.9 \cdot 10^{-6}$	14.12	209.54	0.2004	
T3Sb	$1.770 \cdot 10^6$	$385.2 \cdot 10^{-6}$	25.53	94.43	0.2156	
ReCap Hysteresis Parameters						
	C_s	R_h	a	b	n	m
T3Sa	0.0107	6.9297	1.4953	0.0548	13.0	31.0

calculation the measured voltage waveform is approximated with a rectangular voltage waveform with equivalent magnitude, duration and rise/fall time. The measured voltage signal should not be used without any post processing, due the noise and small oscillations in the measurement, caused by the control of the transformer test device. Large $\mathrm{d}v/\mathrm{d}t$ in the measured voltage signal can cause instabilities during the model calculation. **Figure 4.24** depicts the measured and calculated current and voltage waveform during the DC hysteresis test with the deviation in the calculated current waveform. The corresponding $\Phi - i$ characteristic is depicted in **Figure 4.25**.

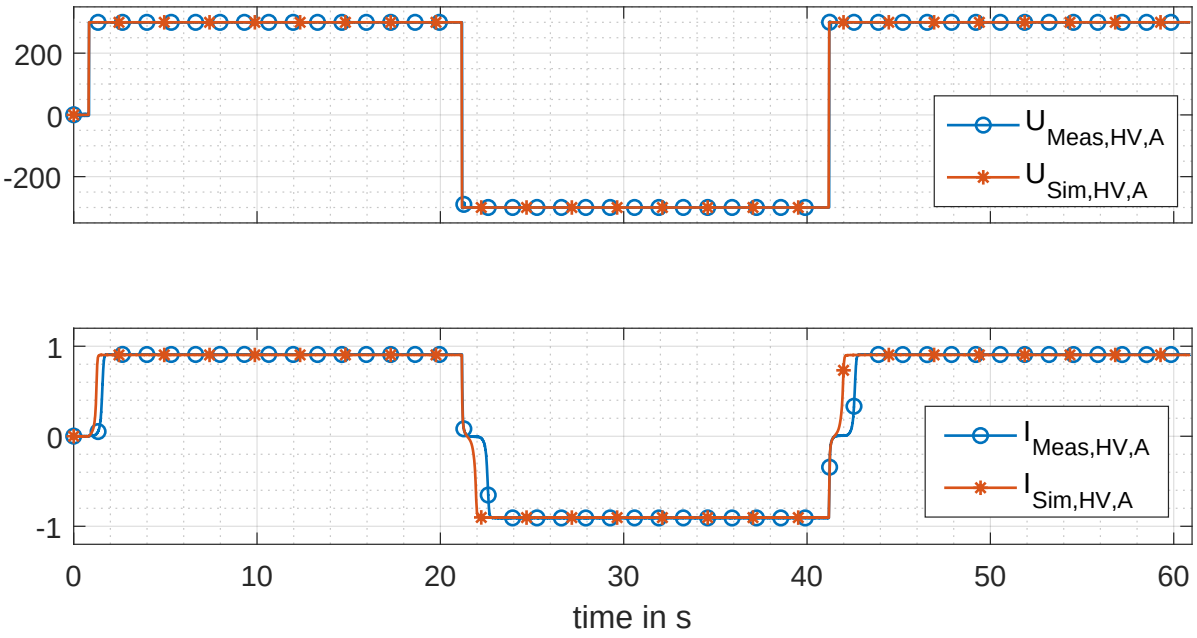

Figure 4.24: Measured and calculated current and voltage waveforms during the DC hysteresis test for the transformer T3Sa via the high-voltage terminals A-C.

The measured and calculated voltage waveforms are almost indistinguishable. A difference in the current waveforms appears during the descending and ascending current around zero-crossing at 22 s and 42 s, respectively. During the time around zero-crossing, the measured current is almost constant for approximately 0.5 s after zero-crossing. An almost constant current in the current waveform corresponds to a steep decrease/increase of flux in the $\Phi - i$ characteristic around zero flux. The small deviation during the first current increase could be related to the measurement uncertainty and a small remanence flux, visible in **Figure 4.25**. The calculated current doesn't show the same characteristic around zero-crossing as the measured current, which leads to the conclusion that the inclination of the modelled hysteresis characteristic is not as steep as the actual major hysteresis loop. Considering the major hysteresis loop (**Figure 2.25**), the branch from the negative coercive field H_c to the negative saturation flux density B_s and the branch from the positive coercive field to the positive saturation flux density in the model are not as steep as the corresponding branch in the measurement. The inclination of the hysteresis characteristic is also affected by the equivalent air gap inductance (rotates the hysteresis characteristic counter-clockwise with increasing L_gap, see **Section 2.4.2 Figure 4.9**). Therefore, the equivalent air gap inductance should be increased or decreased to increase the $\Phi - i$ characteristic inclination around zero-crossing, if a constant equivalent air gap inductance is used. If a non-linear inductance is used to represent the equivalent air gap inductance, the inclination of the saturation characteristic of the non-linear inductance should be increased. The increase of inclination of the saturation characteristic corresponds to a decrease of the equivalent air gap length. The effect of the winding capacitance can be considered as minor, due to the DC measurement.

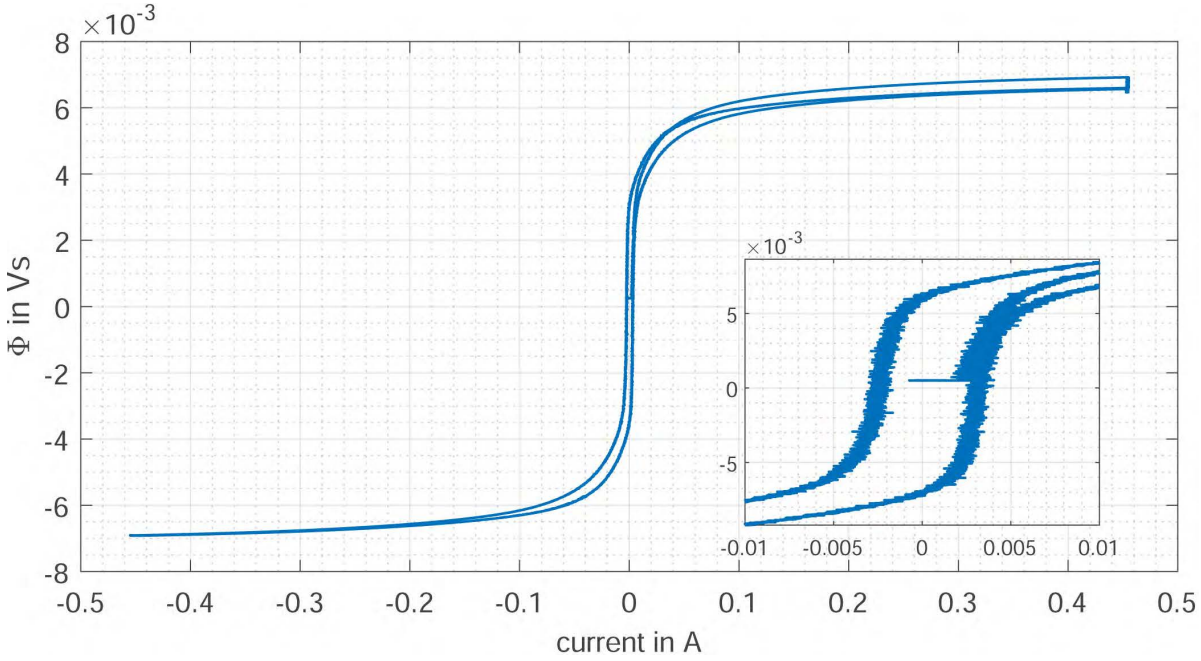

Figure 4.25: $\Phi - i$ characteristic calculated from transformer T3Sa DC hysteresis test via high-voltage terminals A-C.

To improve results obtained from the optimisation process, using the DC hysteresis test, the measured current and voltage waveforms are further processed to reduce the duration of the optimisation. By removing the data point at the time instances with constant current magnitude ($\mathrm{d}i/\mathrm{d}t < 20\,\mathrm{mA/s}$) and by using only the waveform from the initial magnetisation via the positive saturation inductance to the negative saturation inductance (see **Figure 4.26**.), the duration of the measured waveform data was reduced to 4.5 s.

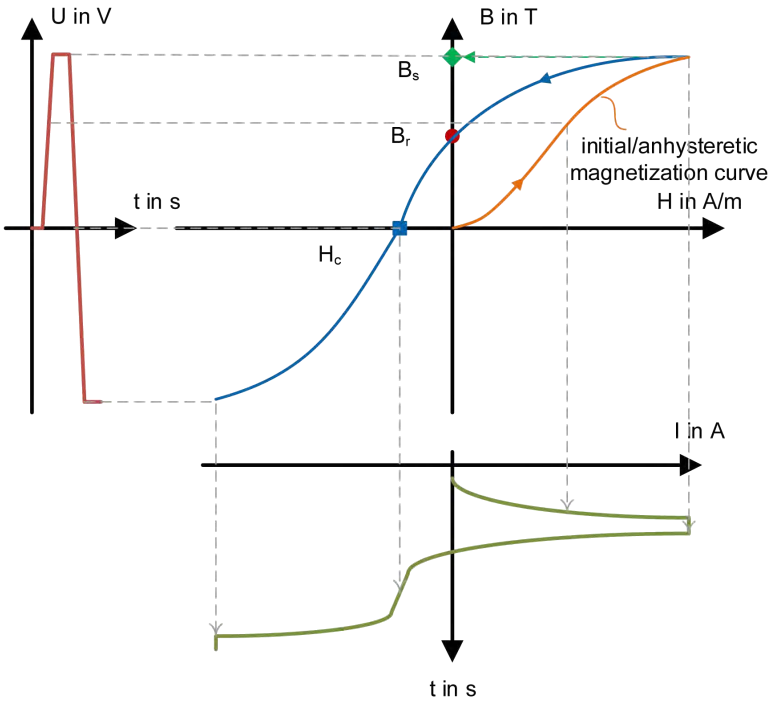

Figure 4.26: Schematic relation between applied voltage waveform, part of the hysteresis characteristic and resulting current waveform during the DC hysteresis test.

Figure 4.27 depicts the measured voltage and corresponding current from the DC hysteresis test after the processing, presented in **Figure 4.24**. Right before 2.5 s in **Figure 4.27** the voltage ringing, caused by the control system of the transformer test device is noticeable.

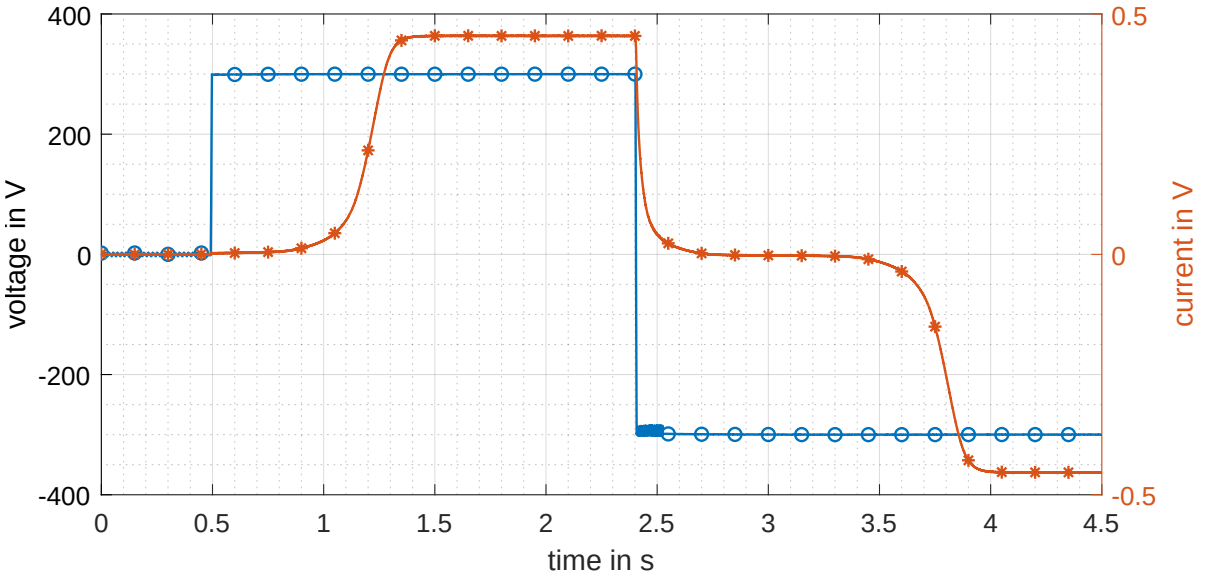

Figure 4.27: Processed DC hysteresis measurement data from transformer T3Sa used during optimisation of the hysteresis models.

AC Saturation Test

Figure 4.28 depicts the measured and calculated phase voltages and currents of the T3Sa transformer during the AC saturation test. The calculated waveforms are derived with the inductance-reluctance model. The small discrepancies between the measured and calculated current waveform are explained partly by the measurement uncertainty and the remaining error during the optimisation (to limit the computational time during the optimisation). In addition to the aforementioned effects, the transformer model parameters, such as the joint equivalent air gap can vary for each transformer limb. In the model, the joint equivalent air gaps are assumed to be equal for each limb.

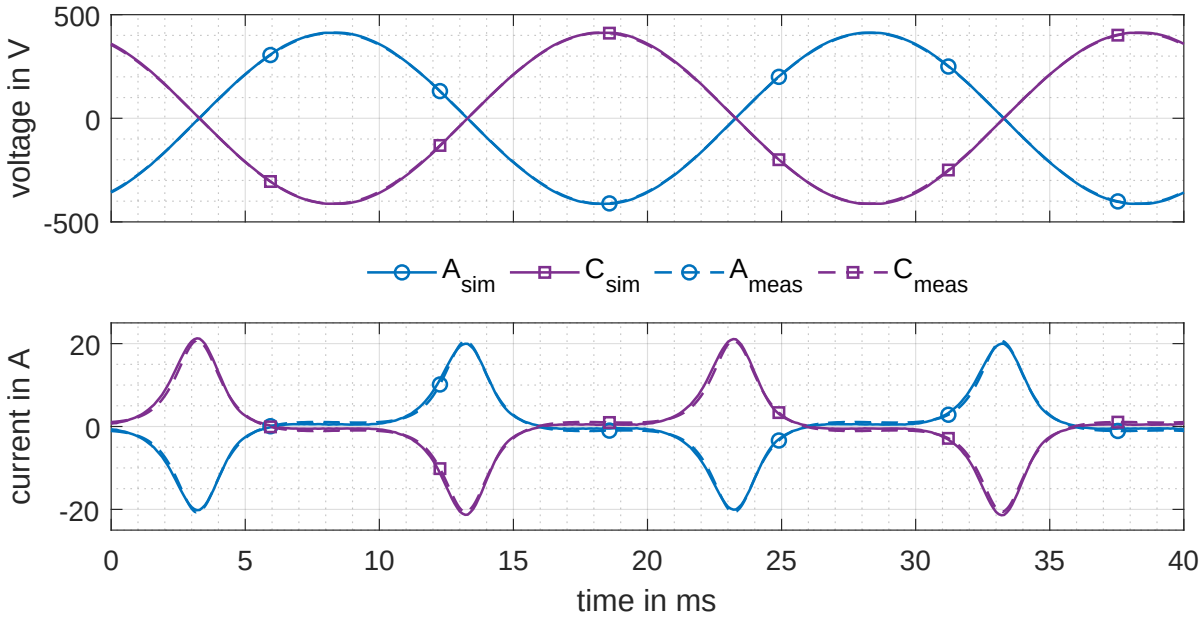

Figure 4.28: Transformer T3Sa inductance-reluctance model: measured and calculated current waveforms, derived from the AC saturation test.

Table 4.12 lists the power demand of the T3Sa transformer for the AC saturation test. The power demand is underestimated in the derived model. The usage of the implemented reactive power Q calculation in Matlab/Simulink overestimates the total reactive power Q_t demand and the fundamental reactive power Q_1 demand, in comparison to the measured values. The discrepancy between the measured and calculated power demand is partly due to the accuracy of the measurement, but mainly to the methods used to measure and calculate the power demand. For example, the CT used for the measurement has a measurement frequency range from 40 Hz - 10 kHz. Therefore, frequency components below 40 Hz may not be measured accurately, introducing an error in the measured power. The deviations between the measured and calculated values are within 15 %, according to the standard IEC 60076-1:2012 [IEC12a] and close to the maximum allow tolerance of 10 % for the total loss.

Figure 4.29 depicts the voltage and current waveform of the measured and calculated AC saturation test from the ReCap model.

Table 4.12: The power demand comparison of transformer T3Sa for the AC saturation test and the inductance-reluctance model.

	calculated	**measured**	**deviation**	**deviation in %**
S in VA	4207.4	4695.2	487.8	10.4
Q_t in var	4199.2	4680.2	481.0	10.3
Q_1 in var	4157.9	3665.8	492.1	13.4
P in W	263.5	375.4	111.9	29.8

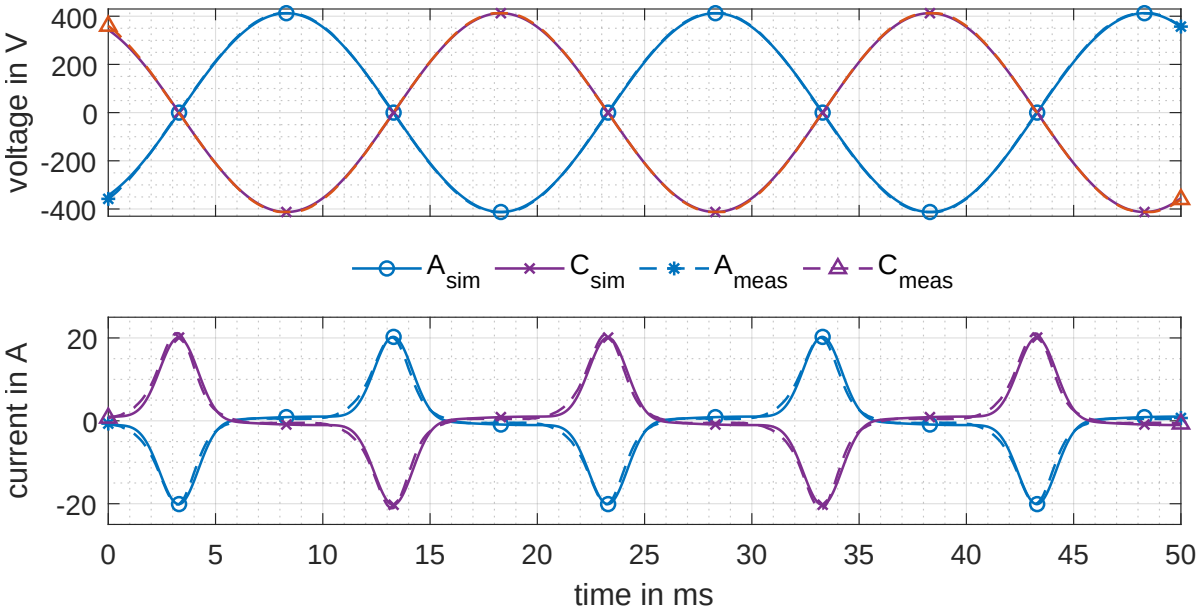

Figure 4.29: Transformer T3Sa capacitance-permeance model: measured and calculated current waveforms, derived from the AC saturation test.

Table 4.13summarises and compares the calculated and measured power demand during the AC saturation test with the capacitance-permeance model. The calculated and measured fundamental reactive and active power demand practically coincides. The total reactive power demand is underestimated by the model. The reason for the deviation should be further evaluated during the modelling procedure.

Table 4.13: The power demand comparison of transformer T3Sa for the AC saturation test and the capacitance-permeance model.

	calculated	**measured**	**deviation**	**deviation in %**
S in VA	3626.2	4695.2	1069	22.77
Q_t in var	3607.49	4680.2	1072.7	22.9
Q_1 in var	3620.1	3665.8	45.7	1.2
P in W	371.66	375.4	3.7	1.0

The AC saturation test was also carried out on the five-limb laboratory transformer T5S (**Appendix C.3**). **Figure 4.30** depicts the voltage and current waveform during the AC saturation test, with a voltage

magnitude of 410 V. The current of phase C is 0.5 A higher than the current magnitude in phase A. Changing the phases from the power amplifier gives the same result for limb C as before. This means the different current magnitude is related to the transformer design. It is assumed that the air gap in the butt joint of limb three is smaller than the air gap in limb one, which results in an increase in current magnitude in limb three (see also **Section 2.4.2**). The assumed magnetic asymmetry is also visible in the neutral point current, which carries the 0.5 A during the current peak of phase A.

Figure 4.30 depicts the AC saturation test of the transformer T5S. Inspecting the transformer core from the side, reveals small deviations in the stacked core sheets. Therefore, the air gap in the joint of limb C or the joint of the adjacent unwounded return limb could be larger in comparison to the corresponding air gap of limb A or the adjacent unwounded return limb. The increased current can be realised in the transformer model by decreasing the equivalent air gap inductance, and thus increasing the equivalent air gap length Δ (see (2.56)).

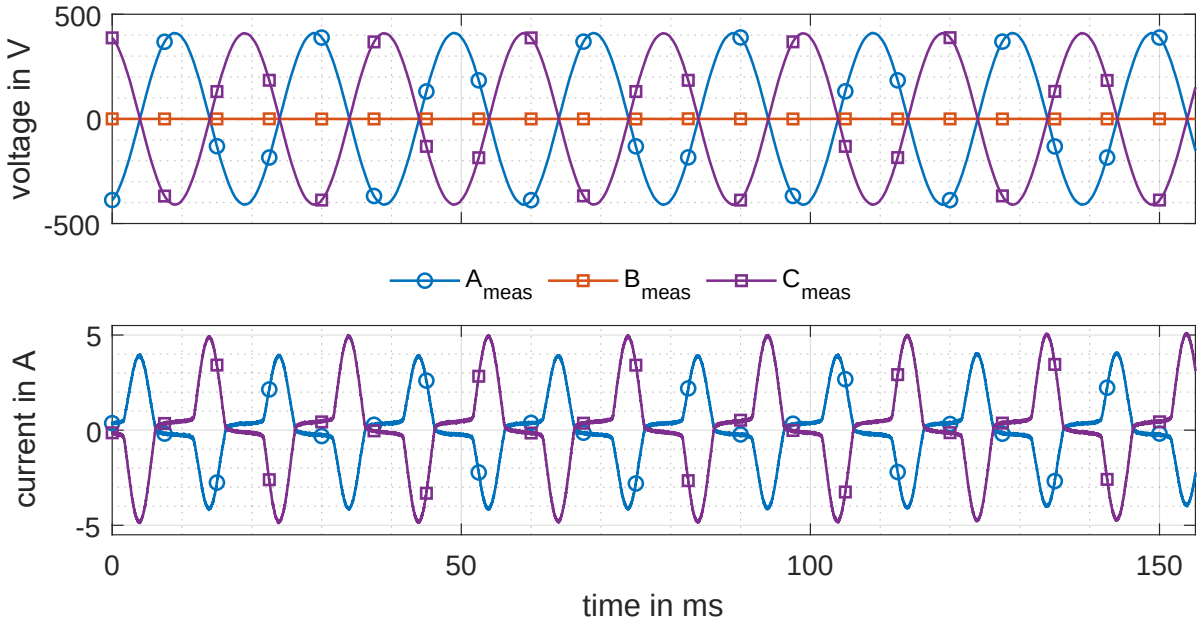

Figure 4.30: Transformer T5S: measured waveforms during the AC saturation test with 290 V_{rms}.

In case of the transformer T3Sb, the AC saturation test at rated frequency of 50 Hz and a peak voltage of 412.5 V per phase could not force the transformer core into saturation conditions. This is due to the use of high grain-oriented (HGO) steel in the transformer T3Sb (**Appendix C.2**) in comparison to conventional grain-oriented (CGO) steel used in the transformer T3Sa (**Appendix C.1**). In order to force the transformer core into saturation, the frequency is reduced to 40 Hz at a constant peak voltage of 380 V per phase. The corresponding measured peak phase current was 111.1 A.

4.4.3 No-Load Test

For the model validation the derived hysteresis parameters from the AC saturation and DC hysteresis test are used to calculate the three-phase no-load currents. The calculated and measured three-phase

no-load currents are compared in the following section.

No-Load Test with Model Parameters derived from AC Saturation Test

Figure 4.31 depicts the measured and calculated three-phase no-load voltage and current waveforms of the T3Sa transformer. The calculated waveforms are derived with the transformer T3Sa inductance-reluctance model with the JA parameters optimised using the AC saturation test. The discrepancies between the measured and calculated current waveform are explained partly by the measurement uncertainty and the remaining error during the optimisation (to limit the computational time during the optimisation). In addition to the aforementioned effects, the transformer model parameters, such as the joint air gap can vary for each transformer limb. In the model the equivalent air gaps are assumed to be equal for each limb. **Table 4.14** presents the power demand components during the standard no-load test carried out with the supply from the power amplifier. The deviation between the measured and calculated active power is well within in the required 15 % from the IEC 60076-1:2012 [IEC12a]. The total reactive power and the apparent power deviation are also within the maximum allowed deviation of 15 %. Further improvements regarding smaller deviations in the power demand could probably be reached by a longer optimization of the JA parameters and the consideration of different equivalent air joint gaps for each limb.

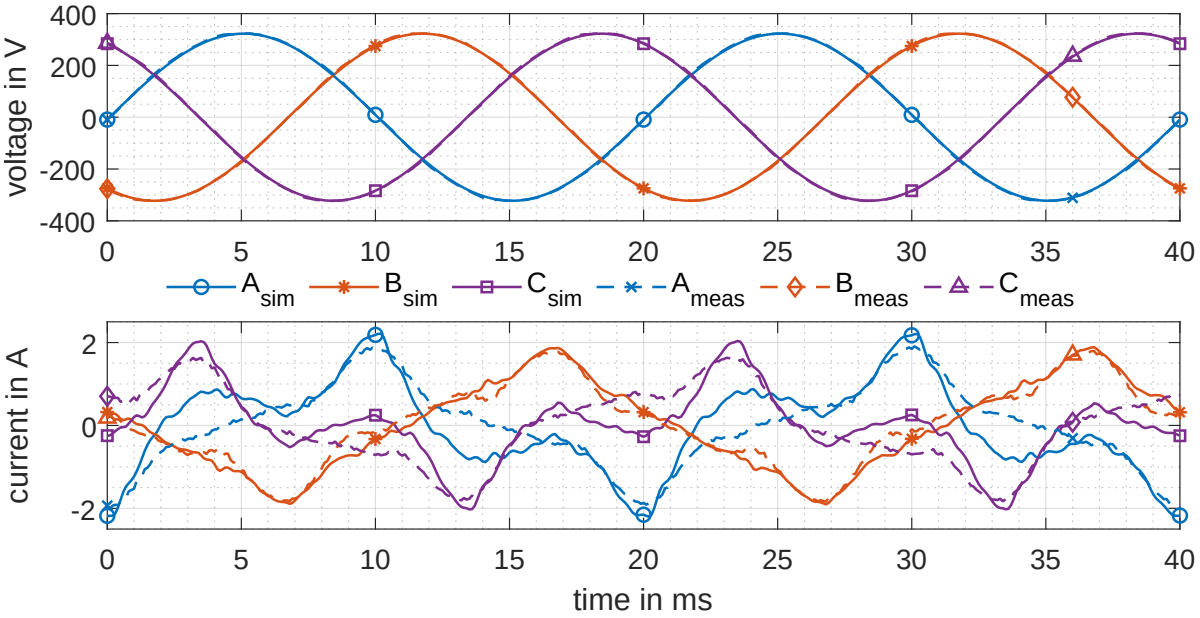

Figure 4.31: Transformer T3Sa no-load test: comparison of calculated and measured current and voltage waveforms derived with the AC saturation test depicted in **Figure 4.28**.

Figure 4.32 depicts the measured and calculated no-load voltage and current waveform of the T3Sa ReCap model, with the hysteresis model parameters derived from the AC saturation test.

Table 4.14: Power demand comparison for no-load test with JA model parameters derived from the AC saturation test.

	calculated	measured	deviation	deviation in %
S in VA	579.8	650.9	71.06	10.9
Q_t in var	556.3	629.7	73.4	11.7
Q_1 in var	531.1	585.8	54.7	6.4
P in W	163.7	164.6	0.9	0.55

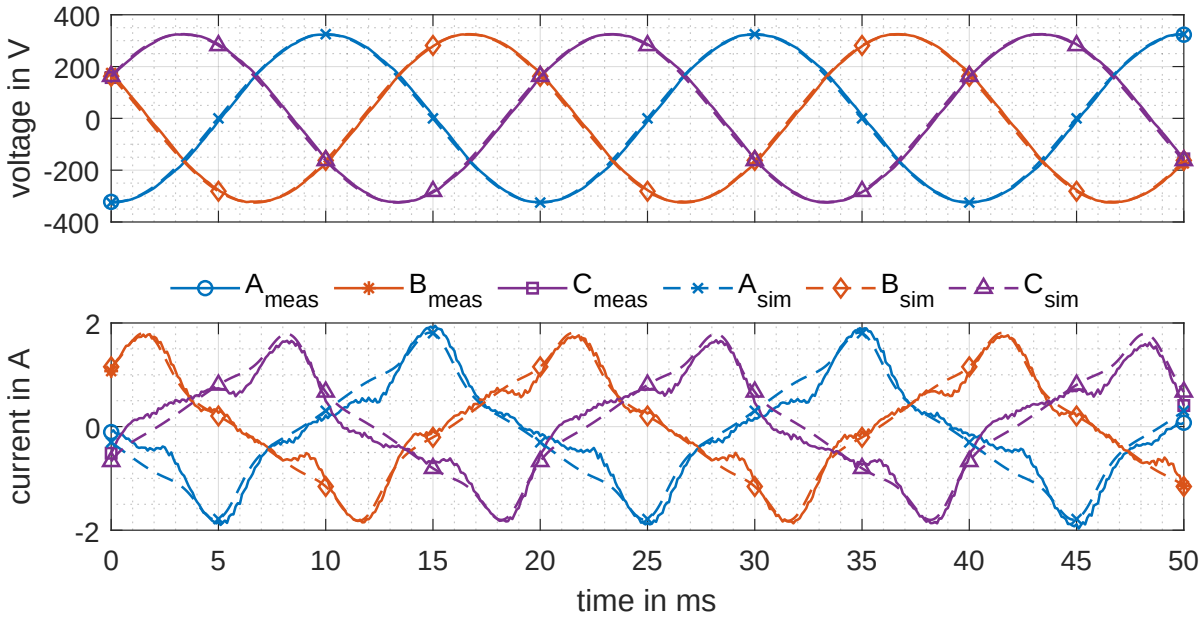

Figure 4.32: Transformer T3Sa ReCap model: comparison of calculated and measured current waveforms during the optimisation, derived from the AC saturation test.

No-Load Test with Model Parameters derived from DC Hysteresis Test

Figure 4.33 depicts the current and voltage waveforms of the derived T3Sa transformer model with the usage of the DC hysteresis test data for the JA hysteresis parameter optimisation. During the parameter optimisation the measurement signal is approximated by a rectangular voltage waveform, as depicted in **Figure 4.27**. The no-load current magnitudes of all phases are underestimated by the calculated currents in the range of 0.1 A to 0.6 A, without any further model adjustments. The result depicted in **Figure 4.33** was derived after 39 iterations during the optimisation with a residual error between the measured and calculated current waveform of 0.002836. During test with a higher number of optimisation iterations, the calculated current waveform was even more underestimated by the model.

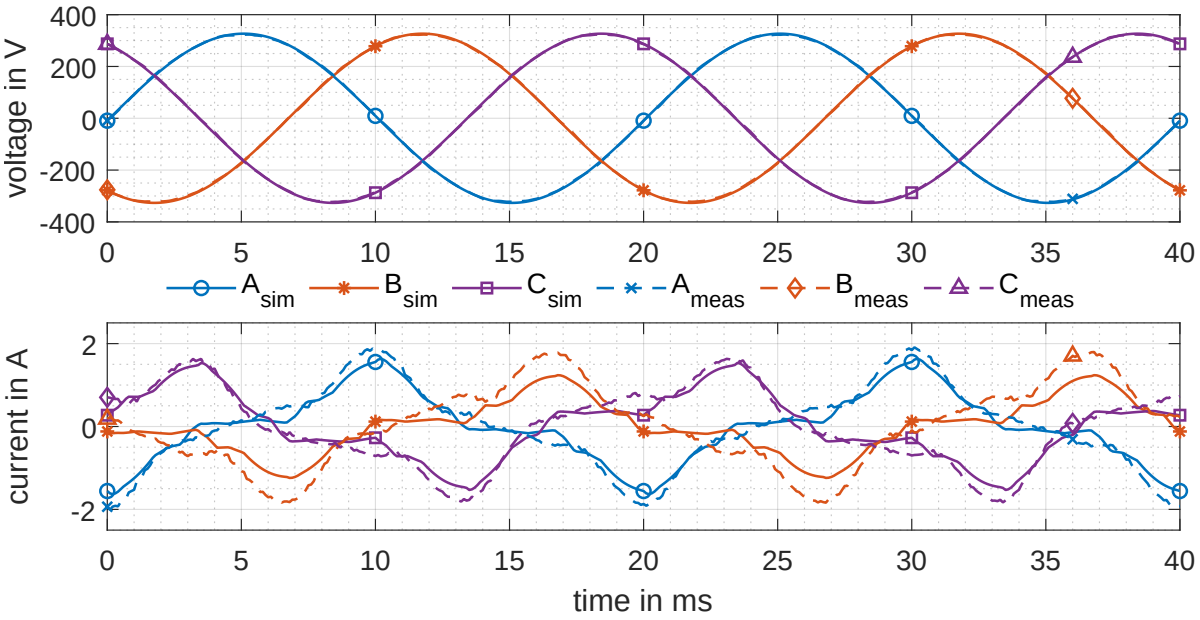

Figure 4.33: Transformer T3Sa JA model: comparison of calculated and measured current waveforms, derived from the DC hysteresis test with the signal depicted in **Figure 4.27**.

Figure 4.34 presents the measured and calculated current waveform, as well as the corresponding absolute error, during the optimisation process after 39 iterations with an error of 0.002836 between the calculated and measured current waveform with the error function (4.3).

$$\text{Error} = \sum \frac{(I_{\text{meas}} - I_{\text{sim}})^2}{Signal\ length} \tag{4.3}$$

The error between calculated and measured currents increase during the initial magnetisation between 0.5 s and with the same error magnitude between 3.5 s and 4 s.

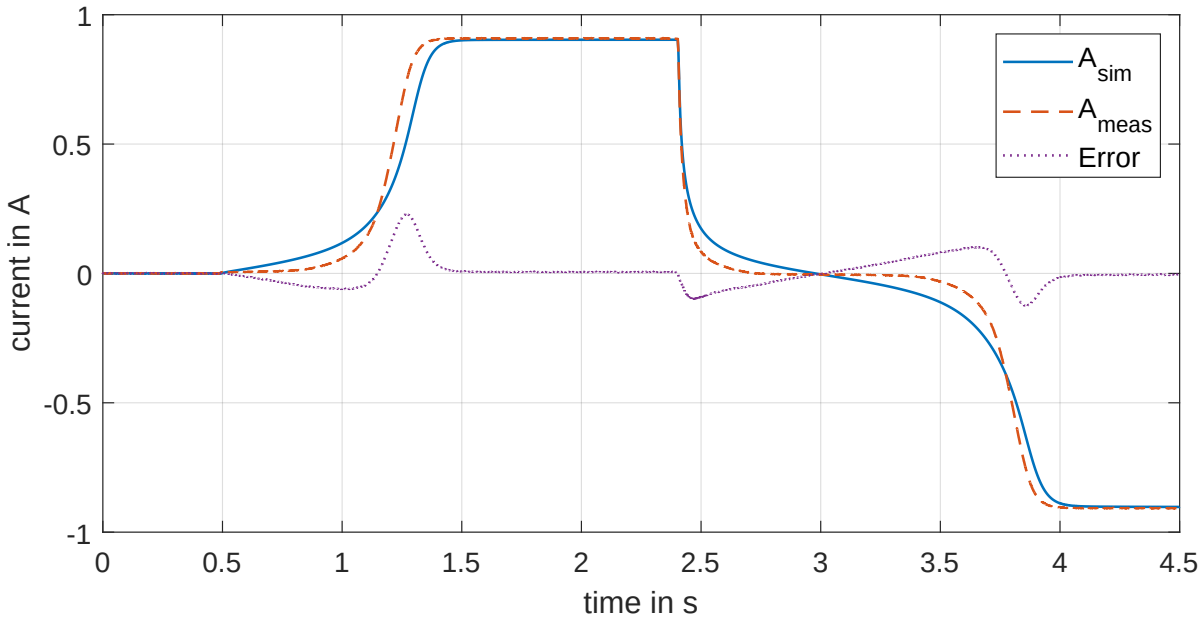

Figure 4.34: Transformer T3Sa JA model: comparison of calculated and measured current waveforms of phase A during the optimisation, derived from the DC hysteresis test.

Table 4.15 compares the power demand during the standard no-load test of the transformer T3Sa model, with the JA hysteresis parameters derived with the DC hysteresis test, and the power demand measured in the laboratory. Without any further adjustments of the model parameters the power calculated with the derived model from the DC hysteresis test underestimates the measured power demand by 0.01 % for the total apparent power, 2.1 % for the total reactive power and 37.8 % for the active power demand. The total reactive and the fundamental reactive power is overestimated by the model.

Table 4.15: Power demand comparison for no-load test with model parameters derived from the DC hysteresis test.

	calculated	**measured**	**deviation**	**deviation in %**
S in VA	650.8	650.9	0.1	0.01
Q_t in var	642.8	629.7	13.1	2.1
Q_1 in var	628.8	585.8	43	7.3
P in W	102.3	164.6	62.3	37.8

No-Load Test Conclusion

Both tests, the AC saturation and the DC hysteresis test, can be used to parametrise the JA hysteresis model, implemented in the inductance-reluctance model of the transformer T3Sa. The duration of the optimisation using the AC saturation test is in the range of ten minutes, with acceptable deviation in power demand and current amplitude. The duration of the optimisation using the DC hysteresis test is in the range of several ten minutes, if the start values for the optimisation

are chosen appropriate and the processed waveforms of the DC hysteresis test are used. The DC hysteresis test has the advantage that the test can be carried out on any transformer in every location, whereas the AC saturation test is limited by an appropriate power source and therefore also limited by the test facility. In terms of power demand accuracy, the model derived from the AC saturation test currently provides higher accuracy than the model derived with the DC hysteresis test. This is explained by the absence of eddy current and excess losses during the DC hysteresis test.

4.4.4 Inrush Current Test

For the further verification of the developed modelling approach, based on the AC saturation test, the inrush current was calculated for the transformer T3Sa and compared to the measured inrush current in [Zir+22b]. The inrush current calculation was carried out in the electromagnetic transient program (EMTP) ATPDraw [HP19] with the topology model of the transformer T3Sa, depicted in **Figure 4.35**. The model is parametrised with the data from the factory acceptance test and the transformer core design data. The transformer core hysteresis characteristic was implemented as DHM (see **Section 2.4.4**).

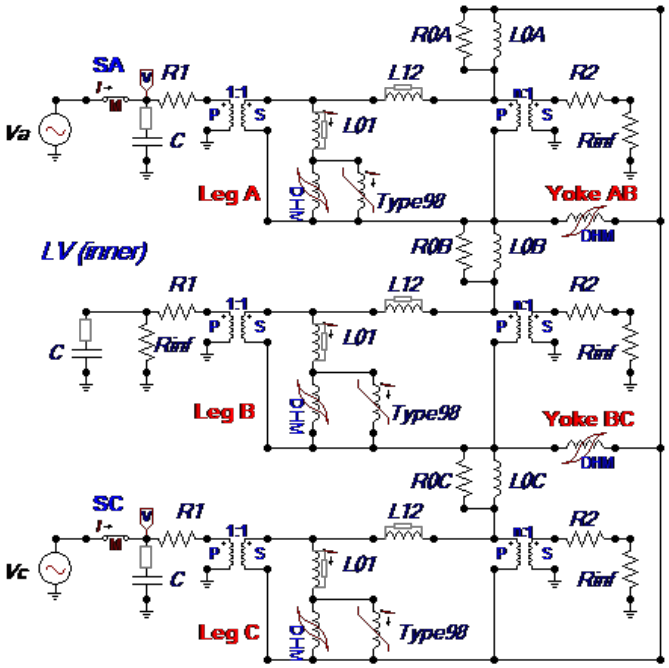

Figure 4.35: Electric model of transformer T3Sa in ATPDraw for the AC saturation test [Zir+22b].

In order to verify the applicability of the transformer models for inrush current calculation, the transformer T3Sa was periodically disconnected and reconnected to the public grid. The goal was to find a case with a maximum current amplitude. The measured voltages and corresponding currents are depicted in **Figure 4.36**. The flux densities in each limb, just before the transformer connection to the grid, are calculated by integrating the phase voltages and recalculating the flux

linkages into flux densities. The flux densities are estimated as $B_{\mathrm{A}}(0) = -0.2\,\mathrm{T}$, $B_{\mathrm{B}}(0) = -0.1\,\mathrm{T}$ and $B_{\mathrm{C}}(0) = 0.3\,\mathrm{T}$. By using these flux densities as initial values, the inrush currents, depicted in **Figure 4.36**, are calculated.

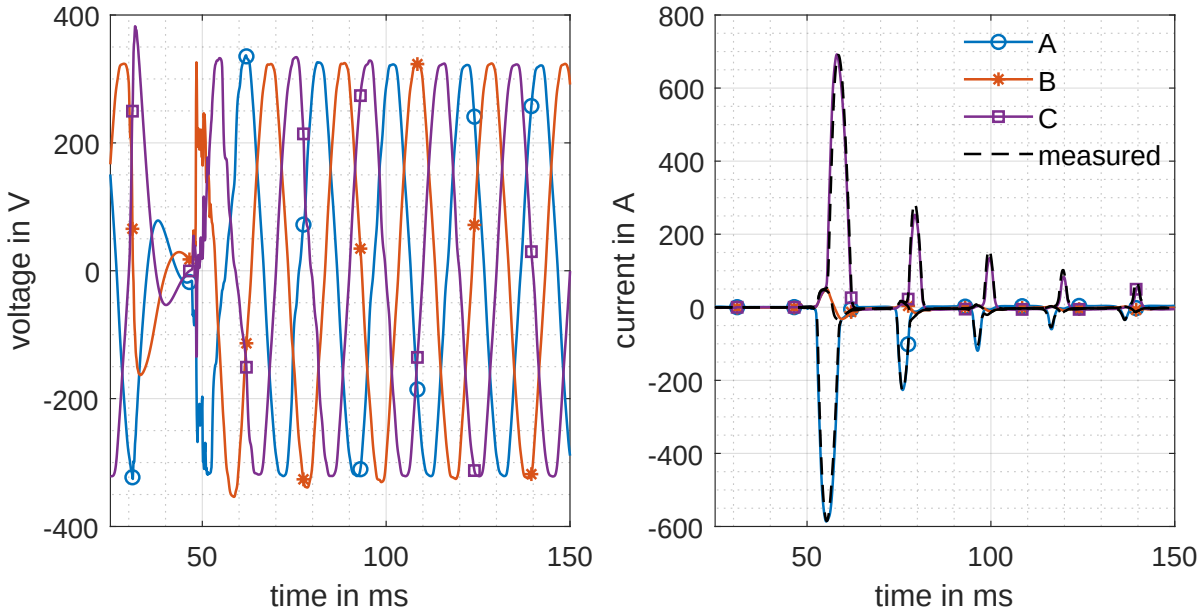

Figure 4.36: Measured and calculated voltage and current waveforms of transformer T3Sa during inrush.

The calculated and measured inrush currents are obtained with an additional impedance between the supply and the transformer, which corresponds to the cable resistance and inductance connecting the T3Sa with the distribution grid transformer. The currents are almost indistinguishable, which gives a further proof for the accurate modelling. Neglecting the grid impedance results in an overestimation of the inrush current peak [Zir+22a].

4.4.5 Back-to-Back Test

For the investigation of transformers during DC bias, a B2B setup with two identical or at least similar transformers can be used [LE02; Zir+18b]. The B2B test requires an accessible transformer neutral terminal on the high-voltage side. For the B2B test, two transformers are connected via their high-voltage terminals. The high-voltage neutral terminals are connected B2B with a DC source in series between the neutral terminals, as depicted in **Figure 4.37**. The transformer T3Sa is energised via the low-voltage terminals from the public grid or from a power amplifier. The second transformer T3Sb is connected to the T3Sa via the high-voltage terminals and/or via the low-voltage terminals. The voltage at the high-voltage neutral terminals is close to 0 V with respect to ground during symmetrical sinusoidal excitation. During non-sinusoidal excitation, e. g. during DC bias accompanied by half-cycle saturation, the voltage at the high-voltage neutral terminal increases. During the laboratory B2B tests with the T3Sa, T3Sb and T5S transformers, the voltage at the high-voltage neutrals reached a maximum voltage of $\pm 10\,\mathrm{V}$ during ungrounded transformers

neutrals. Therefore, a DC can be superimposed via the high-voltage neutrals of the transformers with the source on ground potential, which do not requires an isolation of the DC source for the rated high-voltage of the transformer. For safety reasons, sometimes one high-voltage neutral terminal is solidly grounded, and the second transformer neutral is grounded via a resistance, to ensure the superimposed DC to flow via the high-voltage windings during the B2B tests. As DC source, either a series connections of batteries [Pro+20], a full-wave diode rectifier with an isolating transformer (**Appendix F**) or a welding power supply [LE02] could be used.

The voltage waveform during the supply from the public grid showed a 'rectangular' waveform in comparison to an ideal sinusoidal waveform (see **Figure 4.46**). Therefore, B2B tests were carried out with both supplies and analysed. The analysis revealed that the power amplifier is preferable to the public grid as supply.

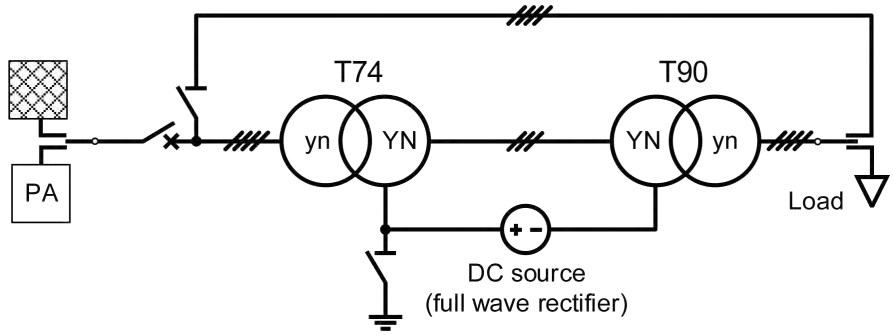

Figure 4.37: B2B test setup with the laboratory transformers T3Sa and T3Sb.

Figure 4.38 depicts the low- and high-voltage phase currents during the B2B test of transformer T3Sa and T3Sb in no-load condition without superimposed DC. The total apparent power demand is 814.15 VA, the total reactive power is 767.21 var, the fundamental reactive power is 722.24 var and the total active power is 272.45 W. The two smaller maxima before and after the current peak, visible on each phase of the low-voltage current waveform, are caused by the B2B operation of the two transformers under test. The first side maximum is to be assigned to transformer T3Sa and the second side maximum is to be assigned to transformer T3Sb (see also **Figure 4.31** for the measured no-load current of transformer T3Sa). The side maxima are caused by the magnetic coupling of the three phases, especially during the current peak of one phase. Besides the magnetic coupling the vector group of the transformer affects the current waveform [Car17].

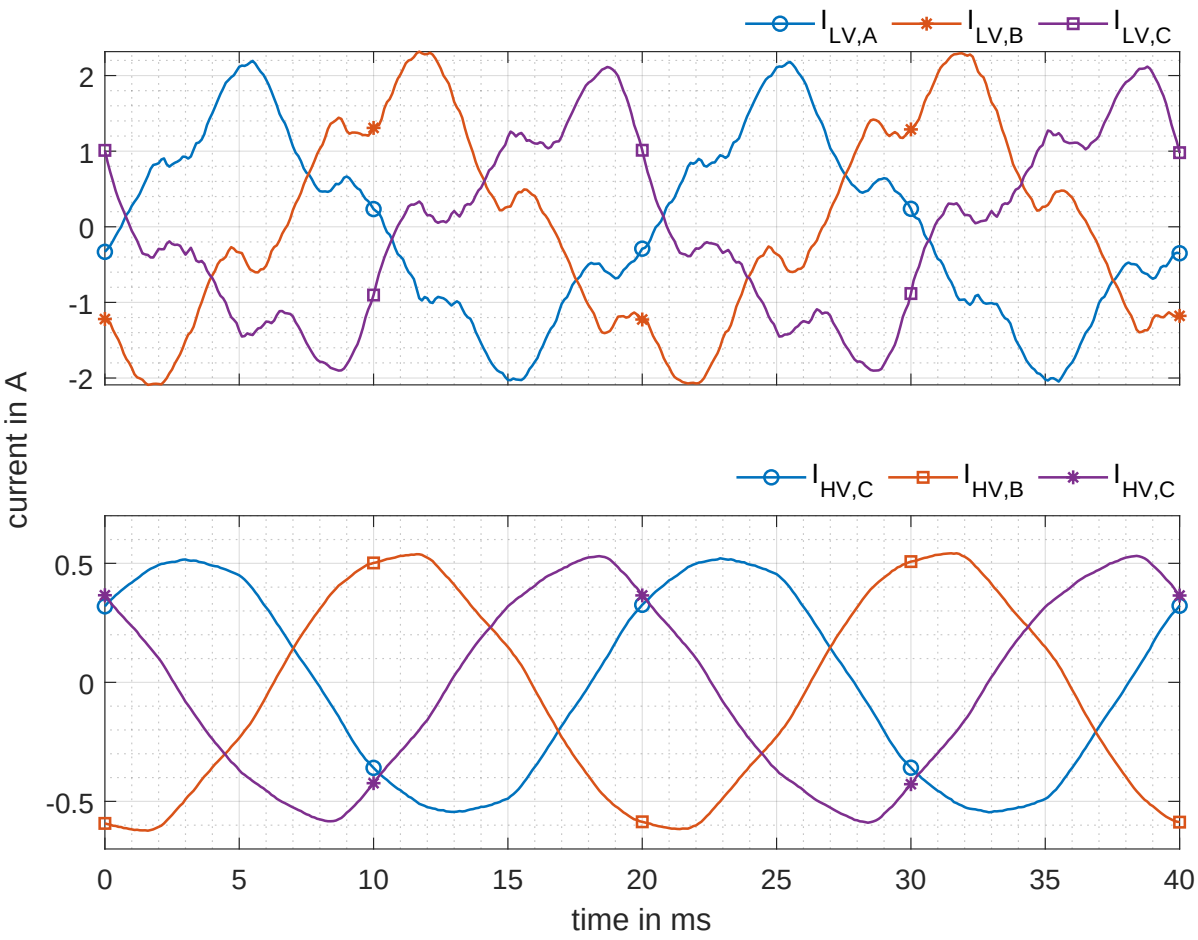

Figure 4.38: Measured current waveforms during the B2B test of the transformers T3Sa YNyn and T3Sb YNyn in no-load condition at the public grid.

4.4.6 Back-to-Back Tests with DC Rectifier at Public Grid

The following **Figure 4.39**, **Figure 4.40** and **Figure 4.41** present the measurement results from a B2B test with the transformer T3Sa and T3Sb with supply from the public grid. The transformer T3Sb is only connected to the transformer T3Sa via the high-voltage terminals. Between the high-voltage neutral of both transformers a full-wave rectifier is used to superimpose a voltage of 63 V_{rms}, which corresponds to a DC of 345 mA. Assuming an equal distribution of the DC between the high-voltage windings, this corresponds to a DC of 115 mA per phase, which corresponds to 13.96 % of the rated current of the transformer T3Sa (824 mA **Appendix C.1**). The current via the high-voltage terminals are measured with Rogowski coils around the transformer bushing. Therefore, no DC component is visible in current measurement on the high-voltage terminals. In **Figure 4.39** the half-cycle saturation in the low-voltage supply current of the transformer T3Sa is visible. Whereas no half-cycle saturation characteristic is noticeable in the high-voltage currents. Therefore, it is assumed that the B2B connected transformer T3Sb didn't reached saturation, while a DC of 340 mA is superimposed via the high-voltage neutrals. The voltage ripple of 1.1 V, caused by the full wave diode rectifier is depicted in **Figure 4.40**.

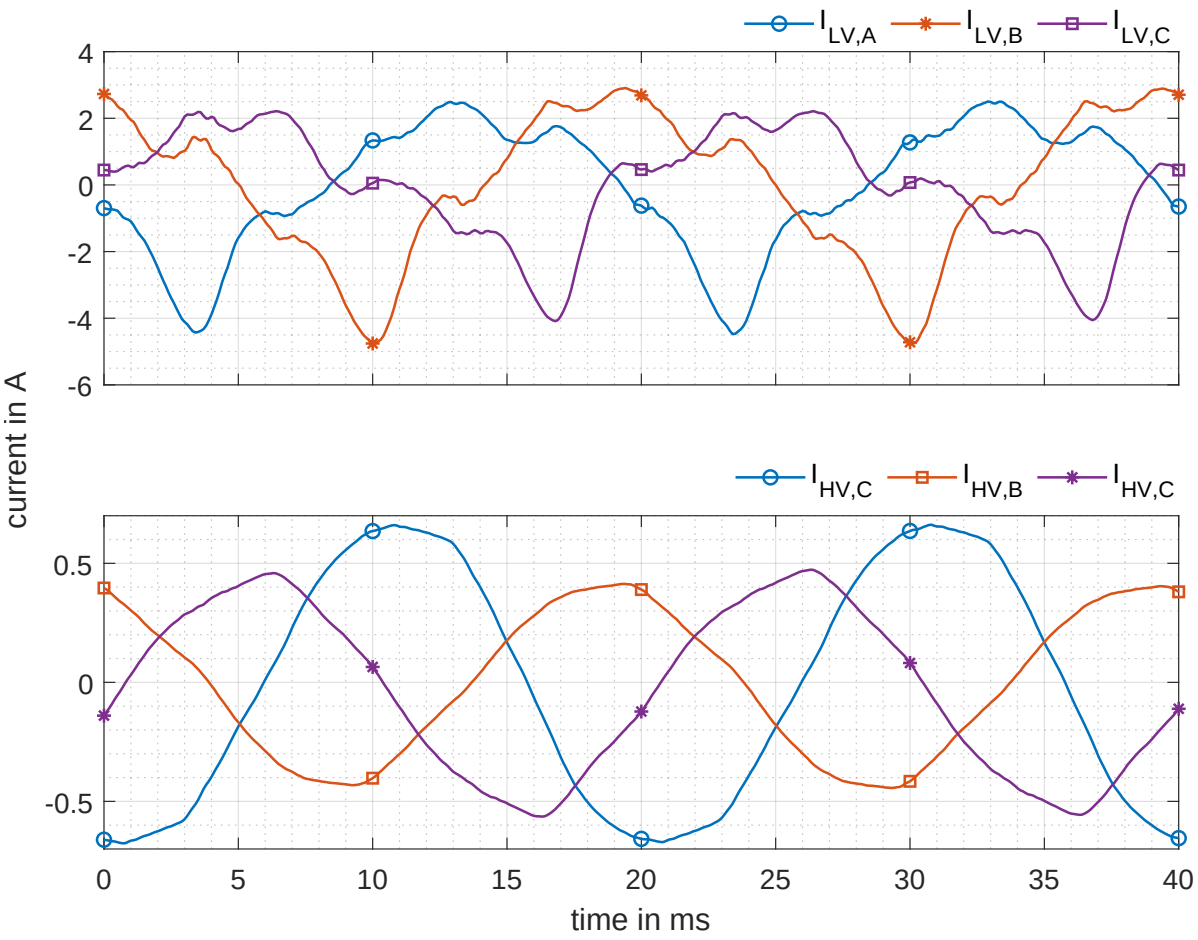

Figure 4.39: Measured low- and high-voltage currents during B2B test of transformers T3Sa and T3Sb with superimposed DC from the full-wave rectifier.

The logarithmic scale in **Figure 4.40** of the ordinate depicts the frequency spectrum of the measured current via the high-voltage neutrals with an AC/DC current clamp. Besides the pronounced peak around 0 Hz, caused by the superimposed DC, dominating frequency components at odd harmonics of the rated frequency of 50 Hz are distinctive indication transformer half-cycle saturation.

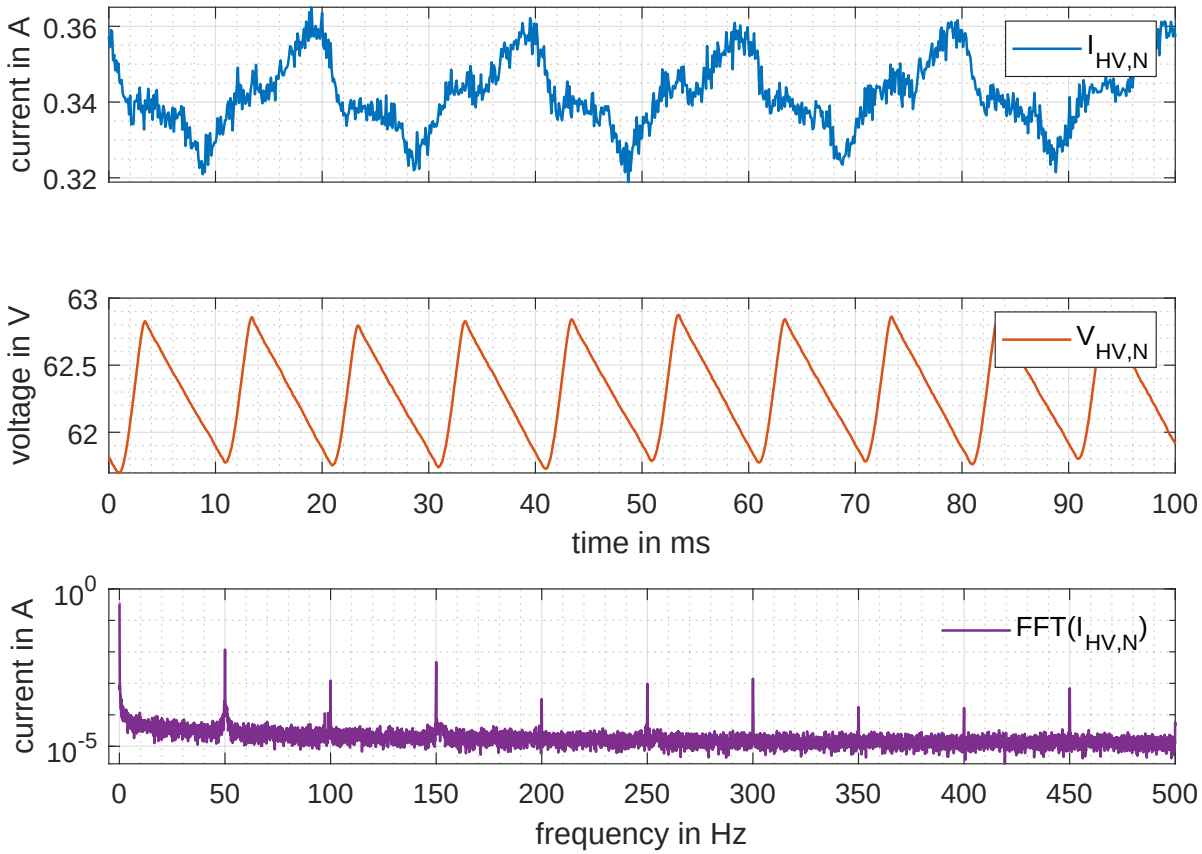

Figure 4.40: Measured current and voltage at high-voltage neutral during B2B test of transformers T3Sa and T3Sb with superimposed DC from the full-wave rectifier and corresponding amplitude spectrum of superimposed DC.

In order to verify the steady-state conditions, under a DC ripple of 40 mA, the power demand was investigated for a timescale of minutes. An excerpt of the power demand versus time is presented in **Figure 4.41**, which depicts a constant power demand during the evaluation period.

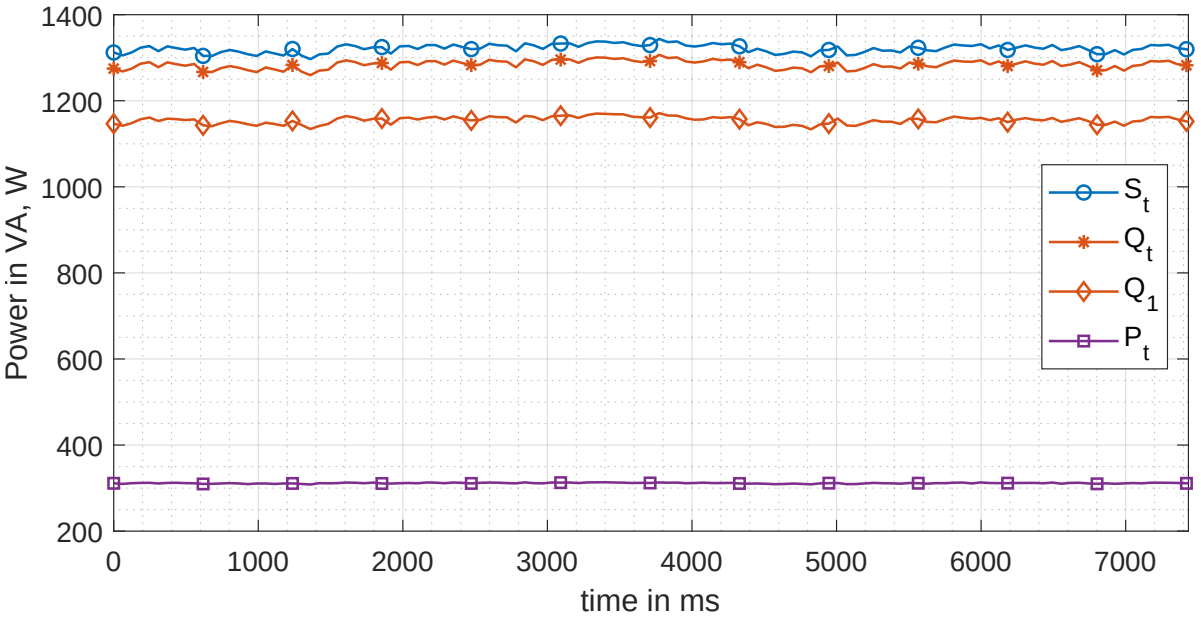

Figure 4.41: Measured power demand during B2B test of transformers T3Sa and T3Sb with superimposed DC from the full-wave rectifier.

4.4.7 Back-to-Back Tests with Batteries at Public Grid

The following **Figure 4.42**, **Figure 4.43** and **Figure 4.44** present the measurement results from a B2B test with the transformer T3Sa and T3Sb with supply from the public grid. The transformer T3Sb is only connected to the transformer T3Sa via the high-voltage terminals. Between the high-voltage neutral of both transformers five 12 V batteries are used in series without bypass capacitor to superimpose a DC. The comparison with the measurement, using a bypass capacitor in parallel to the batteries, reveals no differences. Therefore, further tests are carried out without bypass capacitor.

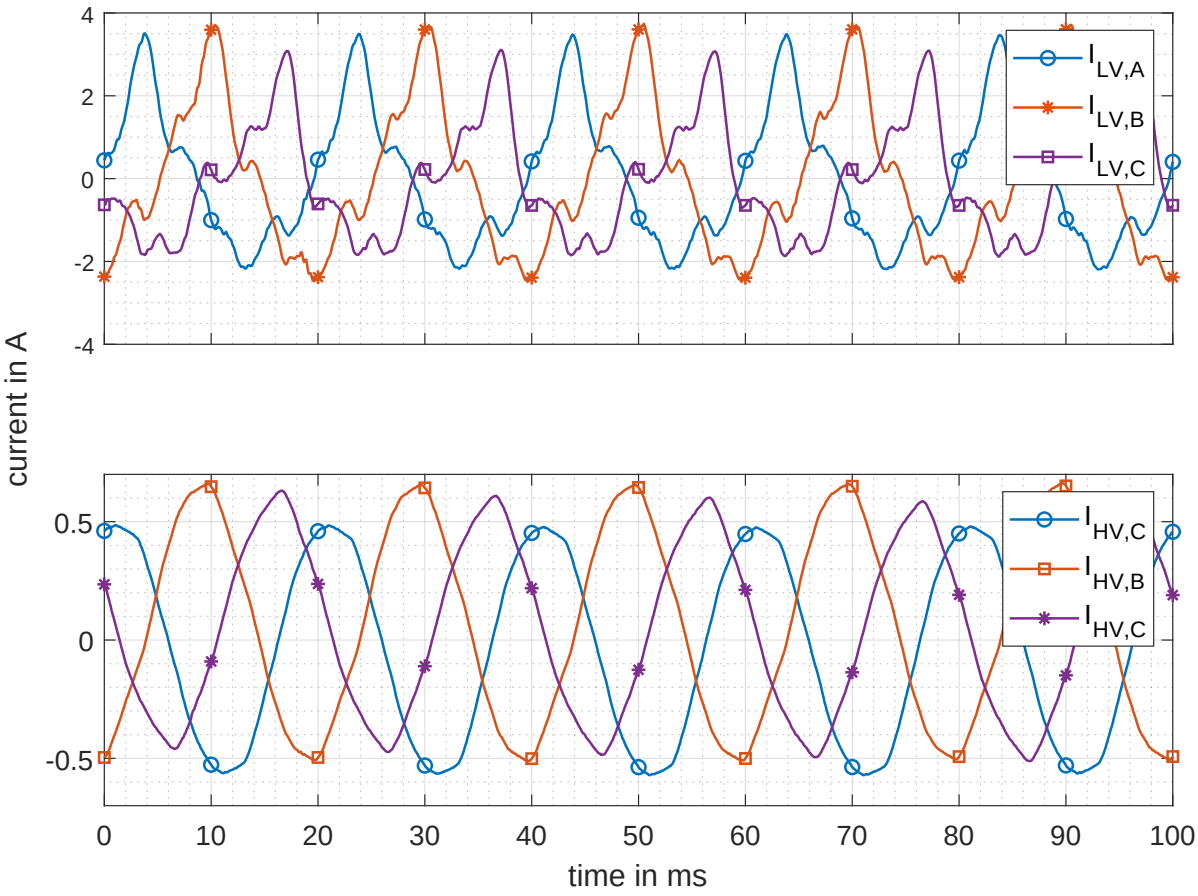

Figure 4.42: Measured low- and high-voltage currents during B2B test of transformers T3Sa and T3Sb with superimposed DC from five 12 V batteries in series without bypass capacitor.

The voltage via the high-voltage neutrals applied with the five batteries is more constant, than the voltage from the full wave rectifier (compare **Figure 4.40**), whereas the current ripple is almost the same as with the full wave rectifier. The frequency spectrum in **Figure 4.43** in purple shows a decaying characteristic, due to the included inrush current recording. The frequency spectrum of an excerpt without the inrush current is depicted in blue, where the odd frequency components are distinctive, as in **Figure 4.40**.

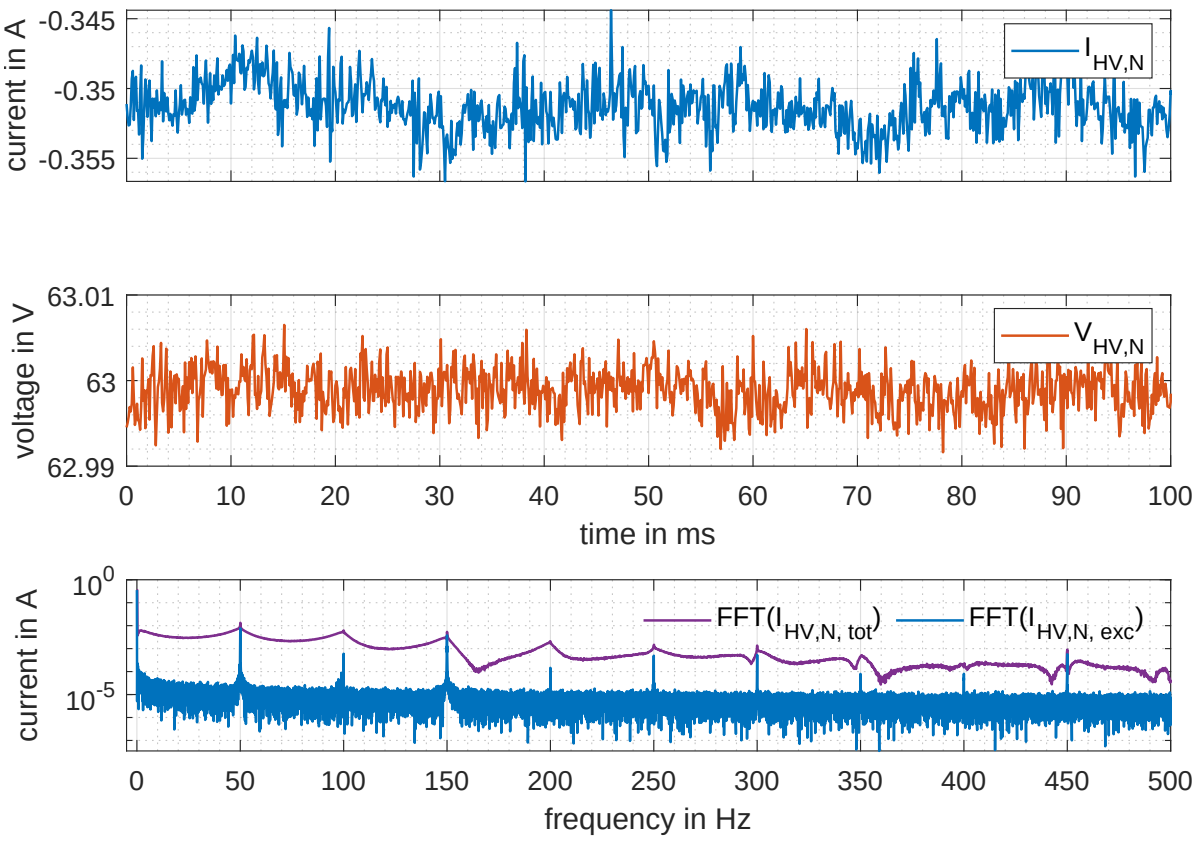

Figure 4.43: Measured current and voltage at high-voltage neutral during B2B test of transformers T3Sa and T3Sb with superimposed DC from five 12 V batteries in series without bypass capacitor and corresponding amplitude spectrum of superimposed DC.

The power demand, depicted in **Figure 4.44** is almost constant at the presented period. The small deviations are caused by deviations in the supply voltage.

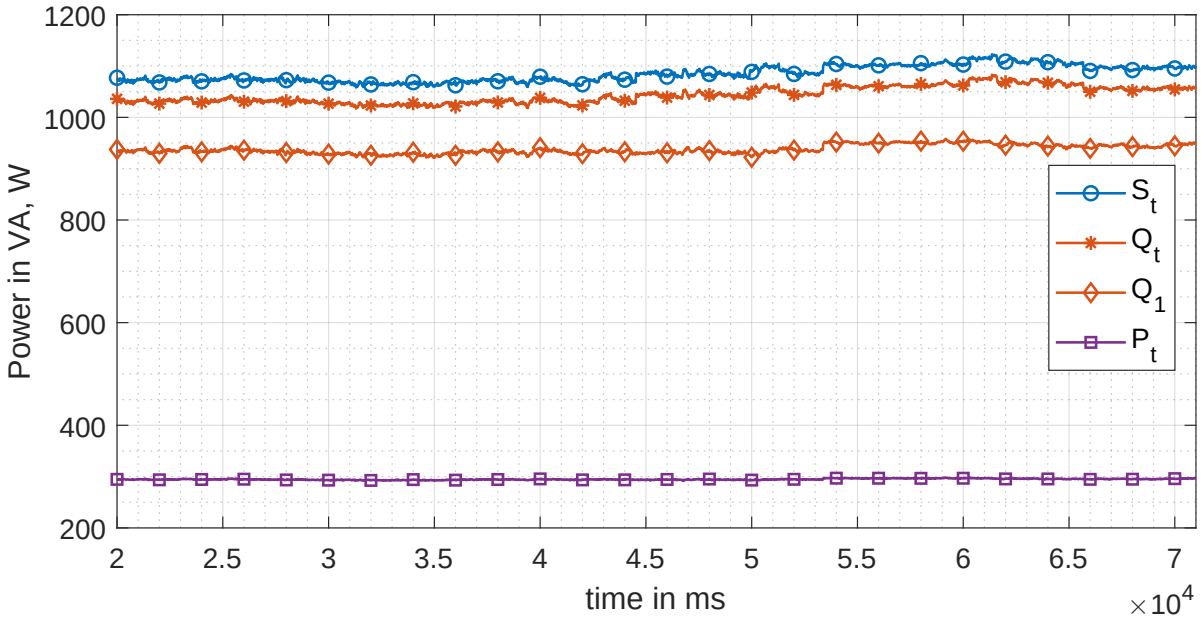

Figure 4.44: Measured power demand during B2B test of transformers T3Sa and T3Sb with superimposed DC from five 12 V batteries in series without bypass capacitor.

The comparison of the supply currents during two B2B tests (only via high-voltage terminals) with supply from the public grid and with superimposed DC of 63 V_{rms} between the high-voltage neutrals from a rectifier and batteries reveals a current peak difference, as depicted in **Figure 4.45**. The rms voltage difference between the test with batteries and the one with the rectifier is 20 mV. Due to the equivalent (winding) resistance of several 100 Ω, the reason for the deviation was suspected to be caused by deviations in the supply voltage. The further analysis reveals a supply voltage amplitude difference of maximum 1.06 V between the two measurements, which caused current amplitude deviations of maximum 33.21 %. Therefore, the measurements should be conducted with the power amplifier, as supply, to guarantee a high amplitude and voltage waveform accuracy.

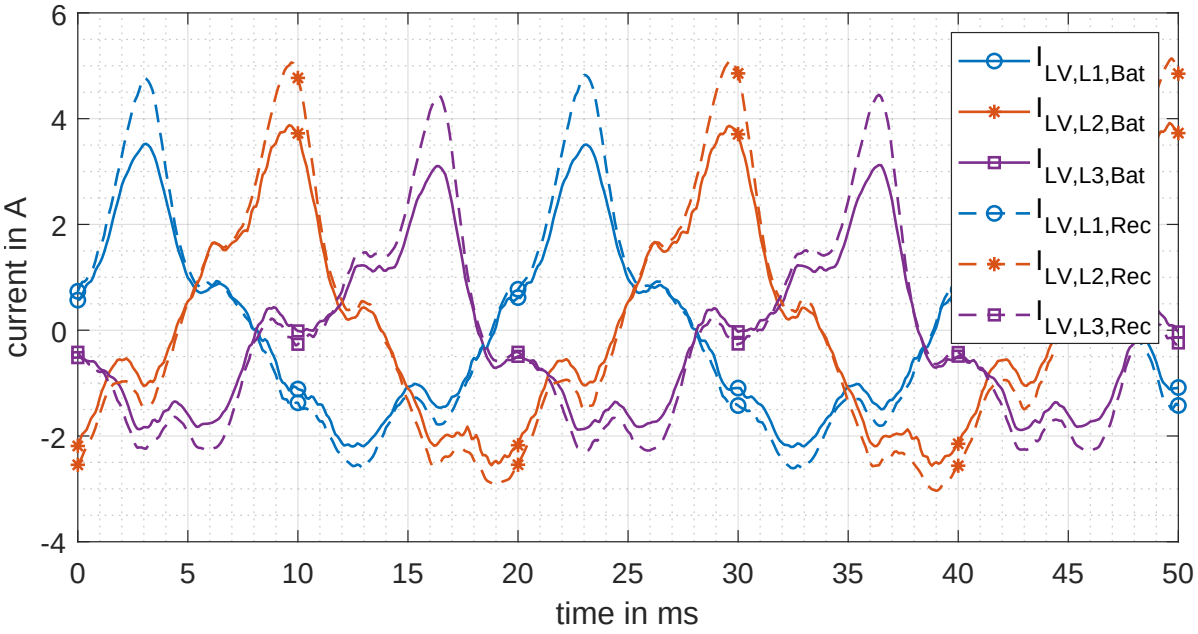

Figure 4.45: Measured supply currents during B2B operation of transformer T3Sa and T3Sb via the high-voltage terminals and with superimposed DC of 63 V_{rms} from the rectifier and batteries.

Table 4.16 lists the voltage and current peaks of the B2B test with 900 mA DC from the DC rectifier and batteries with supply from the public grid, as well as their deviation. Small deviations in the voltage peaks in the range of 1 % cause current peak deviation in the range of 33.21 %.

Table 4.16: Comparison of voltage and current peaks during B2B test with supply form the public grid and with superimposed DC of 900 mA from batteries and a rectifier.

DC Source	V_A	V_B	V_C	I_A	I_B	I_C
		in V			in A	
Batteries	317.94	320.19	318.54	3.57	3.92	3.14
Rectifier	321.30	323.50	322.07	2.68	3.04	2.35
deviation in %	1.06	1.03	1.01	33.21	28.95	25.16

Figure 4.46 depicts the three-phase voltage at the low-voltage terminals of transformer T3Sa during the B2B test with the public grid and the power amplifier as source and an ideal sine-wave (dashed line). The phase voltages during the supply of the public grid show a 'rectangular' shape around the maxima and minima of the sine-wave in comparison to an ideal sine-wave.

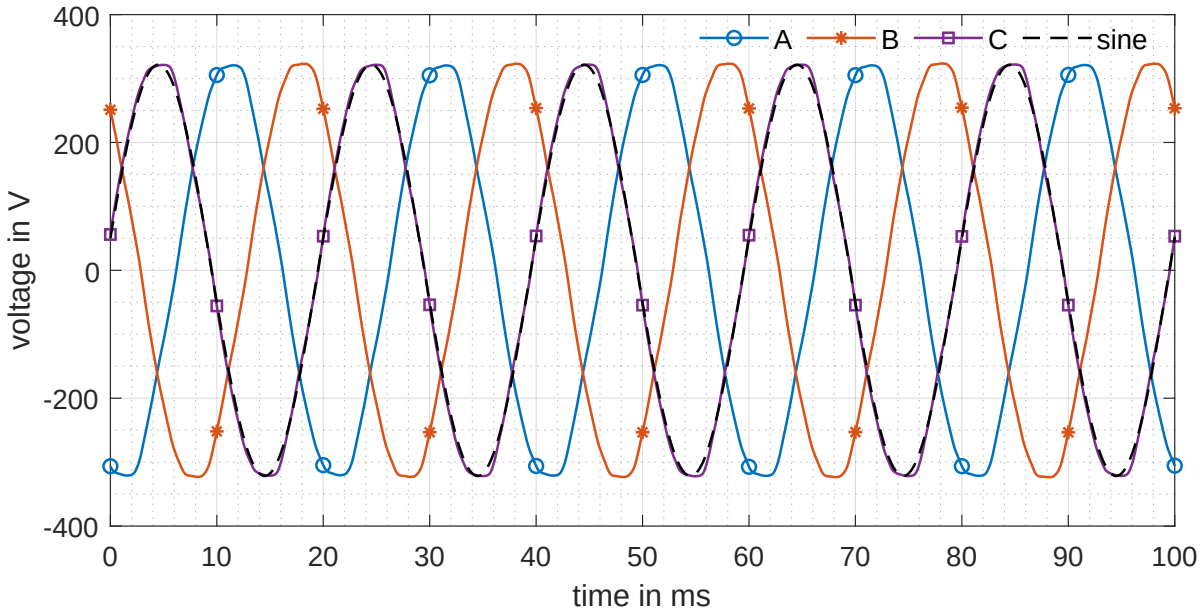

Figure 4.46: Measured three-phase public grid voltage and ideal sine-wave during B2B test of transformer T3Sa and T3Sb.

Figure 4.47 depicts the three-phase voltage with the supply from the power amplifier and for comparison an ideal sine-wave for phase B. Both, the measured and ideal-sine wave coincide and the measured voltage don't show a 'rectangular' shape as in **Figure 4.46**.

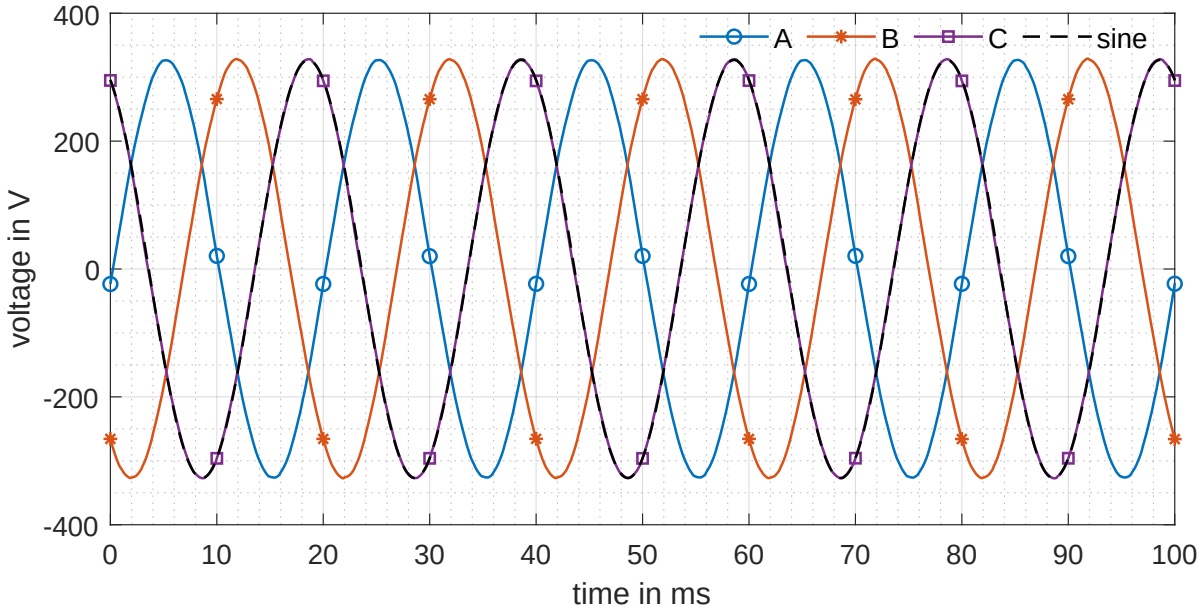

Figure 4.47: Measured three-phase voltage from power amplifier and ideal sine-wave during B2B test of transformer T3Sa and T3Sb.

The comparison of the B2B via the high-voltage terminals with supply from the public grid and the power amplifier during superimposed DC with the rectifier, reveals increased current peaks, while using the public grid as supply, as depicted in **Figure 4.48**.

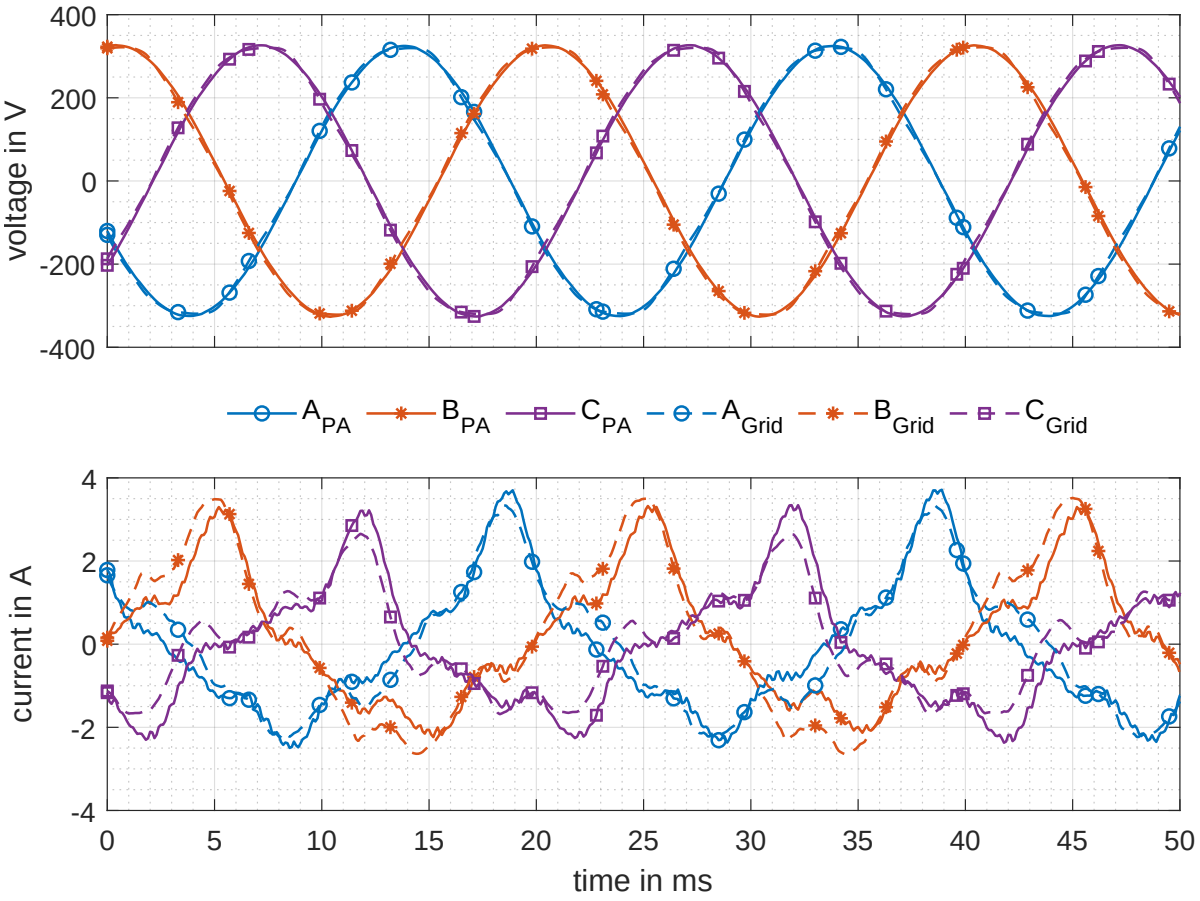

Figure 4.48: Comparison of measured waveforms during the high-voltage B2B test with supply from the public grid and the power amplifier with superimposed DC of 63 V_{rms} via the full-wave rectifier.

The comparison of the current and voltage peaks in **Table 4.17** reveals that voltage amplitude deviations are in the range 2 % can cause current amplitude differences up to 19.43 %.

Table 4.17: Comparison of voltage and current peaks during B2B test with 900 mA DC with supply from the public grid and the power amplifier.

DC Source	V_A	V_B in V	V_C	I_A	I_B in A	I_C
power amplifier	325.26	327.15	326.57	3.77	3.41	3.50
Grid	320.07	321.81	320.52	3.52	3.65	2.82
deviation in %	1.60	1.63	1.85	6.63	7.03	19.43

The B2B test can also be carried out with the transformers T3Sa and T3Sb connected B2B on their high-voltage *and* low-voltage terminals. During the B2B test with the aforementioned transformer connected only via their high-voltage terminals, the second transformer T3Sb can be considered as non-linear load connected to the transformer T3Sa. The (magnetisation) current of the transformer T3Sb is supplied by the transformer T3Sa via the high-voltage terminals. During the B2B test with the low-voltage terminals also in B2B, the magnetisation current of T3Sb is supplied directly from the

supply. The comparison of both B2B setups in no-load conditions (no superimposed DC) and in YNyn vector group reveals an increased current during B2B operation of the low- and high-voltage terminals. According to [IEC97] the short-circuit impedance voltage of the transformers should be within ±10 %. This requirement is not full-filled for the YNyn ($\bar{V}_{\mathrm{T3Sa,sc}} = 17.82\,\mathrm{V}$; $\bar{V}_{\mathrm{T3Sb,sc}} = 21.56\,\mathrm{V}$; $\Delta = 17.34\,\%$) and YNzn5 ($\bar{V}_{\mathrm{T3Sa,sc}} = 20.16\,\mathrm{V}$; $\bar{V}_{\mathrm{T3Sb,sc}} = 26.46\,\mathrm{V}$; $\Delta = 23.8\,\%$) vector group. The differences in the induced no-load voltages, causing circulating currents. The transformer losses of the transformer with the lower DC impedance increase, as it can be seen in **Figure 4.49**. Therefore, tests with low- and high-voltage terminals of the transformers T3Sa and T3Sb will cause an overestimation of the increased losses (LV/HV B2B: P_t=587.52 W; Q_t=1.36 kvar; PF=0.3669 | HV B2B: P_t=268.51 W; Q_t=804.94 var; PF=0.3167) during a test with superimposed DC.

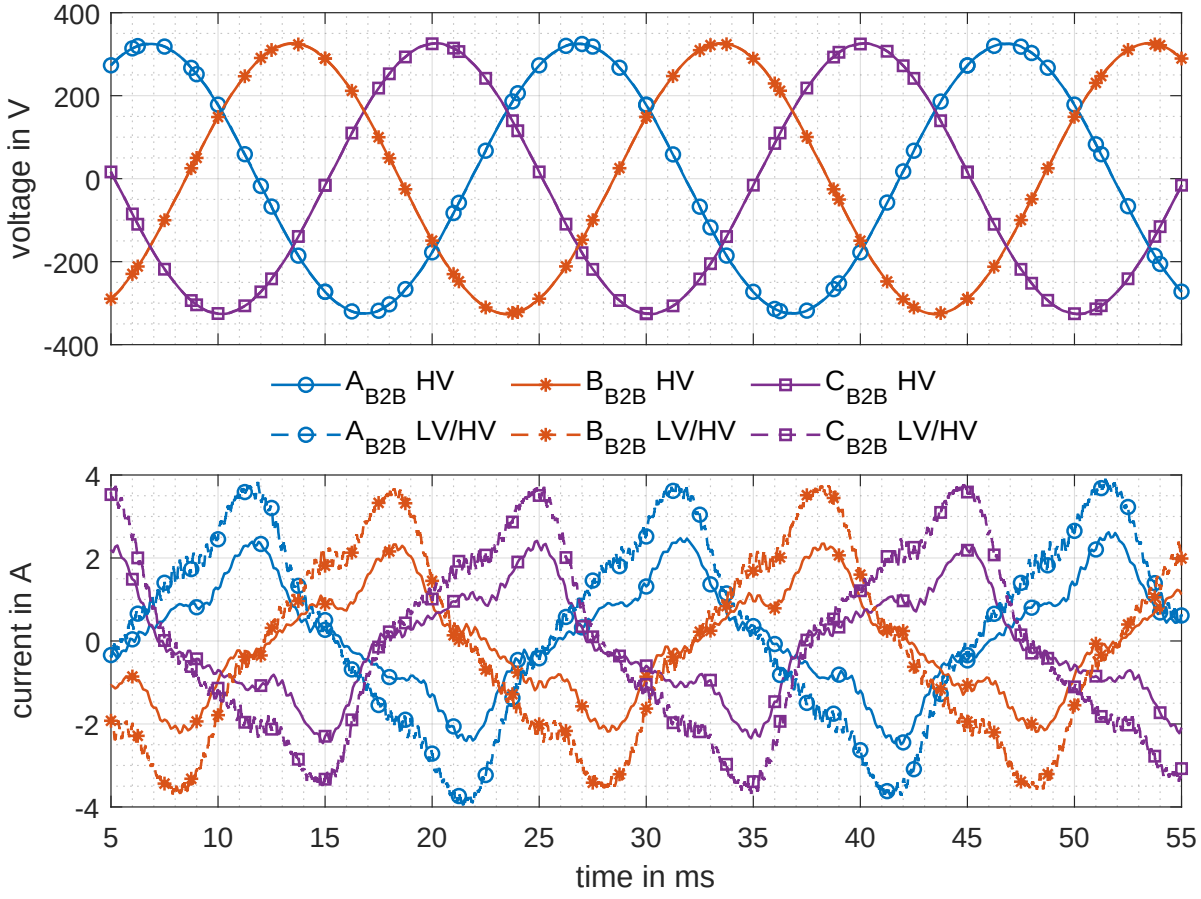

Figure 4.49: Comparison of the measured waveforms during a test with only high-voltage terminals in B2B and a test with low- and high-voltage terminals of T3Sa and T3Sb in B2B operation.

Calculated current waveforms from the B2B test of T3Sa and T3Sb overestimated the actual measured current peaks. The no-load test of T3Sb at the public grid with connected neutral conductor causes in-phase no-load currents. This reveals a dominating zero-sequence impedance in comparison to the positive sequence impedance. This effect can currently not be reproduced with the model of T3Sb. Therefore, further work is required to set up a more accurate model of the transformer T3Sb for further investigation.

4.5 Effect of the Transformer Vector Group on the Power Demand

Figure 4.50a depicts the total power and the fundamental power during a B2B test with transformer T3Sa and T3Sb with different levels of superimposed DC between the high-voltage neutrals of T3Sa and T3Sb (see **Figure 4.37** for the circuit schematic). The low-voltage vector group of T3Sb was yn0, d5 and zn5 for the three measurements, whereas T3Sb was in no-load conditions with solidly grounded low-voltage neutral.

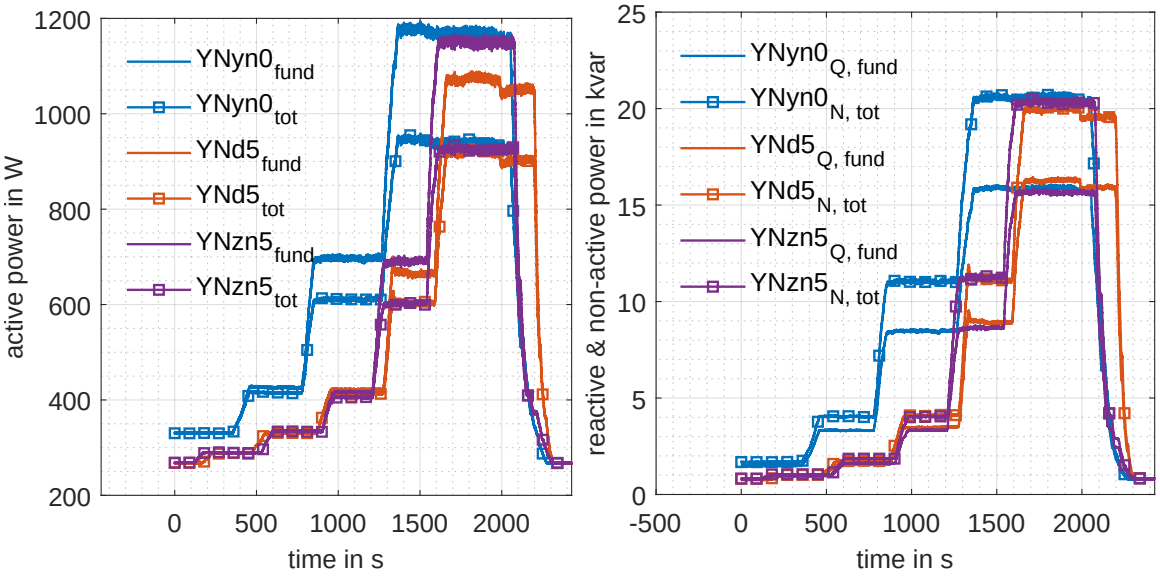

(a) Fundamental active power and total active power demand for different vector groups of transformer T3Sb during B2B superimposed DC test.

(b) Fundamental reactive power and non-active power demand for different vector of transformer T3Sb groups during B2B superimposed DC test.

Figure 4.50: Measured power demand during B2B test with superimposed DC supplying T3Sa with YNyn0 and B2B connected T3Sb with vector groups YNyn0, YNd5 and YNzn5.

During increased levels of superimposed DC (0-1500 mA in 300 mA steps) it can be seen, that the fundamental active power (**Figure 4.50a**) and fundamental reactive power (**Figure 4.50b**) is lower than the total active and non-active power, considering the harmonic contribution up to the 50^{th} harmonic. Therefore, attention need to be paid analysing the power demand during transformer saturation. Considering only the fundamental power drawn by the transformer underestimates the actual power demand. The underestimation of power demand can also cause errors in the thermal assessment of power transformers.

The deviation in power demand for the different vector groups of the transformer T3Sb can be explained by the low voltage delta and zigzag windings. The delta winding is a low impedance path for a circulating current induced from another winding, e. g. the star winding. The magnetic flux caused by the circulating current provides a compensating ampere-turn (in opposite direction to the flux induced by the energised winding), reducing the saturation level inside the transformer core and therefore, the current and power drawn by the transformer during transformer core saturation. The zigzag winding causes the zero-sequence current component to be cancelled out on each

limb, because each limb carries a part winding of two phases with opposite direction, reducing the zero-sequence current component during half-cycle saturation. Thus, the current and power drawn by the transformer setup is reduced.

Taking a closer look at the power demand distribution between the phases during the no-load test of T3Sa and T3Sb in YNyn0, reveals an asymmetric distribution between the phases with $P_{\mathrm{A}} < p_{\mathrm{B}} < P_{\mathrm{C}}$. The asymmetric power distribution between the phases is due to the asymmetric stray losses and the asymmetric mutual coupling between the phases [Esc+07]. The leakage field from the middle limb/winding to the tank is usually smaller than the leakage field from the outer two limbs/windings to the tank, which can intuitive visualised with a top view of a transformer. The asymmetric mutual coupling between the phases is due to the asymmetric distribution of the magnetic field inside the transformer core during a three-phase excitation.

4.6 Transformer Sound Level under Low Frequency Current Bias

Transformer audible sound can be distinguished in load, no-load and cooling plant sound [Plo19; Cig20]. The load sound is caused by the vibration of the transformer windings due to the Lorentz force on the windings. The no-load sound is caused by the magnetised core. In a core, the induced sinusoidal magnetic flux stimulates a variation of the length of the electrical steel sheet with a non-sinusoidal shape, known as magnetostriction. The root cause for magnetostriction are vertical magnetised domains, also called lancet domains, which short circuit energetically high stray flux in order to reduce magnetic energy of the system. This means, the less grain orientated the steel is, the more lanced domains are generated, causing an increased sound level. Higher flux density also increases the density of lancet domains, so that the sound increases sharply with the flux density. Therefore, the sound increase of DC biased transformer cores increases sharply at small DC bias as shown in **Figure 4.51** [Bac+12; Bac+13].

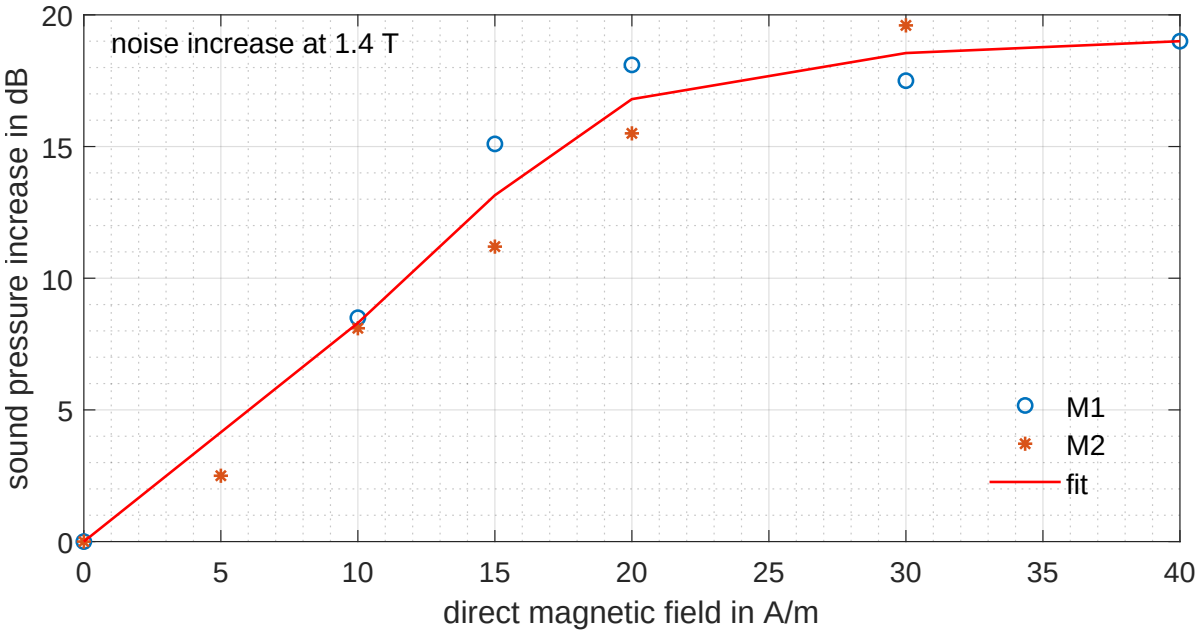

Figure 4.51: Transformer sound increase in dB over DC magnetic field.

The load sound has dominant frequencies of the even multiples of the fundamental frequency (50/60 Hz). The no-load sound has dominant frequencies of the odd multiples of the fundamental frequency, due to the magnetostriction of the material. The magnetostriction force is the dominant audible sound in the power transformer. Under the assumption of linear constrain between magnetisation and magnetic flux density and small linear elastic deformation, the following approximation (4.4) and (4.6) are valid. From (4.7) it can be seen that the force on the transformer core is a function of the instantaneous squared magnetic field B. The material equations can be derived from continuum mechanics [Pre83].

$$F = eEA, \tag{4.4}$$

$$\sigma = eE, \tag{4.5}$$

$$\vec{M} = \frac{\xi}{\mu_0}\left[(1-\psi e)\delta + (\beta-\gamma)\tilde{e}\right], \tag{4.6}$$

$$\sigma = \sigma' - \frac{\xi}{\mu_0}\left[\frac{1}{2}(\beta-\gamma)\vec{B}\times\vec{B} + \frac{1}{2}(1+\gamma)\vec{B}\cdot\vec{B}\gamma\right], \tag{4.7}$$

where E is the modulus of elasticity in the direction of the force in N/m^2, A is the cross-section area of the transformer laminated sheet in m^2, $\vec{B}$ is the instantaneous magnetic flux density vector as function of time, σ is the stress tensor, σ' is the elastic stress tensor, e is the strain tensor, $\tilde{e}$ is

the linearised strain tensor, γ and σ are material constants, ξ is the magnetisability related to the reference status with no strain, μ_0 is the vacuum permeability, δ is the Kronecker delta and $\vec{M}$ is the torque vector.

For the analysis of transformer sound, a narrowband spectrum should be derived from transformer sound measurements. A $1/3$-octave or octave band analysis is insufficient since the spectrum gets blurred and the harmonics cannot be extracted out of the spectral data. **Figure 4.52** shows a comparison between narrowband, $1/3$-octave and octave band analysis of a typical transformer sound. While the narrowband analysis shows the typical comb-like shape with the peaks at the even harmonics of the transformers operating frequencies, this information gets lost in the $1/3$-octave band and octave band analysis.

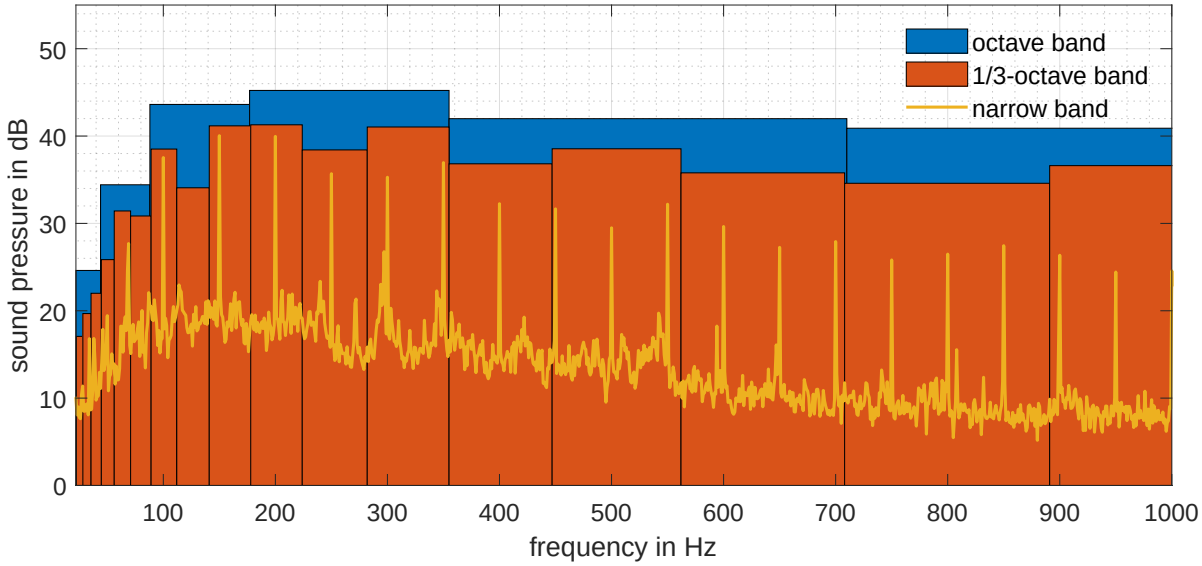

Figure 4.52: Measured transformer sound pressure in dB over frequency with different bands.

To get the narrowband spectrum of the transformers sound, a FFT is applied on the data. During normal operation, the power grid frequency may vary between ± 0.2 Hz around the nominal operating frequency. This frequency deviation multiplies with the higher harmonics and at the 20^{th} harmonic, this deviation is already at ± 4 Hz and must be considered when generating the spectrum. When dealing with non-exact frequencies, the usage of the 'flat top' window function is indicated. It gives a good amplitude representation on cost of exact frequency resolution [Mey17].

Even harmonics in the transformer sound spectrum are always present and are related to even multiples of the operating frequency (100, 200, and 300,... Hz for 50 Hz operating frequency). Odd harmonics in the transformer sound spectrum are related to special operation conditions and therefore are not always present. Odd harmonics (150, 250, and 350,... Hz for 50 Hz operating frequency) in the transformer sound are e. g. caused by LFC or DC biased transformers. Intermediate frequencies of the even and odd harmonics are related to background sound. These intermediate frequencies are shifted by half of the operating frequency (75, 125, 175, and 225,... Hz for 50 Hz operating frequency).

This distinction between the frequency components and the root-cause can be used to identify LFC or DC biased transformer with audible sound measurements [Alb+20].

A commercially available tool to detect a DC bias on a transformer by audible sound measurements can be found via `https://dc-detection.sitram-cam.siemens-energy.cloud/`.

4.7 Low Frequency Current Bias Mitigation in Power Transformers

For the mitigation of LFC or DC flux in transformer core with accessible tertiary delta winding, a single-phase transformer could be connected in series with the tertiary delta winding. On the secondary side of the single-phase transformer, a voltage source with a phase-fired control (PFC) could be used to cause an additional current in the tertiary delta winding, which compensates the LFC or DC flux inside the main transformer core. If no LFC/DC is measured in the tertiary delta winding, the compensation can be turned off and bypassed (circuit configuration in blue). Otherwise, the flux compensation system can switch to operation mode by opening the bypass circuit breaker (red circuit configuration). The system could use the current flowing in the delta winding in combination with a zero control of the 3^{rd} and/or 6^{th} harmonic. The 3^{rd} harmonic and their multiple are caused by transformer half-cycle saturation in the three phases once per cycle. During B2B operation of two power transformers exposed to superimposed DC, the half-cycle saturation in one transformer occurs during the positive half-cycle whereas the half-cycle saturation of the other transformer occur during the negative half-cycle. This behaviour and the frequency spectrum of the current in the delta winding during superimposed DC of 3.3 A via the high-voltage neutral are depicted in **Figure 4.53** and **Figure 4.54**, respectively. The FFT amplitude spectrum is calculated with a line resolution of 0.15 Hz together with a Hanning window (-31 dB, 50 % overlap). The current in the delta winding was measured with a Chauvin Arnoux MN38 AC current clamp with a bandwidth of 40 Hz to 10 kHz [Cha22].

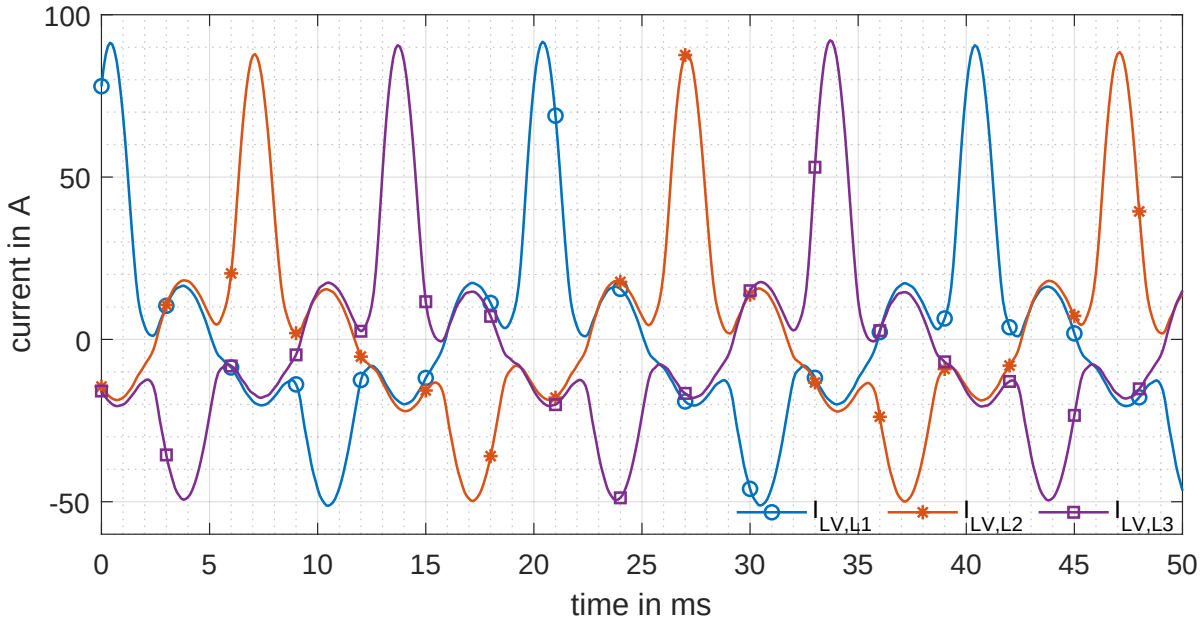

Figure 4.53: Measured phase currents during B2B operation of T3Sa and T3Sb with superimposed DC during with supply from public grid.

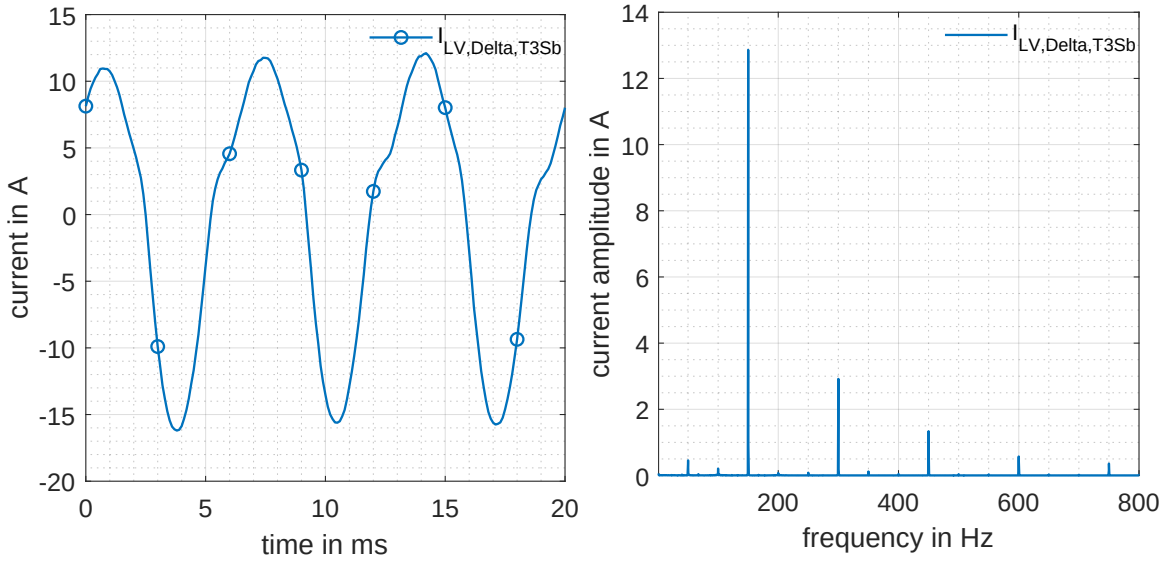

(a) Measured current in delta winding of transformer T3Sb during B2B operation of T3Sa and T3Sb with superimposed DC during with supply from public grid.

(b) Frequency spectrum of current in delta winding of T3Sb during B2B operation with T3Sa and superimposed DC.

Figure 4.54: Transformers T3Sa and T3Sb in B2B operation with 3.3 A superimposed DC via the high-voltage neutral.

Figure 4.55 depicts a schematic of the possible wiring and setup of the tertiary winding with an additional single-phase transformer.

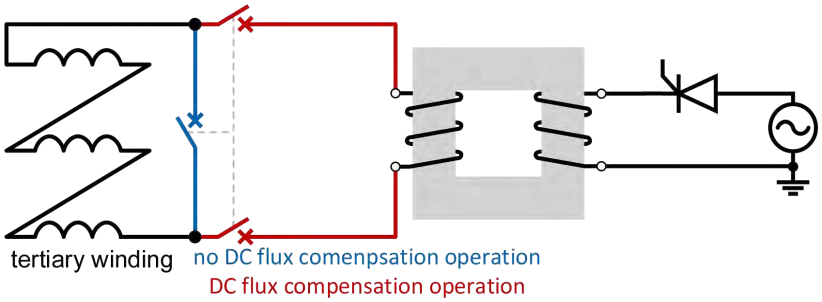

Figure 4.55: LFC mitigation in accessible tertiary delta winding.

The advantages of the proposed method are the following:

- the system can be retrofitted to transformers with accessible delta winding, without any modifications inside the transformer;
- due to the lower voltage rating of the tertiary winding (usually in the 30 $kV_{L\text{-}L}$ range) the size of the additional installation (transformer and power electronics) can be reduced, due to lower insulation distances;
- the system can be disconnected and connected to the transformer during operation, e. g. to decrease losses if no LFC or DC bias is present;
- the current in the tertiary delta winding can be measured easily, e. g. with a Rogowski coil, thus the system do not require any special sensing technique.

4.8 Asset Management and Susceptibility of Power Transformer under Consideration of Low Frequency Currents

GIC/DC bias with high amplitude and long duration can cause transformers to overheat, loose insulation and as a consequence fail. Whether high amplitude and small duration or small amplitude and long duration GIC/DC bias can cause transformers to fail, is still the topic of ongoing research [Alb+21b].

Transformer failure may not be traced back to GICs caused by space weather events, because the time between the failure and event may be in the range of years or only the combination of an already existing weak point with a DC bias causes transformer failure. Although, small DC bias on the transformer can increase the transformer sound level, a major temperature increase due to ohmic heating of the windings or a temperature increase in structural parts due to increased stray flux is not expected [Rai19]. But local hotspots can occur, if weak points such as already degraded insulation are present. In order to trace back transformer failure to possible space weather events, the GIC_{sum} (4.8) can be calculated for different time periods.

$$GIC_{\text{sum}} = \int_{t_1}^{t_2} |\text{GIC}(t)| \, \mathrm{d}t \tag{4.8}$$

For a further risk analysis, a GIC_{sum} value would be required, above which level the specific transformer could be harmed by the bias. This value would depend on the design of each transformer.

A guidance, containing a threshold level, where GICs starts to contribute to an accumulated exposure and different alert levels should be provided. This guidance would be needed to be adapted for different transformer designs. **Figure 4.56** depicts the 1 h-GIC_{sum} value for three different measured transformer neutral point currents during a strong geomagnetic activity (K_p = 7o) and during a geomagnetically comparable quiet period (max. K_p = 1-) during May 2021 [Mat+21c].

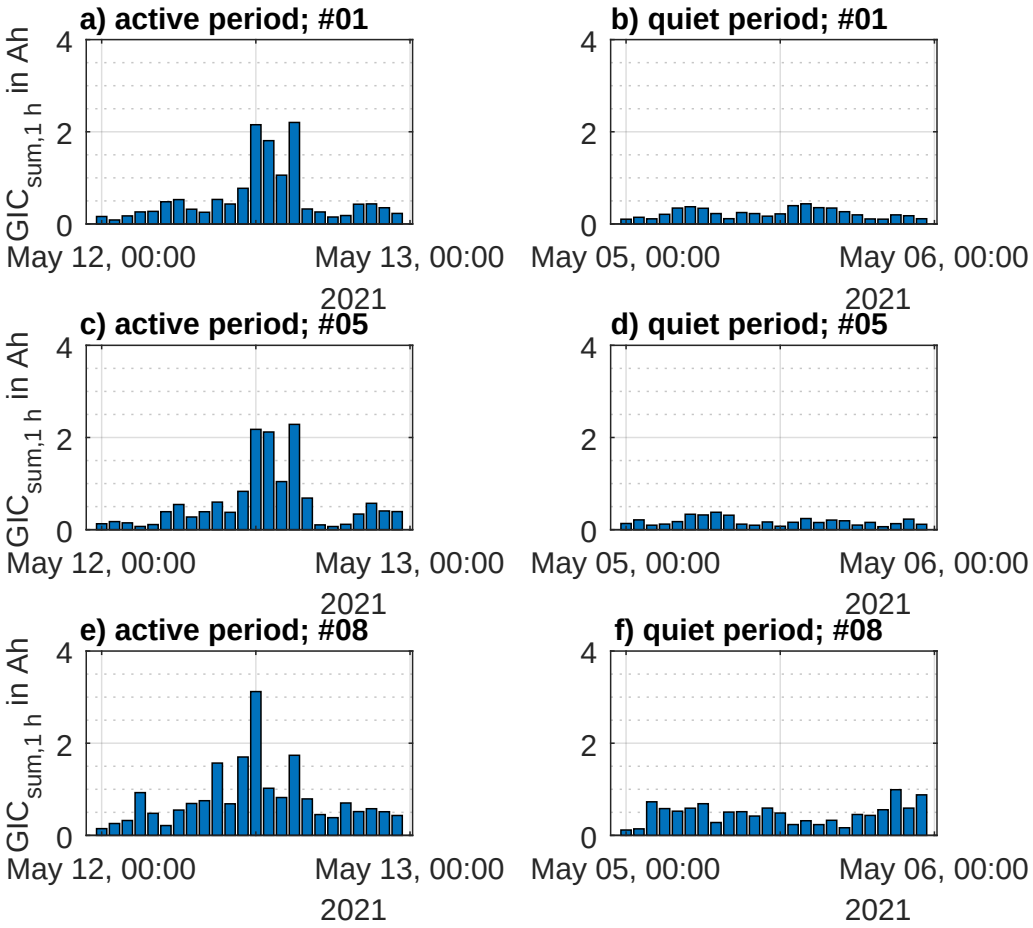

Figure 4.56: Cumulative 1 h GIC_{sum} of client #01 for May 2021 storm (a, c, e) and quiet (b, d, e) period during May 2021.

In [Rai19] a thermal assessment for a specific transformer design was carried out, revealing no overheating (absolute hotspot temperature above 180°) will be caused by a 1 h-GIC_{sum} (NPC of 84 A) value of 84 Ah for the specific transformer design. With 1 h-GIC_{sum} values below 4 Ah during the May 2021 event, we can assume that no major transformer heating would be occurred in the transformer during that event. But the transformer design from [Rai19] is not the same as the

transformer at measurement point #05, where the maximum NPC of 13.83 A occurred during the May 2021 event.

The transformer susceptibility to LFC or DC bias depends on the zero-sequence impedance of the magnetic flux paths and the relative permeability of the core material. Depending on the frequency of the LFC, the LFC adds to further magnetisation of the core (increases offset flux inside the core) or will be transferred/balanced and behave like nominal AC [Alb+20]. The susceptibility v of the transformer to LFC can be quantified by the ration of the AC magnetisation current $i_{\mu,\,\mathrm{AC}}$ to the LFC magnetisation current $i_{\mu,\,\mathrm{LFC}}$. Whereas a high value of v indicates a higher susceptibility to LFC and a low value of v indicates a low susceptibility to LFC.

The transformer can be represented by its π-equivalent circuit. During transformer core saturation, the T (Steinmetz) model [Ste00] cannot accurately represent the transformer behaviour. Thus, the π-equivalent circuit should be used for studies including transformer core saturation [LFJ12; ZMA21; Jaz+13a; Jaz+13b]. Especially during inrush current calculation, the T model can cause the overestimation of the current peaks [ZMA21]. Assuming a single-phase transformer, as depicted in **Figure 4.57**, the susceptibility coefficient can be expresses as follows:

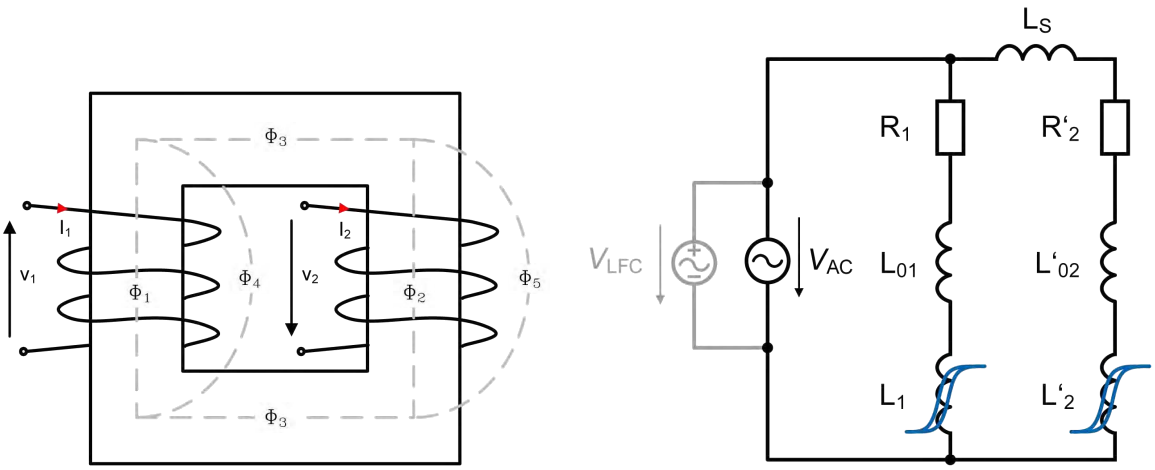

(a) Single-phase transformer schematic.

(b) Single-phase π-equivalent transformer circuit.

Figure 4.57: Single-phase transformer model.

$$v = \frac{i_{\mu,\,\mathrm{LFC}}}{i_{\mu,\,\mathrm{AC}}} = \frac{R_1 + \mathrm{j}\omega(L_{01} + L_1)}{R_2' + \mathrm{j}\omega(L_{02}' + L_2' + L_\mathrm{s})} \cdot \frac{\hat{V}_\mathrm{LFC}}{\hat{V}_\mathrm{AC}}, \tag{4.9}$$

where R_1 and R_2' are the winding resistances, the linear inductances L_{01} and L_{02}' represent the non-magnetic gaps between the thin windings and the limb, L_1 and L_2' are the hysteretical inductances of the corresponding limbs and yokes, L_s is the off-core magnetic leakage inductance between the windings, $\hat{V}_\mathrm{LFC}$ is the peak voltage of the LFC and $\hat{V}_\mathrm{AC}$ is the peak voltage of the AC. Thus, v is exponentially decaying with the frequency, meaning only currents in small frequency range close to 0 Hz can cause transformer core saturation.

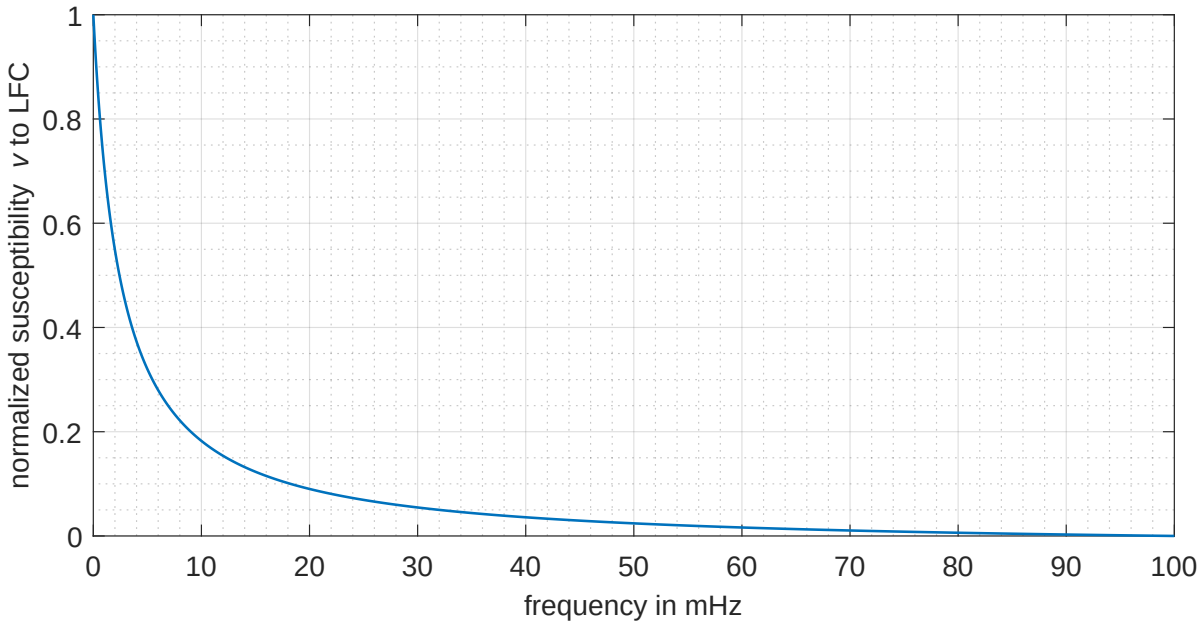

Figure 4.58: Susceptibility of transformer T3Sa to 1 V peak LFC over frequency.

Figure 4.58 presents the normalised susceptibility of the transformer T3Sa to LFC, utilising (4.9), whereas the following values are used: $R_1 = 0.034\,\Omega$, $R_2 = 328.085\,\Omega \cdot (N_{\mathrm{LV}}/N_{\mathrm{HV}})^2$, $L_1 = 400\,\mathrm{V}/(2\pi f \cdot 0.9\,\mathrm{A})$, $L_2 = 35,000\,\mathrm{V}/(2\pi f \cdot 0.9\,\mathrm{A} \cdot N_{\mathrm{LV}}/N_{\mathrm{HV}})$, $L_{1\mathrm{s}} = L_{2\mathrm{s}} = u_{\mathrm{k}} \cdot 35,000\,\mathrm{V}/0.842\,\mathrm{A}$ and $L_{\mathrm{s}} = 0.2308/(2\pi f)$ and $\hat{V}_{\mathrm{LFC}}$, $\hat{V}_{\mathrm{AC}}$ the corresponding voltage amplitudes. Note that the susceptibility scales linear with the LFC amplitude.

4.9 Demagnetisation of multi-phase multi-limb Power Transformers

Residual magnetism in the ferromagnetic core of a transformer can be caused by diagnosis measurement, such as the winding resistance measurement with DC or by GICs. A magnetised core can negatively influence transformer diagnosis measurements (excitation current test, magnetic balancing test or SFRA) or could cause increased inrush currents during transformer energising. Such a remanent flux can be detected by a DC hysteresis measurement, with an asymmetric hysteresis loop with respect to the absicca, as depicted in **Figure 4.59**. For the $\Phi - i$ characteristic, depicted in **Figure 4.59** the 50 MVA T3L transformer (**Appendix C.4**) was demagnetised via the high-voltage terminals V-N, but an offset shift is still visible in the DC hysteresis measurement. This indicates that a remanent flux was still present in the core.

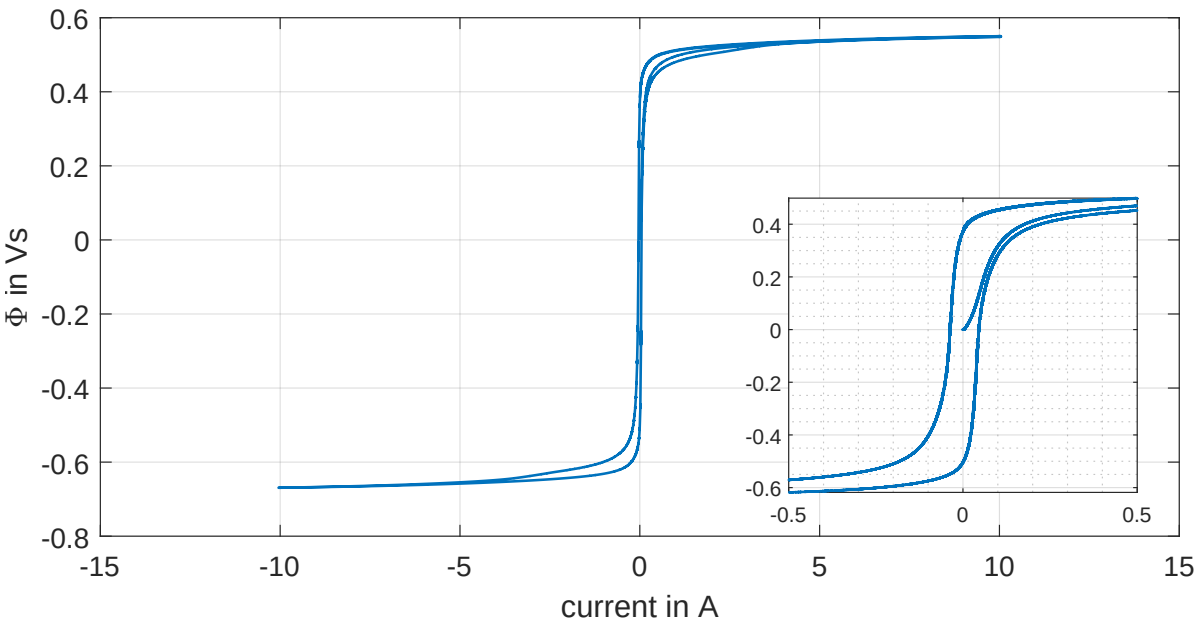

Figure 4.59: Measured hysteresis characteristic with remanence of transformer T3L measured via high voltage terminals A-C with 1212 effective turns.

Therefore, it is recommended by the IEEE Guide C57.152 [IEE13] to demagnetise a transformer before diagnostic tests. Only the electrical demagnetising is a non-destructive method for transformer demagnetisation. Demagnetising with mechanical force or heating above the Curie temperature of the core material will destroy the transformer.

Because the remanence can't be reduced to zero exactly, measurement results are influenced by the remanence of the transformer core, as illustrated in **Figure 4.60**, where the active power demand of each phase varies during the energisation.

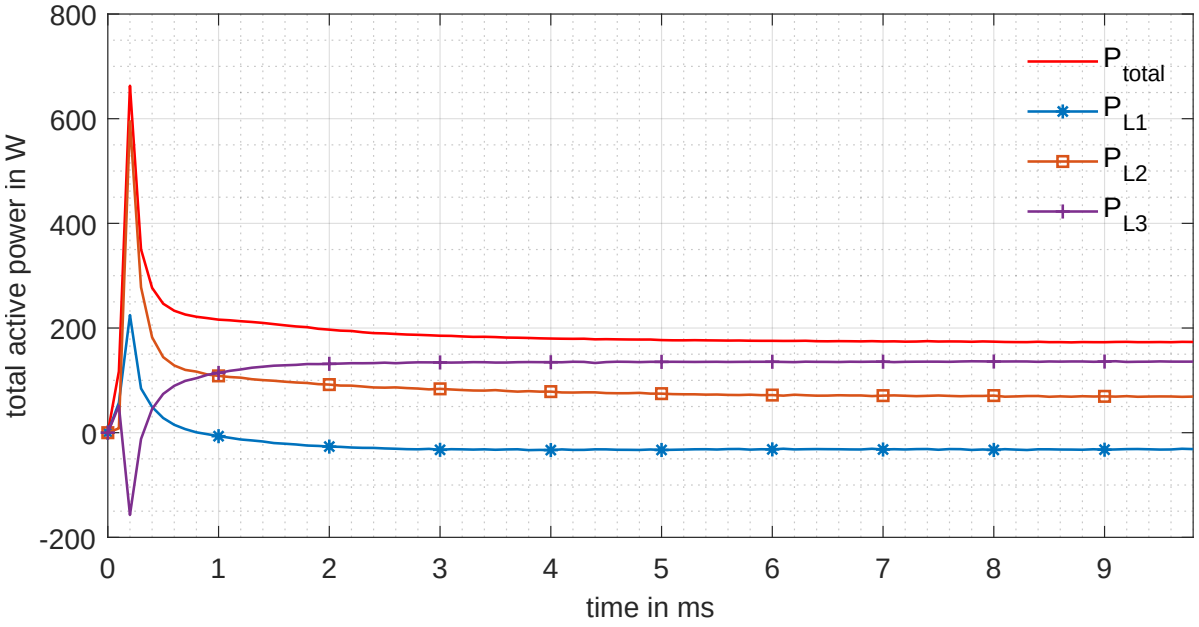

Figure 4.60: Measured active power over time of phase transformer T3Sa during energisation.

The remanence flux causes half-cycle saturation and therefore increases current harmonics, as depicted in **Figure 4.61**, with the accumulated even and odd current harmonics of the phase A.

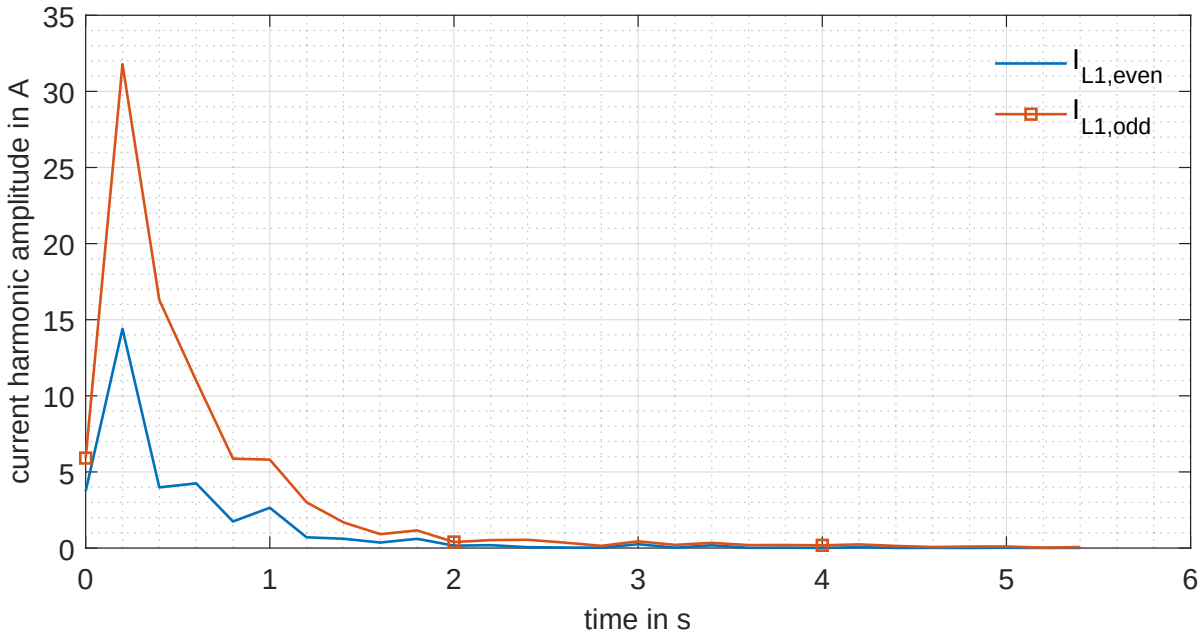

Figure 4.61: Measured rms value of even and odd harmonics over time of phase A from T3Sa during energisation considering current harmonics up to the 50th order calculated over ten periods.

For the demagnetisation of three-phase three-limb and five-limb transformers with two and three windings per limb, an approach with reversible DC polarity, as depicted in **Figure 4.62** is tested with laboratory and large power transformers.

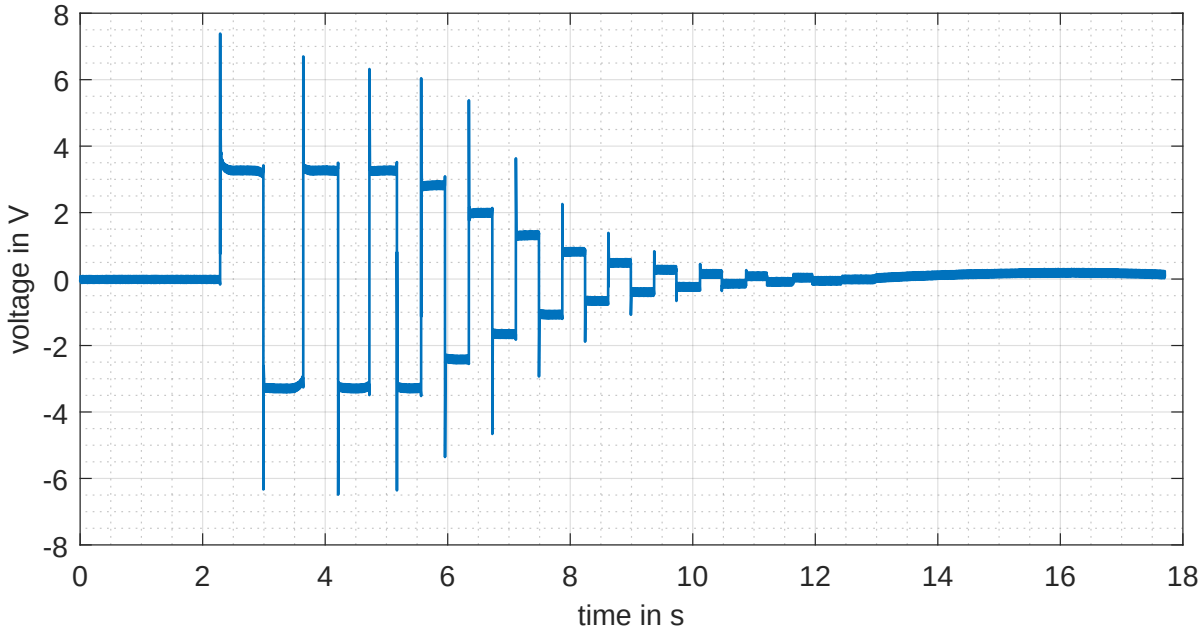

Figure 4.62: Measured voltage during demagnetisation procedure of transformer T3Sa via high-voltage terminal V-N.

The efficiency of the demagnetisation procedure is assessed by DC hysteresis tests on the transformer core, using the approach described in **Section 4.3.2**.

The key to successfully demagnetise transformer cores is to force all magnetic paths of the core (limbs and yokes) into saturation and therefore force them on their major hysteresis loop.

Transformers, equipped with delta winding, can also be demagnetised with the following procedure. A demagnetisation between a phase terminal and the neutral terminal or two-phase terminals will cause the induced current in the delta winding to vanish, because of the 180° phase shift and the corresponding current amplitudes.

If the demagnetisation is carried out between a phase terminal and the neutral terminal, an in-phase (zero-sequence) flux in every limb is caused. Because the demagnetisation with different DC polarities will cause an induced current with a steep increase and a flattening amplitude, it should be considered, if the short current peak can damage the transformer under test. If the delta winding is accessible from outside, a current measurement e. g with a Rogowski coil could be considered.

4.9.1 Demagnetisation of three-limb Transformers

For the demagnetisation of three-limb transformers with YN vector group, the following steps should be carried out:

(1) demagnetise via terminal A-C,
(2) demagnetise via terminals B-N.

Figure 4.63 depicts the magnetic flux density in pu for each of the aforementioned steps.

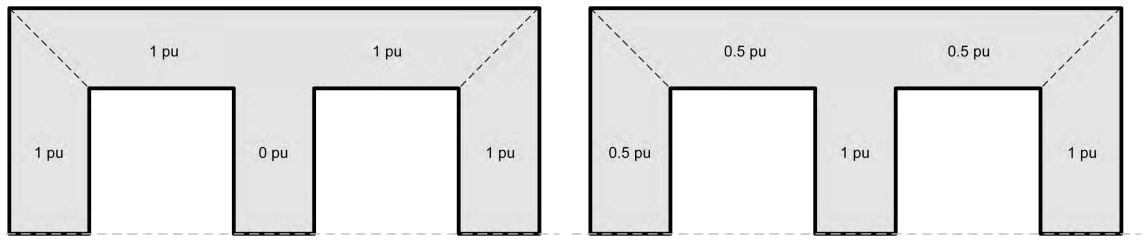

(a) magnetic flux density istribution during step (1). (b) magnetic flux density istribution during step (2).

Figure 4.63: Magnetic flux density distribution for the demagnetisation of three-limb transformer cores in pu.

Thus, every section of the three-limb transformer core forced into saturation during the demagnetisation procedure.

Case Study: Demagnetisation 50 kVA three-limb Transformer

The proposed demagnetisation procedure for three-limb transformer cores was carried out on the three-limb 50 kVA laboratory transformer T3Sb (**Chapter C.2**). For all further tests, the transformer T3Sb winding connection was YNyn. The remanence flux inside the transformer core was caused by a DC winding resistance measurement between the high-voltage terminals A-C. **Figure 4.64a** depicts the DC hysteresis characteristic derived from measurement between the high-voltage terminals A-C, revealing a remanence flux inside the transformer core, due to the asymmetry with respect to the abscissa.

The standard demagnetisation procedure via the high-voltage winding on the middle limb only is not depicted, because the transformer core could always be demagnetised due to the large number of turns on the high-voltage winding (7934 turns). Thus, even with a current of 0.1 A the T3Sb transformer core could successfully be demagnetised. **Figure 4.64b** depicts the DC hysteresis characteristic after the proposed demagnetising procedure, first via the terminals A-C and second via the terminal V-N. It can be seen that the offset shift from **Figure 4.64a** could be successfully removed with the demagnetisation procedure.

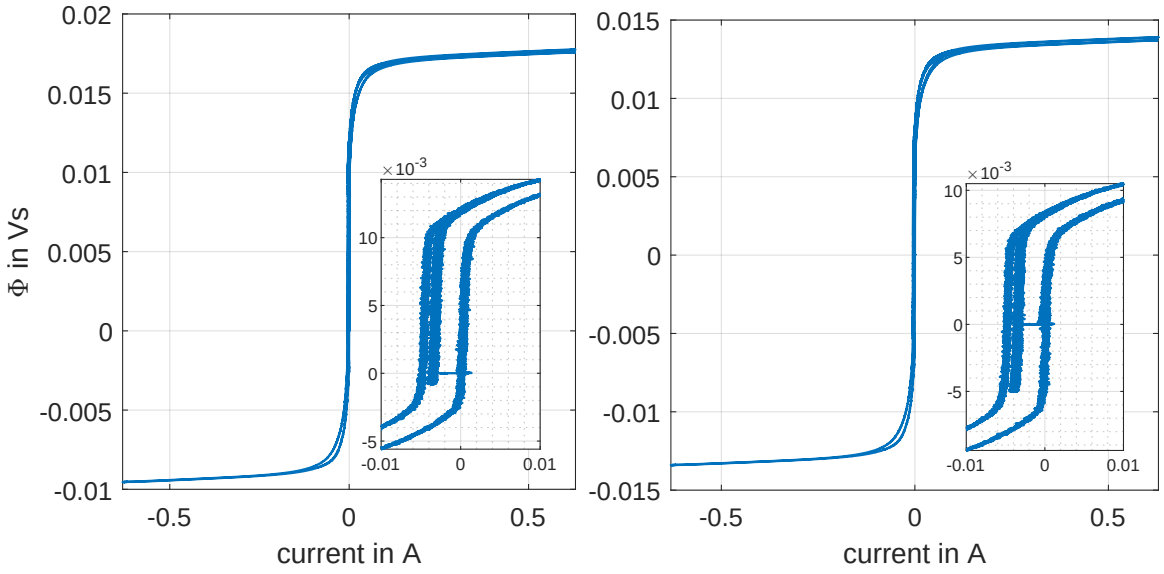

(a) DC hysteresis of T3Sb between high-voltage terminals A-C after DC winding resistance measurement between terminals A-C.

(b) DC hysteresis after proposed demagnetisation procedure.

Figure 4.64: Measured DC hysteresis characteristics after the respective demagnetisation procedure of T3Sb.

4.9.2 Demagnetisation of five-limb Transformers

The demagnetisation of five-limb transformer cores can be done in six steps:

(1) short-circuit terminals A-N and C-N,
(2) demagnetise via terminals B-N,

(3) remove short-circuits,
(4) demagnetise via terminals A-N, B-N, C-N in parallel,
(5) short circuit terminals B-N,
(6) demagnetise via terminals A-C,

Figure 4.65 depicts the magnetic flux density in the five-limb transformer core during the three demagnetisation sequences.

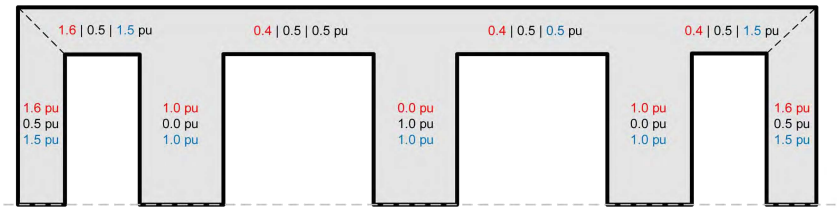

Figure 4.65: Magnetic flux density distribution for the demagnetisation of five-limb transformer cores in pu (step 1: black, step 2: blue, step 3: red).

Form **Figure 4.65** it can be seen, that besides the two adjacent yokes of the middle limb, all other parts of the core reach flux density levels of at least 1 pu. Thus, it can be assumed that all parts with flux density levels of at least 1 pu can be successfully demagnetised with the proposed approach. The approach was successfully tested on a 60 kVA and a 786 MVA five-limb power transformer.

Case Study: Demagnetisation 60 kVA Five-limb Transformer

The proposed demagnetisation approach for five-limb transformer cores was tested on the 60 kVA laboratory transformer T5S (**Appendix C.3**). For the test the transformer windings were connected in YNyn. A remanence flux inside the transformer core was caused by a DC winding resistance measurement (30 A_{DC}, 110 mΩ) between the terminals U and W of the inner windings (low-voltage windings), using the portable transformer test device OMICRON Testrano 600. The DC hysteresis measurement via the same terminals U and W reveals a remanence flux, indicated by the offset in the flux linkage (see **Figure 4.66a**).

The DC winding resistance measurement and the demagnetisation was carried out three times, first only via the middle limb via the terminal connections B-N; second each limb separately in the order A-N, C-N, B-N; and third with the proposed approach. After each demagnetisation a DC hysteresis measurement was carried out between the terminals A-C to check whether an offset/remanence in the DC hysteresis measurement is present or not. The two DC hysteresis characteristics after each demagnetisation approaches are presented in **Figure 4.67b** and **Figure 4.67a**. Both measurements reveal that the sequential demagnetisation of the individual phases and the proposed approach are able to reduce the remanence flux in the transformer core of T5S to a minimum. The demagnetisation only via the middle limb cannot reliably reduce the remanence to a minimum. Also, the demagnetisation of each individual limb cannot reliably reduce the remanence to a minimum.

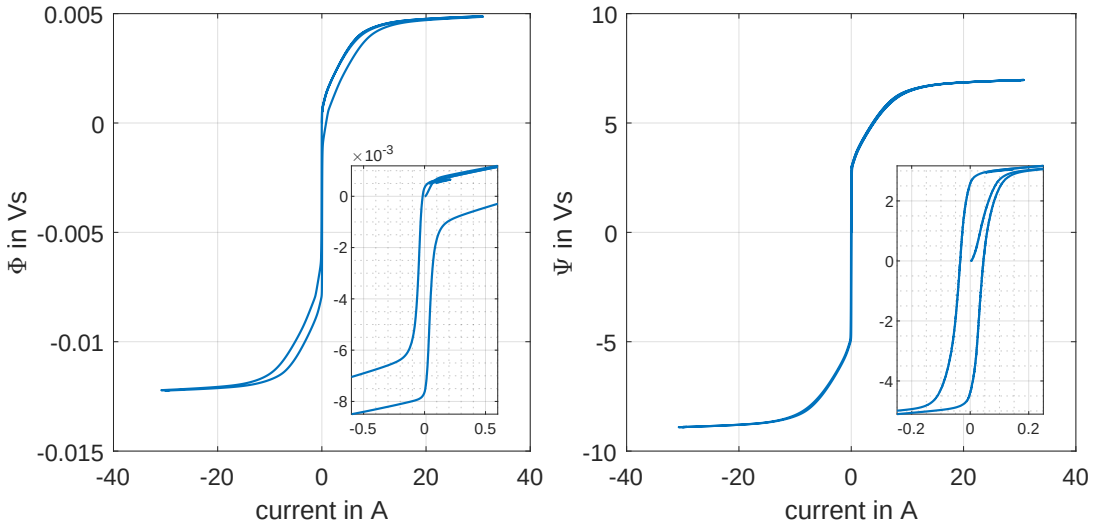

(a) DC hysteresis between high-voltage terminals A-C after DC winding resistance measurement between terminals A-C.

(b) DC hysteresis after demagnetisation between terminals B-N.

Figure 4.66: Measured DC hysteresis characteristics after the respective demagnetisation procedure of T5S.

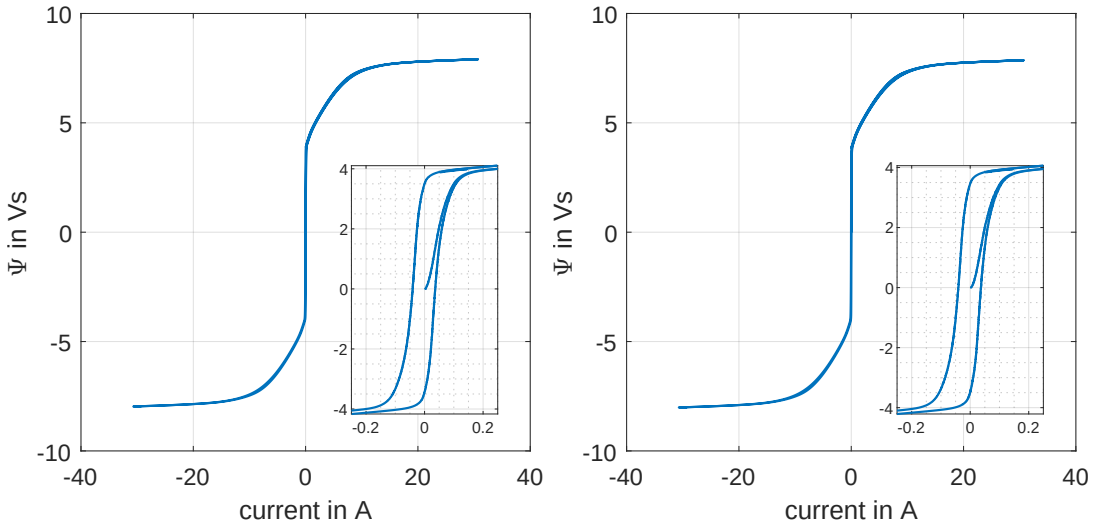

(a) DC hysteresis after demganetisation between terminals A-N, C-N, B-N.

(b) DC hysteresis after proposed demagnetisation procedure.

Figure 4.67: Measured DC hysteresis characteristic after the respective demagnetisation procedure of T5S.

Case Study: Demagnetisation 786 MVA five-limb Transformer

The same comparison, as described in the section before (**Section 4.9.2**), was carried out on 786 MVA power transformer before the factory acceptance test at the transformer manufacturer side on the transformer T5Lb (**Appendix C.6**).

The DC winding resistance measurement (10 A_{DC}, 502.2 mΩ corrected for 20°) via the high-voltage terminals A-C was used to cause a remanence flux inside the transformer core. The winding of the transformer are in YNd11 connection. During the DC winding resistance measurement the current in the delta winding vanishes. **Figure 4.68** depicts the DC hysteresis derived from the measurement between the high voltage terminals A-C. As in the laboratory test, an offset in the flux linkage is visible, revealing a remanence flux inside the transformer core.

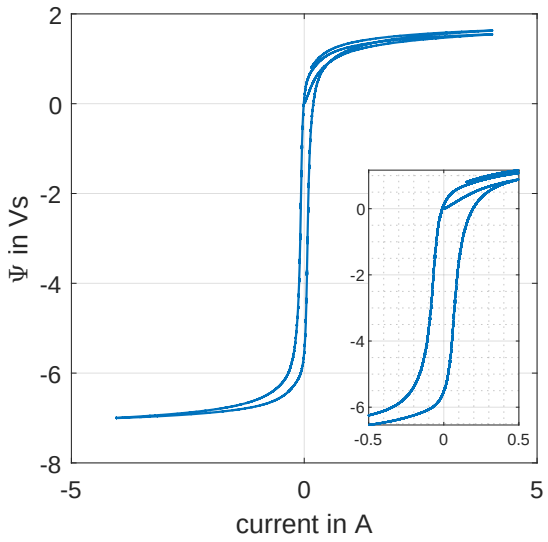

Figure 4.68: Measured DC hysteresis between high-voltage terminals A-C after DC winding resistance measurement between high-voltage terminals A-C with 1170 turns.

After the measured remanence in the transformer core (**Figure 4.68**), the effectiveness of three demagnetisation procedures was tested and verified with DC hysteresis measurements. **Figure 4.69** depicts the DC hysteresis characteristic measured via the high-voltage terminals A-C and B-N. Both $\Psi - i$ characteristics show a symmetrical distribution of the maximum flux linkage, with respect to the abscissa.

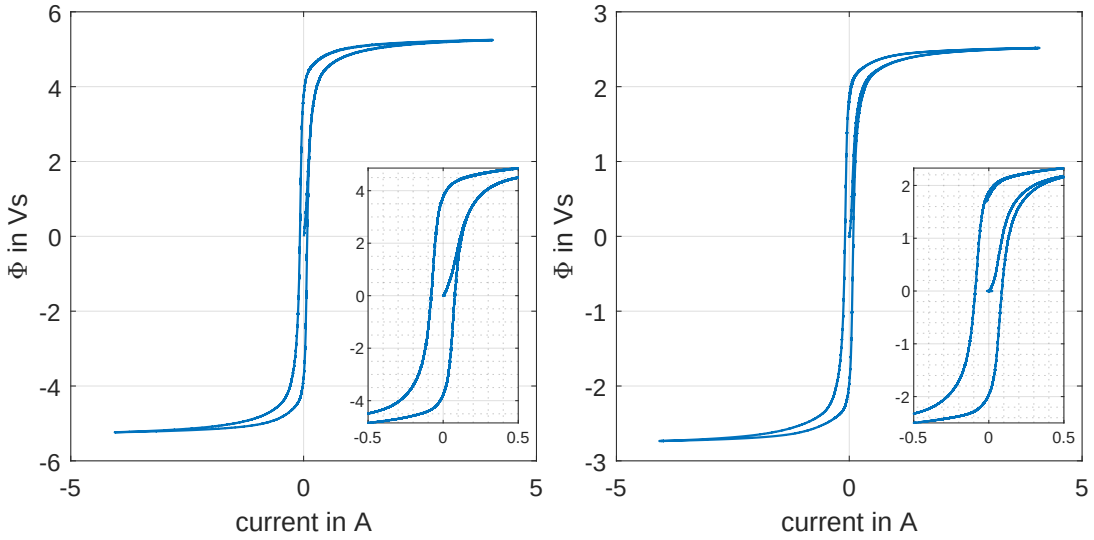

(a) DC hysteresis A-C after proposed demagnetisation procedure.

(b) DC hysteresis between B-N after proposed demagnetisation procedure.

Figure 4.69: DC hysteresis characteristic after demagnetisation procedure (**Section 4.9.1**) of T5Lb.

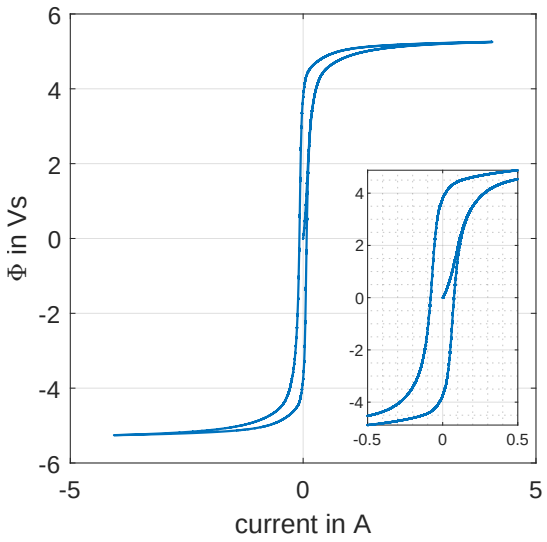

Figure 4.70: Measured DC hysteresis A-C after proposed demagnetisation procedure in **Section 4.9.2** of T5Lb.

Figure 4.69 and **Figure 4.70** proof that the proposed demagnetisation procedure effectively reduces the remanence in a five-limb transformer core.

A third, commonly used demagnetisation procedure was tested after a third DC winding resistance measurement to cause a remanence on the transformer core. During the third demagnetisation procedure, an in-phase voltage is applied simultaneously between the terminals A-B and C-B, where terminal B is used as return. **Figure 4.71** shows an asymmetrical DC hysteresis characteristic with respect to the abscissa. Thus, a remanence is still present in the transformer core, revealing the demagnetisation was not sufficient.

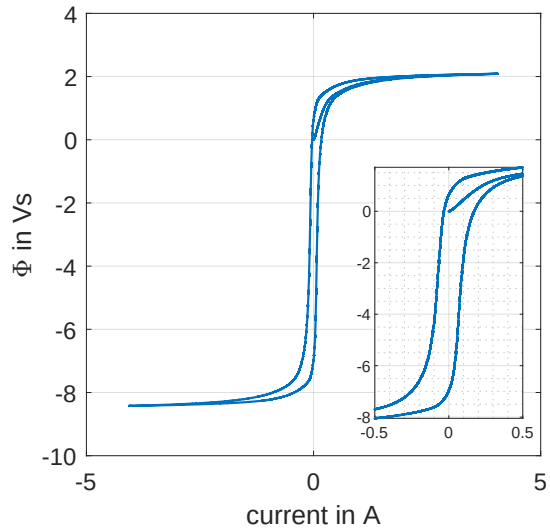

Figure 4.71: Measured DC hysteresis A-C after demagnetisation between A-B and C-B of T5Lb.

4.10 Discussion of Results

It was shown that the transformer core hysteresis characteristic can be measured via the transformer terminals up to saturation conditions. The measurement via the outer two wounded transformer limbs can be carried out with the AC saturation or with the DC hysteresis test. The approach, using the two-phase AC saturation test was tested on two three-limb 50 kVA transformers (T3Sa and T3Sb) and also on a five-limb 60 kVA laboratory transformer. The DC measurement was tested with three and five-limb transformers in the laboratory (T3Sa, T3Sb and T5S) and with three- and five-limb large power transformers (T3L and T5Lb). A further configuration to measure the transformer terminal characteristic under saturation conditions is the use of a power amplifier with a DC voltage on the neutral conductor. This requires the vector group yn on the supply terminals of the transformer. The choice of one of the above methods depends on the availability of the corresponding transformers and the available laboratory equipment. The DC hysteresis test requires only a portable transformer test device and can be carried out in the laboratory and in the field. The drawback of the DC hysteresis test is that the eddy current and excess losses can't be measured during the test. Further investigations are required, to determine if these losses can be considered in the model by using the data from the no-load test. The AC saturation test requires a sufficiently large power source with two anti-phase voltage outputs. This requirement may limit the applicability of the AC saturation test to small transformers. Also the excitation with a superimposed DC on each phase or on the neutral conductor requires an sufficiently large power amplifier, which may also limits the test to small power amplifiers.

Two transformer grey box models are derived from the factory acceptance test data and the transformer core design data, using the inductance-reluctance and the capacitance-permeance analogy. In the two topology models, each core section is represented by an individual branch. The models further include the magnetic stray paths between the limbs and the inner windings, the stray paths between the inner and the middle windings and the stray paths between the middle and outer

windings, if three windings are present. Especially during saturation, the correct representation of the zero-sequence impedance, with equal distribution between the phases, makes the model topological and increases the model accuracy [Zir+22b]. Therefore, the same zero-sequence impedance is derived from the zero-sequence test and included in the model for each limb. Small deviation can be caused by this assumption, because the limbs can have different zero-sequence impedances, but these are not measurable at the transformer terminals. Further improvement of the model accuracy can be reached by considering the air gap between the limb and the core joints. A parameter study with fixed values for the transformer joint air gap revealed a small air gap inductance at low flux density levels and a larger air gap inductance at increased flux density levels. This characteristic can be modelled with a non-linear inductor, which results in an inductance inversely proportional to the equivalent air gap length. Together with the equivalent air gap inductance the winding capacitance should be considered, because the winding capacitance and the equivalent air gap inductance also rotate the $\Psi - i$ characteristic from terminal measurements (counter-)clockwise. The model application range can probably be extended to applications with higher frequencies by split up the magnetic paths into several parallel longitudinal magnetic paths in order to consider the skin effect [Ras+19].

For the parameter estimation of the hysteresis models the AC saturation or DC saturation test are used on the example of the transformer T3Sa, by optimising the error between the measured and calculated terminal current waveforms. The models and model parameters are validated with the standard no-load test by comparing the terminal current waveforms and the power demand. Depending on the numbers of iterations during the optimisation process, the current waveform and amplitude during the no-load is very close to the measured waveforms. The power demand during the no-load test for the model, derived with the AC saturation test, is close to the maximum accepted standardised tolerance of 15 %. Therefore, the modelling approach is suitable for three-limb transformers in the range of 50 kVA rated power. The JA parameters derived with the DC hysteresis and AC saturation test differ roughly by the factor of two, in case of the JA parameter M_{s}. Comparing the standard no-load test with the JA parameters derived from the DC hysteresis and AC saturation test, the data from the AC provides a higher accuracy of the power demand during the no-load test.

The optimisation process is sensitive to the actual voltage waveform. Therefore, the voltage in the calculation should be fitted well to the measured voltage in terms of amplitude, rise time and duration. By removing data samples from the measurement data, where the current is constant, and only using the data from the initial magnetisation curve via the positive saturation inductance to the negative saturation inductance, the overall simulation time can be reduced by 92.6 % from 61 s to 4.5 s in case of the DC hysteresis test. The power demand and current waveform derived from the no-load with the hysteresis parameter optimised, based on the DC hysteresis test, are outside the standardised tolerance of 15 %.

A further improvement during the model optimisation, using the AC saturation or DC hysteresis test, is the usage of simplified model transformer model, representing only a single-phase of the transformer [Zir+22a], as depicted in **Figure 4.72**. Due to the opposite voltages applied to limb A

and C during the AC saturation or DC hysteresis test, the magnetic fluxes are asymmetrical, with respect to the middle limb B of a three-limb transformer core. Therefore, the flux in the middle limb B becomes zero, assuming ideal conditions. Thus, phase A and C are magnetically decoupled. This allows to use either phase A or C for further investigations during the AC saturation test. When comparing the full model with phase A or C, it can be observed that both models produce the same electrical and magnetic outputs. Therefore, the full transformer model can be reduced to a single-phase model, which reduces the computational power significantly.

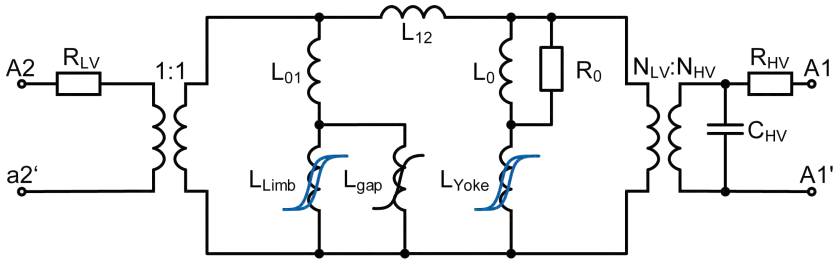

Figure 4.72: single-phase representation of three-limb transformer during AC saturation test, with C'_{HV} of the high-voltage capacity related to the low-voltage side.

It can be expected that the approach is also suitable for five-limb transformers and for transformers with rated power in the MVA-range, a proof is pending by the time of writing, but the required transformer data is given in this thesis.

To investigate the applicability of the transformer topology models, derived with the AC saturation and DC hysteresis test, the calculated and measured data from the inrush current, the short-circuit and the zero-sequence test should be compared and analysed.

As a further test case for the transformer model validation during saturation, the transformer B2B test can be employed with a superimposed DC via the high-voltage neutrals.

The DC hysteresis test is sensitive to remanence flux and signal distortion. Therefore, the transformer under test should be demagnetised before the DC hysteresis test. During a field study on a five-limb 380/110/30 kV 300 MVA power transformer it was found that the available demagnetisation procedures are not sufficient to demagnetise five-limb transformer cores. Therefore, a new procedure using, a DC with reversal polarity was successfully tested on the five-limb laboratory transformer T5S and the large power transformer T5Lb. The key is to force every section of the transformer core on its outer magnetisation curve and decrease the flux sequentially to a minimum.

The B2B tests can be carried out with the high-voltage terminals connected and with low- and high-voltage terminals connected in parallel. If both, the low- and high-voltage terminals are connected B2B, the requirements, given in [IEC97], should be full-filled. The transformer T3Sa and T3Sb can be operated connected via their high-voltage terminals and with one transformer in no-load on its low-voltage terminals. The B2B operation of both the low- and high-voltage terminals will give wrong results, due to the difference in the short-circuit impedance voltage difference. A possible configuration to operate the transformers T3Sa and T3Sb B2B with connected low-

and high-voltage terminals, is the use of two synchronised but independently controllable power amplifiers. In order to prevent difference between the high-voltage terminals of the transformers, each transformer is connected to its own power amplifier with controllable voltage amplitude. Both three-phase supply voltage should be synchronised.

In general, all test should be carried out with the power amplifier as supply, due to voltage distortion with supply from the public grid.

To superimpose a DC either the full-wave rectifier or batteries can be connected between the high-voltage neutrals of the B2B operated transformers. The use of the rectifier is more convenient due to the voltage regulation from outside the test cell. The voltage ripple of the full-wave rectifier does not affect the measurement results.

During the tests with batteries no negative effect with or without the use of a bypass capacitor was noticed. Therefore, no bypass capacitor in parallel to the batteries were used for further tests.

5 Conclusion and Further Research

5.1 Conclusion

The work was motivated by the investigations of geomagnetically induced currents (GICs) in the power transmission grid, including the monitoring of low-frequency currents (LFCs) in general and their effects on power transformers.

In the scope of this work a new transformer terminal measurement setup, the AC saturation test, was developed and successfully tested in the laboratory to characterise the transformer also in deep saturation. The idea of the AC saturation test is to saturate the outer two limbs of an unloaded three-limb transformer by applying two equal 180° increased voltages to the low-voltage windings of the outer two limbs. Because the AC saturation test requires a sufficiently large AC power source, the AC saturation test was further developed to the DC hysteresis test, which uses a DC voltage with changing polarity. The advantage of the DC hysteresis test over the AC saturation test is, that it can be carried out in the laboratory or in the field with a portable transformer test device.

To investigate the effects of GIC bias on transformers, two transformer topology grey box models are derived with the data from the factory acceptance test and the aforementioned AC saturation and DC hysteresis test for the parametrisation of the hysteresis models, implemented in the grey box models. The first topology model is based on the inductance-reluctance analogy with the Jiles-Atherton (JA) hysteresis model. Due to the small calculation step-size required by the model to reproduce smooth current waveforms, a second transformer topology model was employed using the capacitance-permeance analogy. The hysteresis characteristic in the capacitance-permeance topology model uses a non-linear capacitor. The hysteresis model parameters of both models, the JA and the non-linear capacitor are obtained by means of an optimisation with the Nelder-Mead Simplex (NMS) algorithm, utilising the AC saturation or DC saturation test.

During the DC hysteresis test in the field at large power transformers an offset in the measured hysteresis characteristic was observed, indicating a remanence in the transformer core. A demagnetisation with standard procedures could not reduce the remanence. Therefore, two new demagnetisation procedures for three- and five-limb transformers were developed and successfully tested at laboratory and large power transformers. The developed procedures can be carried out and easily be implemented in a portable transformer test device, to reduce the time required for the demagnetisation.

For the measurement of GICs in solidly grounded transformer neutrals, an existing measurement system has been further developed to minimise the constraints of the monitoring system on grid operations. Instead of using a mobile earthing equipment, bypassing the transformer earthing switch and feed through a zero-flux current transducer, a split-core current transducer was mounted around the earthing switch itself. The split-core current transducer uses a Hall sensor as a sensing element. Due to the temperature drift of the Hall sensor, the drift needed to be compensated to provide an acceptable offset drift for long-term measurements. For that propose a reference output signal

characteristic of the measurement system was recorded in a climate chamber. The temperature related offset drift was corrected via the software of the measurement system by a fitted function.

In the following, answers to the research questions related to transformer modelling as stated in **Section 1.1**, are given:

How can the transformer core hysteresis characteristics be modelled and parametrised from transformer terminal measurements?
The transformer core hysteresis can be modelled using the JA hysteresis model. Whereas the JA hysteresis parameters can be derived in the context of an optimisation with the NMS algorithm. To implement the transformer core hysteresis characteristics in the capacitance-permeance analogy a combination of saturation, hysteresis and eddy current element can be used to model the hysteresis characteristics. The six hysteresis parameters are derived during an optimisation with the NMS simplex algorithm from special tests. The hysteresis model, used in the capacitance-permeance analogy model, needs to be further investigated to characterise its behaviour under different operation conditions, such as the inrush current phenomena.

What is an appropriate modelling technique that reproduces the transformer terminal characteristics during saturation?
Transformer grey box topology models are appropriate modelling technique to accurate calculate the transformer terminal characteristics. The model parameters can be derived from the factory acceptance test or can be assumed by rules of thumb. The transformer core design is required to accurately calculate the flux densities in the transformer core sections. For the topology model, either the inductance-reluctance or the capacitance-permeance analogy can be used. The inductance-reluctance analogy is more common to power engineers, but the JA hysteresis model requires a sufficiently small calculation step-size in the area of 10 μs. The capacitance-permeance analogy is more common in power electronics but delivers acceptable current waveforms at higher step-sizes.

What is an appropriate transformer terminal measurement for the parametrisation of transformer hysteresis models including moderate saturation conditions?
The AC saturation and DC hysteresis test, which are developed in this work, are an appropriate transformer terminal measurement in the laboratory and in the field for the parametrisation of the JA and the capacitance-permeance hysteresis model. The two-phase measurement setup mitigates the magnetic coupling of the phases in three- and five-limb transformers. The DC saturation test can be carried out with a portable transformer test device in the field or in the laboratory. A possible drawback of the DC saturation test is the neglect of the eddy current and excess losses, due to measurement with DC. Further test cases and comparisons between models and measurements are required to judge if this drawback can be overcome with the data from the no-load test.

How can five-limb multi-winding power transformers be reliable demagnetised and how can the successful demagnetisation be proofed?
Five-limb multi-winding power transformers can be reliably demagnetised by a sequence of three demagnetisation cycles, using a rectangular DC voltage signal with decaying amplitude. The successfully demagnetisation can be proofed by a DC hysteresis measurement. The demagnetisation

and the DC hysteresis measurement can be carried with a portable transformer test device, in the laboratory and in the field.

The GIC monitoring system, developed in the previous project, was improved with respect the measurement range, accuracy and number of channels. The hardware of the installed measurement systems was updated and three additional measurement systems were employed during the last two years. Five transformers in the Austrian transmission grid are equipped with a direct flux compensation system (DCC). Since 2020, one of these transformers is equipped with a transformer neutral point current (NPC) measurement system and the three additional measurement channels of the improved system are used to monitor the compensating current of the compensation system. The one-year analysis of the measured compensating currents during 2021 reveals an almost homogeneous distribution of the LFC via the three phases of the five-limb 110/380/30 kV 300 MVA transformer. A new version of the measurement system, using a current transformer (CT) with a split core around a transformer neutral switch, was employed in 2021 in a field test. Different other LFC measurement techniques have been investigated regarding their applicability for the measurement of transformer neutral point currents. A possible cost-effective measurement system could use an array of four Hall sensors around the transformer neutral conductor. As main challenge, the drift of the Hall sensors was identified, especially during long-term measurements. By the time of writing the proposed setup was not fully tested in the laboratory.

In the following, answers to the research questions related to low frequency transformer neutral measurement as stated in **Section 1.1**, are given:

What are the specifications for a measurement system to measure low frequency transformer neutral point currents?
For the measurement of transformer neutral point current in geographically mid-latitude countries the following specifications should be fulfilled by a measurement system:

- no restrictions in power grid operation,
- minimum measurement range: ±25 A, (see **Section 3.6**)
- minimum accuracy: 2 % ± 1 mA for ±25 A DC,
- minimum primary current resolution: 5 mA,
- minimum sample rate: 1 Hz,
- compensated temperature related offset drift,
- low long-term offset drift,
- withstand short-circuit currents up to 80 kA.

What is the measurement accuracy of the developed system?
The guaranteed measurement system accuracy of the measurement system developed within this thesis is 2.0 % ±1 mA for the neutral point current measurement in the range of ±(1 A to ± 25 A) DC. The typical accuracy is 0.5 % ± 1 mA in the range of ±(1 A to 25 A) DC and 0.5 % ± 10 mA in the range of ±(1 A to 250 A) DC for the neutral point measurement and the three additional measurement channels respectively. Depending on the used measurement technology it could be

useful also measure the temperature close to the sensor, to provide a temperature compensation of the measurement signal, if required.

5.2 Further Research

Further research in the field of power transformers should address the following topics:

The modelling approach should be further tested and evaluated. E. g. by using other standards tests such as zero-sequence and short-circuit test for the model validation. Furthermore, the modelling approach and the number of case studies should be increased and extended to large power transformers. Further test cases could be the power calculation during machine synchronisation, involving step-up transformers as outlined in [Art91]. Regarding the ReCap model, the ability of accurately reproducing minor hysteresis loops should be evaluated to address possible weak points of the ReCap model.

The modelling approach could be improved in terms of computational speed, e. g. by combining the NMS and PSO algorithms (e. g. as done in [PSS06; FLZ06; LY12; Bha+21]) for the model parameter optimisation and the usage of a single-phase representation of the transformer when using the AC saturation test, as demonstrated in [Zir+22a].

After the model testing, the implementation possibilities in other software environments should be evaluated, to make the model advantages available to a broad number of researchers and users.

The demagnetisation procedure should be applied to a set of test cases, including transformers of different rated power and vector groups, to ensure the reliability of the procedure.

Further research in the field of LFC measurements at transformers should address LFCs caused by power electronics devices and the measurement of LFCs in the environment of hybrid HVAC/DC transmission lines.

Besides the topics mentioned above, the effects of LFC on magnetic (protective) current transformers during DC/LFC bias and the effect on the secondary equipment (such as [DLS06]) should be investigated. Furthermore, the effect on primary equipment.

List of Publications

[Alb+19a] D. Albert, T. Halbedl, H. Renner, R. L. Bailey, and G. Achleitner. "Geomagnetically induced currents and space weather - A review of current and future research in Austria". In: *2019 54th International Universities Power Engineering Conference (UPEC)*. [Piscataway, New Jersey]: IEEE, 2019, pp. 1–6. ISBN: 978-1-7281-3349-2. DOI: 10.1109/UPEC.2019.8893515.

[Alb+19b] D. Albert, S. Polster, R. Schürhuber, C. Obkircher, and G. Rader. "Zero-sequence current blocking device for two phase AC systems". In: *2019 54th International Universities Power Engineering Conference (UPEC)*. [Piscataway, New Jersey]: IEEE, 2019, pp. 1–5. ISBN: 978-1-7281-3349-2. DOI: 10.1109/UPEC.2019.8893601.

[Alb+20] D. Albert, P. Schachinger, H. Renner, P. Hamberger, F. Klammler, and G. Achleitner. "Field experience of small quasi DC bias on power transformers A first classification of low-frequency current pattern and identification of sources". In: *Cigre Session 48*. Ed. by Cigre. Paris, 2020. DOI: 10.1007/s00502-020-00846-1.

[Alb+21a] D. Albert, L. Domenig, D. Maletic, A. Reinbach-Kosestinger, K. Roppert, and H. Renner. "Comparing Two Topology Transformer Hysteresis Models with Power Transformer Measurements". In: *International Conference on the Computation of Electromagnetic Fields (COMPUMAG)*. Ed. by IEEE. 2021. URL: https://www.researchgate.net/publication/357877527_Comparing_Two_Topology_Transformer_Hysteresis_Models_with_Power_Transformer_Measurements.

[Alb+21b] D. Albert, P. Schachinger, R. L. Bailey, H. Renner, and G. Achleitner. "Analysis of long–term GIC measurements in transformers in Austria". In: *Space Weather* (2021). ISSN: 15427390. DOI: 10.1029/2021SW002912.

[Alb+22a] D. Albert, L. Domenig, P. Schachinger, K. Roppert, and H. Renner. "Comparing Two Topology Transformer Hysteresis Models derived from DC Hysteresis Measurements". In: *Electromagnetic Phenomena in Nonlinear Circuits (EPNC 2022)*. 2022, pp. 1–4.

[Alb+22b] D. Albert, P. Schachinger, A. Pirker, C. Engelen, F. Belavic, G. Leber, and H. Renner. "Power Transformer Hysteresis Measurement". In: *17. Sympoisum Energieinnovation EnInnov 2022*. Ed. by U. Bachiesl. 2022.

[AMR21] D. Albert, D. Maletic, and H. Renner. "Measurement based transformer modelling approach". In: *ETG Congress 2021*. 2021, pp. 1–6. URL: https://ieeexplore.ieee.org/document/9469662.

[Pro+20] A. Prohammer, M. Rüschitz, D. Albert, and H. Renner. "Transformer Saturation Methods and Transformer Response to Low Frequency Currents". In: *Power and*

Energy Student Summit (PESS). Ed. by TU Darmstadt. 2020. URL: https://ieeexplore.ieee.org/document/9273802.

[Rac+20] Rachel L. Bailey, R. Leonhardt, C. Möstl, P. Schachinger, and D. Albert. "Historical Analysis of Geomagnetic Stor Scales in Austria". In: *COBS Journal*. Ed. by Zentralanstalt für Meterologie und Geodynamik. 2020, p. 5. ISBN: 978-3-903171-08-4.

[SAR21a] P. Schachinger, D. Albert, and H. Renner. "Low Frequency Currents Source Identification". In: *2022 20th International Conference on Harmonics and Quality of Power (ICHQP)*. 2021, pp. 1–6.

[SAR21b] P. Schachinger, D. Albert, and H. Renner. "Geomagnetically induced currents: A measurement based inverse determination of earth impedances". In: *2021 56th International Universities Power Engineering Conference (UPEC)*. IEEE, 31.08.2021, pp. 1–5. ISBN: 978-1-6654-4389-0. DOI: 10.1109/UPEC50034.2021.9548157.

[Sch+20a] P. Schachinger, D. Albert, Rachel L. Bailey, G. Achleitner, and H. Renner. "Geomagnetically Induced Current Measurement in the Austrian Transmission Grid". In: *COBS Journal*. Ed. by Zentralanstalt für Meterologie und Geodynamik. 2020, p. 6. ISBN: 978-3-903171-08-4.

[Sch+20b] P. Schachinger, D. Albert, H. Renner, R. L. Bailey, G. Achleitner, and G. Leber. "Niederfrequente Sternpunktstroeme im Ubertragungsnetz - Ein Überblick über aktuelle und zukuenftige Forschung in Oesterreich". In: *16. Symposium Energieinnovations*. Ed. by Graz University of Technology. 2020.

[Sch+22] P. Schachinger, D. Albert, H. Renner, and G. Achleitner. "Einfluss von Spannungsänderungen und anderen Quellen auf niederfrequente Sternpunktströme". In: *17. Sympoisum Energieinnovation EnInnov 2022*. Ed. by U. Bachiesl. 2022.

[Zir+22a] S. E. Zirka, D. Albert, Y. I. Moroz, L. Domenig, and H. Renner. "Towards a Topological Model of a Three-Phase Transformer Including Deep Saturation Conditions". In: *20th International IGTE Symposium on Computational Methods in Electromagnetics and Multiphysics (IGTE'22)*. Ed. by Institute of Fundamentals and Theory. Graz, 2022.

[Zir+22b] S. E. Zirka, D. Albert, Y. I. Moroz, and H. Renner. "Further Improvements in Topological Transformer Model Covering Core Saturation". In: *IEEE Access* 10 (2022), pp. 64018–64027. ISSN: 2169-3536. DOI: 10.1109/ACCESS.2022.3183279.

Presentations and Posters

[AA22] D. Albert and G. Achleitner. *Sternpunktsgleichströme im Hoch- und Höchstspannungsnetz - aktueller Stand der Forschung*. online, 22.09.2022.

[Alb21] D. Albert. *Measurement based Transformer Modelling Approach*. Paris, 24.08.2021.

[AS22] D. Albert and P. Schachinger. *Effects of Solar Storms on the Power Grid*. online, 07.04.2022. URL: https://www.netzimpedanz.com/.

[ASB21] D. Albert, P. Schachinger, and R. L. Bailey. *Geomagnetically Induced Currents and Space Weather Prediction in Austria*. Space Weather Workshop, 22.04.2021. URL: https://cpaess.ucar.edu/space-weather-workshop-2021.

[SAB22] P. Schachinger, D. Albert, and R. L. Bailey. *Geomagnetically Induced Currents and Space Weather Prediction in Austria*. Space Weather Workshop, 2022. URL: https://dx.doi.org/10.1029/2021SW00.

[Sch+21] P. Schachinger, D. Albert, R. L. Bailey, H. Renner, and G. Achleitner. *Evaluation of GIC measurements in Austria: SM34A-05*. online, 15.12.2021.

Supervised Theses

[Cul18] S. Culetto. "High-Voltage Direct Current Power Hardware-in-the-Loop Test eines DC/DC-Konverters". Master Thesis. Graz: Graz University of Technology, 2018.

[Frö21] A. Fröhlich. "Versuchsaufbau zur präzisen Messung von Transformatorsternpunktströmen". Bachelor Thesis. Graz: Graz University of Technology, 2021.

[Mal21] D. Maletic. "Eletrocmagnetic Model of a Power Transformer for Low Frequencies". Master Thesis. Graz: Graz University of Technology, 2021.

[Pro20] A. Prohammer. "Messung des Einflusses von niederfrequenten Strömen auf Dreiphasentransformatoren: Measurement of the influence of low-frequency currents on three-phase power transformers". Master Thesis. Graz: Graz University of Technology, 2020.

[Rüs20] M. Rüschitz. "Einfluss und Modellierung von niederfrequenten Strömen auf Leistungstransformatoren: Influence and modelling of low-frequency currents on power transformers". Master Thesis. Graz: Graz University of Technology, 2020.

[Tau20] B. Taupe. "Umbau zweier Leistungstransformatoren zur flexiblen Änderung der Schaltgruppe". Bachelor Thesis. Graz: Graz University of Technology, 2020.

[Woh20] P. E. Wohlfart. "Aufbau und Verifikation eines Systems zur Messung von Sternpunktströmen an Leistungstransformatoren". Bachelor Thesis. Graz: Graz University of Technology, 2020.

Bibliography

[ABB10] ABB. *Transformer Handbook*. Ed. by ABB. 2010.

[ABB11] ABB. *FOCS - Fiber-Optic Current Sensor: Make light work of DC current measurement*. 2011. URL: https://search.abb.com/library/Download.aspx?DocumentID=3BHS362996E01&LanguageCode=en&DocumentPartId=&Action=Launch (visited on 03/16/2021).

[Abb20] L. Abbas. "Off-core magnetic flux paths in power transformers: Modeling and applications". PhD Thesis. Trondheim, Norway: Norwegian University of Science and Technology, 2020. URL: https://hdl.handle.net/11250/2652746.

[Abd+20] Z. M. K. Abda, N. F. A. Aziz, Kadir, M. Z. A. A., and Z. A. Rhazali. "A Review of Geomagnetically Induced Current Effects on Electrical Power System: Principles and Theory". In: *IEEE Access* 8 (2020), pp. 200237–200258. ISSN: 2169-3536. DOI: 10.1109/ACCESS.2020.3034347.

[Ach22] G. Achleitner. *Transformer Protection Settings using a DCC System*. Ed. by D. Albert. 21.02.2022.

[AHH95] R. Allcock, S. Holland, and L. Haydock. "Calculation of zero phase sequence impedance for power transformers using numerical methods". In: *IEEE Transactions on Magnetics* 31.3 (1995), pp. 2048–2051. ISSN: 0018-9464. DOI: 10.1109/20.376446.

[AHS12] J. Allmeling, W. Hammer, and J. Schonberger. "Transient simulation of magnetic circuits using the permeance-capacitance analogy". In: *2012 IEEE 13th Workshop on Control and Modeling for Power Electronics (COMPEL 2012)*. Piscataway, NJ: IEEE, 2012, pp. 1–6. ISBN: 978-1-4244-9373-9. DOI: 10.1109/COMPEL.2012.6251786.

[AKP15] D. Alekseev, A. Kuvshinov, and N. Palshin. "Compilation of 3D global conductivity model of the Earth for space weather applications". In: *Earth, Planets and Space* 67.1 (2015), p. 377. DOI: 10.1186/s40623-015-0272-5.

[Al-13] D. Al-Halbouni. "The European Alps as an interrupter of the Earth's conductivity structures". In: *Solid Earth Discussions* 5.2 (2013), pp. 1031–1079. DOI: 10.5194/sed-5-1031-2013.

[AL07] Alakula, M. A. F. K. and S. Lindahl. "Method and equipment for the protection of power systems against geomagnetically induced currents". EP1766746 (A1). 2007.

[Alb+19] D. Albert, T. Halbedl, H. Renner, R. L. Bailey, and G. Achleitner. "Geomagnetically induced currents and space weather - A review of current and future research in Austria". In: *2019 54th International Universities Power Engineering Conference*

(UPEC). [Piscataway, New Jersey]: IEEE, 2019, pp. 1–6. ISBN: 978-1-7281-3349-2. DOI: 10.1109/UPEC.2019.8893515.

[Alb+20] D. Albert, P. Schachinger, H. Renner, P. Hamberger, F. Klammler, and G. Achleitner. "Field experience of small quasi DC bias on power transformers A first classification of low-frequency current pattern and identification of sources". In: *Cigre Session 48*. Ed. by Cigre. Paris, 2020. DOI: 10.1007/s00502-020-00846-1.

[Alb+21a] D. Albert, L. Domenig, D. Maletic, A. Reinbach-Kosestinger, K. Roppert, and H. Renner. "Comparing Two Topology Transformer Hysteresis Models with Power Transformer Measurements". In: *International Conference on the Computation of Electromagnetic Fields (COMPUMAG)*. Ed. by IEEE. 2021. URL: https://www.researchgate.net/publication/357877527_Comparing_Two_Topology_Transformer_Hysteresis_Models_with_Power_Transformer_Measurements.

[Alb+21b] D. Albert, P. Schachinger, R. L. Bailey, H. Renner, and G. Achleitner. "Analysis of long–term GIC measurements in transformers in Austria". In: *Space Weather* (2021). ISSN: 15427390. DOI: 10.1029/2021SW002912.

[Alb+22a] D. Albert, L. Domenig, P. Schachinger, K. Roppert, and H. Renner. "Comparing Two Topology Transformer Hysteresis Models derived from DC Hysteresis Measurements". In: *Electromagnetic Phenomena in Nonlinear Circuits (EPNC 2022)*. 2022, pp. 1–4.

[Alb+22b] D. Albert, P. Schachinger, A. Pirker, C. Engelen, F. Belavic, G. Leber, and H. Renner. "Power Transformer Hysteresis Measurement". In: *17. Sympoisum Energieinnovation EnInnov 2022*. Ed. by U. Bachiesl. 2022.

[Ami+20] S. Amirdehi, B. Trajin, P.-E. Vidal, J. Vally, and D. Colin. "Power Transformer Model in Railway Applications Based on Bond Graph and Parameter Identification". In: *IEEE Transactions on Transportation Electrification* 6.2 (2020), pp. 774–783. DOI: 10.1109/TTE.2020.2979598.

[AMR21] D. Albert, D. Maletic, and H. Renner. "Measurement based transformer modelling approach". In: *ETG Congress 2021*. 2021, pp. 1–6. URL: https://ieeexplore.ieee.org/document/9469662.

[Ann+00] U. D. Annakkage, P. G. McLaren, E. Dirks, R. P. Jayasinghe, and A. D. Parker. "A current transformer model based on the Jiles-Atherton theory of ferromagnetic hysteresis". In: *IEEE Transactions on Power Delivery* 15.1 (2000), pp. 57–61. ISSN: 08858977. DOI: 10.1109/61.847229.

[Ant+12] E. E. Antonova, M. S. Pulinets, M. O. Riazantseva, S. S. Znatkova, I. P. Kirpichev, Stepanova, and M. V. "Turbulence in the Magnetosheath and the Problem of Plasma

Penetration Inside the Magnetosphere". In: *Exploring the Solar Wind*. Ed. by M. Lazar. InTech, 2012. ISBN: 978-953-51-0339-4. DOI: 10.5772/36791.

[ÁPW12] A. Ádám, E. Prácser, and V. Wesztergom. "Estimation of the electric resistivity distribution (EURHOM) in the european lithosphere in the frame of the eurisgic WP2 project". In: *Acta Geodaetica et Geophysica Hungarica* 47.4 (2012), pp. 377–387. ISSN: 1217-8977. DOI: 10.1556/AGeod.47.2012.4.1.

[Art16] Arteche Group. *Optical Current Transformer*. 2016. URL: https://www.arteche.com/en/products/optical-current-transformer.

[Art91] C. M. Arturi. "Transient simulation and analysis of a three-phase five-limb step-up transformer following an out-of-phase synchronization". In: *IEEE Transactions on Power Delivery* 6.1 (1991), pp. 196–207. ISSN: 08858977. DOI: 10.1109/61.103738.

[ASB21] D. Albert, P. Schachinger, and R. L. Bailey. *Geomagnetically Induced Currents and Space Weather Prediction in Austria*. Space Weather Workshop, 22.04.2021. URL: https://cpaess.ucar.edu/space-weather-workshop-2021.

[ASR21] D. Albert, P. Schachinger, and H. Renner. "Method for measuring magnetic flux in a magnetic component". 2021.

[Aus21] Austrian Power Grid. *Media-Center*. 2021. URL: https://www.apg.at/de/Media-Center/Download-Bereich.

[Ave+18] A. Avendano, B. A. Mork, D. Ishchenko, and F. Gonzalez. "Advanced Leakage Inductance Model for Transformer Transient Simulation". In: *2018 IEEE Power & Energy Society General Meeting (PESGM)*. Ed. by IEEE. Piscataway, NJ: IEEE, 2018, pp. 1–5. ISBN: 978-1-5386-7703-2. DOI: 10.1109/PESGM.2018.8586015.

[Bac+12] F. Bachinger, A. Hackl, P. Hamberger, A. Leikermoser, G. Leber, H. Passath, and M. Stoessl. "Direct current in transformers: Effects and compensation". In: *44th International Conference on Large High Voltage Electric Systems 2012* (2012).

[Bac+13] F. Bachinger, P. Hamberger, A. Leikermoser, G. Leber, and H. Passath. *Direct current in transformers - experience, compensation: Paper PS1-34: Cigre SC A2 & C4 Joint Colloquium*. Zurich, Switzerland, 2013.

[Bai+17] R. L. Bailey, T. Halbedl, I. Schattauer, A. Römer, G. Achleitner, C. D. Beggan, V. Wesztergom, R. Egli, and R. Leonhardt. "Modelling geomagnetically induced currents in midlatitude Central Europe using a thin-sheet approach". In: *Annales Geophysicae* 35.3 (2017), pp. 751–761. DOI: 10.5194/angeo-35-751-2017.

[Bai+18] R. L. Bailey, T. Halbedl, I. Schattauer, G. Achleitner, and R. Leonhardt. "Validating GIC Models With Measurements in Austria: Evaluation of Accuracy and Sensitivity to

Input Parameters". In: *Space Weather* 16.7 (2018), pp. 887–902. ISSN: 15427390. DOI: 10.1029/2018SW001842.

[Bai18] R. L. Bailey. "Space weather and geomagnetically induced currents in Austria". PhD Thesis. Vienna: Universität Wien, 2018.

[Bar+15] C. Barbosa, L. Alves, R. Caraballo, G. A. Hartmann, A. R. R. Papa, and R. J. Pirjola. "Analysis of geomagnetically induced currents at a low-latitude region over the solar cycles 23 and 24: comparison between measurements and calculations". In: *Journal of Space Weather and Space Climate* 5.5 (2015), A35. DOI: 10.1051/swsc/2015036.

[BCP03] A. Benabou, S. Clénet, and F. Piriou. "Comparison of Preisach and Jiles–Atherton models to take into account hysteresis phenomenon for finite element analysis". In: *Journal of Magnetism and Magnetic Materials* 261.1-2 (2003), pp. 139–160. ISSN: 03048853. DOI: 10.1016/S0304-8853(02)01463-4.

[Ber08] G. Bertotti. *Hysteresis in magnetism: For physicists, materials scientists and engineers*. Digitaler Nachdr. Academic Press series in electromagnetism. San Diego, Calif.: Acad. Press, 2008. ISBN: 0120932709.

[Ber88] G. Bertotti. "General properties of power losses in soft ferromagnetic materials". In: *IEEE Transactions on Magnetics* 24.1 (1988), pp. 621–630. ISSN: 0018-9464. DOI: 10.1109/20.43994.

[Bha+21] B. Bhardwaj, J. Jaiharie, R. Sorabh Dadhich, S. I. Ahmed, and M. Ganesan. "Windfarm optimization using Nelder-Mead and Particle Swarm optimization". In: *Proceedings of the 7th International Conference on Electrical Energy Systems (ICEES 2021)*. Piscataway, NJ: IEEE, 2021, pp. 524–529. ISBN: 978-1-7281-7612-3. DOI: 10.1109/ICEES51510.2021.9383684.

[Bis85] J. E. L. Bishop. "Enhanced eddy current loss due to domain displacement". In: *Journal of Magnetism and Magnetic Materials* 49.3 (1985), pp. 241–249. ISSN: 03048853. DOI: 10.1016/0304-8853(85)90154-4.

[Blo46] A. Bloch. "On methods for the construction of networks dual to non-planar networks". In: *Proceedings of the Physical Society* 58.6 (1946), pp. 677–694. ISSN: 0959-5309. DOI: 10.1088/0959-5309/58/6/306.

[BLU+38] L. F. BLUME, G. Camilli, A. Boyajian, and B. A. Mork. *Transformer engineering: A treatise on the theory, operation and application of transformers*. New York: Wiley, 1938. URL: https://archive.org/details/transformer-engineering-blume-camilli-boyajian-1938/page/n41/mode/2up.

[Boh+05] K. Bohnert, H. Brandle, M. Brunzel, P. Gabus, and P. Guggenbach. "Highly Accurate Fiber-Optic DC Current Sensor for the Electro-Winning Industry". In: *52nd Annual*

petroleum and chemical industry conference. IEEE, 2005, pp. 121–128. ISBN: 0-7803-9272-8. DOI: 10.1109/PCICON.2005.1524547.

[Bol02] L. Bolduc. "GIC observations and studies in the Hydro-Québec power system". In: *Journal of Atmospheric and Solar-Terrestrial Physics* 64.16 (2002), pp. 1793–1802. ISSN: 13646826. DOI: 10.1016/S1364-6826(02)00128-1.

[Bot19] D. H. Boteler. "A 21st Century View of the March 1989 Magnetic Storm". In: *Space Weather* 17.10 (2019), pp. 1427–1441. ISSN: 15427390. DOI: 10.1029/2019SW002278.

[Bot94] D. H. Boteler. "Geomagnetically induced currents: present knowledge and future research". In: *IEEE Transactions on Power Delivery* 9.1 (1994), pp. 50–58. ISSN: 08858977. DOI: 10.1109/61.277679.

[BP17] D. H. Boteler and R. J. Pirjola. "Modeling geomagnetically induced currents". In: *Space Weather* 15.1 (2017), pp. 258–276. ISSN: 15427390. DOI: 10.1002/2016SW001499.

[BP22] D. H. Boteler and R. J. Pirjola. "Electric field calculations for real-time space weather alerting systems". In: *Geophysical Journal International* 230.2 (2022), pp. 1181–1196. ISSN: 0956-540X. DOI: 10.1093/gji/ggac104.

[BP98] D. H. Boteler and R. J. Pirjola. "The complex-image method for calculating the magnetic and electric fields produced at the surface of the Earth by the auroral electrojet". In: *Geophysical Journal International* 132.1 (1998), pp. 31–40. ISSN: 0956-540X. DOI: 10.1046/j.1365-246x.1998.00388.x.

[Bro44] A. Bronwell. "Transmission-Line Analogies of Plane Electromagnetic-Wave Reflections". In: *Proceedings of the IRE* 32.4 (1944), pp. 233–241. ISSN: 0096-8390. DOI: 10.1109/JRPROC.1944.230657.

[Bun68] R. W. Buntenbach. *Improved circuit models for inductors wound on dissipative magnetic cores*. 1968. URL: https://www.osti.gov/biblio/4832990,journal%20=.

[Bun69] R. W. Buntenbach. "Analogs between magnetic and electrical circuits". In: *Electronic Products*. Vol. 5. 1969, pp. 108–113.

[But+17] M. D. Butala, M. Kazerooni, J. J. Makela, F. Kamalabadi, J. L. Gannon, H. Zhu, and T. J. Overbye. "Modeling Geomagnetically Induced Currents From Magnetometer Measurements: Spatial Scale Assessed With Reference Measurements". In: *Space Weather* 15.10 (2017), pp. 1357–1372. ISSN: 15427390. DOI: 10.1002/2017SW001602.

[Cag53] L. Cagniard. "Basic theory of the magneto-telluric method of geophysical prospecting: BASIC THEORY OF THE MAGNETO–TELLURIC METHOD OF GEOPHYSICAL

PROSPECTING". In: *GEOPHYSICS* 18.3 (1953), pp. 605–635. ISSN: 0016-8033. DOI: 10.1190/1.1437915.

[Car+03] A. Carlson, J. Fuhr, G. Schemel, and F. Wegscheider. *Testing of Transformers: Routine tests, Type tests and Special tests*. 2003. URL: https://library.e.abb.com/public/c1256b3c00492da6852570f8006d6175/1LAB000074_Testbook_intro.pdf.

[Car+19] R. Caraballo, J. A. González–Esparza, M. Sergeeva, and C. R. Pacheco. "First GIC estimates for the Mexican power grid". In: *Space Weather* (2019). ISSN: 15427390. DOI: 10.1029/2019SW002260.

[Car16] R. Caraballo. "Geomagnetically induced currents in Uruguay: Sensitivity to modelling parameters". In: *Advances in Space Research* 58.10 (2016), pp. 2067–2075. ISSN: 02731177. DOI: 10.1016/j.asr.2016.03.006.

[Car17] C. Carrander. *Magnetizing Currents in Power Transformers - Measurements, Simulations, and Diagnostic Methods: Doctoral Thesis*. Schweden, 2017. URL: https://www.diva-portal.org/smash/get/diva2:1106261/FULLTEXT02.pdf.

[CBG18] H. K. Chisepo, L. D. Borrill, and C. T. Gaunt. "Measurements show need for transformer core joint details in finite element modelling of GIC and DC effects". In: *COMPEL - The international journal for computation and mathematics in electrical and electronic engineering* 37.3 (2018), pp. 1011–1028. ISSN: 0332-1649. DOI: 10.1108/COMPEL-11-2016-0511.

[CD13] E. W. Cliver and W. F. Dietrich. "The 1859 space weather event revisited: limits of extreme activity". In: *Journal of Space Weather and Space Climate* 3 (2013), A31. DOI: 10.1051/swsc/2013053.

[CH09] N. Chiesa and H. K. Høidalen. "Systematic switching study of transformer inrush current: simulations and measurements". In: (2009). URL: https://www.ipstconf.org/papers/Proc_IPST2009/09IPST046.pdf.

[Cha+03] W. Chandrasena, P. G. McLaren, U. D. Annakkage, and R. P. Jayasinghe. "Modeling GIC effects on power systems: the need to model magnetic status of transformers". In: *2003 IEEE Bologna PowerTech: conference proceedings*. [Place of publication not identified]: IEEE, 2003, pp. 981–986. ISBN: 0-7803-7967-5. DOI: 10.1109/PTC.2003.1304679.

[Cha+04] W. Chandrasena, P. G. McLaren, U. D. Annakkage, and R. P. Jayasinghe. "An Improved Low-Frequency Transformer Model for Use in GIC Studies". In: *IEEE Transactions on Power Delivery* 19.2 (2004), pp. 643–651. ISSN: 08858977. DOI: 10.1109/TPWRD.2004.824429.

[Cha+06] W. Chandrasena, P. G. McLaren, U. D. Annakkage, R. P. Jayasinghe, D. Muthumuni, and E. Dirks. "Simulation of hysteresis and eddy current effects in a power transformer". In: *Electric Power Systems Research* 76.8 (2006), pp. 634–641. ISSN: 03787796. DOI: 10.1016/j.epsr.2005.12.009.

[Cha18] D. Chatrefou. *Post Intelligent - French Power Grid Smart Substation*. 2018. URL: https://docplayer.net/56685409-Poste-intelligent-french-power-grid-smart-substation.html.

[Cha22] Chauvin Arnoux. *Current clamps for AC current: MN series*. 2022. URL: https://www.chauvin-arnoux.at/sites/default/files/HLHBDAMR.PDF.

[Che+09] Q. Chen, L. Xu, X. Ruan, S. C. Wong, and C. K. Tse. "Gyrator-Capacitor Simulation Model of Nonlinear Magnetic Core". In: *2009 IEEE Applied Power Electronics Conference and Exposition*. Piscataway, NJ: IEEE, 2009, pp. 1740–1746. ISBN: 978-1-4244-2811-3. DOI: 10.1109/APEC.2009.4802905.

[Che49] E. C. Cherry. "The Duality between Interlinked Electric and Magnetic Circuits and the Formation of Transformer Equivalent Circuits". In: *Proceedings of the Physical Society. Section B* 62.2 (1949), pp. 101–111. ISSN: 0370-1301. DOI: 10.1088/0370-1301/62/2/303.

[Chi10] N. Chiesa. "Power Transformer Modeling for Inrush Current Calculation". PhD Thesis. Trondheim, Norway: Norwegian University of Science and Technology, 2010. URL: https://ntnuopen.ntnu.no/ntnu-xmlui/bitstream/handle/11250/256440/322811_FULLTEXT02.pdf?sequence=2&isAllowed=y.

[Cho+15] K.-C. Choi, M.-Y. Park, Y. Ryu, Y. Hong, J.-H. Yi, S.-W. Park, and J.-H. Kim. "Installation of Induced Current Measurement Systems in Substations and Analysis of GIC Data during Geomagnetic Storms". In: *Journal of Astronomy and Space Sciences* 32.4 (2015), pp. 427–434. ISSN: 2093-5587. DOI: 10.5140/JASS.2015.32.4.427.

[Cig14] Cigre. *Electrical Transient Interaction Between Transformers and the Power System: Part 1- Expertise: Joint Working Group A2/C4.39*. 2014.

[Cig15] Cigre. *Transformer reliability survey: WG A2.37*. 2015. ISBN: 978-2-85873-346-0. URL: https://e-cigre.org/publication/642-transformer-reliability-survey.

[Cig20] Cigre. *Load sound power levels for specification purposes of three-phase 50 Hz and 60 Hz liquid-filled power transformers*. Ed. by Cigre. 2020. URL: https://e-cigre.org/publication/WGR_310_1-load-sound-power-levels-for-specification-purposes-of-three-phase-50-hz-and-60-hz-liquid-filled-power-transformers.

[Cig90] Cigre. *Guidelines for represantation of network elements when calculating transients: Working Group 02 (Internal overvoltages) Of Study Committee 33 (Overvoltages and Insulation Coordination)*. 1990. URL: https://e-cigre.org/publication/039-guidelines-for-representation-of-network-elements-when-calculating-transients.

[Cig96] Cigre TF 13.00.1. "Controlled Switching – A State-of-the-Art Survey, Part II". In: *ELECTRA No. 164*. Ed. by Cigre. Electra. Feburary 1996, pp. 39–61. URL: https://e-cigre.org/publication/ELT_164_1-controlled-switching-a-state-of-the-art-survey-part-ii.

[Cla16] C. Clauser. *Einführung in die Geophysik: Globale physikalische Felder und Prozesse in der Erde*. 2., aktualisierte und korrigierte Auflage. Berlin and Heidelberg: Springer Spektrum, 2016. ISBN: 978-3-662-46883-8. DOI: 10.1007/978-3-662-46884-5.

[Cli+20] M. A. Clilverd, C. J. Rodger, J. B. Brundell, M. Dalzell, I. Martin, D. H. Mac Manus, and N. R. Thomson. "Geomagnetically Induced Currents and Harmonic Distortion: High Time Resolution Case Studies". In: *Space Weather* 18.10 (2020). ISSN: 15427390. DOI: 10.1029/2020SW002594.

[Con07] C. Constable. "Geomagnetic Spectrum, Temporal". In: *Encyclopedia of geomagnetism and paleomagnetism*. Ed. by D. Gubbins and E. Herrero-Bervera. Encyclopedia of earth sciences series. Dordrecht: Springer, 2007, pp. 353–355. ISBN: 978-1-4020-3992-8. DOI: 10.1007/978-1-4020-4423-6.

[CPT11] G. Chicco, P. Postolache, and C. Toader. "Triplen harmonics: Myths and reality". In: *Electric Power Systems Research* 81.7 (2011), pp. 1541–1549. ISSN: 03787796. DOI: 10.1016/j.epsr.2011.03.007.

[Dag+99] I. A. Daglis, R. M. Thorne, W. Baumjohann, and S. Orsini. "The terrestrial ring current: Origin, formation, and decay". In: *Reviews of Geophysics* 37.4 (1999), pp. 407–438. ISSN: 87551209. DOI: 10.1029/1999RG900009.

[DB12] T. Demiray and G. Beccuti. "Geomagnetisch induzierte Ströme im Schweizer Übertragungsnetz: Geomagnetically induced currents in the Swiss Transmission Network". In: (2012). URL: https://www.swissgrid.ch/dam/swissgrid/current/News/2013/Schlussbericht_GIC.pdf.

[DDY05] K. Dizheng, W. Da, and Z. Yun. "The Analysis and Handling of the Impact of Ground Current in DC Transmission on Power Grid Equipment". In: *Paper abstracts*. Piscataway, N.J: IEEE, 2005, pp. 1–4. ISBN: 0-7803-9114-4. DOI: 10.1109/TDC.2005.1547164.

[Dea94] J. H. B. Deane. "Modeling the dynamics of nonlinear inductor circuits". In: *IEEE Transactions on Magnetics* 30.5 (1994), pp. 2795–2801. ISSN: 0018-9464. DOI: 10.1109/20.312521.

[Deu] Deutsches GeoForschungsZentrum. *Planetarische Kennziffer der geomagnetischen Aktivität*. URL: https://www.gfz-potsdam.de/kp-index/.

[DEW19] DEWESoft. *Power Manuel: Version: 2.0*. Ed. by DEWESoft. 2019.

[DIN02] DIN. *Deutsche Norm 40110-2:2002 Wechselstromgrößen - Teil 2: Mehrleiter-Stromkreise: Quantities used in alternating current theory - Part 2: Multi-line circuits*. Berlin, 2002. DOI: 10.31030/9413829.

[Div+20] T. Divett, D. H. Mac Manus, G. S. Richardson, C. D. Beggan, C. J. Rodger, M. Ingham, E. Clarke, A. W. P. Thomson, M. Dalzell, and Y. Obana. "Geomagnetically Induced Current Model Validation From New Zealand's South Island". In: *Space Weather* 18.8 (2020). ISSN: 15427390. DOI: 10.1029/2020SW002494.

[DLS06] J. Dickert, R. Luxenburger, and P. Schegner. "Investigation on the Behavior of the Remanence Level of Protective Current Transformers". In: *Proceedings of the International Symposium Modern Electric Power Systems*. Ed. by E. Rosolowski. Wroclaw, 2006, pp. 348–353. ISBN: 9788392131526.

[Dom22] L. Domenig. "Hysteresis Network Model for 3-Phase Transformer". Master Theses. Graz: Graz University of Technology, 2022.

[DS13] C.-I. Dobrotă and A. Stancu. "What does a first-order reversal curve diagram really mean? A study case: Array of ferromagnetic nanowires". In: *Journal of Applied Physics* 113.4 (2013), p. 043928. ISSN: 0021-8979. DOI: 10.1063/1.4789613.

[Dub+13] W. Dubitzky, O. Wolkenhauer, K.-H. Cho, and H. Yokota. *Encyclopedia of systems biology: With 148 tables*. New York, NY: Springer Reference, 2013. ISBN: 978-1-4419-9862-0. DOI: 10.1007/978-1-4419-9863-7.

[Dun61] J. W. Dungey. "Interplanetary Magnetic Field and the Auroral Zones". In: *Physical Review Letters* 6.2 (1961), pp. 47–48. ISSN: 0031-9007. DOI: 10.1103/PhysRevLett.6.47.

[Dup+01] L. R. Dupre, R. van Keer, J. A. A. Melkebeek, Y. I. Moroz, and S. E. Zirka. "Hysteresis Models for Transient Simulation". In: *Scientific computing in electrical engineering*. Ed. by M. Griebel, D. E. Keyes, R. M. Nieminen, D. Roose, T. Schlick, U. van Rienen, M. Günther, and D. Hecht. Vol. 18. Lecture Notes in Computational Science and Engineering. Berlin et al.: Springer, 2001, pp. 105–112. ISBN: 978-3-540-42173-3. DOI: 10.1007/978-3-642-56470-3.

[DW81] E. P. Dick and W. Watson. "Transformer Models for Transient Studies Based on Field Measurements". In: *IEEE Transactions on Power Apparatus and Systems* PAS-100.1 (1981), pp. 409–419. ISSN: 0018-9510. DOI: 10.1109/TPAS.1981.316870.

[Dyn18] Dynamicratings. *GIC-4: Geomagnetic Induced Current Sensor*. PDF. 2018. URL: https://www.dynamicratings.com/wp-content/uploads/2020/03/181109-GIC-Sensor.pdf.

[Eas+15] J. P. Eastwood, H. Hietala, G. Toth, T. D. Phan, and M. Fujimoto. "What Controls the Structure and Dynamics of Earth's Magnetosphere?" In: *Space Science Reviews* 188.1-4 (2015), pp. 251–286. ISSN: 0038-6308. DOI: 10.1007/s11214-014-0050-x.

[Eas+17] J. P. Eastwood, E. Biffis, M. A. Hapgood, L. Green, M. M. Bisi, R. D. Bentley, R. Wicks, L.-A. McKinnell, M. Gibbs, and C. Burnett. "The Economic Impact of Space Weather: Where Do We Stand?" In: *Risk analysis : an official publication of the Society for Risk Analysis* 37.2 (2017), pp. 206–218. DOI: 10.1111/risa.12765.

[Eat94] M. Eaton. "Modeling magnetic devices using the gyrator re-cap core model". In: *Conference record / Northcon 94, Washington State Convention and Trade Center, Seattle, Washington, October 11 - 13, 1994*. Piscataway, NJ: IEEE Operations Center, 1994, pp. 60–66. ISBN: 0-7803-9995-1. DOI: 10.1109/NORTHC.1994.638970.

[EGT11] E. Echer, W. D. Gonzalez, and B. T. Tsurutani. "Statistical studies of geomagnetic storms with peak Dst≤ -50nT from 1957 to 2008". In: *Journal of Atmospheric and Solar-Terrestrial Physics* 73.11-12 (2011), pp. 1454–1459. ISSN: 13646826. DOI: 10.1016/j.jastp.2011.04.021.

[EH00] S. L. Eliassen and S. M. Hesjevik. "Varied pipeline conditions complicate mitigation strategies". In: *Oil and Gas Journal* 98.26 (2000), pp. 60–63. URL: https://www.scopus.com/inward/record.uri?eid=2-s2.0-1642633522&partnerID=40&md5=b780a8a9330b6a4342f658c0294d22ff.

[Elo+92] J. Elovaara, P. Lindblad, A. Viljanen, T. Mäkinen, R. Pirjola, S. Larsson, and B. Kielen. "Geomagnetically Induced Current sin the Nordic Power System and theri Effects on Equipment, Control, Protection and Operation". In: *Cigre Session 1992*. Ed. by Cigre. 1992, pp. 1–10.

[Ema07] A. E. Emanuel. "About the Rejection of Poynting Vector in Power Systems Analysis". In: *Electrical Power Quality and Utilisation. Journal* Vol. 13.nr 1 (2007), pp. 43–49. ISSN: 1896-4672. URL: http://yadda.icm.edu.pl/yadda/element/bwmeta1.element.baztech-article-BAT1-0029-0028/c/Emanuel_v13i1_07.pdfUR%20-%20http://yadda.icm.edu.pl/yadda/element/bwmeta1.element.baztech-article-BAT1-0029-0028.

[Ema90] A. E. Emanuel. "Powers in nonsinusoidal situations-a review of definitions and physical meaning". In: *IEEE Transactions on Power Delivery* 5.3 (1990), pp. 1377–1389. ISSN: 08858977. DOI: 10.1109/61.57980.

[emp22] emprimus. *Protecting the Power grid from solar Storms and Electromagnetic Pulse (EMP)*. 2022. URL: http://www.emprimus.com/.

[Eng20] C. Engelen. *Demganetization of 5-limb transformer cores: E-Mail*. Ed. by D. Albert. 08.09.2020.

[EP97] M. Elleuch and M. Poloujadoff. "A contribution to the modeling of the transformer joints using a new concept of equivalent variable air-gap length". In: *Acta Technica CSAV (Ceskoslovensk Akademie Ved)* 42.3 (1997), pp. 245–262. URL: https://www.scopus.com/inward/record.uri?eid=2-s2.0-0343295434&partnerID=40&md5=47ac7c121261179bb11699df4c7d6f70.

[EP98] M. Elleuch and M. Poloujadoff. "New transformer model including joint air gaps and lamination anisotropy". In: *IEEE Transactions on Magnetics* 34.5 (1998), pp. 3701–3711. ISSN: 0018-9464. DOI: 10.1109/20.718532.

[Eri+02] I. A. Erinmez, S. Majithia, C. Rogers, T. Yasuhiro, S. Ogawa, H. Swahn, and J. G. Kappenman. "Application of modelling techniques to assess geomagnetically induced current risks on the NGC transmission system". In: (2002). URL: https://e-cigre.org/publication/39-304_2002-application-of-modelling-techniques-to-assess-geomagnetically-induced-current-risks-on-the-ngc-transmission-system.

[Ero+10] E. A. Eroshenko, A. V. Belov, D. Boteler, S. P. Gaidash, S. L. Lobkov, R. Pirjola, and L. Trichtchenko. "Effects of strong geomagnetic storms on Northern railways in Russia". In: *Advances in Space Research* 46.9 (2010), pp. 1102–1110. ISSN: 02731177. DOI: 10.1016/j.asr.2010.05.017.

[Esc+07] R. Escarela-Perez, S. V. Kulkarni, N. K. Kodela, and J. C. Olivares-Galvan. "Asymmetry During Load-Loss Measurement of Three-Phase Three-Limb Transformers". In: *2007 IEEE Power Engineering Society general meeting*. Piscataway, NJ: IEEE Service Center, 2007, p. 1. ISBN: 1-4244-1296-X. DOI: 10.1109/PES.2007.386017.

[EUR21] EURISGIC. *GIC records*. 2021. URL: http://eurisgic.org/.

[Fax+17] F. R. Faxvog, G. Fuchs, W. Jensen, D. Wojtczak, M. B. Marz, and S. R. Dahman. *HV Power Transformer Neutral Blocking Device Operating Experience in Wisconsin*. 2017. URL: https://static1.squarespace.com/static/57bc8a4a414fb50147550a88/t/59fb4629084665d0199f607d/1509639730091/2017+11+07+

+HV+Power+Transformer+Neutral+Blocking+Device+%28NBD%29+Operating+Experience+in+Wisconsin.pdf.

[FBG14] R. A. D. Fiori, D. H. Boteler, and D. M. Gillies. "Assessment of GIC risk due to geomagnetic sudden commencements and identification of the current systems responsible". In: *Space Weather* 12.1 (2014), pp. 76–91. ISSN: 15427390. DOI: 10.1002/2013SW000967.

[Fer12] P. Fernberg. *One-Dimensional Earth Resistivity Models for Selected Areas of Continental United States and Alaska: EPRI Technical Update 1026430*. 2012. URL: http://jupiter.ethz.ch/~kuvshinov/For_Dima_Alexeev/150116_Relevant_Papers_for_Revision/1D_profiles_for_North_America.pdf (visited on 04/08/2019).

[FFM94] A. A. Fardoun, E. F. Fuchs, and M. Masoum. "Experimental analysis of a DC bucking motor blocking geomagnetically induced currents". In: *IEEE Transactions on Power Delivery* 9.1 (1994), pp. 88–99. ISSN: 08858977. DOI: 10.1109/61.277683.

[FL92] P. S. Filipski and P. W. Labaj. "Evaluation of reactive power meters in the presence of high harmonic distortion". In: *IEEE Transactions on Power Delivery* 7.4 (1992), pp. 1793–1799. ISSN: 08858977. DOI: 10.1109/61.156980.

[FLM01] A. Ferrero, S. Leva, and A. P. Morando. "An approach to the non-active power concept in terms of the poynting-park vector". In: *European Transactions on Electrical Power* 11.5 (2001), pp. 291–299. ISSN: 1430144X. DOI: 10.1002/etep.4450110503.

[Flu97] Fluke corporation. *80K-40 High Voltage Probe: Instruction Sheet*. Ed. by Fluke corporation. 1997. URL: https://docs.rs-online.com/1033/0900766b812677d9.pdf.

[FLZ06] S.-K. S. Fan, Y.-C. Liang, and E. Zahara. "A genetic algorithm and a particle swarm optimizer hybridized with Nelder–Mead simplex search". In: *Computers & Industrial Engineering* 50.4 (2006), pp. 401–425. ISSN: 03608352. DOI: 10.1016/j.cie.2005.01.022.

[Frö21] A. Fröhlich. "Versuchsaufbau zur präzisen Messung von Transformatorsternpunktströmen". Bachelor Thesis. Graz: Graz University of Technology, 2021.

[FS08] K. F. Forbes and O. C. St. Cyr. "Solar activity and economic fundamentals: Evidence from 12 geographically disparate power grids". In: *Space Weather* 6.10 (2008), pp. 1–20. ISSN: 15427390. DOI: 10.1029/2007SW000350.

[FS10] K. F. Forbes and O. C. St. Cyr. "An anatomy of space weather's electricity market impact: Case of the PJM power grid and the performance of its 500 kV transformers". In: *Space Weather* 8.9 (2010). ISSN: 15427390. DOI: 10.1029/2009SW000498.

[Fuc+14] K. Fuchs, A. Novitskiy, F. Berger, and D. Westermann. *Hochspannungsgleichstromübertragung - Eigenschaften des Übertragungsmediums Freileitung*. [Online-Ausg.] Vol. 7. Ilmenauer Beiträge zur elektrischen Energiesystem-, Geräte- und Anlagentechnik. Ilmenau: Univ.-Verl. Ilmenau, 2014. URL: https://www.db-thueringen.de/receive/dbt_mods_00023044.

[FWD82] K. Foster, F. E. Werner, and R. M. Del Vecchio. "Loss separation measurements for several electrical steels". In: *Journal of Applied Physics* 53.11 (1982), pp. 8308–8310. ISSN: 0021-8979. DOI: 10.1063/1.330350.

[FY02] E. F. Fuchs and Y. You. "Measurement of Psi-i characteristics of asymmetric three-phase transformers and their applications". In: *IEEE Power Engineering Review* 22.8 (2002), pp. 69–70. ISSN: 0272-1724. DOI: 10.1109/MPER.2002.4312518.

[FYR99] E. F. Fuchs, Y. You, and D. J. Roesler. "Modeling and simulation, and their validation of three-phase transformers with three legs under DC bias". In: *IEEE Transactions on Power Delivery* 14.2 (1999), pp. 443–449. ISSN: 08858977. DOI: 10.1109/61.754087.

[Gau14] C. T. Gaunt. "Reducing uncertainty – responses for electricity utilities to severe solar storms". In: *Journal of Space Weather and Space Climate* 4.4 (2014), A01. DOI: 10.1051/swsc/2013058.

[GD77] S. Glasstone and P. J. Dolan. *The Effects of Nuclear Weapons*. 3rd ed. U.S. Government Printing Office, 1977.

[GE 16] GE Grid Solutions. *COSI-CT: Optical Current transformer*. 2016. URL: https://www.gegridsolutions.com/products/brochures/grid-ga-l3-cosi_ct-0907-2016_07-en.pdf.

[GE18] G. G. González and M. Ehsani. "Power-Invariant Magnetic System Modeling". In: *International Journal of Magnetics and Electromagnetism* 4.1 (2018), pp. 1–9. DOI: 10.35840/2631-5068/6512.

[Gil+10] J. Gilbert, J. G. Kappenman, W. A. Radasky, and E. Savage. *The Late-Time (E3) High-Altitude Electromagnetic Pulse (HEMP) and Its Impact on the U.S. Power Grid*. Ed. by Metatech Corporation. 2010. URL: http://www.futurescience.com/emp/ferc_Meta-R-321.pdf.

[Gil+20] A. Gil, R. Modzelewska, S. Moskwa, A. Siluszyk, M. S., A. Wawrzynczak, M. Pozoga, and S. Domijanski. "Transmission Lines in Poland and Space Weather Effects". In: *Energies* 13.9 (2020), p. 2359. DOI: 10.3390/en13092359.

[GKS05] L. Gertmar, P. Karlsson, and O. Samuelsson. "On DC injection to AC grids from distributed generation". In: *European Conference on Power Electronics and Applications,*

2005. Piscataway, NJ: IEEE Service Center, 2005, pp. 1–10. ISBN: 90-75815-09-3. DOI: 10.1109/EPE.2005.219420.

[GLD18] N. Y. Ganushkina, M. W. Liemohn, and S. Dubyagin. "Current Systems in the Earth's Magnetosphere". In: *Reviews of Geophysics* 56.2 (2018), pp. 309–332. ISSN: 87551209. DOI: 10.1002/2017RG000590.

[GM01] J. Gyselinck and J. Melkebeek. "Two–dimensional finite element modelling of overlap joints in transformer cores". In: *COMPEL - The international journal for computation and mathematics in electrical and electronic engineering* 20.1 (2001), pp. 253–268. ISSN: 0332-1649. DOI: 10.1108/03321640110359976.

[GM12] C. T. Gaunt and M. Malengret. "Why we use the term non-active power, and how it can be measured under non-ideal power supply conditions". In: *IEEE Power Engineering Society [i.e. Power & Energy Society] conference and exposition in Africa (PowerAfrica), 2012*. Piscataway, NJ: IEEE, 2012, pp. 1–4. ISBN: 978-1-4673-2550-9. DOI: 10.1109/PowerAfrica.2012.6498641.

[Gra82] C. D. Graham. "Physical origin of losses in conducting ferromagnetic materials (invited)". In: *Journal of Applied Physics* 53.11 (1982), pp. 8276–8280. ISSN: 0021-8979. DOI: 10.1063/1.330306.

[Hal+14] T. Halbedl, H. Renner, M. Sakulin, and G. Achleitner. "Measurement and analysis of neutral point currents in a 400-kV-network". In: *2014 Electric Power Quality and Supply Reliability Conference (PQ)*. Piscataway, NJ: IEEE, 2014, pp. 65–68. ISBN: 978-1-4799-5022-5. DOI: 10.1109/PQ.2014.6866785.

[Hal+16] T. Halbedl, H. Renner, R. L. Bailey, R. Leonhardt, and G. Achleitner. "Analysis of the impact of geomagnetic disturbances on the Austrian transmission grid". In: *19th Power Systems Computation Conference*. Piscataway, NJ: IEEE, 2016, pp. 1–5. ISBN: 978-88-941051-2-4. DOI: 10.1109/PSCC.2016.7540833.

[Hal14] T. Halbedl. "Messung von Gleichströmen am Sternpunkt von Drehstromtransformatoren im Höchstspannungsnetz". Masterarbeit. Graz: Graz University of Technology, 2014.

[Hal19] T. Halbedl. "Low Frequency Neutral Point Currents on Transformer in the Austrian power Transmission Network". PhD Thesis. Graz: Graz University of Technology, 2019. URL: https://diglib.tugraz.at/download.php?id=5cc8220f5d096&location=browse (visited on 11/11/2021).

[Ham+17] P. Hamberger, G. Leber, H. Passath, H. Pregartner, and A.-K. Schrammel. "Messanordnung zum Erfassen eines magnetischen Gleichflusses im Kern eines Transformators - European Patent Office - EP 2952997 B1". EP 2 952 997 B1. 2017. URL: https:

//patentimages.storage.googleapis.com/ee/b4/e8/c743062828b620/EP2952997B1.pdf.

[Ham16] P. Hamberger. "Apparatus for reducing a magnetic unidirectional flux component in the core for a transformer". US 2016/0125999 A1. 2016. URL: https://patentimages.storage.googleapis.com/1d/1f/94/dd3b0b20572685/US20160125999A1.pdf.

[Ham93] D. C. Hamill. "Lumped equivalent circuits of magnetic components: the gyrator-capacitor approach". In: *IEEE Transactions on Power Electronics* 8.2 (1993), pp. 97–103. ISSN: 0885-8993. DOI: 10.1109/63.223957.

[Ham94] D. C. Hamill. "Gyrator-capacitor modeling: a better way of understanding magnetic components". In: *Conference proceedings 1994 / APEC '94, Ninth Annual Applied Power Electronics Conference and Exposition, February 13 - 17, 1994, Orlando, FL*. New York: Inst. of Electrical and Electronics Engineers, 13-17 Feb. 1994, pp. 326–332. ISBN: 0-7803-1456-5. DOI: 10.1109/APEC.1994.316381.

[HD21] M. Hayerikhiyavi and A. Dimitrovski. "Comprehensive Analysis of Continuously Variable Series Reactor Using G-C Framework". In: *2021 IEEE Power & Energy Society General Meeting (PESGM)*. Piscataway, NJ: IEEE, 2021, pp. 1–5. ISBN: 978-1-6654-0507-2. DOI: 10.1109/PESGM46819.2021.9637971.

[Hei+20] T. Heid, T. Neumeier, F. Renaud, M. VO, and M. Yanin. "Monitoring of asymmetric short circuit currents at a hydro power plant using electronic fibre optical current transformers: A3-223". In: *Cigre Session 48*. Ed. by Cigre. Paris, 2020. URL: https://e-cigre.org/publication/SESSION2020_A3-223.

[Her+18] H. Herterich, F. Klammler, P. Hamberger, and G. Leber. "Restoring efficiency, removing sound: Ready for DC in the grid with DC compensation and DC-ready transformers". In: *Transformers Magazine* 4 (2018), pp. 92–99. URL: https://hrcak.srce.hr/index.php?show=clanak&id_clanak_jezik=314150.

[Hey+17] M. J. Heyns, S. I. Lotz, P. J. Cilliers, and C. T. Gaunt. "Ensemble Estimation of Network Parameters: A Tool to Improve the Real-time Estimation of GICs in the South African Power Network". In: *The Proceedings of SAIP2017* (2017). URL: http://arxiv.org/pdf/1912.04742v1.

[HG90] F. Heppner and U. Grenander. "A stochastic nonlinear model for coordinated bird flocks". In: *The ubiquity of chaos* (1990).

[HL14] P. Hamberger and A. Leikermoser. "Verfahren und Vorrichtung zum Detektieren einer magnetischen Kenngröße in einem Kern". WO 2011/127969. 2014. URL: https://patentimages.storage.googleapis.com/34/f9/4a/9143f8e9ace166/EP2558875B1.pdf.

[HL93] G. S. Heinson and F. Lilley. "An application of thin-sheet electromagnetic modelling to the Tasman Sea". In: *Physics of the Earth and Planetary Interiors* 81.1-4 (1993), pp. 231–251. ISSN: 00319201. DOI: 10.1016/0031-9201(93)90133-T.

[Høi+09] H. K. Høidalen, B. A. Mork, F. Gonzalez, D. Ishchenko, and N. Chiesa. "Implementation and verification of the Hybrid Transformer model in ATPDraw". In: *Electric Power Systems Research* 79.3 (2009), pp. 454–459. ISSN: 03787796. DOI: 10.1016/j.epsr.2008.09.003.

[Hon+18] I. Honkonen, A. Kuvshinov, L. Rastätter, and A. Pulkkinen. "Predicting Global Ground Geoelectric Field With Coupled Geospace and Three-Dimensional Geomagnetic Induction Models". In: *Space Weather* 16.8 (2018), pp. 1028–1041. ISSN: 15427390. DOI: 10.1029/2018SW001859.

[Hor+03] W. Horton, R. S. Weigel, D. Vassiliadis, and I. Doxas. "Substorm classification with the WINDMI model". In: *Nonlinear Processes in Geophysics* 10.4/5 (2003), pp. 363–371. DOI: 10.5194/npg-10-363-2003.

[Hor+12] R. Horton, D. H. Boteler, T. J. Overbye, R. J. Pirjola, and R. C. Dugan. "A Test Case for the Calculation of Geomagnetically Induced Currents". In: *IEEE Transactions on Power Delivery* 27.4 (2012), pp. 2368–2373. ISSN: 08858977. DOI: 10.1109/TPWRD.2012.2206407.

[Hor+19] R. Horton, C. Perry, B. Leonhardi, B. Philipps, J. Snider, J. Butterfield, N. Bhatt, and B. M. Arritt. *High-altitude electromagnetic pulse and the bulk power system - potential impacts and mitigation strategies: Potential Impacts and Mitigation Strategies*. Ed. by EPRI. 2019. URL: https://www.epri.com/pages/product/3002014979/.

[Hor17] R. Horton. "The Potential for Long-Term and Large-Scale Disruptions to the Bulk–Power System". In: *Reliability Technical Conference*. Ed. by Federal Energy Regulatory Commission. 2017, pp. 1–9.

[HP19] H. K. Hoidalen and L. Prikler. *ATPDRAW Users' Manual: version 7.0 for Windows*. 2019.

[HR21] H. K. Høidalen and A. C. Rocha. "Analysis of gray Box Modelling of Transformers". In: *Electric Power Systems Research* 197 (2021), p. 107266. ISSN: 03787796. DOI: 10.1016/j.epsr.2021.107266.

[HRA18] T. Halbedl, H. Renner, and G. Achleitner. *Geomagnetically induced currents modelling and monitoring transformer neutral currents in Austria*. 2018. URL: https://link.springer.com/content/pdf/10.1007%2Fs00502-018-0665-9.pdf.

[Hug+22] J. Hughes, R. Mcgranaghan, A. C. Kellerman, J. Bortnik, R. F. Arrit, K. Venkataramani, C. H. Perry, J. McCormick, C. M. Ngwira, and M. Cohen. "Revealing Novel Connections

Between Space Weather and the Power Grid: Network Analysis of Ground–Based Magnetometer and Geomagnetically Induced Currents (GIC) Measurements". In: *Space Weather* 20.2 (2022). ISSN: 15427390. DOI: 10.1029/2021SW002727.

[Hut+08] K. E. J. Huttunen, S. P. Kilpua, A. Pulkkinen, A. Viljanen, and E. Tanskanen. "Solar wind drivers of large geomagnetically induced currents during the solar cycle 23". In: *Space Weather* 6.10 (2008). ISSN: 15427390. DOI: 10.1029/2007SW000374.

[IEC01a] IEC. *International Standard 60422:2013 Mineral insulating oils in electrical equipment – Supervision and maintenance guidance*. Vienna, 2013-12-01.

[IEC01b] IEC. *International Standard 61936-1:2021 Power installations exceeding 1 kV AC and 1,5 kV DC – Part 1: A*. 2021-07-01.

[IEC01c] IEC. *International Standard IEC 61672-1:2013 Electroacoustics – Sound level meters Part 1: Specifications*. Vienna, 2015-08-01. URL: https://effects.austrian-standards.at/action/effectsDownload/547593/4/OEVE_OENORM_EN_61672-1_2015_08_01_en.pdf.

[IEC01d] IEC. *Power Transformers - Part 23: DC magnetic bia ssuppression devices*. 2018-01.

[IEC07a] IEC. *International Standard 60076-18:2012 Power transformers - Part 18: Measurement of frequency response*. 2012-07.

[IEC07b] IEC. *International Standard 60076-3:2014 Power transformers - Part 3: Insulation levels, dielectric tests and external clearances in air*. 2013-07. URL: https://www.vde-verlag.de/iec-normen/preview-pdf/info_iec60076-3%7Bed3.0%7Db.pdf.

[IEC09] IEC. *International Standard 60404-2:2009 Magnetic materials – Part 2: Methods of measurement of the magnetic properties of electrical steel sheet and strip by means of an Epstein frame*. Berlin, 2009. DOI: 10.31030/1495294.

[IEC12a] IEC. *International Standard 60076-1:2012 Power Transformers - Part1: General: (IEC 60076-1:2011)*. Vienna, 2012.

[IEC12b] IEC. *International Standard 61869-2:2012 Instrument transformers - Part 2: Additional requirements for current transformers*. 2012. URL: https://www.vde-verlag.de/iec-normen/preview-pdf/info_iec61869-2%7Bed1.0%7Db.pdf.

[IEC21] IEC. *International Standard 61000-2-10:2021 Electromagnetic compatibility (EMC) - Part 2-10: Environment - Description of HEMP environment - Conducted disturbance*. 2021. URL: https://effects.austrian-standards.at/action/de/private/details/1163372/IEC_61000-2-10_2021_Ed__2_0_2021_11_18.

[IEC97] IEC. *International Standard 60076-8: 1997 Power transformers - Application guide*. 1997.

[IEE03] IEEE. *IEEE Standard for Interconnecting Distributed Resources with Electric Power Systems*. Piscataway, NJ, USA, 2003. DOI: 10.1109/IEEESTD.2003.94285.

[IEE13] IEEE. *IEEE Guide for Diagnostic Field Testing of Fluid-Filled Power Transformers, Regulators, and Reactors*. Piscataway, NJ, USA, 2013. DOI: 10.1109/IEEESTD.2013.6544533.

[IEE15] IEEE Standard Association. *IEEE Guide for Safety in AC Substation Grounding: IEEE Power and Energy Society*. Piscataway, NJ, USA, 2015. DOI: 10.1109/IEEESTD.2015.7109078.

[III10] IEEE Power Engineering Society, Institute of Electrical and Electronics Engineers, and IEEE-SA Standards Board. *IEEE standard definitions for the measurement of electric power quantities under sinusoidal, nonsinusoidal, balanced, or unbalanced conditions: 1459-2010*. New York, 2010. DOI: 10.1109/IEEESTD.2010.5439063.

[Int18] Intermagnet. *Intermagnet*. 2018. URL: http://www.intermagnet.org/index-eng.php (visited on 11/12/2018).

[Isa14] Isabellenhütte Heusler GmbH & Co. KG. *MANGANIN*. 2014. URL: https://www.isabellenhuette.de/fileadmin/Daten/Praezisionslegierungen/Datenblaetter_Widerstand/MANGANIN.pdf.

[Iva+18] E. Ivannikova, M. Kruglyakov, A. Kuvshinov, L. Rastätter, and A. Pulkkinen. "Regional 3-D Modeling of Ground Electromagnetic Field Due To Realistic Geomagnetic Disturbances". In: *Space Weather* 16.5 (2018), pp. 476–500. ISSN: 15427390. DOI: 10.1002/2017SW001793.

[JA84] D. C. Jiles and D. L. Atherton. "Theory of ferromagnetic hysteresis (invited)". In: *Journal of Applied Physics* 55.6 (1984), pp. 2115–2120. ISSN: 0021-8979. DOI: 10.1063/1.333582.

[Jaz+13a] S. Jazebi, A. Farazmand, B. P. Murali, and F. de Leon. "A Comparative Study on pi and T Equivalent Models for the Analysis of Transformer Ferroresonance". In: *IEEE Transactions on Power Delivery* 28.1 (2013), pp. 526–528. ISSN: 1937-4208. DOI: 10.1109/TPWRD.2012.2220637.

[Jaz+13b] S. Jazebi, F. de Leon, A. Farazmand, and D. Deswal. "Dual Reversible Transformer Model for the Calculation of Low-Frequency Transients". In: *IEEE Transactions on Power Delivery* 28.4 (2013), pp. 2509–2517. ISSN: 1937-4208. DOI: 10.1109/TPWRD.2013.2268857.

[Joi95] Joint Committee for Guides in Metrology. *Guide to the expression of uncertainty in measurement*. 1. ed., corr. and reprinted. Genève, 1995. ISBN: 9267101889.

[JTD92] D. C. Jiles, J. B. Thoelke, and M. K. Devine. "Numerical determination of hysteresis parameters for the modeling of magnetic properties using the theory of ferromagnetic hysteresis". In: *IEEE Transactions on Magnetics* 28.1 (1992), pp. 27–35. ISSN: 0018-9464. DOI: 10.1109/20.119813.

[Kam+16] M. Kamel, H. Saeed, A. Karrar, A. Eltom, M. Bowman, T. Womack, and P. Cooper. "On-site low voltage determination of zero sequence impedances for station auxiliary transformers". In: *2016 IEEE Power and Energy Society General Meeting (PESGM)*. Piscataway, NJ: IEEE, 2016, pp. 1–5. ISBN: 978-1-5090-4168-8. DOI: 10.1109/PESGM.2016.7741771.

[Kap06] J. G. Kappenman. "Great geomagnetic storms and extreme impulsive geomagnetic field disturbance events – An analysis of observational evidence including the great storm of May 1921". In: *Advances in Space Research* 38.2 (2006), pp. 188–199. ISSN: 02731177. DOI: 10.1016/j.asr.2005.08.055.

[Kaz+15] M. Kazerooni, T. Hutchins, T. J. Overbye, and H. Zhu. *Use of PMU Data for Geomagnetic Distrubance Model Validation*. 2015. URL: https://www.naspi.org/sites/default/files/2016-09/07%20-%20Naspi%20pres_032115.pdf.

[KE27] J. Kennedy and R. Eberhart. "Particle swarm optimization". In: *Proceedings / 1995 IEEE International Conference on Neural Networks*. Piscataway, NJ: IEEE, 1995-11-27, pp. 1942–1948. ISBN: 0-7803-2768-3. DOI: 10.1109/ICNN.1995.488968.

[Kel+17] G. S. Kelly, A. Viljanen, C. D. Beggan, and A. Thomson. "Understanding GIC in the UK and French high-voltage transmission systems during severe magnetic storms". In: *Space Weather* 15.1 (2017), pp. 99–114. ISSN: 15427390. DOI: 10.1002/2016SW001469.

[Kel+21] A. C. Kellerman, R. Mcgranaghan, J. Bortnik, B. A. Carter, J. Hughes, R. F. Arritt, K. Venkataramani, C. H. Perry, J. McCormick, C. M. Ngwira, M. Cohen, and J. Yue. "Geomagnetically Induced Currents at Middle Latitudes: 1. Quiet–time Variability". In: *Space Weather* (2021). ISSN: 15427390. DOI: 10.1029/2021SW002729.

[Khu+22] Z. M. Khurshid, N. F. Ab Aziz, Z. A. Rhazali, and M. Z. A. Ab Kadir. "Effect of GIC Neutral Blocking Devices (NBDs) on Power Network Ferroresonance in Malaysia". In: *IEEE Access* 10 (2022), pp. 77225–77238. ISSN: 2169-3536. DOI: 10.1109/ACCESS.2022.3184424.

[Kis06] P. Kis. "Jiles-Atherton Model implementation to Edge Finite Element Method". PhD Thesis. Budapest: Budapest University of Technology and Economics, 2006.

URL: https://repozitorium.omikk.bme.hu/bitstream/handle/10890/563/ertekezes.pdf;sequence=1.

[KK13] S. V. Kulkarni and S. A. Khaparde. *Transformer engineering: Design, technology, and diagnostics*. 2. ed. Boca Raton, Fla.: CRC Press, 2013. ISBN: 9781439854181.

[KL20] A. Kelbert and G. M. Lucas. "Modified GIC Estimation Using 3–D Earth Conductivity". In: *Space Weather* 18.8 (2020). ISSN: 15427390. DOI: 10.1029/2020SW002467.

[Kni+16] D. J. Knipp, A. C. Ramsay, E. D. Beard, A. L. Boright, W. B. Cade, I. M. Hewins, R. H. McFadden, W. F. Denig, L. M. Kilcommons, M. A. Shea, and D. F. Smart. "The May 1967 great storm and radio disruption event: Extreme space weather and extraordinary responses". In: *Space Weather* 14.9 (2016), pp. 614–633. ISSN: 15427390. DOI: 10.1002/2016SW001423.

[Kov+11] B. Kovan, F. de Leon, C. Czarkowski, Z. Zabar, and L. Birenbaum. "Mitigation of Inrush Currents in Network Transformers by Reducing the Residual Flux With an Ultra-Low-Frequency Power Source". In: *IEEE Transactions on Power Delivery* 26.3 (2011), pp. 1563–1570. ISSN: 1937-4208. DOI: 10.1109/TPWRD.2010.2102778.

[KW18] H. Kirkham and D. R. White. "Reactive Power and GIC: the Problems of an Unrecognized Operationalist Measurement". In: *AMPS 2018*. Piscataway, NJ, USA: IEEE, 2018, pp. 1–6. ISBN: 978-1-5386-5375-3. DOI: 10.1109/AMPS.2018.8494870.

[KZO18] M. Kazerooni, H. Zhu, and T. J. Overbye. "Mitigation of Geomagnetically Induced Currents Using Corrective Line Switching". In: *IEEE Transactions on Power Systems* 33.3 (2018), pp. 2563–2571. ISSN: 0885-8950. DOI: 10.1109/TPWRS.2017.2753840.

[Lan01] L. J. Lanzerotti. "Space Weather Effects on Technologies". In: *Space Weather (eds P. Song, H.J. Singer and G.L. Siscoe)*. (2001), pp. 11–22. DOI: 10.1029/GM125p0011.

[LAT85] J. R. Legro, N. C. Abi-Samra, and F. M. Tesche. "Study to assess the effects of magnetohydrodynamic electromagnetic pulse on electric power systems. Phase I, final report. Volume 3". In: (1985). URL: https://www.osti.gov/biblio/5768774,%20journal%20=.

[LBP20] C. Liu, D. H. Boteler, and R. J. Pirjola. "Influence of shield wires on geomagnetically induced currents in power systems". In: *International Journal of Electrical Power and Energy Systems* 117 (2020), p. 105653. ISSN: 01420615. DOI: 10.1016/j.ijepes.2019.105653.

[LC89] E. Lombardini and G. Cariani. "EMC/NEMP technology from military applications to telecommunications". In: *Conference Proceedings., Eleventh International Telecommunications Energy Conference*. IEEE, 15-18 Oct. 1989, pp. 13.1/1–13.110. DOI: 10.1109/INTLEC.1989.88294.

[LCF90] M. Lockwood, S. W. H. Cowley, and M. P. Freeman. "The excitation of plasma convection in the high-latitude ionosphere". In: *Journal of Geophysical Research: Space Physics* 95.A6 (1990), p. 7961. ISSN: 01480227. DOI: 10.1029/JA095iA06p07961.

[LE02] M. Lahtinen and J. Elovaara. "GIC occurrences and GIC test for 400 kV system transformer". In: *IEEE Transactions on Power Delivery* 17.2 (2002), pp. 555–561. ISSN: 08858977. DOI: 10.1109/61.997938.

[Led+99] D. Lederer, H. Igarashi, A. Kost, and T. Honma. "On the parameter identification and application of the Jiles-Atherton hysteresis model for numerical modelling of measured characteristics". In: *IEEE Transactions on Magnetics* 35.3 (1999), pp. 1211–1214. ISSN: 0018-9464. DOI: 10.1109/20.767167.

[LEM20a] LEM. *LEM IT 65-S ULTRASTAB*. 2020. URL: https://www.lem.com/en/it-65s-ultrastab.

[LEM20b] LEM. "LF 306-S". In: (2020). URL: https://www.lem.com/sites/default/files/products_datasheets/lf%20306-s%20e.pdf.

[LEM20c] LEM. *LA 200-SD/SP3*. 30.11.2020. URL: https://www.lem.com/en/la-200sdsp3.

[Len+20] M. Lenner, A. Frank, L. Yang, T. M. Roininen, and K. Bohnert. "Long-Term Reliability of Fiber-Optic Current Sensors". In: *IEEE Sensors Journal* 20.2 (2020), pp. 823–832. ISSN: 1530-437X. DOI: 10.1109/JSEN.2019.2944346.

[Leo+15] F. de Leon, A. Farazmand, S. Jazebi, D. Deswal, and R. Levi. "Elimination of Residual Flux in Transformers by the Application of an Alternating Polarity DC Voltage Source". In: *IEEE Transactions on Power Delivery* 30.4 (2015), pp. 1727–1734. ISSN: 1937-4208. DOI: 10.1109/TPWRD.2014.2377199.

[Leo+20] R. Leonhardt, R. Egli, B. Leichter, I. Herzog, R. Kornfeld, R. L. Bailey, N. Kompein, P. Arneitz, R. Mandl, and R. Steiner. *Conrad Observatory, GMO Bulletin 6*. 2020. DOI: 10.13140/RG.2.2.13444.45443.

[LFJ12] F. de Leon, A. Farazmand, and P. Joseph. "Comparing the T and pi Equivalent Circuits for the Calculation of Transformer Inrush Currents". In: *IEEE Transactions on Power Delivery* 27.4 (2012), pp. 2390–2398. ISSN: 1937-4208. DOI: 10.1109/TPWRD.2012.2208229.

[LGK18] A. J. C. Lackey, R. A. Goubran, and F. Kwamena. "Geomagnetically induced current measurement using an integrated magnetometer platform". In: *2018 IEEE Sensors Applications Symposium*. Ed. by I. S. A. Symposium. Piscataway, NJ: IEEE, 2018, pp. 1–6. ISBN: 978-1-5386-2092-2. DOI: 10.1109/SAS.2018.8336773.

[LHC16] Lotfi, A., H. K. Høidalen, and N. Chiesa. "Effect of DC biasing in 3-legged 3-phase transformers taking detailed model of off-core path into account". In: *Electric Power Systems Research* 138 (2016), pp. 18–24. ISSN: 03787796. DOI: 10.1016/j.epsr.2016.01.015.

[Lid96] D. R. Lide, ed. *CRC handbook of chemistry and physics: A ready-reference book of chemical and physical data*. 76. ed. Boca Raton: CRC Press, 1996. ISBN: 0849305977.

[Liu+09] C.-M. Liu, L.-G. Liu, R. J. Pirjola, and Z.-Z. Wang. "Calculation of geomagnetically induced currents in mid- to low-latitude power grids based on the plane wave method: A preliminary case study". In: *Space Weather* 7.4 (2009). ISSN: 15427390. DOI: 10.1029/2008SW000439.

[LLK18] G. M. Lucas, J. J. Love, and A. Kelbert. "Calculation of Voltages in Electric Power Transmission Lines During Historic Geomagnetic Storms: An Investigation Using Realistic Earth Impedances". In: *Space Weather* 16.2 (2018), pp. 185–195. ISSN: 15427390. DOI: 10.1002/2017SW001779.

[Lot+16] Lotfi, A., Zirka, S., Y. Moroz, N. Chiesa, and B. A. Mork. "Benchmarking of hysteretic elements in topological transformer model". In: *Electric Power Systems Research* 138 (2016), pp. 33–40. ISSN: 03787796. DOI: 10.1016/j.epsr.2016.02.030.

[Lov12] J. J. Love. "Credible occurrence probabilities for extreme geophysical events: Earthquakes, volcanic eruptions, magnetic storms". In: *Geophysical Research Letters* 39.10 (2012), n/a–n/a. ISSN: 00948276. DOI: 10.1029/2012GL051431.

[LPA00] F. Liorzou, B. Phelps, and D. L. Atherton. "Macroscopic models of magnetization". In: *IEEE Transactions on Magnetics* 36.2 (2000), pp. 418–428. ISSN: 0018-9464. DOI: 10.1109/20.825802.

[LQC12] F. de Leon, L. Qaseer, and J. Cohen. "AC Power Theory From Poynting Theorem: Identification of the Power Components of Magnetic Saturating and Hysteretic Circuits". In: *IEEE Transactions on Power Delivery* 27.3 (2012), pp. 1548–1556. ISSN: 1937-4208. DOI: 10.1109/TPWRD.2012.2188652.

[Lun06] H. Lundstedt. "The sun, space weather and GIC effects in Sweden". In: *Advances in Space Research* 37.6 (2006), pp. 1182–1191. ISSN: 02731177. DOI: 10.1016/j.asr.2005.10.023.

[Lur08] A. I. Lur'e. "Transformer connection under no-load and short-circuit events". In: *Russian Electrical Engineering* 79.2 (2008), pp. 57–70. ISSN: 1068-3712. DOI: 10.3103/S1068371208020016.

[LWB89] E. V. Larsen, R. A. Walling, and C. J. Bridenbaugh. "Parallel AC/DC transmission lines steady-state induction issues". In: *IEEE Transactions on Power Delivery* 4.1 (1989), pp. 667–674. ISSN: 08858977. DOI: 10.1109/61.19259.

[LY12] Liu and M.-T. Yang. "A New Hybrid Nelder-Mead Particle Swarm Optimization for Coordination Optimization of Directional Overcurrent Relays". In: *Mathematical Problems in Engineering* 2012 (2012), pp. 1–18. ISSN: 1024-123X. DOI: 10.1155/2012/456047.

[Mad+19] A. Madaschi, M. Brunero, M. Ferrario, P. Martelli, P. Boffi, and M. Martinelli. "N-Matrix Jones Analysis of a Fiber-Optic Current Sensor". In: *2019 CLEO/Europe - EQEC Conference Digest*. [S. l.]: IEEE, 2019, p. 1. ISBN: 978-1-7281-0469-0. DOI: 10.1109/CLEOE-EQEC.2019.8873093.

[Mah12] J. Mahseredjian. *Literature survey on transformer models for the simulation of eletromagnetic transients with emphasis on geomagnetic-induced currents (GIC) aplications: 1025844*. 2012.

[Man+21] J. M. Mandl, R. Klammbauer, A. Bergmann, D. Albert, P. Schachinger, and H. Renner. *FORESEEN - Fiber Optical Current Measurement*. Ed. by Graz University of Technology. 2021. URL: https://online.tugraz.at/tug_online/fdb_detail.ansicht?cvfanr=F46970&cvorgnr=37&sprache=1.

[Mar+12] R. A. Marshall, M. Dalzell, C. L. Waters, P. Goldthorpe, and E. A. Smith. "Geomagnetically induced currents in the New Zealand power network". In: *Space Weather* 10.8 (2012), pp. 1–13. ISSN: 15427390. DOI: 10.1029/2012SW000806.

[Mar+13] R. A. Marshall, H. Gorniak, T. van der Walt, C. L. Waters, M. d. Sciffer, M. Miller, M. Dalzell, T. Daly, G. Pouferis, G. Hesse, and P. Wilkinson. "Observations of geomagnetically induced currents in the Australian power network". In: *Space Weather* 11.1 (2013), pp. 6–16. ISSN: 15427390. DOI: 10.1029/2012SW000849.

[Mar+17] R. A. Marshall, A. Kelly, T. van der Walt, A. Honecker, C. Ong, D. Mikkelsen, A. Spierings, G. Ivanovich, and A. Yoshikawa. "Modeling geomagnetic induced currents in Australian power networks". In: *Space Weather* 15.7 (2017), pp. 895–916. ISSN: 15427390. DOI: 10.1002/2017SW001613.

[Mat+21a] A. Matthee, P. W. Futter, R. Vogt-Ardatjew, and F. Leferink. "Lightning Strike EMP Effect On Local Grids". In: *2021 Asia-Pacific International Symposium on Electromagnetic Compatibility (APEMC)*. IEEE, 9/27/2021 - 9/30/2021, pp. 1–4. ISBN: 978-1-7281-7621-5. DOI: 10.1109/APEMC49932.2021.9596729.

[Mat+21b] J. Matzka, C. Stolle, Y. Yamazaki, O. Bronkalla, and A. Morschhauser. "The Geomagnetic Kp Index and Derived Indices of Geomagnetic Activity". In: *Space Weather* 19.5 (2021). ISSN: 15427390. DOI: 10.1029/2020SW002641.

[Mat+21c] J. Matzka, O. Bronkalla, K. Tornow, K. Elger, and C. Stolle. *Geomagnetic Kp index*. 2021. DOI: 10.5880/KP.0001.

[Mat22] MathWorks. *Calculate single-phase real and reactive power - Simulink*. 2022. URL: https://de.mathworks.com/help/physmod/sps/ref/powermeasurement.html.

[May03] I. D. Mayergoyz. *Mathematical models of hysteresis and their applications*. 1st ed. Elsevier series in electromagnetism. Amsterdam and Boston: Elsevier, 2003. ISBN: 9780124808737. DOI: 10.1016/B978-0-12-480873-7.X5000-2.

[MB02] S. Mohr and T. Bosselmann. "A high dynamic magnetooptic current transformer with optimized signal processing". In: *Proceedings of IEEE sensors 2002*. Piscataway, NJ: IEEE Operations Center, 2002, pp. 1354–1359. ISBN: 0-7803-7454-1. DOI: 10.1109/ICSENS.2002.1037317.

[McI+20] S. W. McIntosh, S. Chapman, R. J. Leamon, R. Egeland, and N. W. Watkins. "Overlapping Magnetic Activity Cycles and the Sunspot Number: Forecasting Sunspot Cycle 25 Amplitude". In: *Solar Physics* 295.12 (2020), pp. 1–14. ISSN: 1573-093X. DOI: 10.1007/s11207-020-01723-y.

[McK03] A. J. McKay. "Geoelectric Fields and Geomagnetically Induced Currents in the United Kingdom". PhD Thesis. Edinburgh, England: University of Edinburgh, 2003. URL: http://hdl.handle.net/1842/639.

[McN90] W. J. McNutt, ed. *The Effect of GIC on Power Transformers: Special Panel Session Report "Geomagnetically Storm Cycle 22: Power System Problems on the Horizon,"* 1990.

[Mel13] Melexis. *Melexis MLX91205 Datasheet*. 2013. URL: https://media.melexis.com/-/media/files/documents/datasheets/mlx91205-datasheet-melexis.pdf?la=en.

[Mes15] D. Meschede. *Gerthsen Physik*. 25. Aufl. Springer-Lehrbuch. Berlin: Springer Spektrum, 2015. ISBN: 9783662459768. DOI: 10.1007/978-3-662-45977-5.

[Mey17] M. Meyer. *Signalverarbeitung: Analoge und digitale Signale, Systeme und Filter*. 8., verbesserte Auflage. Lehrbuch. Wiesbaden: Springer Vieweg, 2017. ISBN: 9783658183202. DOI: 10.1007/978-3-658-18321-9.

[MGI05] B. A. Mork, F. Gonzalez, and D. Ishchenko. "Leakage Inductance Model for Autotransformer Transient Simulation". In: *IPST - International Conference on Power Systems Transients*. 2005. URL: https://www.ipstconf.org/papers/Proc_IPST2005/05IPST248.pdf.

[Min+17] T. Minteer, T. Mooney, S. Artz, and D. E. Whitehead. "Understanding design, installation, and testing methods that promote substation IED resiliency for high-altitude electromagnetic pulse events". In: *70th Annual Conference for Protective Relay Engineers*. Piscataway, NJ: IEEE, 2017, pp. 1–18. ISBN: 978-1-5386-1581-2. DOI: 10.1109/CPRE.2017.8090057.

[ML92] J. C. Moreira and T. A. Lipo. "Modeling of saturated AC machines including air gap flux harmonic components". In: *IEEE Transactions on Industry Applications* 28.2 (1992), pp. 343–349. ISSN: 1939-9367. DOI: 10.1109/28.126740.

[MM05] J. A. Martinez and B. A. Mork. "Transformer Modeling for Low- and Mid-Frequency Transients—A Review". In: *IEEE Transactions on Power Delivery* 20.2 (2005), pp. 1625–1632. ISSN: 08858977. DOI: 10.1109/TPWRD.2004.833884.

[MN21] F. Müllner and H. Neudorfer. "Semi-empirisches Hysteresemodell für Elektroblech mit Berücksichtigung von Oberschwingungen und hoher Sättigung". In: *e & i Elektrotechnik und Informationstechnik* 138.2 (2021), pp. 70–77. ISSN: 1613-7620. DOI: 10.1007/s00502-021-00871-8.

[Mol02] T. S. Molinski. "Why utilities respect geomagnetically induced currents". In: *Journal of Atmospheric and Solar-Terrestrial Physics* 64.16 (2002), pp. 1765–1778. ISSN: 13646826. DOI: 10.1016/S1364-6826(02)00126-8.

[Mor+07] B. A. Mork, F. Gonzalez, D. Ishchenko, D. L. Stuehm, and J. Mitra. "Hybrid Transformer Model for Transient Simulation—Part I: Development and Parameters". In: *IEEE Transactions on Power Delivery* 22.1 (2007), pp. 248–255. ISSN: 08858977. DOI: 10.1109/TPWRD.2006.883000.

[MRB14] L. Marti, A. Rezaei-Zare, and D. H. Boteler. "Calculation of Induced Electric Field During a Geomagnetic Storm Using Recursive Convolution". In: *IEEE Transactions on Power Delivery* 29.2 (2014), pp. 802–807. ISSN: 08858977. DOI: 10.1109/TPWRD.2013.2273833.

[Myl+14] M. Myllys, A. Viljanen, Ø. A. Rui, and T. M. Ohnstad. "Geomagnetically induced currents in Norway: the northernmost high-voltage power grid in the world". In: *Journal of Space Weather and Space Climate* 4 (2014), A10. DOI: 10.1051/swsc/2014007.

[Nak+18] S. Nakamura, Y. Ebihara, S. Fujita, T. Goto, N. Yamada, S. Watari, and Y. Omura. "Time Domain Simulation of Geomagnetically Induced Current (GIC) Flowing in 500-kV

Power Grid in Japan Including a Three-Dimensional Ground Inhomogeneity". In: *Space Weather* 66.1 (2018), p. 164. ISSN: 15427390. DOI: 10.1029/2018SW002004.

[Nan+88] J. E. Nanevicz, E. F. Vance, W. Radasky, M. A. Uman, G. K. Soper, and J. Ma Pierre. "EMP susceptibility insights from aircraft exposure to lightning". In: *IEEE Transactions on Electromagnetic Compatibility* 30.4 (1988), pp. 463–472. ISSN: 0018-9375. DOI: 10.1109/15.8760.

[Nar16] K. Narendra. *White Paper on "Wide Area Real Time GIC Monitoring using TESLA Phasor Measurement Unit (PMU)"*. 2016. DOI: 10.13140/RG.2.1.4024.2168.

[Nas17] Nasa. *Earth Magnetosphasere*. 2017. URL: https://www.nasa.gov/sites/default/files/images/470162main_magnetosphere-orig_full.jpg.

[Ngn+12] T. Ngnegueu, F. Marketos, F. Devaux, T. Xu, R. Bardsley, and S. Barker. "Behaviour of transformers under DC/GIC excitation: Phenomenon, Impact on design/design evaluation process and Modelling aspects in support of Design". In: *Cigre Session 2012*. Ed. by Cigre. 2012.

[Ngw+09] C. M. Ngwira, L.-A. McKinnell, P. J. Cilliers, A. Viljanen, and R. J. Pirjola. "Limitations of the modeling of geomagnetically induced currents in the South African power network". In: *Space Weather* 7.10 (2009). ISSN: 15427390. DOI: 10.1029/2009SW000478.

[NM65] J. A. Nelder and R. Mead. "A Simplex Method for Function Minimization". In: *The Computer Journal* 7.4 (1965), pp. 308–313. ISSN: 0010-4620. DOI: 10.1093/comjnl/7.4.308.

[NN20] National Centers for Environmental Information (NCEI) and National Centers for Environmental Information (NCEI). *World Magnetic Model - Maps of Magnetic Elements*. 2020. URL: https://www.ngdc.noaa.gov/geomag/WMM/image.shtml.

[NOA20] NOAA. *NOAA / NWS Space Weather Prediction Center*. 2020. URL: https://www.swpc.noaa.gov/.

[Nos+15] Nose Masahito, Sugiura Masahisa, Kamei Toyohisa, Iyemori Toshihiko, and Koyama Yukinobu. *Dst Index*. 2015. DOI: 10.17593/14515-74000.

[ODA22] A. Ovalle, R. Dugan, and R. Arritt. "GICharm: A System Level Analysis Tool for Geomagnetic Disturbance Related Harmonics". In: *IEEE Transactions on Industry Applications* 58.2 (2022), pp. 1406–1415. ISSN: 1939-9367. DOI: 10.1109/TIA.2022.3145770.

[OMe83] K. O'Meara. "Passive balancing of transformer flux in power converters". In: *Proceedings of Powercon: International Solid-State Power Electronics Conference* (1983). URL:

https://www.scopus.com/inward/record.uri?eid=2-s2.0-0020941384&partnerID=40&md5=752bb922a4cb3636da306383fb5ab17e.

[OO18] K. C. Okpala and C. E. Ogbonna. "On the mid-latitude ionospheric storm association with intense geomagnetic storms". In: *Advances in Space Research* 61.7 (2018), pp. 1858–1872. ISSN: 02731177. DOI: 10.1016/j.asr.2017.08.017.

[Ort+14] G. Ortiz, L. Fassler, J. W. Kolar, and O. Apeldoorn. "Flux Balancing of Isolation Transformers and Application of "The Magnetic Ear" for Closed-Loop Volt–Second Compensation". In: *IEEE Transactions on Power Electronics* 29.8 (2014), pp. 4078–4090. ISSN: 0885-8993. DOI: 10.1109/TPEL.2013.2294551.

[Ove+22] T. J. Overbye, J. Snodgrass, A. Birchfield, and M. Stevens. "Towards Developing Implementable High Altitude Electromagnetic Pulse E3 Mitigation Strategies for Large-Scale Electric Grids". In: *2022 IEEE Texas Power and Energy Conference (TPEC)*. [Piscataway, New Jersey]: IEEE, 2022, pp. 1–6. ISBN: 978-1-6654-7902-8. DOI: 10.1109/TPEC54980.2022.9750778.

[Pal+22] C. I. Paleari, F. Mekhaldi, F. Adolphi, M. Christl, C. Vockenhuber, P. Gautschi, J. Beer, N. Brehm, T. Erhardt, H.-A. Synal, L. Wacker, F. Wilhelms, and R. Muscheler. "Cosmogenic radionuclides reveal an extreme solar particle storm near a solar minimum 9125 years BP". In: *Nature communications* 13.1 (2022), p. 214. DOI: 10.1038/s41467-021-27891-4.

[PB04] G. W. Prölss and M. K. Bird. *Physics of the Earth's space environment: An introduction*. Berlin: Springer, 2004. ISBN: 3540214267.

[PDM95] D. A. Philips, L. R. Dupre, and J. A. Melkebeek. "Comparison of Jiles and Preisach hysteresis models in magnetodynamics". In: *IEEE Transactions on Magnetics* 31.6 (1995), pp. 3551–3553. ISSN: 0018-9464. DOI: 10.1109/20.489566.

[PE05] A. Pulkkinen and M. Engels. "The role of 3-D geomagnetic induction in the determination of the ionospheric currents from the ground geomagnetic data". In: *Annales Geophysicae* 23.3 (2005), pp. 909–917. DOI: 10.5194/angeo-23-909-2005.

[PHF18] M. Pfeiffer, S. Hedtke, and C. M. Franck. "Corona Current Coupling in Bipolar HVDC and Hybrid HVAC/HVDC Overhead Lines". In: *IEEE Transactions on Power Delivery* 33.1 (2018), pp. 393–402. ISSN: 08858977. DOI: 10.1109/TPWRD.2017.2713603.

[Phi14] T. Philips. *Near Miss: The Solar Superstorm of July 2012*. 2014. URL: https://science.nasa.gov/science-news/science-at-nasa/2014/23jul_superstorm.

[Pir82] R. Pirjola. "Electromagnetic induction in the earth by a plane wave or by fields of line currents harmonic in time and space". Phd Thesis. Helsinki: Finnish Meteorological Institute, 1982.

[Pir89] R. Pirjola. "Geomagnetically induced currents in the Finnish 400 kV power transmission system". In: *Physics of the Earth and Planetary Interiors* 53.3-4 (1989), pp. 214–220. ISSN: 00319201. DOI: 10.1016/0031-9201(89)90005-8.

[Plo19] C. Ploetner. *Power transformer audible sound requirements: Interim Report prepared by Christoph Ploetner (Convenor): WG A2.54 Report*. 2019. URL: https://e-cigre.org/publication/WGR_302_1-power-transformer-audible-sound-requirements.

[Pre35] F. Preisach. "Über die magnetische Nachwirkung". In: *Zeitschrift fr Physik* 94.5-6 (1935), pp. 277–302. ISSN: 1434-6001. DOI: 10.1007/BF01349418.

[Pre83] A. Prechtl. *Dynamik elektromechanischer Systeme: Vorlesung im Wintersemester 1983/84*. 1983. URL: https://www.ew.tu-darmstadt.de/media/ew/privatissimum/DES_Teil_1.pdf.

[PRI49] A. T. PRICE. "The induction of electric currents in non-uniform thin sheets and shells". In: *The Quarterly Journal of Mechanics and Applied Mathematics* 2.3 (1949), pp. 283–310. ISSN: 0033-5614. DOI: 10.1093/qjmam/2.3.283.

[Pro+20] A. Prohammer, M. Rüschitz, D. Albert, and H. Renner. "Transformer Saturation Methods and Transformer Response to Low Frequency Currents". In: *Power and Energy Student Summit (PESS)*. Ed. by TU Darmstadt. 2020. URL: https://ieeexplore.ieee.org/document/9273802.

[PS18] S. K. Pukkalla and B. Subbarao. "Study on Modeling & Simulation Analysis of Electromagnetic Pulse (EMP) Coupling to Cables". In: *15th International Conference on Electromagnetic Interference & Compatibility (INCEMIC-2018)*. Piscataway, NJ: IEEE, 2018, pp. 1–4. ISBN: 978-1-7281-0476-8. DOI: 10.1109/INCEMIC.2018.8704564.

[PSS06] Praveen Koduru, Sanjoy Das, and Stephen M. Welch. "A Particle Swarm Optimization-Nelder Mead Hybrid Algorithm for Balanced Exploration and Exploitation in Multidimensional Search Space". In: *Proceedings of the 2006 International Conference on Artificial Intelligence, ICAI 2006, Las Vegas, Nevada, USA, June 26-29, 2006, Volume 2*. Ed. by Hamid R. Arabnia. CSREA Press, 2006, pp. 457–464.

[Pul+05] A. Pulkkinen, S. Lindahl, A. Viljanen, and R. Pirjola. "Geomagnetic storm of 29-31 October 2003: Geomagnetically induced currents and their relation to problems in the Swedish high-voltage power transmission system". In: *Space Weather* 3.8 (2005). ISSN: 15427390. DOI: 10.1029/2004SW000123.

[Pul+12] A. Pulkkinen, E. Bernabeu, J. Eichner, C. Beggan, and A. W. P. Thomson. "Generation of 100-year geomagnetically induced current scenarios". In: *Space Weather* 10.4 (2012). ISSN: 15427390. DOI: 10.1029/2011SW000750.

[Pul+17] A. Pulkkinen, E. Bernabeu, A. Thomson, A. Viljanen, R. Pirjola, D. H. Boteler, J. Eichner, P. J. Cilliers, Welling, N. P. Savani, R. S. Weigel, J. J. Love, C. Balch, C. M. Ngwira, G. Crowley, A. Schultz, R. Kataoka, B. Anderson, Fugate, J. J. Simpson, and M. MacAlester. "Geomagnetically induced currents: Science, engineering, and applications readiness". In: *Space Weather* 15.7 (2017), pp. 828–856. ISSN: 15427390. DOI: 10.1002/2016SW001501.

[PVP07] R. J. Pirjol, A. T. Viljanen, and A. A. Pulkkineni. "Research of Geomagnetically Induced Currents (GIC) in Finland". In: *7th International Symposium on Electromagnetic Compatibility and Electromagnetic Ecology, 2007*. Piscataway, NJ: IEEE Service Center, 2007, pp. 269–272. ISBN: 978-1-4244-1269-3. DOI: 10.1109/EMCECO.2007.4371707.

[RA14] J. Raith and S. Ausserhofer. *GIC Strength verification of Power Transformers in a high voltage Laboratory*. Cape Town, South Africa, 2014.

[Rab87] M. Rabinlowitz. "Effect of the Fast Nuclear Electromagnetic Pulse on the Electric Power Grid Nationwide: A Different View". In: *IEEE Transactions on Power Delivery* 2.4 (1987), pp. 1199–1222. ISSN: 08858977. DOI: 10.1109/TPWRD.1987.4308243.

[Rad+19] W. A. Radasky, R. Adams, C. Balch, Z. Emin, A. Halley, T. Ohnstad, A. Pinhel, Y. Sakharov, E. Salinas, E. Savage, P. Smith, and J. van Baellen. *Understanding of geomagnetic storm environment for high voltage power grids: WG C4.32*. 2019. URL: https://e-cigre.org/publication/780-understanding-of-geomagnetic-storm-environment-for-high-voltage-power-grids.

[Rad12] W. Radasky. *GIC Measurement Systems: E-Mail*. Ed. by D. Albert. 2020-02-12.

[Rah+19] M. A. Rahman, M. R. Islam, A. M. Mahfuz-Ur-Rahman, K. M. Muttaqi, and D. Sutanto. "Investigation of the Effects of DC Current Injected by Transformer-Less PV Inverters on Distribution Transformers". In: *IEEE Transactions on Applied Superconductivity* 29.2 (2019), pp. 1–4. ISSN: 1051-8223. DOI: 10.1109/TASC.2019.2895580.

[Rai19] J. Raith. "Risk Assessment of Power Transformers under the Influence of Geomagnetically Induced Currents (GIC)". PhD Thesis. Graz: TU Graz, 2019. URL: https://diglib.tugraz.at/risk-assessment-of-power-transformers-under-the-influence-of-geomagnetically-induced-currents-gic-2019.

[Ram+13] A. Ramos, J. C. Burgos, A. Moreno, and E. Sorrentino. "Determination of Parameters of Zero-Sequence Equivalent Circuits for Three-Phase Three-Legged YNynd Transformers Based on Onsite Low-Voltage Tests". In: *IEEE Transactions on Power Delivery* 28.3 (2013), pp. 1618–1625. ISSN: 1937-4208. DOI: 10.1109/TPWRD.2013.2259184.

[Ras+19] P. Rasilo, W. Martinez, K. Fujisaki, J. Kyyra, and A. Ruderman. "Simulink Model for PWM-Supplied Laminated Magnetic Cores Including Hysteresis, Eddy-Current, and

Excess Losses". In: *IEEE Transactions on Power Electronics* 34.2 (2019), pp. 1683–1695. ISSN: 0885-8993. DOI: 10.1109/TPEL.2018.2835661.

[RB17a] A. Ramos and J. C. Burgos. "Influence of tertiary stabilizing windings on zero-sequence performance of three-phase three-legged YNynd transformers. Part I: Equivalent circuit models". In: *Electric Power Systems Research* 144 (2017), pp. 32–40. ISSN: 03787796. DOI: 10.1016/j.epsr.2016.10.065.

[RB17b] A. Ramos and J. C. Burgos. "Influence of tertiary stabilizing windings on zero-sequence performance of three-phase three-legged YNynd transformers. Part II: Tank overheating hazard and short-circuit duty". In: *Electric Power Systems Research* 145 (2017), pp. 149–156. ISSN: 03787796. DOI: 10.1016/j.epsr.2017.01.003.

[RDS13] P. Ripka, K. Draxler, and R. Styblikova. "Measurement of DC Currents in the Power Grid by Current Transformer". In: *IEEE Transactions on Magnetics* 49.1 (2013), pp. 73–76. ISSN: 0018-9464. DOI: 10.1109/TMAG.2012.2216862.

[RH19] L. Rosenqvist and J. O. Hall. "Regional 3-D Modeling and Verification ofGeomagnetically Induced Currents in Sweden". In: *Space Weather* 17.1 (2019), pp. 27–36. ISSN: 15427390. DOI: 10.1029/2018SW002084.

[RI10] A. Rezaei-Zare and R. Iravani. "On the Transformer Core Dynamic Behavior During Electromagnetic Transients". In: *IEEE Transactions on Power Delivery* 25.3 (2010), pp. 1606–1619. ISSN: 1937-4208. DOI: 10.1109/TPWRD.2010.2046678.

[Ria18] I. U. Rian. "Application of Optical Current Transformers in Digital Substations". Master Thesis. Trondheim, Norway: Norwegian University of Science and Technology, 2018. URL: https://ntnuopen.ntnu.no/ntnu-xmlui/bitstream/handle/11250/2563522/18823_FULLTEXT.pdf?sequence=1&isAllowed=y.

[Ril12] P. Riley. "On the probability of occurrence of extreme space weather events". In: *Space Weather* 10.2 (2012), pp. 1–12. ISSN: 15427390. DOI: 10.1029/2011SW000734.

[Rod+20] C. J. Rodger, M. A. Clilverd, D. H. Mac Manus, I. Martin, M. Dalzell, J. B. Brundell, T. Divett, N. R. Thomson, T. Petersen, Y. Obana, and N. R. Watson. "Geomagnetically Induced Currents and Harmonic Distortion: Storm–Time Observations From New Zealand". In: *Space Weather* 18.3 (2020). ISSN: 15427390. DOI: 10.1029/2019SW002387.

[Ros+22] L. Rosenqvist, T. Fristedt, A. P. Dimmock, P. Davidsson, R. Fridström, J. O. Hall, L. Hesslow, J. Kjäll, M. Y. Smirnov, Welling, and P. Wintoft. "3D Modeling of Geomagnetically Induced Currents in Sweden—Validation and Extreme Event Analysis". In: *Space Weather* 20.3 (2022). ISSN: 15427390. DOI: 10.1029/2021SW002988.

[Ros05] G. Rosselli. "Transformer test to calculate Z0 for interconnected windings transformers using symmetrical sequence components". In: *2005 IEEE Power Engineering Society General Meeting*. Piscataway: IEEE, 2005, pp. 852–857. ISBN: 0-7803-9157-8. DOI: 10.1109/PES.2005.1489258.

[Rus+13] B. Rusek, C. Neumann, S. Steevents, U. Sundermann, K. Kleinkorte, J. Wulff, F. Jenau, and K.-H. Weck. *Ohmic coupling between AC and DC circuits on hybrid voerhead lines*. Auckland, 2013. URL: https://e-cigre.org/publication/SYMP_AUC_2013-symposium-auckland---2013.

[Rus05] R. Russel. *Charged Particle Motion in Earth's Magnetosphere*. 2005. URL: https://www.windows2universe.org/earth/Magnetosphere/tour/tour_earth_magnetosphere_07.html.

[Rus87] P. Rustan. "Description of an Aircraft Lightning And Simulated Nuclear Electromagnetic Pulse (NEMP) Threat Based on Experimental Data". In: *IEEE Transactions on Electromagnetic Compatibility* EMC-29.1 (1987), pp. 49–63. ISSN: 0018-9375. DOI: 10.1109/TEMC.1987.304332.

[Sad+02] N. Sadowski, N. J. Batistela, J. Bastos, and M. Lajoie-Mazenc. "An inverse Jiles-Atherton model to take into account hysteresis in time-stepping finite-element calculations". In: *IEEE Transactions on Magnetics* 38.2 (2002), pp. 797–800. ISSN: 0018-9464. DOI: 10.1109/20.996206.

[SAN12] V. A. Sergeev, V. Angelopoulos, and R. Nakamura. "Recent advances in understanding substorm dynamics". In: *Geophysical Research Letters* 39.5 (2012). ISSN: 00948276. DOI: 10.1029/2012GL050859.

[SAR21a] P. Schachinger, D. Albert, and H. Renner. "Low Frequency Currents Source Identification". In: *2022 20th International Conference on Harmonics and Quality of Power (ICHQP)*. 2021, pp. 1–6.

[SAR21b] P. Schachinger, D. Albert, and H. Renner. "Geomagnetically induced currents: A measurement based inverse determination of earth impedances". In: *2021 56th International Universities Power Engineering Conference (UPEC)*. IEEE, 31.08.2021, pp. 1–5. ISBN: 978-1-6654-4389-0. DOI: 10.1109/UPEC50034.2021.9548157.

[SAW22] P. Schachinger, D. Albert, and P. Wohlfart. *LFC Simulator*. 2022. URL: https://github.com/IEAN-TUGraz/LFC-Simulator.

[SB12] E. Sorrentino and J. C. Burgos. "Comparison of methods for measuring zero sequence impedances in 3-phase core-type transformers". In: *2012 47th International Universities Power Engineering Conference (UPEC 2012)*. Piscataway, NJ: IEEE, 2012, pp. 1–5. ISBN: 978-1-4673-2856-2. DOI: 10.1109/UPEC.2012.6398626.

[Sch+22] P. Schachinger, D. Albert, H. Renner, and G. Achleitner. "Einfluss von Spannungsänderungen und anderen Quellen auf niederfrequente Sternpunktströme". In: *17. Sympoisum Energieinnovation EnInnov 2022*. Ed. by U. Bachiesl. 2022.

[SF02] M. Steurer and K. Frohlich. "The impact of inrush currents on the mechanical stress of high voltage power transformer coils". In: *IEEE Transactions on Power Delivery* 17.1 (2002), pp. 155–160. ISSN: 08858977. DOI: 10.1109/61.974203.

[SH99] R. C. Smith and C. L. Hom. *A Domain Wall Model for Ferroelectric Hysteresis: CRSC-TR99-07 Technical Report*. 1999. URL: https://projects.ncsu.edu/crsc//reports/ftp/pdf/crsc-tr99-07.pdf.

[Sil+12] R. M. Silva, H. Martins, I. Nascimento, J. M. Baptista, A. L. Ribeiro, J. L. Santos, P. Jorge, and O. Frazão. "Optical Current Sensors for High Power Systems: A Review". In: *Applied Sciences* 2.3 (2012), pp. 602–628. DOI: 10.3390/app2030602.

[Sim01] E. Simmon. *Optical Current Transducer for Electrical Power Systems: Overview and Literature Survey*. Gathersburg, MD, 2001. URL: https://nvlpubs.nist.gov/nistpubs/Legacy/IR/nistir6805.pdf.

[Sim05] F. Simpson. *Practical magnetotellurics*. Cambridge, UK and New York: Cambridge University Press, 2005. ISBN: 9780521817271. DOI: 10.1017/CBO9780511614095.

[Sim71] K. Simonyi. *Theoretische Elektrotechnik*. 4., überarbeitete und ergänzte Auflage. Vol. Band 20. Hochschulbücher für Physik. Berlin: VEB Deutscher Verlag der Wissenschaften, 1971.

[SK55] R. P. Sallen and E. L. Key. "A practical method of designing RC active filters". In: *IRE Transactions on Circuit Theory* 2.1 (1955), pp. 74–85. ISSN: 0096-2007. DOI: 10.1109/TCT.1955.6500159.

[SK91] M. Sugiura and T. Kamei. *Dst index*. 1991. URL: http://wdc.kugi.kyoto-u.ac.jp/dstdir/dst2/onDstindex.html.

[Sme+20] R. P. P. Smeets, A. B. Hofstee, R. M. Nijman, N. A. Belda, and B. Baum. "Innovative T&D Switching Equipment and Development of its Testing Technology: A3-104". In: *Cigre Session 48*. Ed. by Cigre. Paris, 2020.

[Sor+19] K. A. Sorathia, V. G. Merkin, A. Y. Ukhorskiy, R. C. Allen, K. Nykyri, and S. Wing. "Solar Wind Ion Entry Into the Magnetosphere During Northward IMF". In: *Journal of geophysical research. Space physics* 124.7 (2019), pp. 5461–5481. ISSN: 2169-9380. DOI: 10.1029/2019JA026728.

[SPS18] V. V. Surkov, V. A. Pilipenko, and A. K. Sinha. "Possible mechanisms of co-seismic electromagnetic effect". In: *Acta Geodaetica et Geophysica* 53.1 (2018), pp. 157–170. ISSN: 2213-5820. DOI: 10.1007/s40328-018-0211-6.

[SS08] F. Sulla and O. Samuelsson. "Estimation of the zero sequence voltage on the D-side of a Dy transformer by using one voltage transformer on the D-side". In: *The Institution of Engineering and Technology 9th international conference on developments in power systems protection*. London: IET, 2008, pp. 516–521. ISBN: 978 0 86341 902 7. DOI: 10.1049/cp:20080091.

[Ste00] C. P. Steinmetz. *Theory and calculation of alternating current phenomena*. 3rd ed., rev. and enl. Nineteenth Century Collections Online (NCCO). New York: Electrical World and Engineer Inc, 1900. URL: http://ncco.galegroup.com/gdc/ncco/MonographsDetailsPage/MonographsDetailsWindow?disableHighlighting=false&prodId=NCCO&action=1&activityType=BasicSearch&javax.portlet.action=viewPortletAction&documentId=GALE%7CBCIFHA857476068&dviSelectedPage=1.

[Sze+21] R. Szewczyk, O. Petruk, M. Nowicki, A. Ostaszewska-Liżewska, A. Kolano-Burian, P. Gazda, A. Bieńkowski, P. Nowak, and T. Charubin. "LTspice Implementation of Gyrator-Capacitor Magnetic Circuit Model Considering Losses and Magnetic Saturation for Transient Simulations of Switching Mode Power Supplies Utilizing Inductive Elements with Cores Made of Amorphous Alloys". In: *Automation 2021: Recent Achievements in Automation, Robotics and Measurement Techniques*. Ed. by R. Szewczyk, C. Zieliński, and M. Kaliczyńska. Vol. 1390. Advances in Intelligent Systems and Computing. Cham: Springer International Publishing, 2021, pp. 416–424. ISBN: 978-3-030-74892-0. DOI: 10.1007/978-3-030-74893-7.

[SZK21] R. Szewczyk, C. Zieliński, and M. Kaliczyńska, eds. *Automation 2021: Recent Achievements in Automation, Robotics and Measurement Techniques*. Vol. 1390. Advances in Intelligent Systems and Computing. Cham: Springer International Publishing, 2021. ISBN: 978-3-030-74892-0. DOI: 10.1007/978-3-030-74893-7.

[Tau20] B. Taupe. "Umbau zweier Leistungstransformatoren zur flexiblen Änderung der Schaltgruppe". Bachelor Thesis. Graz: Graz University of Technology, 2020.

[Tex18] Texas Instrument. *ADS111x ADC Datasheet*. 2018.

[Tho+05] A. W. P. Thomson, A. J. McKay, E. Clarke, and S. J. Reay. "Surface electric fields and geomagnetically induced currents in the Scottish Power grid during the 30 October 2003 geomagnetic storm". In: *Space Weather* 3.11 (2005), n/a–n/a. ISSN: 15427390. DOI: 10.1029/2005SW000156.

[Thy80] Thyssen Grillo Funke GmbH. *Lieferprogramm ORSI H*. Ed. by Thyssen Grillo Funke GmbH. 1980.

[Tor+12] J. M. Torta, L. Serrano, J. R. Regué, A. M. Sánchez, and E. Roldán. "Geomagnetically induced currents in a power grid of northeastern Spain". In: *Space Weather* 10.6 (2012). ISSN: 15427390. DOI: 10.1029/2012SW000793.

[Tre21] Trench Group. *Optical Current Transformers - Trench Group*. 16.11.2021. URL: https://trench-group.com/products/optical-current-transformers/.

[Tri+07] N. B. Trivedi, Í. Vitorello, W. Kabata, S. L. G. Dutra, A. L. Padilha, M. S. Bologna, M. B. de Pádua, A. P. Soares, G. S. Luz, F. d. A. Pinto, R. Pirjola, and A. Viljanen. "Geomagnetically induced currents in an electric power transmission system at low latitudes in Brazil: A case study". In: *Space Weather* 5.4 (2007). ISSN: 15427390. DOI: 10.1029/2006SW000282.

[Tsu03] B. T. Tsurutani. "The extreme magnetic storm of 1–2 September 1859". In: *Journal of Geophysical Research: Space Physics* 108.A7 (2003). ISSN: 01480227. DOI: 10.1029/2002JA009504.

[Tuv+16] M. Tuvenson, T. Evan, A. Coburn, D. Ralph, S. Ruffle, E. Oughton, A. Skelton, J. Copic, V. Kesaite, J. Z. Yeo, S. Malik, E. Leverett, L. Pryor, D. Needham, J. C. D. Jung, A. Cahplin, A. Mahalingam, A. Shaghaghi, J. Tsang, and S. Asante. *Helios Solar Storm Scenario*. Ed. by University of Cambridge. 2016. URL: https://www.jbs.cam.ac.uk/wp-content/uploads/2020/08/aig-helios-solar-storm-16-june.pdf.

[UMK82] M. Uman, M. Master, and E. Krider. "A Comparison of Lightning Electromagnetic Fields with the Nuclear Electromagnetic Pulse in the Frequency Range 104-107 Hz". In: *IEEE Transactions on Electromagnetic Compatibility* EMC-24.4 (1982), pp. 410–416. ISSN: 0018-9375. DOI: 10.1109/TEMC.1982.304056.

[UYM98] J. Ulleryd, M. Ye, and G. Moreau. "Fundamental frequency coupling between HVAC and HVDC lines in the Quebec-New England multiterminal system-comparison between field measurements and EMTDC simulations". In: *Proceedings / 1998 International Conference on Power System Technology, August 18 - 21, 1998 Beijing, China*. Piscataway, NJ: IEEE, 1998, pp. 498–502. ISBN: 0-7803-4754-4. DOI: 10.1109/ICPST.1998.729013.

[VCK20] V. Vakhnina, A. Chernenko, and D. Kretov. "Integrating Monitoring Systems and Power Transformer Protections to Curb Destructive Effects of Quasi-Direct Currents". In: *Proceedings 2020 International Conference on Industrial Engineering, Applications and Manufacturing (ICIEAM)*. Piscataway, NJ: IEEE, 2020, pp. 1–5. ISBN: 978-1-7281-4590-7. DOI: 10.1109/ICIEAM48468.2020.9111896.

[VGK20] V. Vakhnina, I. Gorohov, and D. Kretov. "Impact of Lithospheric Quasi-Direct Current Sources on Electric Power Systems". In: *2020 International Multi-Conference on Industrial Engineering and Modern Technologies (FarEastCon)*. [Piscataway, NJ]: IEEE, 2020, pp. 1–4. ISBN: 978-1-7281-6951-4. DOI: 10.1109/FarEastCon50210.2020.9271082.

[VŠ19] T. Výbošt'oková and M. Švanda. "Statistical Analysis of the Correlation Between Anomalies in the Czech Electric Power Grid and Geomagnetic Activity". In: *Space Weather* 17.8 (2019), pp. 1208–1218. ISSN: 15427390. DOI: 10.1029/2019SW002181.

[VU88] E. F. Vance and M. A. Uman. "Differences between lightning and nuclear electromagnetic pulse interactions". In: *IEEE Transactions on Electromagnetic Compatibility* 30.1 (1988), pp. 54–62. ISSN: 0018-9375. DOI: 10.1109/15.19889.

[VW77] G. Vasseur and P. Weidelt. "Bimodal electromagnetic induction in non-uniform thin sheets with an application to the northern Pyrenean induction anomaly". In: *Geophysical Journal International* 51.3 (1977), pp. 669–690. ISSN: 0956-540X. DOI: 10.1111/j.1365-246X.1977.tb04213.x.

[Wal57] C. S. Walker. "The Excitation Requirements of 3-Phase Core-Type 3-Legged Y-Connected Transformers". In: *Transactions of the American Institute of Electrical Engineers. Part III: Power Apparatus and Systems* 76.3 (1957), pp. 1113–1119. ISSN: 0097-2460. DOI: 10.1109/AIEEPAS.1957.4499731.

[WB02] M. Willsch and T. Bosselmann. "Optical current sensor application in the harsh environment of a 120 MVA power generator". In: *Ofs 2002*. Piscataway, NJ: Institute of Electrical and Electronics Engineers, 2002, pp. 407–410. ISBN: 0-7803-7289-1. DOI: 10.1109/OFS.2002.1000653.

[Wik+08] M. Wik, A. Viljanen, R. Pirjola, A. Pulkkinen, P. Wintoft, and H. Lundstedt. "Calculation of geomagnetically induced currents in the 400 kV power grid in southern Sweden". In: *Space Weather* 6.7 (2008). ISSN: 15427390. DOI: 10.1029/2007SW000343.

[Wil11] J. L. Willems. "Budeanu's Reactive Power and Related Concepts Revisited". In: *IEEE Transactions on Instrumentation and Measurement* 60.4 (2011), pp. 1182–1186. ISSN: 0018-9456. DOI: 10.1109/TIM.2010.2090704.

[WNE21] S. Watari, S. Nakamura, and Y. Ebihara. "Measurement of geomagnetically induced current (GIC) around Tokyo, Japan". In: *Earth, Planets and Space* 73.1 (2021), pp. 1–19. ISSN: 1880-5981. DOI: 10.1186/s40623-021-01422-3.

[WNM21] W. Wang, A. Nysveen, and N. Magnusson. "Power losses in the three–phase three–limb transformer due to common and differential mode of dc–bias". In: *IET Electric Power*

Applications 15.11 (2021), pp. 1488–1498. ISSN: 17518660. DOI: 10.1049/elp2.12113.

[Woh20] P. E. Wohlfart. "Aufbau und Verifikation eines Systems zur Messung von Sternpunktströmen an Leistungstransformatoren". Bachelor Thesis. Graz: Graz University of Technology, 2020.

[WRB01] P. R. Wilson, J. N. Ross, and A. D. Brown. "Optimizing the Jiles-Atherton model of hysteresis by a genetic algorithm". In: *IEEE Transactions on Magnetics* 37.2 (2001), pp. 989–993. ISSN: 0018-9464. DOI: 10.1109/20.917182.

[Xu+94] W. Xu, T. G. Martinich, J. H. Sawada, and Y. Mansour. "Harmonics from SVC transformer saturation with direct current offset". In: *IEEE Transactions on Power Delivery* 9.3 (1994), pp. 1502–1509. ISSN: 08858977. DOI: 10.1109/61.311218.

[YFB94] Y. You, E. F. Fuchs, and P. R. Barnes. "Reactive power demand of transformers with DC bias". In: *Conference Record of the IEEE Industry Applications Society Annual Meeting, 1994*. Piscataway: IEEE, 1994, pp. 339–346. ISBN: 0-7803-1993-1. DOI: 10.1109/IAS.1994.377489.

[YM17] Y. Yamazaki and A. Maute. "Sq and EEJ—A Review on the Daily Variation of the Geomagnetic Field Caused by Ionospheric Dynamo Currents". In: *Space Science Reviews* 206.1-4 (2017), pp. 299–405. ISSN: 0038-6308. DOI: 10.1007/s11214-016-0282-z.

[You+16] M. Young, A. Dimitrovski, Z. Li, and Y. Liu. "Gyrator-Capacitor Approach to Modeling a Continuously Variable Series Reactor". In: *IEEE Transactions on Power Delivery* 31.3 (2016), pp. 1223–1232. ISSN: 1937-4208. DOI: 10.1109/TPWRD.2015.2510642.

[You+96] Y. You, E. F. Fuchs, Lin, and P. R. Barnes. "Reactive power demand of transformers with DC bias". In: *IEEE Industry Applications Magazine* 2.4 (1996), pp. 45–52. ISSN: 10772618. DOI: 10.1109/2943.503528.

[ZAM19] ZAMG. *Jahrbuch — ZAMG*. 2019. URL: https://www.zamg.ac.at/cms/de/klima/klimauebersichten/jahrbuch.

[Zaw+20] A. A. Zawawi, N. F. Ab Aziz, M. Z. A. Ab Kadir, H. Hashim, and Z. Mohammed. "Evaluation of Geomagnetic Induced Current on 275 kV Power Transformer for a Reliable and Sustainable Power System Operation in Malaysia". In: *Sustainability* 12.21 (2020), p. 9225. DOI: 10.3390/su12219225.

[Zen18] Zentralanstalt für Meterologie und Geodynamik. *Conrad Observatorium*. 2018. URL: http://www.conrad-observatory.at/zamg/index.php/de/.

[Zha+20] J. Zhao, S. E. Zirka, Y. I. Moroz, and C. M. Arturi. "Structure and properties of the hybrid and topological transformer models". In: *International Journal of*

Electrical Power and Energy Systems 118 (2020), p. 105785. ISSN: 01420615. DOI: 10.1016/j.ijepes.2019.105785.

[Zha+21] J. Zhao, Y. Gao, J. Tang, S. L. Klemperer, J. Wen, C.-.-H. Chen, and J. Chong. "Electromagnetic Field Generated by an Earthquake Source Due to Motional Induction in 3D Stratified Media, and Application to 2008 Mw 6.1 Qingchuan Earthquake". In: *Journal of Geophysical Research: Solid Earth* 126.10 (2021). ISSN: 2169-9313. DOI: 10.1029/2021JB022102.

[Zir+04] S. E. Zirka, Y. I. Moroz, P. Marketos, and A. J. Moses. "Congruency-Based Hysteresis Models for Transient Simulation". In: *IEEE Transactions on Magnetics* 40.2 (2004), pp. 390–399. ISSN: 0018-9464. DOI: 10.1109/TMAG.2004.824137.

[Zir+06] S. E. Zirka, Y. I. Moroz, P. Marketos, A. J. Moses, and D. C. Jiles. "Measurement and Modeling of B–H Loops and Losses of High Silicon Nonoriented Steels". In: *IEEE Transactions on Magnetics* 42.10 (2006), pp. 3177–3179. ISSN: 0018-9464. DOI: 10.1109/TMAG.2006.880090.

[Zir+08] S. E. Zirka, Y. I. Moroz, P. Marketos, A. J. Moses, D. C. Jiles, and T. Matsuo. "Generalization of the Classical Method for Calculating Dynamic Hysteresis Loops in Grain-Oriented Electrical Steels". In: *IEEE Transactions on Magnetics* 44.9 (2008), pp. 2113–2126. ISSN: 0018-9464. DOI: 10.1109/TMAG.2008.2000662.

[Zir+11] S. E. Zirka, Y. I. Moroz, A. J. Moses, and C. M. Arturi. "Static and Dynamic Hysteresis Models for Studying Transformer Transients". In: *IEEE Transactions on Power Delivery* 26.4 (2011), pp. 2352–2362. ISSN: 1937-4208. DOI: 10.1109/TPWRD.2011.2140404.

[Zir+12a] S. E. Zirka, Y. I. Moroz, C. M. Arturi, N. Chiesa, and H. K. Hoidalen. "Topology-Correct Reversible Transformer Model". In: *IEEE Transactions on Power Delivery* 27.4 (2012), pp. 2037–2045. ISSN: 1937-4208. DOI: 10.1109/TPWRD.2012.2205275.

[Zir+12b] S. E. Zirka, Y. I. Moroz, R. G. Harrison, and K. Chwastek. "On physical aspects of the Jiles-Atherton hysteresis models". In: *Journal of Applied Physics* 112.4 (2012), p. 043916. ISSN: 0021-8979. DOI: 10.1063/1.4747915.

[Zir+14] S. E. Zirka, Y. I. Moroz, R. G. Harrison, and N. Chiesa. "Inverse Hysteresis Models for Transient Simulation". In: *IEEE Transactions on Power Delivery* 29.2 (2014), pp. 552–559. ISSN: 1937-4208. DOI: 10.1109/TPWRD.2013.2274530.

[Zir+15] S. E. Zirka, Y. I. Moroz, N. Chiesa, R. G. Harrison, and H. K. Hoidalen. "Implementation of Inverse Hysteresis Model Into EMTP—Part II: Dynamic Model". In: *IEEE Transactions on Power Delivery* 30.5 (2015), pp. 2233–2241. ISSN: 1937-4208. DOI: 10.1109/TPWRD.2015.2416199.

[Zir+17] S. E. Zirka, Y. I. Moroz, H. K. Hoidalen, A. Lotfi, N. Chiesa, and C. M. Arturi. "Practical Experience in Using a Topological Model of a Core-Type Three-Phase Transformer—No-Load and Inrush Conditions". In: *IEEE Transactions on Power Delivery* 32.4 (2017), pp. 2081–2090. ISSN: 1937-4208. DOI: 10.1109/TPWRD.2016.2618900.

[Zir+18a] S. E. Zirka, Y. I. Moroz, C. M. Arturi, and D. Bonnman. "Topological transient Models of three-phase five-limb Transformer". In: *Electrical Engineering and Power Engineering* 0.2 (2018), pp. 18–25. ISSN: 1607-6761. DOI: 10.15588/1607-6761-2017-2-2.

[Zir+18b] S. E. Zirka, Y. I. Moroz, J. Elovaara, M. Lahtinen, R. A. Walling, H. K. Høidalen, D. Bonmann, C. M. Arturi, and N. Chiesa. "Simplified models of three-phase, five-limb transformer for studying GIC effects". In: *International Journal of Electrical Power and Energy Systems* 103 (2018), pp. 168–175. ISSN: 01420615. DOI: 10.1016/j.ijepes.2018.05.035.

[Zir+21] S. E. Zirka, Y. I. Moroz, A. V. Zhuykov, D. A. Matveev, M. A. Kubatkin, M. V. Frolov, and M. Popov. "Eliminating VT uncertainties in modeling ferroresonance phenomena caused by single phase-to-ground faults in isolated neutral network". In: *International Journal of Electrical Power and Energy Systems* 133 (2021), p. 107275. ISSN: 01420615. DOI: 10.1016/j.ijepes.2021.107275.

[Zir+22a] S. E. Zirka, D. Albert, Y. I. Moroz, L. Domenig, and H. Renner. "Towards a Topological Model of a Three-Phase Transformer Including Deep Saturation Conditions". In: *20th International IGTE Symposium on Computational Methods in Electromagnetics and Multiphysics (IGTE'22)*. Ed. by Institute of Fundamentals and Theory. Graz, 2022.

[Zir+22b] S. E. Zirka, D. Albert, Y. I. Moroz, and H. Renner. "Further Improvements in Topological Transformer Model Covering Core Saturation". In: *IEEE Access* 10 (2022), pp. 64018–64027. ISSN: 2169-3536. DOI: 10.1109/ACCESS.2022.3183279.

[ZMA14] S. E. Zirka, Y. I. Moroz, and C. M. Arturi. "Accounting for the Influence of the Tank Walls in the Zero-Sequence Topological Model of a Three-Phase, Three-Limb Transformer". In: *IEEE Transactions on Power Delivery* 29.5 (2014), pp. 2172–2179. ISSN: 08858977. DOI: 10.1109/TPWRD.2014.2307117.

[ZMA21] S. E. Zirka, Y. I. Moroz, and C. M. Arturi. "Once again about the Steinmetz transformer model and the ongoing subdivision of its leakage inductance". In: *COMPEL - The international journal for computation and mathematics in electrical and electronic engineering* (2021). ISSN: 0332-1649. DOI: 10.1108/COMPEL-06-2021-0190.

[ZMR17] S. E. Zirka, Y. I. Moroz, and E. Rahimpour. "Towards a transformer transient model as a lumped-distributed parameter system". In: *COMPEL - The international journal for computation and mathematics in electrical and electronic engineering* 36.3 (2017), pp. 741–750. ISSN: 0332-1649. DOI: 10.1108/COMPEL-09-2016-0389.

A Transformer Neutral Point Current Measurement System

A.1 Measurement System Versions

Table A.1 lists the measurement system history, according to the used hardware.

Table A.1: Measurement system version and corresponding PCB versions.

System Version	Supply PCB	Measurement PCB	DCC PCB
v2019	v2	v3	v1
v2021	v3	v3	v2

A.2 Version v2019

The LFC measurement system v2019 can record up to four voltage channels simultaneously and the temperature inside the measurement cabinet or in the current sensors cabinet. It is built from up to five blocks, as presented in **Figure A.2** and **Figure 3.4**. Channel one is used to measure the transformer NPC. Channel two to four are used to measure the injected current of a DCC system at equipped transformers. For the NPC measurement, the LEM IT65-S ULTRASTAB closed-loop zero-flux CT [LEM20a] is used in combination with a 50 Ω measurement burden. The currents of the DCC are measured with a LEM LF-306 S [LEM20b] with a 33 Ω burden. The LEM LA200SD/SP3 is used with a burden of 350 Ω.

Block 1 includes the CT and the measurement burden. In order to measure positive and negative current amplitude, the measurement signal is shifted +2.0496 V with an operation amplifier (op amp) based adder in *Block 2*. The offset shift is required, because the ADC is used with a voltage input range of 0 V to +4.096 V [Tex18].

Block 3 includes the Sallen-Key topology of a second-order active low-pass filter. The op amp is primarily used as a buffer. For that reason, the performance of the filter is essentially independent of the op amps performance [SK55]. An active low-pass filter is used, because of the higher linearity of the active filter, compared to the passive filter, where the amplitude of the output is lower than the input signal. With the active filter design, also the input impedance does not affect the linearity.

In *Block 4* the signal is sampled with a 16-bit ADC and sent via I^2C protocol to the Raspberry Pi single board computer. The Raspberry Pi is used for data storage and the remote access via the Universal Mobile Telecommunications System (UMTS).

Block 5 connects the DCC measurement signals from the DCC cabinet, on the transformer tank, to the rest of the measurement system, installed at the scaffold of the neutral point switch. The measurement electronic and the cabinet are depicted in **Figure A.1**. The top PCB is the power supply PCB with a D-Sub9 connector to the NPC transducer LEM IT65-S ULTRASTAB. The middle PCB includes the channel two to four, with the adder, filter circuit and ADC. The bottom PCB is the single board computer Raspberry Pi 4 model B.

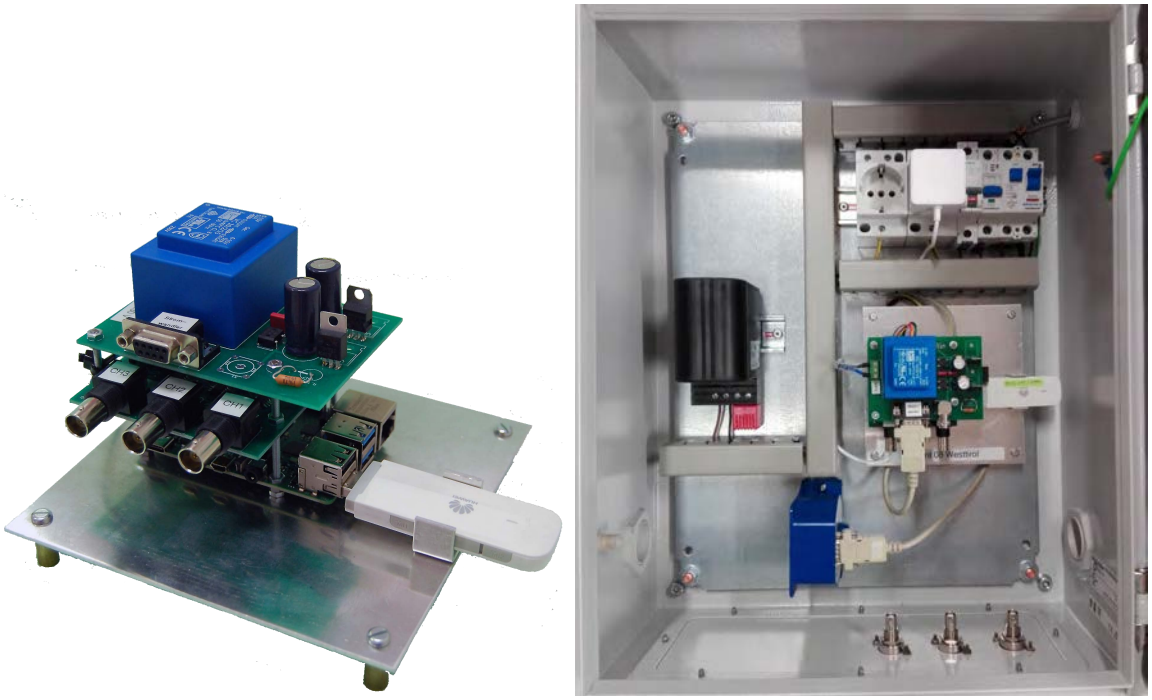

(a) Measurement electronic with power supply PCB, signal processing PCB and single board computer.

(b) Measurement cabinet with 230 V/50 Hz power supply, measurement electronic, CT and cabinet heating.

Figure A.1: Neutral point current measurement system.

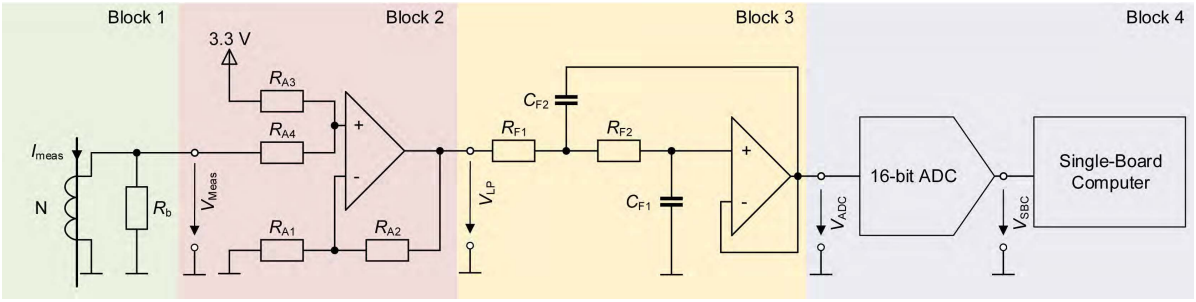

Figure A.2: Neutral point current measurement electronic layout.

A demonstrator of the v2019 measurement system, including the DCC measurement system, is depicted in **Figure A.3**. On the screen, a live view of the measured transformer NPCs from the nine measurement locations is displayed.

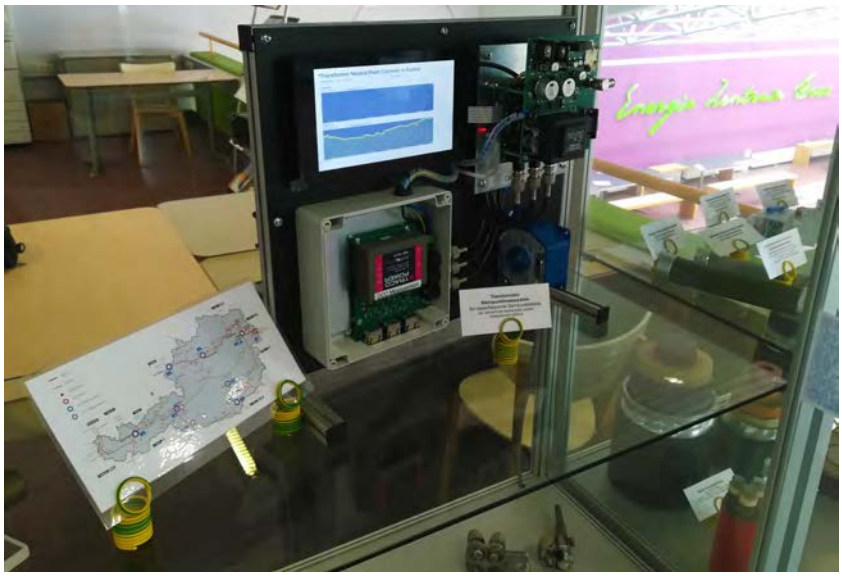

Figure A.3: Measurement system demonstrator with DCC measurement electronic and measurement location map.

Figure A.4 depicts the guaranteed and typical measurement accuracy of the measurement system with the CT LEM IT65-S ULTRASTAB.

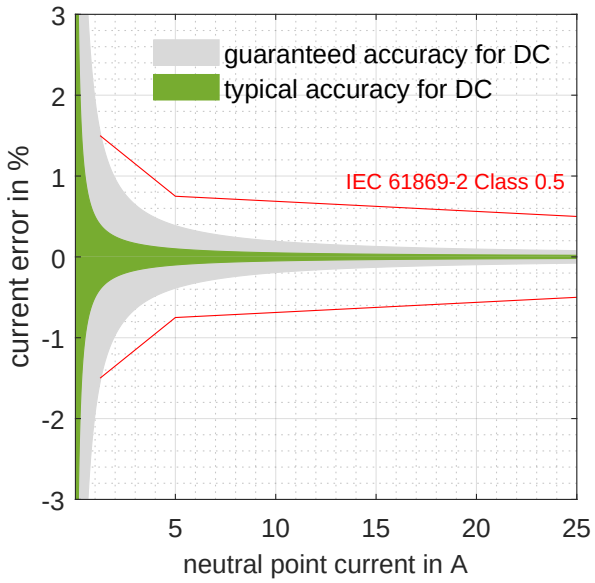

Figure A.4: Guaranteed and typical measurement system accuracy for LEM IT65-S ULTRASTAB.

Table A.2 gives an overview of the versions, runtime and their location. In the column 'Direction' the measurement direction of the CT, used in the measurement system, is indicated. The positive sign (+) indicates the current is measured in positive direction from substation ground into the power grid via the transformer neutral; the negative sign (−) indicates the current is measured in positive direction from the power grid via the transformer neutral into the substation ground. The

positive current direction of the DCC measurement is from the DCC system into the transformer winding.

Table A.2: Measurement client information.

Client	**State**	**V. Level** in kV	**Runtime**	**Vers.**	**Direc.**
#01	Vienna	380	2016-08-26 - 2020-09-23	v2014	+
			2020-09-23 - present	v2019	+
#02	Styria	380	2016-11-08 - 2018-04-12	v2014	+
	Styria	220	2018-04-23 - 2020-09-04	v2014	−
			2020-09-04 - present	v2019	−
#03	Salzburg	380	2017-04-10 - 2021-07-23	v2014	−
			2021-07-23 - present	v2021	−
#04	Vienna	220	2017-05-11 - 2020-09-23	v2014	+
			2020-09-23 - present	v2021	+
#05	Up. Austria	380	2017-10-10 - 2020-12-10	v2014	−
			2020-12-10 - present	v2019	−
#06	Low. Austria	220	2021-10-21 - 2021-12-07	v2019	+
	Low. Austria		2021-12-07 - present	v2019	+
#07	Low. Austria	380	2020-01-20 - present	v2019	−
#08	Tyrol	380	2021-03-15 - present	v2019	−
#09	Carinthia	220	2021-03-15 - present	v2021	−

A.3 Measurement System Design Data

The error of an ADC in general given as least significant bit (LSB)[1] full scale range (FSR)/2. The LSB, for the ADC Texas Instruments ADS1115 in FSR $\pm 4.096\,\mathrm{V}$ differential operation mode, is $125\,\mu\mathrm{V}$. Summing up all errors (integral non-linearity, offset error, long-term offset drift, offset drift over temperature, offset power supply rejection, max. gain error [Tex18]) from the data sheet gives 13 LSB. Thus, the overall measurement error of the ADC is $1.625\,\mu\mathrm{V}$.

$$u(V_{\mathrm{ADC}}) = \frac{U_{\mathrm{LSB}}}{2} \cdot 19 = 19 \cdot \frac{4.096\mathrm{V}}{2 \cdot 2^{16}} = 19 \cdot 31.25\mu\mathrm{V} = 593.75\mu\mathrm{V} \tag{A.1}$$

(A.2) to (A.5) are the transfer functions of the neutral point current measurement system, depicted in **Figure A.2**. The function parameters are given in **Table A.3**.

$$V_{\mathsf{meas}}(t) = \frac{I_{\mathsf{meas}} \cdot R_b}{N}, \tag{A.2}$$

$$V_{\mathsf{LP}}(t) = \left(1 + \frac{R_{A2}}{R_{A1}}\right) \cdot \left(\frac{R_{A4}}{R_{A3} + R_{A4}} \cdot 3.3\ V + \frac{R_{A3}}{R_{A3} + R_{A4}} \cdot V_{\mathsf{meas}}\right), \tag{A.3}$$

[1] LSB is the smallest level an ADC can convert

Table A.3: Measurement system component tolerances; component designation refers to **Figure 3.3**, **Figure 3.4**, and **Figure A.2**.

Component	Description	Version	Value	Tolerance
LEM IT65-S				0.003 %
LEM LF306S				0.4 %
LA200SD/SP3				1 %
R_{b}	NPC	50 Ω	v2019	1 %
R_{b}	NPC	50 Ω	v2021	0.1 %
R_{b}	NPC	350 Ω	v2021	0.1 %
R_{b}	DCC	33 Ω	v2019	0.5 %
R_{b}	DCC	33 Ω	v2021	0.5 %
R_{A1}	NPC	33.2 kΩ	v2019/2021	0.1 %
$R_{\mathrm{A2}}, R_{\mathrm{A4}}$	NPC	20 kΩ	v2019/2021	1 %
R_{A3}	NPC	31.6 kΩ	v2019/2021	1 %
R_{A21}	NPC	100 kΩ	v2021	1 %
R_{A22}	NPC	19 kΩ	v2021	1 %
R_{A10}	DCC	30 kΩ	v2019/21	0.1 %
R_{A11}	DCC	20 kΩ	v2019/21	1 %
$R_{\mathrm{F1}}, R_{\mathrm{F2}}$	DCC	4.7 kΩ	v2019/21	1 %
$C_{\mathrm{F1}}, C_{\mathrm{F2}}$	DCC	33 μF	v2019/21	20 %
ADC ADS1115 (FSR ±4.096 V)			v2019/21	1.625 mV
V_{ras}	DCC	3.3 V	v2019/21	10 %

$$V_{\mathrm{ADC}}(s_n) = \frac{V_{\mathrm{LP}}}{1 + \omega_c C_1 (R_1 + R_2) + \omega_c^2 R_1 R_2 C_1 C_2}, \tag{A.4}$$

$$V_{\mathrm{SBC}} = V_{\mathrm{ADC}} \tag{A.5}$$

A.4 Alternative Current Measurement Technique: Resistive Measurement

Table A.4: Physical properties of MANGANIN® [Isa14].

Property	Value
Electric resistivity (@ 20°C), ρ_{R}	43 $\mu\Omega \cdot \mathrm{cm}$
Temperature coefficient (@ 20°C)	$\pm 10 \cdot 10^{-6}$/K
Density, ρ	8.4 $\mathrm{g/cm^3}$
Specific heat capacity, c	410 J/kg·K
Thermoelectric voltage, α (@ 20°C)	-1 μV/K
Melting point, T_m	960°C

On the example of a 380 kV transformer earthing switch with a quadratic U-shaped profile arm, a possible setup is evaluated. The quadratic arm should have the outer dimensions of $50 \cdot 50$ mm, assuming a thickness of 2 mm and aluminium as the main material (red) of the switching arm. The MANGANIN® (detail information on the material is given in **Table A.4**) shunt-inlet (blue) is also

assumed to be quadratic with a thickness of 2 mm and a length of 100 mm. The lower part of the switching arm is also assumed with a quadratic shape out of aluminium (yellow) with an outer dimension of $42 \cdot 42$ mm and a thickness of 2 mm. The MANGANIN® shunt-inlet therefore has the following dimensions:

- volume V: 35,200 mm^3
- conductive surface area A: 16,800 mm^2 ($=$0.0168 m^2)
- length l: 100 mm
- equivalent resistance: $R = \rho \cdot l/A = 2.56\,\mu\Omega$

In order to check if a short-circuit current cause the material to heat up and to become mechanically unstable, the relative temperature increase (in comparison to the ambient temperature) of the material is compared to the melting point. In (A.6) the energy introduced to the shunt is calculated. In (A.7) the total temperature rise of the shunt resistor, due to a 50 kA short-circuit current for 300 ms is calculated to be $+$14.95 K. Assuming an ambient temperature of $+$40°C the absolute temperature of the shunt would be 54.95°C. This temperature is far away from the melting point of 960°C. Therefore, no considerable decrease of mechanical strength is assumed.

$$E = I^2 \cdot R_{\mathrm{Shunt}} = (50\,\mathrm{kA})^2 \cdot 2.56\mu\Omega \cdot 0.3\,\mathrm{s} = 1920\,\mathrm{J} \tag{A.6}$$

$$\Delta T = \frac{E}{c\rho V} = \frac{1920\,\mathrm{J}}{410\,\mathrm{J/kg \cdot K} \cdot 8.4 \cdot 10^3\,\mathrm{kg/m^3} \cdot 35.2 \cdot 10^{-6}\mathrm{m^3}} = +14.95\,\mathrm{K} \tag{A.7}$$

The ideal measured voltage across the shunt (neglect all errors) for 10 mA and 25 A is calculated to $\pm$25.6 nV to $\pm$64 μV, according to (A.8) and (A.9).

$$U_{\mathrm{Shunt,min}} = R_{\mathrm{Shunt}} \cdot I_{\mathrm{min}} = 2.92\mu\Omega \cdot \pm 10\,\mathrm{mA} = \pm 25.6\,\mathrm{nV} \tag{A.8}$$

$$U_{\mathrm{Shunt,max}} = R_{\mathrm{Shunt}} \cdot I_{\mathrm{min}} = 2.92\mu\Omega \cdot \pm 25\,\mathrm{A} = \pm 64\,\mu\mathrm{V} \tag{A.9}$$

The thermoelectric voltage is caused by a temperature difference between the contact area of two thermal elements [Mes15], in this case the MANGANIN® shunt and the aluminium. Assuming the rest of the switching arm is made out of aluminium with a thermoelectric voltage of $+3.5\,\mu$V/K, the thermoelectric voltage between MANGANIN® and aluminium is calculated according to (A.10) with an assumed temperature difference of 0.1 K. Because the interface between Aluminium and MANGANIN® is present between the upper switching arm and the lower part of the switching arm, the thermoelectric voltage arises two times. Thus, the thermoelectric voltage itself would lead to a measurement of 13.18 A.

$$U_{\text{thermo}} = \begin{array}{l}(\kappa_{\text{Al}} - \kappa_{\text{MAN}}) \cdot (T_1 - T_2) = (35\,\mu\text{V/K} - (-35\,\mu\text{V/K})) \cdot 0.1\,\text{K} \\ = 38.5\,\mu\text{V}\end{array} \tag{A.10}$$

In Order to neglect the thermoelectric voltage, the shunt resistance need to be increased by the factor 10^6, which means the shunt resistance would need to be in the range of 2.52 Ω. With additional 2.52 Ω the DC network parameters would already be influenced (typical winding resistance power transformer 0.2...0.6 Ω/phase). Also, the loss dissipation during a short circuit current event limits the maximum shunt resistance.

Due to the different electron attraction of metals, merging two different metals will result in a galvanic corrosion (oxidation) of the less noble metal. The galvanic series lists the materials according to their standard electrode potential E^0. Standard refers to activity of the ions, which need to be 1 mol/l. MANGANIN® is a mixture of 86 % copper ($E^0 = +0.52\,\text{V}$), 2 % nickel ($E^0 = -0.23\,\text{V}$), 12 % Manganese ($E^0 = -1.18\,\text{V}$). Therefore, the overall standard potential of MANGANIN® is assumed to be $+0.301\,\text{V}$. The standard potential of aluminium is -1.66 V. Thus, aluminium is the less noble material and will be oxidised (loss electrons) by MANGANIN®, causing an additional voltage between the two materials.

B Jiles-Atherton Model

B.1 Jiles-Atherton Hysteresis Model

The JA model generates a sigmoid-shaped hysteresis loop by considering the pinning sites on domain wall motions. An equation describing the sigmoid-shape was derived by the idea of energy change (E) per unit volume.

$$E = -\mu_0 m \cdot H, \tag{B.1}$$

where μ_0 is the vacuum permeability, m is the magnetic moment per unit area and H is the magnetic field. The coupling between domains in ferromagnetic solid is taken into account by introducing the parameter α.

$$E = -\mu_0 m \cdot (H + \alpha M), \tag{B.2}$$

where M is the bulk magnetisation. By substitution $H + \alpha M = H_\mathrm{e}$ in (B.2), where H_e is the effective field intensity the magnetisation can be derived as follows:

$$H_\mathrm{e} = M_\mathrm{s} \cdot f(H_\mathrm{e}). \tag{B.3}$$

Where M_s is the magnetisation state. This holds true only if the ferromagnetic material is in equilibrium state. This is only the case of a perfect solid ferromagnetic material with no impedance to change in magnetisation. For a real solid the ideal magnetisation characteristic M_an, also referred to as anhysteretic characteristic, can be described as follows:

$$M_\mathrm{an} = M_\mathrm{s} \cdot f(H_\mathrm{e}), \tag{B.4}$$

The function $f(H_\mathrm{e})$ is zero for $H_\mathrm{e} = 0$ and converges to 1 when H_e approaches infinity. This behaviour is described by the following function [JA84]:

$$M_\mathrm{an}(H_\mathrm{e}) = M_\mathrm{s} \left(\coth\left(\frac{H_\mathrm{e}}{a}\right) - \left(\frac{a}{H_\mathrm{e}}\right) \right), \tag{B.5}$$

where the parameter a affects the shape of the characteristic. Increasing a twisted the characteristic anti-clockwise and vice versa, whereas M_s influences the peak value of the characteristic at $H_\mathrm{e} \to \infty$.

So far no material defects, are considered, which cause the hysteretical characteristic. The JA attempts to take into account two domain wall movements. First, the domain wall displacement and second, the domain wall bulging. The domain wall displacement is an irreversible process

(M_{irr}), which is caused by a permanent displacement of the domain walls even if the external field is removed. The domain wall bulging is a reversible process (M_{rev}). Thus, the magnetisation M is the sum of both effects:

$$M = M_{\mathrm{irr}} + M_{\mathrm{rev}}. \tag{B.6}$$

The magnetisation of irreversible displacement (M_{irr}) of the domain wall, which cannot be deformed, just displaced, can be described with:

$$M_{\mathrm{irr}} = M_{\mathrm{an}} - \delta k \left(\frac{\mathrm{d}M_{\mathrm{irr}}}{\mathrm{d}H_{\mathrm{e}}} \right), \tag{B.7}$$

where δ considers the domain wall pinning opposes the change of the magnetisation with $\delta = +1$ for $\mathrm{d}H/\mathrm{d}t > 0$ and $\delta = -1$ for $\mathrm{d}H/\mathrm{d}t < 0$. Rearranging (B.7), results in:

$$\frac{\mathrm{d}M_{\mathrm{irr}}}{\mathrm{d}H_{\mathrm{e}}} = \frac{M_{\mathrm{an}} - M_{\mathrm{irr}}}{\delta k}. \tag{B.8}$$

Inserting $H_{\mathrm{e}} = H + \alpha M$ at both sides results in:

$$\frac{\mathrm{d}(H + \alpha M)}{\mathrm{d}M_{\mathrm{irr}}} = \frac{\delta k}{M_{\mathrm{an}} - M_{\mathrm{irr}}}, \tag{B.9}$$

whereas the left side can be rewritten to:

$$\frac{\mathrm{d}H}{\mathrm{d}M_{\mathrm{irr}}} + \alpha = \frac{\delta k}{M_{\mathrm{an}} - M_{\mathrm{irr}}}. \tag{B.10}$$

Subtracting α from both sides of the equation and reformulate the right site to a common denominator gives:

$$\frac{\mathrm{d}H}{\mathrm{d}M_{\mathrm{irr}}} = \frac{\delta k - \alpha(M_{\mathrm{an}} - M_{\mathrm{irr}})}{M_{\mathrm{an}} - M_{\mathrm{irr}}}. \tag{B.11}$$

Inverting both sides of (B.11) results in

$$\frac{\mathrm{d}M_{\mathrm{irr}}}{\mathrm{d}H} = \frac{M_{\mathrm{ab}} - M_{\mathrm{irr}}}{\delta k - \alpha(M_{\mathrm{an}} - M_{\mathrm{irr}})}. \tag{B.12}$$

The aforementioned assumption of rigid domain walls do not hold true in reality. The domain walls rather flex with increasing magnetic field before the domain wall moves. The domain wall flex is a reversible process, causing also reversible magnetisation change. This reversible magnetisation is

taking into account with the following equation, introducing the parameter c which is a measure for the domain wall before breaking free.

$$M_{\mathrm{rev}} = c(M_{\mathrm{an}} - M_{\mathrm{irr}}) \tag{B.13}$$

The reversible differential susceptibility component is:

$$\frac{\mathrm{d}M_{\mathrm{rev}}}{\mathrm{d}H} = c\left(\frac{\mathrm{d}M_{\mathrm{an}}}{\mathrm{d}H} - \frac{\mathrm{d}M_{\mathrm{irr}}}{\mathrm{d}H}\right). \tag{B.14}$$

Combining the reversible (B.12) and irreversible component (B.14) into one equation with the following steps. Starting with the sum of the differential susceptibility:

$$\frac{\mathrm{d}M}{\mathrm{d}H} = \frac{\mathrm{d}M_{\mathrm{irr}}}{\mathrm{d}H} + \frac{\mathrm{d}M_{\mathrm{rev}}}{\mathrm{d}H}. \tag{B.15}$$

Inserting (B.14) and (B.12) into (B.15) gives:

$$\frac{\mathrm{d}M}{\mathrm{d}H} = \frac{\mathrm{d}M_{\mathrm{irr}}}{\mathrm{d}H} + c\left(\frac{\mathrm{d}M_{\mathrm{an}}}{\mathrm{d}H} - \frac{\mathrm{d}M_{\mathrm{irr}}}{\mathrm{d}H}\right). \tag{B.16}$$

Reformulating (B.16) results in:

$$\frac{\mathrm{d}M}{\mathrm{d}H} = (1-c)\frac{\mathrm{d}M_{\mathrm{irr}}}{\mathrm{d}H} + c\frac{\mathrm{d}M_{\mathrm{an}}}{\mathrm{d}H}. \tag{B.17}$$

Inserting (B.12) into the last equation results in the final first-order non-linear differential equation of the JA model:

$$\frac{\mathrm{d}M}{\mathrm{d}H} = (1-c)\frac{M_{\mathrm{an}} - M_{\mathrm{irr}}}{\delta k - \alpha(M_{\mathrm{an}} - M_{\mathrm{irr}})} + c\frac{\mathrm{d}M_{\mathrm{an}}}{\mathrm{d}H}. \tag{B.18}$$

Further developments of the JA model and (B.18) exist. To mitigate the non-physical behaviour at the hysteresis loop tips, stated in [JTD92], the implementation of the parameter δ_{M} is proposed in [Dea94]. By multiplying (B.12) with the parameter δ_{M} the non-physical behaviour is mitigated.

$$\delta_{\mathrm{m}} = \begin{cases} 0 & H < 0 \text{ and } M_{\mathrm{an}} - M > 0 \\ 0 & H > 0 \text{ and } M_{\mathrm{an}} - M < 0 \\ 1 & \text{otherwise} \end{cases} \tag{B.19}$$

B.2 Jiles-Atherton Model Implementation

Figure B.1 depicts the JA hysteresis element implementation in MATLAB/Simulink, including the eddy current ($R_{\mathrm{fe}}/\mathrm{le}$) and rate dependent excess loss ($\mathrm{d}B/\mathrm{d}t$) components. A is the core element's cross-section area, N_{LV} the number of turns of the low-voltage winding, $k20$ scaling factor for the rate dependent excess loss. The factor $k20$ is roughly adjusted manually before the JA parameter optimisation and le is the mean magnetic path length, R_{fe} is the total iron path resistance.

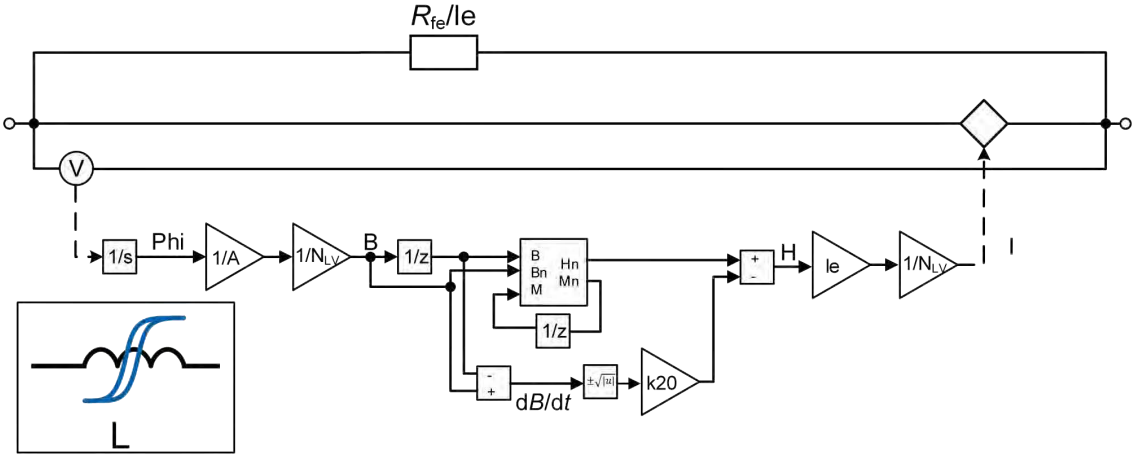

Figure B.1: JA hysteresis model implementation in MATLAB/Simulink, including eddy current and excess loss components.

B.3 Jiles-Atherton Parameter Deviation

The calculation procedure of the JA parameters is based on [JTD92]. In order to calculate the five JA model parameters in [JTD92] it is suggested to use the normal initial susceptibility χ'_{in}, the initial anhysteretic susceptibility χ'_{an}, the coercitivity H_{c}, the differential susceptibility at the coercive point χ'_{Hc}, the remanence M_{r}, the differential susceptibility at remanence χ'_{M}, and the coordinates H_{m}, M_{m} of the hysteresis loop tip, together with the differential susceptibility of the initial magnetisation characteristic at the hysteresis loop tip χ'_{m}. From these measured magnetic properties, the JA parameters can be calculated or can serve as first approximation.

B.3.1 Determine Jiles-Atherton Parameter M_{s}

The saturation magnetisation M_{s} is often known, or at least the region of M_{s} is known. Common values for M_{s} are in the range of 1.55 to $1.80 \cdot 10^6$ A/m.

B.3.2 Determine Jiles-Atherton Parameter c

The JA parameter c is determined from the normal initial susceptibility χ'_{in} and the initial anhysteretic susceptibility χ'_{an}:

$$\chi_{\mathrm{in}} = \left.\frac{\mathrm{d}M}{\mathrm{d}H}\right|_{H=0,M=0} = \frac{(1-c)M_{\mathrm{an}}}{k\delta - \alpha M_{\mathrm{an}}} + c\frac{\mathrm{d}M_{\mathrm{an}}}{\mathrm{d}H}. \tag{B.20}$$

Using (B.47) with $H_{\mathrm{e}} = H + \alpha M$ in (B.20) gives:

$$\chi_{\mathrm{in}} = \frac{(1-c)M_{\mathrm{s}}\left[coth\left(\frac{H}{a}\right) - \frac{a}{H}\right]}{k\delta - \alpha M_{\mathrm{s}}\left[coth\left(\frac{H}{a}\right) - \frac{a}{H}\right]} + m_{\mathrm{s}} \cdot \frac{c}{a}\left[1 - coth^2\left(\frac{H}{a}\right) + \frac{a^2}{H^2}\right], \tag{B.21}$$

taking into account for $H \to 0$ $\coth(H/a) - (a/H) \to 0$ results in:

$$\chi_{\mathrm{in}} = 0 + c\frac{\mathrm{d}M_{\mathrm{an}}}{\mathrm{d}H}. \tag{B.22}$$

Because $M = 0$ at the origin of the magnetisation characteristic,

$$\chi_{\mathrm{in}} = \frac{cM_{\mathrm{s}}}{3a}, \tag{B.23}$$

which can be solves for c:

$$c = \frac{3a\chi_{\mathrm{in}}}{M_{\mathrm{s}}}. \tag{B.24}$$

The initial susceptibility $\chi_{\mathrm{in}} = \mu_{\mathrm{r}} - 1$, thus approximating the initial μ_{r} of the magnetic material can be used to solve (B.24).

B.3.3 Determine the Relationship of the JA Parameter a and α

From (B.47) with $H_{\mathrm{e}} = H + \alpha M$ it can be seen that the JA parameters a and α are affected by χ_{an} as follows:

$$\chi_{\mathrm{an}} = \lim_{H,M\to 0}\left\{\frac{\mathrm{d}}{\mathrm{d}H}M_{\mathrm{an}}(h)\right\} = \frac{M_{\mathrm{s}}}{3a - \alpha M_{\mathrm{s}}}, \tag{B.25}$$

solving (B.25) a results in:

$$a = \frac{M_{\mathrm{s}}}{3}\left(\frac{1}{\chi_{\mathrm{an}}} + \alpha\right). \tag{B.26}$$

(B.26) is used as constrain for the further calculation of the JA parameters a and α.

B.3.4 Determine Jiles-Atherton Parameter k

The JA parameter k affects the area of the hysteresis characteristic and therefore the losses. The JA parameter k accounts for the pinning and therefore for the coercitivity of the material. The pinning force acts like a magnetic field opposing the external magnetic field H. For the derivation of k the conditions at the coercive point are considered. The differential susceptibility at the coercive point χ_c is assumed as maximum differential susceptibility χ_max, due to the natural of the hysteresis characteristic. Then χ_max can be described by:

$$\chi_\mathrm{max} = \frac{1}{k\delta - \alpha(M_\mathrm{an}(h_\mathrm{c}) - M_\mathrm{irr})}(M_\mathrm{an}(H_\mathrm{c}) - M_\mathrm{irr}) + c\left(\frac{\mathrm{d}M_\mathrm{an}(H_\mathrm{c})}{\mathrm{d}H} - \frac{\mathrm{d}M_\mathrm{irr}}{\mathrm{d}H}\right), \tag{B.27}$$

for the coercive point the following parameters apply: $\delta = 1$, $H = H_\mathrm{c}$, $M = 0$. Using these conditions in (B.27) gives:

$$k = \frac{M_\mathrm{an}(H_\mathrm{c}) - M_\mathrm{irr}}{\chi_\mathrm{max} - c\left(\frac{\mathrm{d}M_\mathrm{an}(H_\mathrm{c})}{\mathrm{d}H} - \frac{\mathrm{d}M_\mathrm{irr}}{\mathrm{d}H}\right)} + \alpha(M_\mathrm{an}(H_\mathrm{c}) - M_\mathrm{irr}). \tag{B.28}$$

For the further derivation of k the terms M_irr and $\mathrm{d}M_\mathrm{irr}/\mathrm{d}H$ at the coercive point can be expressed as function of $M_\mathrm{an}(H_\mathrm{c})$, χ_max, and $\mathrm{d}M_\mathrm{an}(H_\mathrm{c})/\mathrm{d}H$ with the following equations:

$$M = M_\mathrm{rev} + M_\mathrm{irr}, \tag{B.29}$$

with $M_\mathrm{rev} = c(M_\mathrm{an} - M_\mathrm{irr})$ (B.29) results in:

$$M = cM_\mathrm{an} + (1-c)M_\mathrm{irr}, \tag{B.30}$$

which can be reformulated to:

$$M_\mathrm{irr} = \frac{M - cM_\mathrm{an}}{1-c}, \tag{B.31}$$

With $M = 0$ at the coercive point, (B.31) results in:

$$M_\mathrm{irr} = -\frac{c}{1-c}M_\mathrm{an}(H_\mathrm{c}). \tag{B.32}$$

Differentiating (B.31) with respect to H and considering the following values at the coercive point $\mathrm{d}M(H_\mathrm{c})/\mathrm{d}H = \chi'_\mathrm{max}$:

$$\frac{\mathrm{d}M_\mathrm{irr}(H_\mathrm{c})}{\mathrm{d}H} = \frac{\chi_\mathrm{max}}{1-c} - \frac{c}{1-c}\cdot\frac{\mathrm{d}M_\mathrm{an}(H_\mathrm{c})}{\mathrm{d}H}. \tag{B.33}$$

Substituting (B.33) into (B.28) yields the following equation for k:

$$k = \frac{M_{\mathrm{an}}(H_{\mathrm{c}})}{\chi_{\mathrm{max}} - c\frac{\mathrm{d}M_{\mathrm{an}}(H_{\mathrm{c}})}{\mathrm{d}H}} \cdot \frac{1+\alpha}{1-c}. \tag{B.34}$$

B.3.5 Conditions at Remanence Point

The JA parameter α can be calculated if the parameters a, k and c are known, using the remanence M_{r}. Taking into account the conditions at the remanence point with $\delta = -1$, $H = 0$ and $M = M_{\mathrm{r}}$, with:

$$\frac{\mathrm{d}M}{\mathrm{d}H} = (1-c)\frac{M_{\mathrm{an}} - M_{\mathrm{irr}}}{k\delta - \alpha(M_{\mathrm{an}} - M_{\mathrm{irr}})} + c\frac{\mathrm{d}M_{\mathrm{an}}}{\mathrm{d}H}, \tag{B.35}$$

yields:

$$\chi_{\mathrm{r}} = \frac{M_{\mathrm{an}}(M_{\mathrm{r}}) - M_{\mathrm{irr}}}{-k - \alpha(M_{\mathrm{an}}(M_{\mathrm{r}}) - M_{\mathrm{irr}})} + c\left(\frac{\mathrm{d}M_{\mathrm{an}}(M_{\mathrm{r}})}{\mathrm{d}H} - \frac{\mathrm{d}M_{\mathrm{irr}}}{\mathrm{d}H}\right). \tag{B.36}$$

Taking into account that $M_{\mathrm{r}} = M_{\mathrm{rev}} + M_{\mathrm{irr}}$ and $M_{\mathrm{rev}} = c(M_{\mathrm{an}} - M_{\mathrm{irr}})$ the irreversible magnetisation can be expressed as follows:

$$M_{\mathrm{irr}} = \frac{M_{\mathrm{r}} - cM_{\mathrm{an}}(M_{\mathrm{r}})}{1-c}, \tag{B.37}$$

and

$$\frac{\mathrm{d}M_{\mathrm{irr}}}{\mathrm{d}H} = \frac{1}{1-c} \cdot \frac{\mathrm{d}M_{\mathrm{r}}}{\mathrm{d}H} - \frac{c}{1-c}\frac{\mathrm{d}M_{\mathrm{an}}(M_{\mathrm{r}})}{\mathrm{d}H}. \tag{B.38}$$

Substituting (B.38) into (B.36) yields:

$$\chi r = \frac{M_{\mathrm{an}}(M_{\mathrm{r}}) - M_{\mathrm{r}}}{-(1-c)k - \alpha(M_{\mathrm{an}}(M_{\mathrm{r}}) - M_{\mathrm{r}}} + \frac{c}{1-c} \cdot \left(\frac{\mathrm{d}M_{\mathrm{an}}(M_{\mathrm{r}})}{\mathrm{d}H} - \frac{\mathrm{d}M_{\mathrm{r}}}{\mathrm{d}H}\right), \tag{B.39}$$

which can be solved for M_{r}:

$$M_{\mathrm{r}} = M_{\mathrm{an}}(M_{\mathrm{r}}) + \frac{k}{\frac{\alpha}{1-c} + \frac{1}{\chi_{\mathrm{r}} - c\frac{\mathrm{d}M_{\mathrm{an}}(M_{\mathrm{r}})}{\mathrm{d}H}}}. \tag{B.40}$$

B.3.6 Determine Jiles-Atherton Parameter a and α at Hysteresis loop tips

The last step includes the explicit calculation of α and a by using the conditions at the hysteresis loop tip M_m and H_m. At the loop tips the following conditions are applied: $\delta = 1$, assuming the loop tip is close to saturation, the differential susceptibility of the initial magnetisation characteristic approaches the differential susceptibility of the anhysteretic characteristic $\mathrm{d}M/\mathrm{d}H \approx \mathrm{d}M_\mathrm{an}/\mathrm{d}H$. With the general equation for the irreversible magnetisation $M_\mathrm{irr} = (M - cM_\mathrm{an})/(1-c)$ the approximation yields $\mathrm{d}M_\mathrm{irr}/\mathrm{d}H = \mathrm{d}M/\mathrm{d}H = \mathrm{d}M_\mathrm{an}(H_\mathrm{m})/\mathrm{d}H$. Taking into account that $M_\mathrm{irr} = M_\mathrm{m}$ (B.36) yields:

$$\chi_\mathrm{m} = \frac{M_\mathrm{an}(H_\mathrm{m}) - M_\mathrm{m}}{k\delta - \alpha(M_\mathrm{an}(H_\mathrm{m}) - M_\mathrm{m})} + c\left(\frac{\mathrm{d}M_\mathrm{an}(H_\mathrm{m})}{\mathrm{d}H} - \frac{\mathrm{d}M_\mathrm{irr}(H_\mathrm{m})}{\mathrm{d}H}\right). \tag{B.41}$$

With the aforementioned approximations, the term on the right-hand side of (B.41) becomes zero and results in:

$$\chi_\mathrm{m} = \frac{M_\mathrm{an}(H_\mathrm{m}) - M_\mathrm{m}}{k\delta - \alpha(M_\mathrm{an}(H_\mathrm{m}) - M_\mathrm{m})}, \tag{B.42}$$

which can be reformulated for M_m:

$$M_\mathrm{m} = M_\mathrm{an}(H_\mathrm{m}) - \frac{(1-c)k\chi_\mathrm{m}}{\alpha\chi_\mathrm{m} + 1}. \tag{B.43}$$

Due to the dependency of the parameters and the derived equations, the JA parameters need to be derived iteratively. The parameter c is obtained from (B.24), whereas the JA parameters a, α and k are obtained with (B.34), (B.40), and (B.43) in an integrative procedure. With (B.26) and a seed value for α, a first estimation for a can be found. Afterwards, k is calculated using (B.34). The derived values for k, α and a from (B.40) are used subsequently in (B.43) to derive the values of α, a and k. This procedure for α, a and k is then repeated.

B.4 Inverse Jiles-Atherton Model

The implemented inverse JA model is based on [Sad+02] with implemented parameter δ_M to mitigate the non-physical behaviour at the hysteresis loop tips.

$$\Delta B = B(t + \Delta t) - B(t), \tag{B.44}$$

where $B(t)$ is the magnetic flux density known from the previous simulation step. Δ is a discrete simulation time step.

The magnetisation is calculates as follows:

$$M(t) = \frac{B(t)}{\mu_0} - H(t). \tag{B.45}$$

The effective magnetic field is given by:

$$H_\mathrm{e}(t) = H(t) - \alpha M(t), \tag{B.46}$$

$$M_\mathrm{an}(t) = M_\mathrm{s}\left(\coth\frac{H_\mathrm{e}(t)}{a} - \frac{a}{H_\mathrm{e}(t)}\right), \tag{B.47}$$

$$\frac{\mathrm{d}M_\mathrm{an}}{\mathrm{d}H_\mathrm{e}} = \frac{M_\mathrm{s}}{a}\left(1 - \coth^2\frac{H_\mathrm{e}(t)}{a} + \left(\frac{a}{H_\mathrm{e}(t)}\right)^2\right), \tag{B.48}$$

$$M_\mathrm{irr}(t) = \frac{M(t) - cM_\mathrm{an}(t)}{1-c}, \tag{B.49}$$

$$\delta_\mathrm{m} = \begin{cases} 0 & H < 0 \text{ and } M_\mathrm{an} - M > 0 \\ 0 & H > 0 \text{ and } M_\mathrm{an} - M < 0 \\ 1 & \text{otherwise} \end{cases} \tag{B.50}$$

$$\frac{\mathrm{d}M_\mathrm{irr}}{\mathrm{d}B_\mathrm{e}} = \delta_\mathrm{M}\frac{M_\mathrm{an}(t) - M_\mathrm{irr}(t)}{\mu_0 k\delta}, \tag{B.51}$$

$$\frac{\mathrm{d}M}{\mathrm{d}B} = \frac{(1-c)\frac{\mathrm{d}M_\mathrm{irr}}{\mathrm{d}B_\mathrm{e}} + \frac{c}{\mu_0}\cdot\frac{\mathrm{d}M_\mathrm{an}}{\mathrm{d}H_\mathrm{e}}}{1 + \mu_0(1-\alpha)(1-c)\frac{\mathrm{d}M_\mathrm{irr}}{\mathrm{d}B_\mathrm{e}} + c(1-\alpha\frac{\mathrm{d}M_\mathrm{an}}{\mathrm{d}H_\mathrm{e}})}, \tag{B.52}$$

$$M(t+\Delta t) = M(t) + \frac{\mathrm{d}M}{\mathrm{d}B}\Delta B, \tag{B.53}$$

$$H(t+\Delta t) = \frac{B(t+\Delta t)}{\mu_0} - M(t+\Delta t). \tag{B.54}$$

C Power Transformer Data

The apparent, active and non-active power was measured with the Dewetron DEWE2-A4 power analyser (**Chapter G.1**). **Figure C.1** depicts the defined transformer core dimensions.

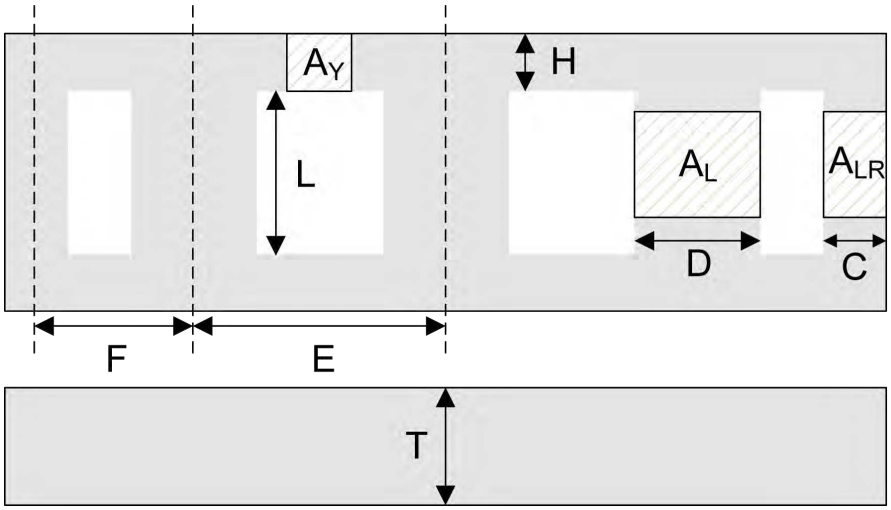

Figure C.1: Transformer core dimension nomenclature.

C.1 Transformer T3Sa

Transformer Nameplate

Manufacturing Year	1974
Manufacturer	EBG Elektro Bau AG Linz
Rated Frequency/Power	50 Hz/50 kVA
Vector Group	YNyn0, YNyn6, YNd5, YNd11, YNz5, YNz11
Primary/Secondary Rated Voltage rms, L-L	35,000 V/400 V
Primary/Secondary Rated Current rms	0.824 A/72.1 A
Primary/Tap Changer Position/Secondary Winding Turns	7730/2/51+51

Measured Transformer Data

Low-Voltage Winding Resistances 2A/2B/2C (1)	59.74/79.92/104.3 mΩ
High-Voltage Winding Resistances 1A/1B/1C (1)	282/277/287 Ω
Total no-load active power losses P	178.3 W
Total no-load apparent power S	650.3 VA
Total no-load non-active power N	625.46 var
Short circuit impedance Z_{12} (2)	0.228 Ω/phase
Zero-sequence impedance Z_0 (2)	2.244 Ω/phase @ 70.5 A
Winding capacity to ground C_H 1U/1V/1W (5)	3.51/2.30/2.98 nF

Transformer Core

Cross-section limb A_l/yoke A_y (3)	6740 mm^2/6740 mm^3
Window height L	330 mm
Distance limb to limb A	230 mm

Diameter limb/yoke	101 mm/101 mm
Core material & thickness	Thyssen Krupp ORIS89 0.27 mm
Core material density	7.65 g/cm^3
Core material spec. electric conductivity	48 $\mu\Omega$·cm
Min. saturation inductance limb/yoke [4]	1.746 T/1.746 T
Filling factor	0.955
Primary (HV) winding design	17 (axial) x 32 (radial) layered
Secondary (LV) winding design	2-layer flat

[1] OMICRON CPC100 @ 20°C 0.697 $\mu\Omega$ connection resistance | [2] secondary (LV) to primary (HV) winding | [3] filling factor included | [4] maximum allowed secondary voltage of 266.65 V_{rms} | [5] @ 50 Hz with OMICRON DIRANA

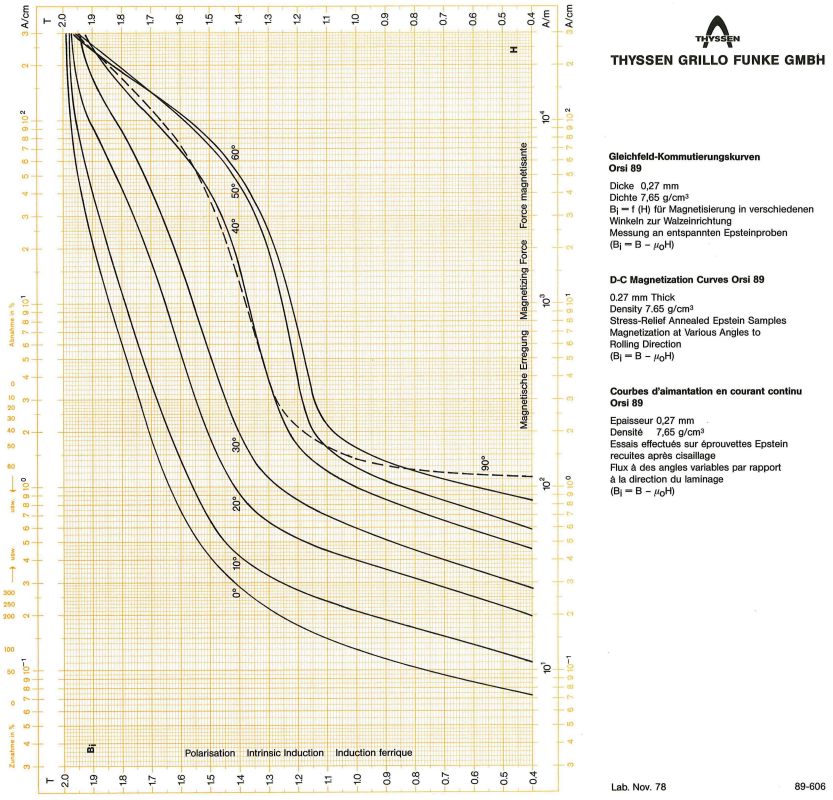

Figure C.2: DC magnetisation characteristic of T3Sa core material [Thy80]

C.2 Transformer T3Sb

Transformer Nameplate

Manufacturing Year	1990
Manufacturer	EBG Elektro Bau AG Linz
Rated Frequency/Power	50 Hz/50 kVA

Vector Group	YNyn0, YNyn6, YNd5, YNd11, YNz5, YNz11
Primary/Secondary Rated Voltage rms, L-L	34,965 V/420 V
Primary/Secondary Rated Current rms	0.87 A/68.7 A
Primary/Tap Changer Position/Secondary Winding Turns	7792/2/54+54
Measured Transformer Data	
Low-Voltage Winding Resistances 2A/2B/2C [1]	65.62/64.0/61.6 mΩ
High-Voltage Winding Resistances 1A/1B/1C [1]	227/230/222 Ω
Total no-load active power losses P	98.61 W
Total no-load apparent power S	187.44 VA
Total no-load non-active power N	159.41 var
Short-circuit impedance X_{12} [2]	0.114 Ω/phase
Zero-sequence impedance Z_0 [2]	3.35 Ω/phase @ 15.88 A/phase
Winding capacity to ground C_H/C_L [5]	1.043/2.131 nF
Transformer Core	
Cross-section limb A_l/yoke A_y [3]	6570 mm^2/6570 mm^3
Window height L	300 mm
Distance limb to limb A	233 mm
Diameter limb/yoke	102 mm/102 mm
Core material & thickness	M2H 0.30 mm
Min. saturation inductance limb/yoke [4]	2.03 T/2.03 T
Filling factor	0.965
Primary (HV) winding design	28 layered
Secondary (LV) winding design	2-layer flat

[1] OMICRON CPC100 @ 20°C 0.697 μΩ connection resistance | [2] secondary (LV) to primary (HV) winding | [3] filling factor included | [4] maximum allowed secondary voltage of 319.98 V_{rms} | [5] @ 50 Hz with OMICRON DIRANA

C.3 Transformer T5S

Transformer Nameplate	
Manufacturing Year	2021
Manufacturer	Siemens Energy AG Linz/Weiz
Rated Frequency/Power	50 Hz/60 kVA
Vector Group	YNyn0, YNyn6, YNd5, YNd111
Inner/Outer Rated Voltage rms, L-L	400 V/400 V
Inner/Outer Rated Current rms	60 A/60 A
Inner/Outer Winding Turns	122/122
Measured Transformer Data	
Inner Winding Resistances 2A/2B/2C (1-9 con.) [1]	54.12/53.26/54.14 mΩ

Outer Winding Resistances 1A/1B/1C (1-9 con.) [1]	68.5/68.56/68.53 mΩ
Total no-load active power losses P	99.58 W
Total no-load apparent power S	198.31 VA
Total no-load non-active power N	171.50 var
Short circuit reactance X_{12} [2]	0.133 Ω/phase
Zero-sequence impedance Z_0 [2]	9.8 Ω/phase @ 70.71 A
Winding capacity to ground C_H [5]	0.003457 nF

Transformer Core

Core cross-section	rectangular
Core joints	90 °
Cross-section wounded limbs A_l [3]	8,022 mm²
Cross-section unwounded limbs A_l/yoke A_y [2]	4,679.5 mm³/4,679.5 mm²
Window height L	500 mm
Distance wounded limb to limb A	400 mm
Distance un-wounded limb to wounded limb A	235 mm
Width limb/height yoke	120 mm/70 mm
Core material	CGO steel; ET 110-30LS (110-30M)
Core material coating on each side	1.5-3.0 μm
Core material density	7650 kg/m³
Core material spez. electric conductivity	$2.08 \cdot 10^6$ S/m
Min. saturation inductance limb/yoke [4]	1.8 T/1.8 T
Filling factor	0.955
Primary (HV) winding design	1 layered
Secondary (LV) winding design	1 layered

Further information on the transformer design can be found in the transformer design proposal "5-Schenkel Labortransformator".

[1] OMICRON CPC100 @ 20°C with 0.697 μΩ connection resistance | [2] secondary (LV) to primary (HV) winding | [3] filling factor included | [4] maximum allowed secondary voltage of 266.65 V_{rms} | [5] @ 50 Hz with OMICRON DIRANA

C.4 Transformer T3L

Transformer Nameplate

Manufacturing Year	2021
Manufacturer	Siemens Energy Austria GmbH Linz
Rated Frequency/Power	50 Hz/50 MVA
Vector Group	YNd5d5
Primary/Secondary/Tertiary Rated Voltage rms, L-L	110.0 kV/10.5 kV/6.0 kV
Primary/Secondary/Tertiary Rated Current rms	289 A/1,925 A/1,925 A

Nominal Primary/Secondary Winding Turns	497+109/105
Measured Transformer Data	
Nominal Primary Winding Resistances 1A-/1B-/1C-N (1)	423.8/424.4/423.9,mΩ
Secondary Winding Resistances 2A-B/2B-C/2C-A (1,2)	17.81/17.83/17.78,Ω
Tertiary Winding Resistances 3A-B/3B-C/3C-A (1)	6.79/6.82/6.83,Ω
Total no-load active power losses P (3)	13.08 kW
Total no-load apparent power S (3)	4.577 MVA
Total no-load non-active power Q (3)	5.575 Mvar
Short circuit impedance Z_{12} (4)	1.95+j53.55 Ω/phase
Zero-sequence impedance Z_0 (2)	1.3+j46.93 Ω/phase @ 164.6 A
Winding capacity to ground $C_H/C_M/C_L$ 5	3797/1433/13240 pF
Transformer Core	
Cross-section limb A_l/yoke A_y (6)	2065.49 cm^2/2065.49 cm^2
Window height L	1410 mm
Distance limb to limb A	1630 mm
Diameter limb/yoke	536 mm/536 mm
Core material	080-23 Domain Refined
Min. saturation inductance limb/yoke	2.03 T/2.03 T
Filling factor	0.965
Primary (HV) winding design	28 layered
Secondary (LV) winding design	2-layer flat

(1) at 20°C | (2) nominal tap changer position 10 | (3) @ 100 % U_n | (4) HV to MV | (5) @ 50 Hz with OMICRON CPC 100 | (6) filling factor included

C.5 Transformer T5La Auto Transformer

Transformer Nameplate	
Manufacturing Year	2021
Manufacturer	Siemens Energy AG Weiz
Rated Frequency/Power	60 Hz/600/600/75 MVA
Vector Group	YNa0d1
HV/LV/MV Rated Voltage rms, L-L	345 kV/141.5 kV/13.8 kV
HV/LV/MV Rated Current rms	1116 A/2448 A/3138 A
HV/LV/MV Winding Turns	284-340-396/236/40
Measured Transformer Data	
Mean HV Winding Resistance (OLTC: 17-9-1) (1)	125.02/115.75/125.02 mΩ
MV Winding Resistance (1)	31.990/32.011/31.972 mΩ
LV Winding Resistance (1)	5.301/5.258/5.232 mΩ
Total no-load active power losses P (@13,8 kV)	185.1 kW
Total no-load apparent power S (@13,8 kV)	198.81 kVA

Short circuit impedance X_{12} (OLTC:10)	53.55 Ω/phase
Zero-sequence impedance Z_0 (Z1NS)	23.15 Ω/phase @ 514.7 A
Winding capacity to ground C_H 1U/1V/1W, C_L 2U/2V/2W[2]	592/588/590, 726/720/723 pF
Transformer Core	
Core joints	45 °
Cross-section wounded/unwounded limbs A_l/yoke A_y[3]	75.41 dm^2 37.84 dm^2/42.93 dm^2
Window height L	2,900 mm
Diameter yoke H	580 mm
Diameter wounded limb D	1034 mm
Diameter un-wounded limb D	510 mm
Distance wounded limb to limb A	2060 mm
Distance un-wounded limb to wounded limb A	1315 mm
Core material	Posco 110-30M

[1] OMICRON Testrano @ 22.5°C | [2] Doble M4100 | [3] filling factor included

C.6 Transformer T5Lb GSU Transformer

Transformer Nameplate	
Manufacturing Year	2022
Manufacturer	Siemens Energy AG Weiz
Rated Frequency/Power	50 Hz/786/786 MVA
Vector Group	YNd5
HV/LV Rated Voltage rms, L-L	525 kV/22.8 kV
HV/LV Rated Current rms	843.3 A/19,903.4 A
HV(OLTC: 3)/LV Winding Turns	557+2x14/44
Measured Transformer Data	
HV Winding Resistance (OLTC: 1) [1]	251.3 mΩ
MV Winding Resistance [1]	7.55 mΩ
LV Winding Resistance [1]	10.22 mΩ
Total no-load active power losses P (@22.8 kV)	165.6 kW
Total no-load apparent power S (@22.8 kV)	185.4 kVA
Short circuit impedance X_{12} (OLTC:1)	111.66 Ω/phase
Zero-sequence impedance Z_0 (Z1N0 OLTC:1)	64.14 Ω/phase @ 656.95 A
Winding capacity to ground C_H, C_L [2]	16185.3 pF/0.0553 μF
Transformer Core	
Core joints	45 °
Cross-section wounded/unwounded limbs A_L/main yoke A_Y [3]	137.41 dm^3 69.23 dm^2/78.75 dm^3

Window height L	2,590 mm
Distance E wounded limb to limb A	2328 mm
Distance F un-wounded limb to wounded limb A	1,539 mm
Core material	080-23DR (0.23 mm grain oriented HiB silicon steel laser treated)

(1) Agilent Datalogger, Fluke 8846A @ 20°C | (2) HV/LV to LV/HV+tank @ 10 kV | (3) filling factor 0.965 included

D Power Amplifier Characteristic Data

All measurements are performed with the Regatron full 4-Q grid simulators switched power amplifiers connected in parallel or on one single power amplifier. In both cases, the 'DC rejection' is turned on in the control of the power amplifier. This option is recommended by the manufacturer of the power amplifier if inductive components are connected to the amplifiers. Also, the neutral conductor N and PE should be connected together, because the power amplifier uses the PE conductor as control reference.

AC load side ratings

Power Range	0 - 30 kVA
Voltage Range	0 - 305 $V_{rms,L-N}$
Current Range	3 x 0 - 43 A
Frequency Range	0 - 1 kHz
Modulation Bandwidth	5 kHz
DC Offset	$\leq$ 10 mV

Static Accuracy

Voltage @50/60 Hz	0.05 % F.S.
Voltage	$\leq$ 1.5 V
Frequency	2 mHz
Phase Angle	1 °

DC Ripple and Noise

16 Hz - 200 kHz	230 mV_{rms}
9 kHz - 20 MHz	700 mV_{p-p}

Figure D.1: Power amplifiers in power hardware-in-the-loop laboratory.

E Audio and Acoustic Analyser

For the transformer sound level measurement, the electroacoustic equipment according to **Table E.1** was used, which fulfils the requirements of class 1 according to [IEC01c].

Table E.1: Measurement system component tolerances.

Device	**Specific Data**
Audio Recorder	NTI XL2
Microphone	NTI M2230
Sample Rate	48 kHz
Calibrator	Brüel & Kjaer 4231
Calibration accuracy	±0.2 dB
Microphone	NTI MA220
Frequency Range	5 Hz - 20 kHz
Frequency response tolerance (20 Hz - 4 kHz)	±1 dB
Frequency response tolerance (4 Hz - 10 kHz)	±1.5 dB

F DC Source / Rectifier

A 230 V/230 V isolation transformer is used to supply a full-wave rectifier (GBPC2506) with smoothing capacitor (FELSIC 2200 μF) to superimpose a DC between the high-voltage neutrals during the B2B tests in the laboratory. The schematic and a figure of the DC source are depicted in **Figure F.1** and in **Figure F.2** respectively.

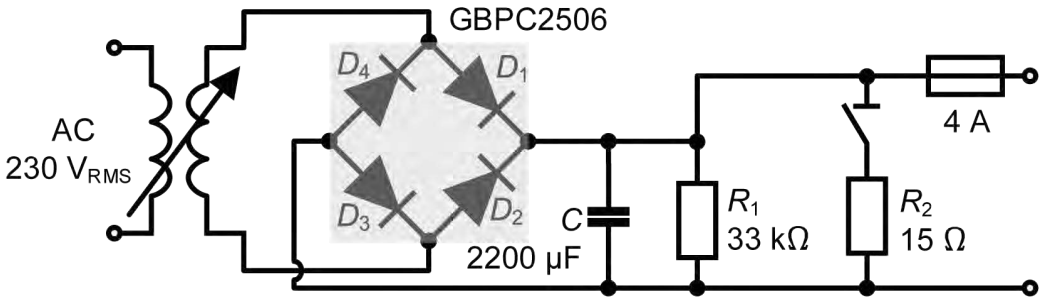

Figure F.1: Schematic of DC source used during B2B laboratory tests.

Figure F.2: Figure of the full-wave rectifier and the smoothing capacitor with parallel resistor R_1.

G Transformer Laboratory Measurement System

G.1 Data Acquisition System DEWETRON DEWE2-A4

As data acquisition system, the Dewetron DEWE2-A4 power analyser was used, with a sample frequency of 10 kHz. The used voltage measurement channels and signals are listed in **Table G.1**. The TRION-2402-V module was calibrated on 2020-08-25.

Table G.1: Dewetron voltage modules and measurement setup.

Voltage Module	**Measurement Point**	**Measurement Range** in V
DAQP-HV	voltage A/B/C_{LV},	$\pm$800 V
DAQP-LV	current CA MN38 DC shunt A/B/C_{LV}	$\pm$2.5 V
TRION-2402-V	voltage A/B/C_{HV}	$\pm$100 V

G.2 Measurement Probes and Shunt

Table G.2 lists measurement probes used in the laboratory measurements. For further analysis, the current from current clamps are used. A comparison of deviation over the current frequency between the current clamp Chauvin Arnoux MN38 and the Lumel DC shunt (100 A/60 mV) was done for a short-circuit test of T3Sb. The amplitude and phase deviation at 1 kHz is below 100 mA and 0.48 ° at 10 A peak current per phase, whereas these values are within the accuracy of the current clamp ($\leq 2.5\% + 5\,\mathrm{mV}$, $\leq 5°$) and the DC shunt ($0.2\,\%$). Also, the comparison between the shunt and Chauvin Arnoux MN38 clamp in the frequency spectrum of the current reveals nearly the same spectrum up tp 1 kHz. Comparing the power measurement, the largest deviation was observed in the fundamental active power at 1 kHz with 685.22 mW for the Chauvin Arnoux MN38 current clamp and 4.48 W for the DC shunt. This deviation can be explained by the frequency measurement range of the Chauvin Arnoux MN3, which is specified between 40 Hz and 10 kHz. Therefore, the current frequency spectrum below 40 Hz cannot be measured, whereas this range is measured via the shunt. The high-voltage probe Fluke 80K-40 has a measurement accuracy for 60 Hz AC of 5 % [Flu97]. A frequency sweep from 50 Hz to 1,000 Hz reveals a high damping of the voltage amplitude for frequencies above 50 Hz. Therefore, the measured voltage with probes is only used for proof-of-concept measurements.

Table G.2: Dewetron voltage modules and measurement setup.

Probe Type	**Product Name**	**Conversion Ratio**
Voltage	Fluke 80k-40	1:1000 V
Current	Chauvin Arnoux MN38	100 A/V, 10 A/V
Current	Chauvin Arnoux E3N	100 A/V, 10 A/V
Current	Chauvin Arnoux C173	1 mV/A
Shunt	Lumel DC 100 A/60 mV	1:1666.67 A/V

G.3 Power Measurement

For the power measurement, with an accessible dedicated neutral conductor, the voltage between the terminal connection and the neutral conductor is used. In case of delta connected windings, the line-to-line voltage is used for the power calculation. The power calculation was done in the measurement system with the software Oxygen 5.7. All voltages were measured from line-to-neutral. As current signal for the power calculation the signal from the current clamps were used. The power calculation in the Oxgyen 5.7 software is done applying the IEEE Standard 1459 [III10].

Figure G.1 depicts the measured phase currents with the Lumel DC shunts and the Chauvin Arnoux MN38 current clamps during the short-circuit test of transformer T3Sb at 50 Hz. The phase shift between the signal from the shunt and current clamp is 1.8°, 3.6°, and 5.4° for phase A, B and C, respectively. The normalised deviation between the waveforms of the shunt and current clamp of phase B reveals a constant offset in one of the measurement channels. These values are almost all within the range of the specified phase shift of the Chauvin Arnoux current clamp [Cha22]. The phase shift between the waveforms of the neutral conductor is 99°, whereas no phase shift is specified for the current clamps below 10 A.

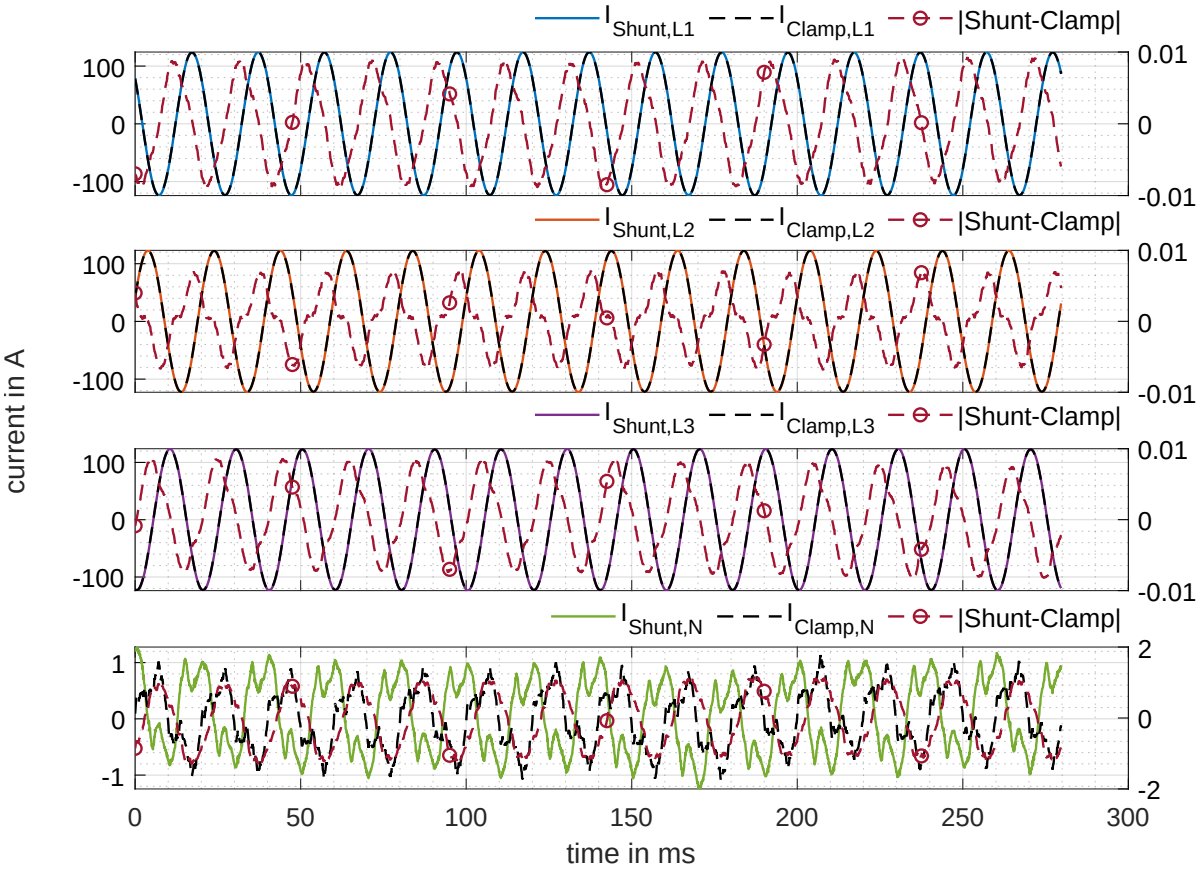

Figure G.1: Deviation between currents measured with Chauvin Arnoux MN38 and Lumel DC 100 A/60 mV over current @ 50 Hz.

Figure G.2 depicts the deviation between the calculated power, using the Chauvin Arnoux current

clamps, and the Lumel DC shunts, as well as the resulting power factor. The power factor, using the DC shunts, is 2 % lower than the power factor measured with the current clamps.

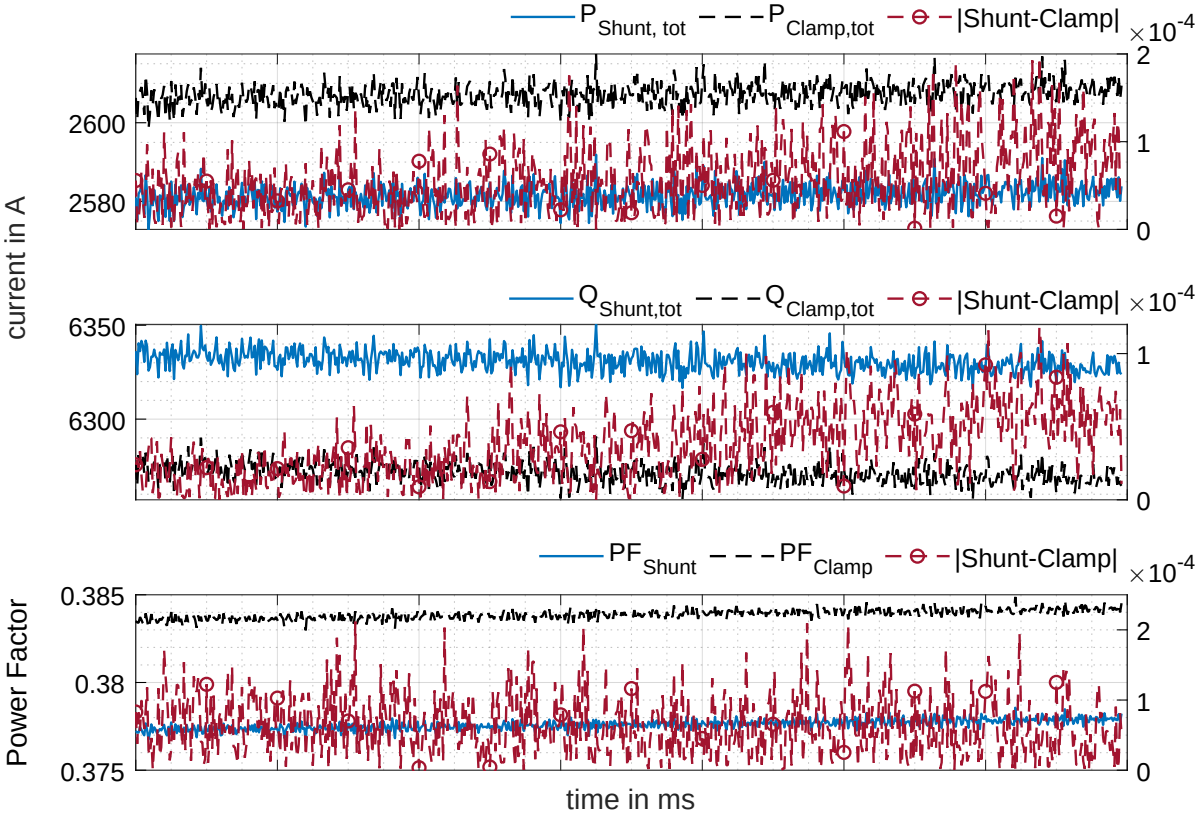

Figure G.2: Deviation of Power and Power Factor between Chauvin Arnoux MN38 and Lumel DC 100 A/60 mV over current @ 50 Hz.

Figure G.3 depicts the frequency spectrum of the current clamps and the shunts. The frequency spectrum with both measurement equipments coincides. The maximum deviation of the normalised current amplitude is below $2.7 \cdot 10^{-4}$.

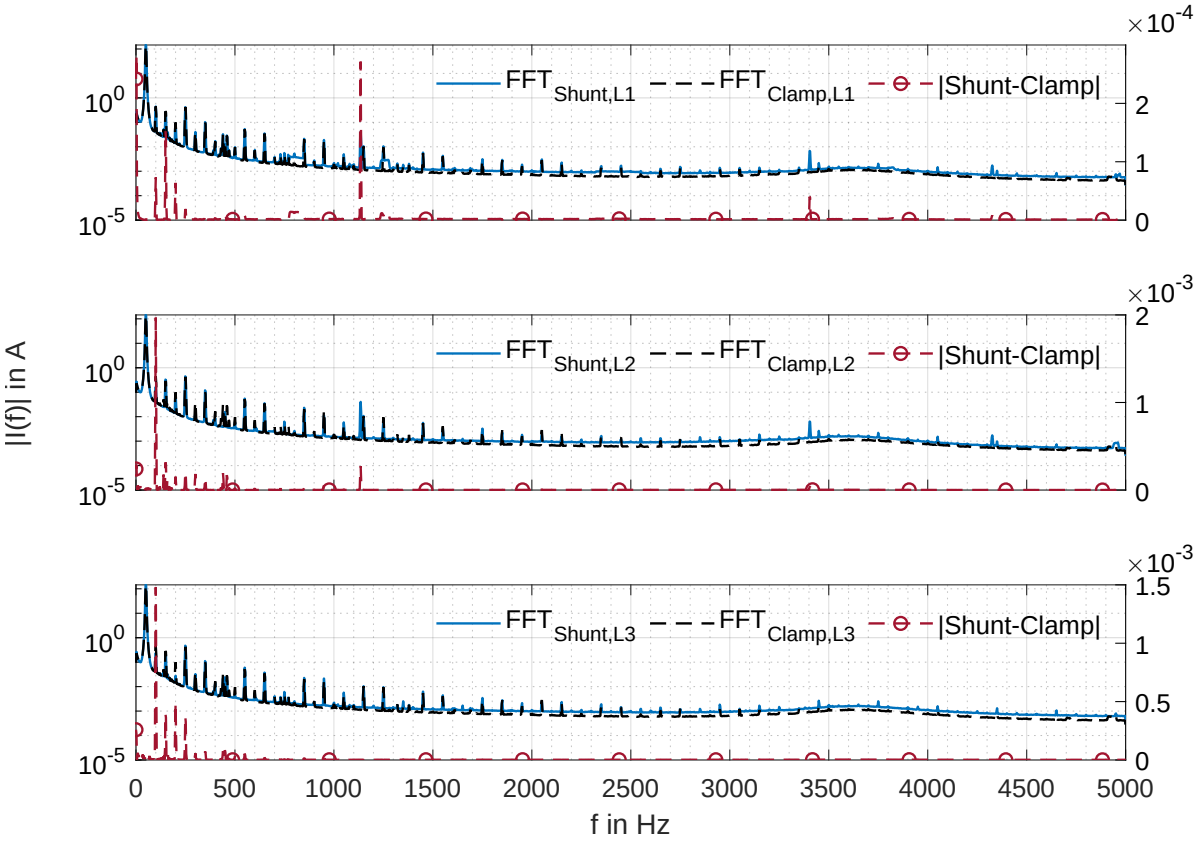

Figure G.3: Single-side amplitude spectrum of phase currents measured with Chauvin Arnoux MN38 current clamps and Lumel DC 100 A/60 mV shunts over frequency.

G.3.1 IEEE 1459 Power Calculation

The IEEE Standard 1459 [III10] provides a definition for the power calculation in multi-wire systems during unbalanced and non-sinusoidal conditions. During unbalanced three-phase four wire system, triplen harmonics can form in the neutral conductor. Therefore, the neutral conductor needs to be taking into account during the power analysis.

Figure G.4 depicts the power separation of apparent power S into active power P, harmonic reactive power Q_h, reactive power Q and distortion reactive power D.

Note, that the constants need to be adjusted, if more or less than three plus one neutral conductor are used.

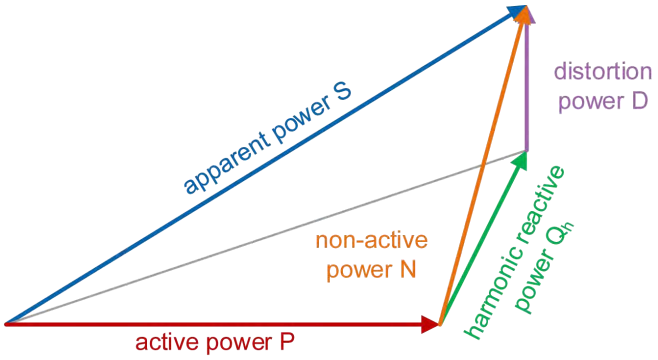

Figure G.4: Extended power triangle.

For the further power calculation [III10] introduces an effective current I_e and voltage V_e.

$$I_\mathrm{e} = \sqrt{\frac{1}{3}(I_\mathrm{a}^2 + I_\mathrm{b}^2 + I_\mathrm{c}^2 + \rho I_\mathrm{n}^2)}, \tag{G.1}$$

where $\rho = r_\mathrm{n}/r$ with the phase conductor resistance r and the neutral conductor resistance r.

The effective voltage V_e is given by:

$$V_\mathrm{e} = \sqrt{\frac{3(V_\mathrm{a}^2 + V_\mathrm{b}^2 + V_\mathrm{c}^2) + \xi(V_\mathrm{ab}^2 + V_\mathrm{bc}^2 + V_\mathrm{ca}^2)}{9(1+\xi)}}, \tag{G.2}$$

where

$$\xi = \frac{P_\Delta}{P_\mathrm{Y}} = \frac{9V_\mathrm{e}^2}{R_\Delta} \cdot \frac{R_\mathrm{Y}}{3V_\mathrm{e}^2} = \frac{3R_\mathrm{Y}}{R_\Delta}, \tag{G.3}$$

with the effective line-to-neutral voltage V_e. If the ration ξ is unknown, it is recommended to assume $\xi = 1.0$ [III10]. With this assumption (G.2) yields:

$$V_\mathrm{e} = \sqrt{\frac{3(V_\mathrm{a}^2 + V_\mathrm{b}^2 + V_\mathrm{c}^2) + \xi(V_\mathrm{ab}^2 + V_\mathrm{bc}^2 + V_\mathrm{ca}^2)}{18}}. \tag{G.4}$$

A further simplification of (G.4), assuming the line-to-neutral voltages are with the range of $\pm 10\,\%$, yields:

$$V_\mathrm{e} = \sqrt{\frac{V_\mathrm{ab}^2 + V_\mathrm{bc}^2 + V_\mathrm{ca}^2}{9}}, \tag{G.5}$$

which results in an error less than 0.2 %. The effective apparent power is calculated by:

$$S_{\mathrm{e}} = 3V_{\mathrm{e}}I_{\mathrm{e}}. \tag{G.6}$$

The calculation of the power components is based on the separation between fundamental effective and non-fundamental effective current and voltage components. With further simplification explained in [III10], the current and voltage components are calculated as follows, assuming the ratios ρ_1, $\rho_1\mathrm{h}$ are unknown and therefore assumed to be 1.0 (the further definition can be found in [III10]). This simplification yields:

$$I_{\mathrm{e}} = \sqrt{\frac{I_{\mathrm{a}}^2 + I_{\mathrm{b}}^2 + I_{\mathrm{c}}^2 + I_{\mathrm{n}}^2}{3}}, \tag{G.7}$$

$$I_{\mathrm{e1}} = \sqrt{\frac{I_{\mathrm{a1}}^2 + I_{\mathrm{b1}}^2 + I_{\mathrm{c1}}^2 + I_{\mathrm{n1}}^2}{3}}, \tag{G.8}$$

$$I_{\mathrm{eH}} = \sqrt{\frac{I_{\mathrm{aH}}^2 + I_{\mathrm{bH}}^2 + I_{\mathrm{cH}}^2 + I_{\mathrm{nH}}^2}{3}} = \sqrt{I_{\mathrm{e}}^2 - I_{\mathrm{e1}}^2}, \tag{G.9}$$

$$V_{\mathrm{e}} = \sqrt{\frac{3(V_{\mathrm{a}}^2 + V_{\mathrm{b}}^2 + V_{\mathrm{c}}^2) + (V_{\mathrm{ab}}^2 + V_{\mathrm{bc}}^2 + V_{\mathrm{ca}}^2)}{18}}, \tag{G.10}$$

$$V_{\mathrm{e}} = \sqrt{\frac{3(V_{\mathrm{a1}}^2 + V_{\mathrm{b1}}^2 + V_{\mathrm{c1}}^2) + (V_{\mathrm{ab1}}^2 + V_{\mathrm{bc1}}^2 + V_{\mathrm{ca1}}^2)}{18}}, \tag{G.11}$$

$$V_{\mathrm{eH}} = \sqrt{\frac{3(V_{\mathrm{aH}}^2 + V_{\mathrm{bH}}^2 + V_{\mathrm{cH}}^2) + (V_{\mathrm{abH}}^2 + V_{\mathrm{bcH}}^2 + V_{\mathrm{caH}}^2)}{18}}. \tag{G.12}$$

Therefore, the effective apparent power consists of four terms:

$$S_{\mathrm{e}}^2 = (3V_{\mathrm{e1}}I_{\mathrm{e1}})^2 + (3V_{\mathrm{e1}}I_{\mathrm{eH}})^2 + (3V_{\mathrm{eh}}I_{\mathrm{e1}})^2 + (3V_{\mathrm{eH}}I_{\mathrm{eH}})^2. \tag{G.13}$$

The non-fundamental effective apparent power S_{eN} yields:

$$S_{\mathrm{eN}} = \sqrt{S_{\mathrm{e}}^2 - S_{\mathrm{e1}}^2} = \sqrt{D_{\mathrm{e1}}^2 + D_{\mathrm{eV}}^2 + S_{\mathrm{eH}}^2}, \tag{G.14}$$

with D_{e1} is the effective current distortion power, D_{eV} is the effective voltage distortion power and S_{eH} is the effective harmonic apparent power. Whereas the terms can be calculated as follows:

$$D_{\mathrm{e1}} = 3V_{\mathrm{e1}}I_{\mathrm{eH}}, \tag{G.15}$$

$$D_{\mathrm{eV}} = 3V_{\mathrm{eH}}I_{\mathrm{e1}}, \tag{G.16}$$

$$S_{\mathrm{eH}} = 3V_{\mathrm{eH}}I_{\mathrm{eH}}, \tag{G.17}$$

The distortion power is yields:

$$D_{\mathrm{eH}} = \sqrt{S_{\mathrm{eH}}^2 + P_{\mathrm{H}}^2}, \tag{G.18}$$

whereas the effective total apparent power S_{e} can be split up into active power P (in W) and non-active power N in (var).

$$S_{\mathrm{e}}^2 = P^2 + N^2 \tag{G.19}$$

The power factor PF yields:

$$PF = \frac{P}{S_{\mathrm{e}}}, \tag{G.20}$$

whereas for non-sinusoidal conditions the following holds true:

$$PF \neq \cos(\varphi), \tag{G.21}$$

with $S_{\mathrm{e}} > P$.

The arithmetic mean active, reactive and apparent power from measurements and simulations in this thesis are calculated in MATLAB/Simulink, using the single phase 'Power Measurement' block from the library 'Simscape/Electrical/Control/Measurements' [Mat22], which uses the current and voltage wave forms as input and calculates the active and reactive power harmonic components.

The active and reactive power is calculated for each harmonic $k = 0, 1, 2, 3, ...$, where $k = 0$ is the DC component and $k = 1$ corresponds to th fundamental frequency component.

$$P_{\mathrm{k}} + \mathrm{j}Q_{\mathrm{k}} = G\left(U_{\mathrm{k}}e^{\mathrm{j}\theta_{\mathrm{U,k}}}\right)\left(\overline{I_{\mathrm{k}}e^{\mathrm{j}\theta_{\mathrm{I,k}}}}\right), \tag{G.22}$$

with

$$U_k e^{\mathrm{j}\theta_{U,k}} = \frac{2}{\mathrm{T}}\int_{t-\mathrm{T}}^{t} U(t)\sin(2\pi k f_{\mathrm{b}} t)\mathrm{d}t + \mathrm{j}\frac{2}{\mathrm{T}}\int_{t-\mathrm{T}}^{t} U(t)\cos(2\pi k f_{\mathrm{b}} t)\mathrm{d}t, \tag{G.23}$$

$$I_k e^{\mathrm{j}\theta_{I,k}} = \frac{2}{\mathrm{T}} \int_{t-\mathrm{T}}^{t} I(t)\sin(2\pi k f_\mathrm{b} t)\mathrm{d}t + \mathrm{j}\frac{2}{\mathrm{T}} \int_{t-\mathrm{T}}^{t} I(t)\cos(2\pi k f_\mathrm{b} t)\mathrm{d}t. \tag{G.24}$$

In the phasor equations, T is the inverse of the base frequency f_b, which is a fixed pre-defined value. G in (G.22) equals 0.25 for the DC component ($k = 0$) and 0.5 for the fundamental and harmonics ($k > 0$). $G = 0.5$ results from complex power calculation $\underline{S} = \underline{U} \cdot \underline{I}^*$. Because the current and voltage amplitudes are larger by factor $\sqrt{2}$, $\underline{U} = \hat{u}/\sqrt{2}$ and $\underline{I} = \hat{i}/\sqrt{2}$, the multiplication yields the factor 2 in the denominator. $G = 0.25$ for the DC component results from the instantaneous power formulation $p(t) = u(t) \cdot i(t) = \Re(\underline{u}) \cdot \Re(\underline{i})$, which can be reformulated with the relation $\Re(\underline{a}) = 1/2 \cdot (\underline{a} + \underline{a}^*)$. Thus, $p(t) = 1/4 \cdot (\underline{u} + \underline{u}^*) \cdot (\underline{i} + \underline{i}^*)$. The total active power P and reactive power Q is defined as follows

$$P = \sum_{k=0}^{n} P_k, \tag{G.25}$$

$$Q = \sum_{k=1}^{n} Q_k, \tag{G.26}$$

excluding the DC component ($k = 0$) in case of the reactive power, because DC only contributes to active power.

G.3.2 Not Standardised Power Calculation Methods

Besides the standardised power calculation approaches mentioned in the section before, different other approaches are discussed and developed. The following list attempts to give a general overview of the other proposed methods. A comparison of different theories can be found in [Wil11]. A comparison of different power meters with different operation principle can be found in [FL92]. A review of definitions and physical meaning of powers in non-sinusoidal conditions can be found in [Ema90].

- General Power Theory [GM12], which is based on compensating power
- Power definition by the mean of the Poynting vector [FLM01; Ema07; LQC12]

H Space Weather

H.1 Magnetospheric Current Systems

The region 1 field-aligned Birkenland currents (schematic in **Figure H.1**) are dominated by electrons and can penetrate into the ionosphere at altitudes of 100 km to 150 km, where they can become visible as Aurora. Note that Auroras are particles from the magnetosphere precipitating into the polar regions of the earth, and not only particles from the Sun.

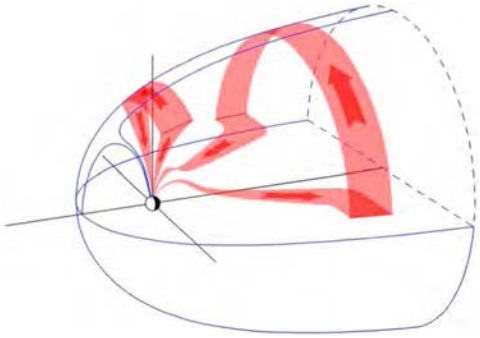

Figure H.1: Region 1 field-aligned currents [GLD18].

In the polar region, the inward and outward orientated Birkenland currents (region 1 field) are connected by the Pedersen currents. On the dayside and Northern Hemisphere in north-south direction; on the nightside of the Northern Hemisphere in south-north direction. The Pedersen currents itself cause the Hall currents in east-west and west-east direction, respectively. Those currents are also known as the polar ring current system. In the Southern Hemisphere an analogue current system exists. **Figure H.2a** illustrates the polar ring current system of the northern earth hemisphere [Rus05].

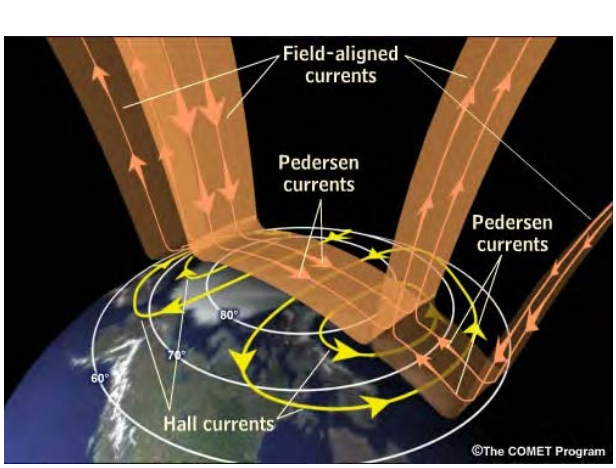

(a) Polar ring current system of northern earth hemisphere [Rus05].

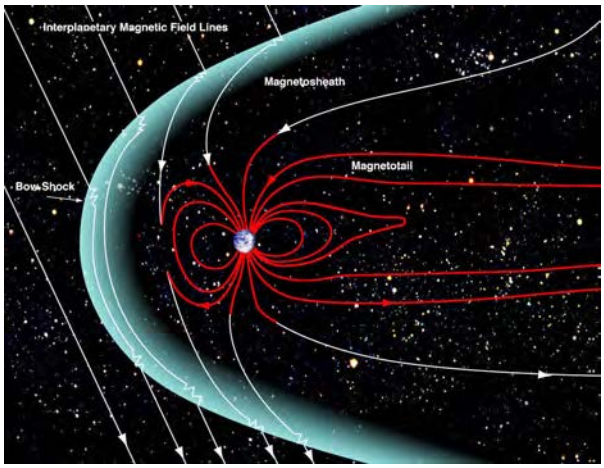

(b) Structure of magnetosphere [Nas17].

Figure H.2: Current systems and structure of magnetosphere.

The magnetosphere is highly susceptible to upstream solar wind conditions. Southward interplanetary magnetic fields (IMFs) cause magnetic reconnection between the magnetospheric field (**Figure H.3A**, red line) and the solar wind magnetic field (**Figure H.3A**, blue line).

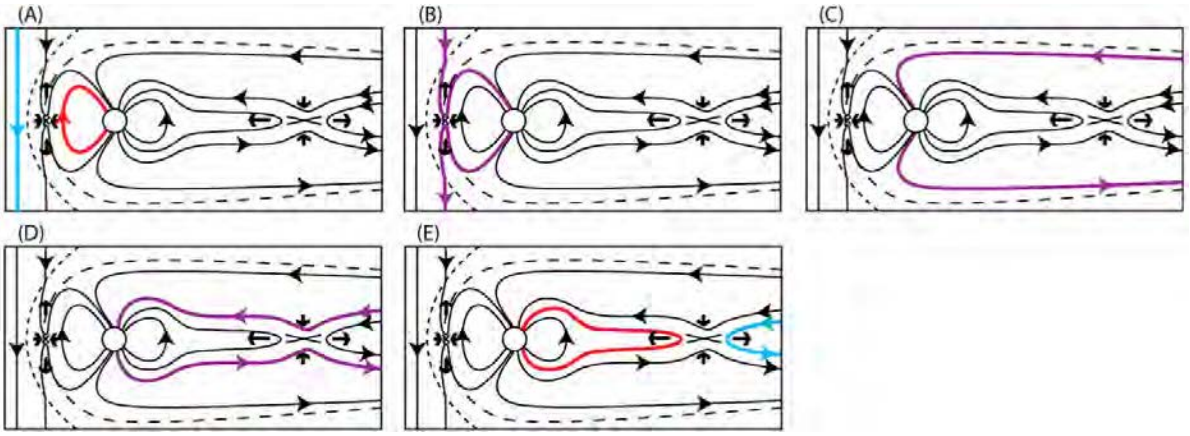

Figure H.3: Dungey cycle [Eas+15].

This reconnection causes open magnetic field lines with connection to the earth on one end (**Figure H.3B**, purple line). The open magnetic field lines move via the polar caps to the nightside and transport plasma towards the poles, through the cusps and into the magnetotail. This causes magnetic flux accumulation in the tail. Magnetic reconnection via the tail current sheet returns plasma on closed field lines (**Figure H.3E**, red line) to the nightside of the earth. This basic cycle is known as Dungey cycle [Dun61]. Whereas the Dungey cycle do not explain the highly dynamic processes in the magnetosphere. Region 1 current system varies with the IMF strength and orientation [LCF90]. The region 2 current system has changes with longer timescales [Hor+03].

Periodic releases of open flux in the magnetotail and stored energy in the lobe magnetic field causes magnetospheric substorms, which causes magnetic field disturbances in the magnetosphere, especially on the nightside. These substorms are also called Substorm Current Wedge (SCW) and last in a range of hours. The upward and downward current of the SCW running in the same region as the boundaries of the auroral bulge. The auroral bulge forms the nightside auroral oval during the substorm onset. Auroral substorms start with a transition of the solar wind from day- to nightside magnetopause. The transition takes place by magnetic reconnections, as indicated in **Figure H.3**. This transition occurs in the timescale of tens of minutes. During the second phase, the current sheet thickness is reduced upon a point where magnetic reconnections occur. The reconnections form two plasma jets with opposite motion direction, one towards the earth and the other one away from the earth. The plasma cloud moving away from the earth is also called plasmoid. This flux and energy transition causes currents from the magnetotail into the ionosphere and energy transport into the earth atmosphere, where they can become visible as Aurora Borealis. These transitions last in the range of ten minutes. During the recovery phase, magnetic field is transported from the tail to the dayside via the dawn- and duskside. Detailed information on substorm dynamics can be found in [SAN12]. **Figure H.4** shows a simplified schematic of the SCW current paths.

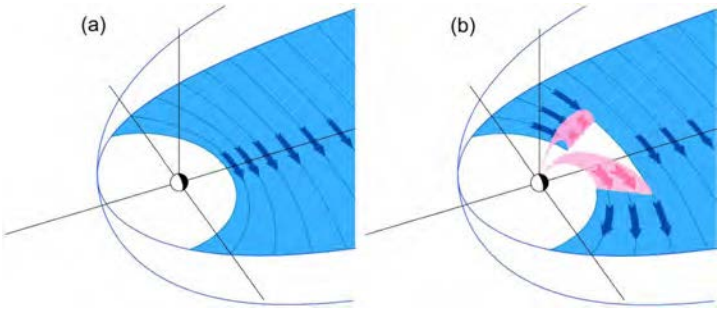

Figure H.4: SCW development; SCW field-aligned currents diverting a part of the tail current [GLD18].

Geomagnetic storms result from convection of plasma from the tail through the inner magnetosphere and out the dayside of the magnetopause. This convection can be caused e. g. by CME. Geomagnetic storms usually start with the dayside compression of the magnetosphere in the time range of minutes, whereas the compression of the nightside occurs in a longer scale of hours. After the compression, the magnetosphere expands back to the original size, which happens in the range of days. **Figure H.5** depicts the Dst value and the storm phases. The Dst minimum of about -150 nT indicates a magnetic field weakening by the ring current, which corresponds to a ring current of many million amps. This enhanced ring current is caused by the injection of energetic particles into the inner magnetosphere [PB04]. **Figure H.6** illustrates the current path transition of the near earth nightside region via the different current systems during geomagnetic storms. During the recovery phase, the ring current decays. One possible main loss process is that of the exchange with exospheric neutral hydrogen atoms. Due to the expected shorter lifetime of oxygen atoms, compared to hydrogen atoms, the recovery can be distinct into two phases. A rapid decay rate followed by a slower decay rate. The second possible main loss process is the that the rapid phase during the recovery is caused by drift induced removal of ring current particles from the inner magnetosphere. A sudden initial increase of the magnetic field can occur during the initial phase of the storm. A sudden impulse (SI) is when there is a short increase in the magnetic field that is not followed by a magnetic storm. If it is followed by a magnetic storm, it is referred to as SSC [PB04].

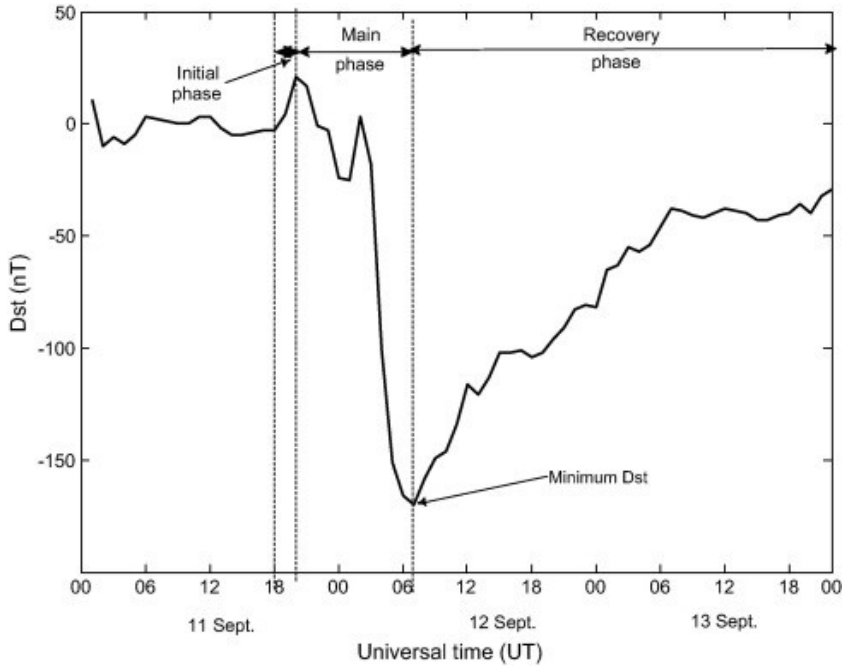

Figure H.5: Geomagnetic storm phases [OO18].

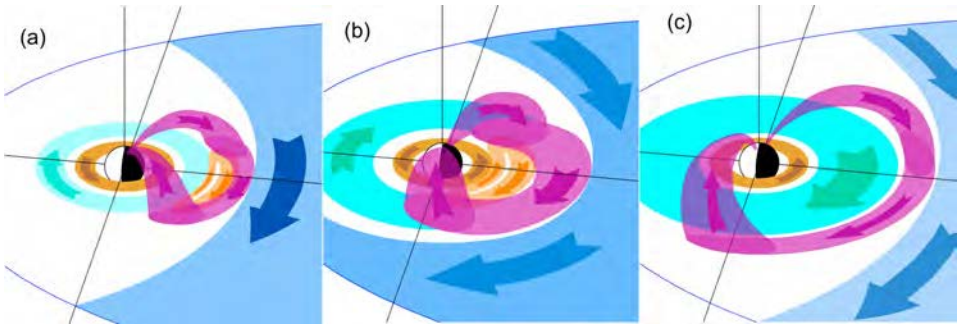

Figure H.6: current path transition of near earth nightside region due to geomagnetic storms [GLD18].

In rare cases, a northward IMF can also trigger geomagnetic storms. The Bz component of the IMF is the major control factor for the geomagnetic activity. The energy availability and the process of energy transportation into the magnetosphere [Sor+19] during this IMF condition are in focus of ongoing research. **Figure H.8** depicts the magnetic field lines in the magnetosheath during northward IMF conditions. Large magnetic field fluctuations at high latitudes and a low magnetic field strength create favourable conditions for field line interconnection and an area where magnetosheath plasma can penetrate into the magnetosphere [Ant+12]. During the appearance of a strong northward IMF the Bz component, can cause an additional current system (**Figure H.7b**). The northward Bz (NBZ) current is driven by plasma entering through the magnetopause during northward IMF. Further information on this entering process can be found in [Eas+15].

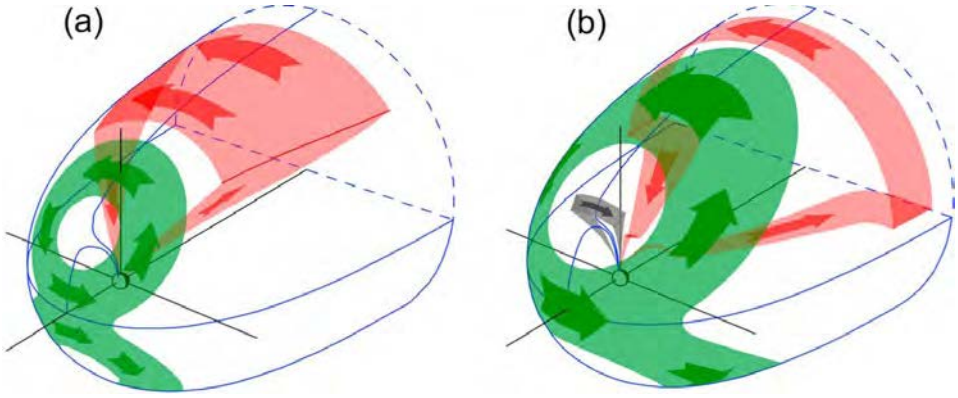

Figure H.7: a) absence of strong northward IMF; b) appearance of dayside field-aligned current system (grey) [GLD18].

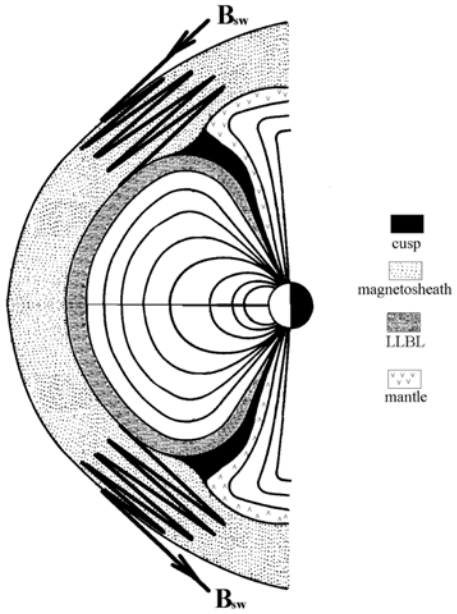

Figure H.8: scheme of magnetic field in the magnetosheath under northward IMF condition [Ant+12].

Magnetic variation occurs on all time scales. It is important to distinguish between regular and irregular variation, the latter often referred to as magnetic activity. Regular variations have different signatures, depending on the geographical latitude. This is due to the different current systems around the earth. **Figure H.9** depicts the frequency spectrum and the corresponding time periods for different geomagnetic variations.

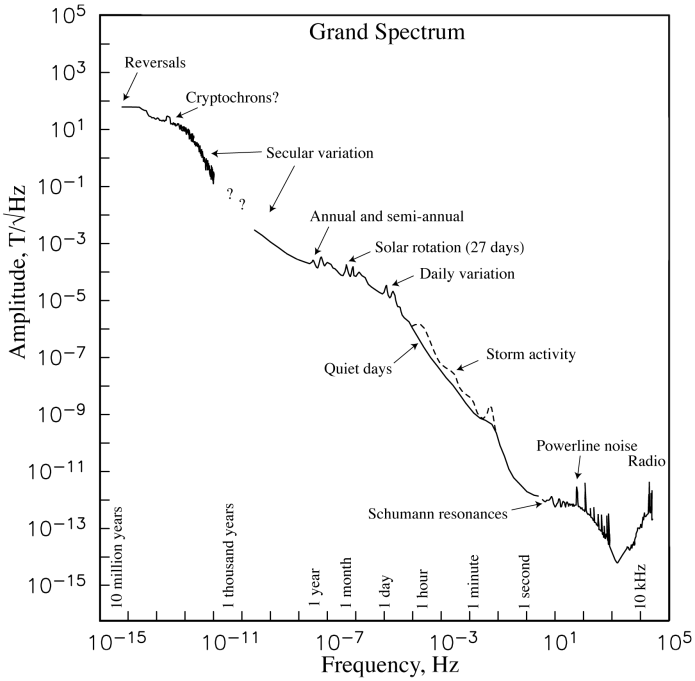

Figure H.9: Frequency spectrum of geomagnetic variations [Con07]. *Reproduced with permission from Springer Nature.*

H.2 Space Weather Events Probability and Economic Impact

- Carrinton Event in the next 10 years: 12 % [Ril12]
- Carrinton Event in the next 50 years: 50 % [Ril12]
- Super storm (CE) in the next 10 years: approx. 6.3 %
- Quebec event in the next 10 years: approx. 17.8 % [Lov12]
- Costs related to space weather events [Tuv+16; Eas+17]

H.3 Historical Space Weather Events

- 7176 before common era (BCE): signs of a very strong solar radiation event in ice cores [Pal+22]
- 775 anna domini (AD): signs of a very strong solar radiation event in ice cores [Pal+22]
- 1859: Carrington Event (1760 nT) [Tsu03]
- 1921: Magnetic storm, which was probably similar in strength to the Carrington event. Aurora observations in Samoa, several fires caused by GICs in telegraph lines in Sweden [Kap06; CD13]
- 1967: Strong solar flare and CME led to widespread communications blackout [Kni+16]

- 1989: Hydro-Quebec blackout [Bol02; Bot19]
- 2003: strong solar flare; 90-minute outage in southern Swedish power grid [Pul+05]
- 2012: A "Carrington" class storm misses the earth, but is recorded by the Stereo A satellite [Phi14]

I Worldwide Research on GIC related Topics

Czech Republic: [RDS13; VŠ19]
Swiss: [DB12]
Austria: [Bai+17]
Finland: [PVP07]
Sweden: [Wik+08; PE05; Ros+22]
Norway: [Elo+92; EH00; Hut+08; Myl+14]
Canada:[BP22]
Russia: [Ero+10]
Poland: [Gil+20]
USA: [Hug+22; ODA22]
Spain: [Tor+12]
Mexico: [Car+19]
Brazil: [Tri+07; Bar+15]
Uruguay: [Car16]
South-Africa: [Hey+17]
China: [Liu+09]
Japan: [Nak+18; WNE21] UK: [Kel+17; Eri+02]
Australia: [Mar+13; Mar+17]
New Zealand: [Mar+12]
France: [Kel+17]
Malaysia: [Abd+20; Zaw+20; Khu+22]
Korea: [Cho+15]

J Implemented Heuristic Optimisation Algorithms

J.1 Nelder-Mead Simplex Algorithm

```
fun = @(JA) ErrorEstimation(JA, MeasData_UI, OptimasationType);
options = optimset('Display','iter','MaxIter',2,'TolFun',...
1e-15,'TolX',1e-15);
[x_star,fval] = fminsearch(fun,JA_0,options);
```

J.2 Particle Swarm Optimisation Algorithm

```
N = 25; % population size (total evaluations will be itmax*N)
itmax = 40;
c1 = 1.05; c2 = 1.05;
wmax = 1; wmin = 0.3; %set to same value for constant w
w = linspace(wmax,wmin,itmax); %linear variation of w

% Problem and velocity bounds
a(1:N,1) = 1.50e6; b(1:N,1) = 1.76e6; %bounds on var. x1-MS
a(1:N,2) = 1;      b(1:N,2) = 1e3;    %bounds on var. x2-JAa
a(1:N,3) = 1e-6;   b(1:N,3) = 1e-1;   %bounds on var. x3-alpha
a(1:N,4) = 1;      b(1:N,4) = 1e4;    %bounds on var. x4-k
a(1:N,5) = 0.1;    b(1:N,5) = 0.999;  %bounds on var. x5-c

d = (b-a);          % Parameter range
m = a; n = b;
q = (n-m)/4; %initial velocities are 1/4 (original) of parameter
  space size/range

% Random initialisation of positions and velocities
D = 5;                  % Number of variables
x = a+d.*rand(N,D);
v = q.*rand(N,D);

% Evaluate Object for all Particles
Ms_Set = x(:,1);
JAa_Set = x(:,2);
alpha_Set = x(:,3);
k_Set = x(:,4);
c_Set = x(:,5);

% Initialise Init_T74_BHfit.m
```

```
run('C:\T74\Init_T74_BHfit_PSO.m')
% Initialise Error Vector
Error = NaN(N,1);

% Simulation for first set op particles/parameters
for IterParam = 1:N
    % Set JA Parameter
    Ms = Ms_Set(IterParam);
    JAa = JAa_Set(IterParam);
    alpha = alpha_Set(IterParam);
    k = k_Set(IterParam);
    c = c_Set(IterParam);

    Ms2 = Ms;
    JAa2 = JAa;
    alpha2 = alpha;
    k2 = k;
    c2 = c;

    % Execute Simulink Model
    try
        open_system('T74_elec_Hys.slx');
        % Save simulation data
        out = sim('T74_elec_Hys.slx');
    catch
        disp('Simulation terminated with an error.
             Next JA-Parameter set is choosen.')
        continue
    end

    if OptimiseI
        % Get Hsim
        Isim = out.IsimLVL1*2*102*(1/0.431);

        % Conditioning of Hsm
        Ism_length = length(Ism);
        Isim_length = length(Isim);
        Scale = Isim_length/Ism_length;

        Isim_resample = resample(Isim,1,Scale);
```

```
        % Calculate Root-Mean Square-Error (RSME) between
        % smoothed measured H and simulated H
        Error(IterParam) = sqrt(sum(((-Ism(100:end-100))-...
        Isim_resample(100:end-100)).^2)/...
        length(Ism(100:end-100)));
    end

    % Find gbest and pbest (in this case coincides with x)
    [fgbest,igbest] = min(Error);
    gbest = x(igbest,:);
    pbest = x; fpbest = Error;
end

% Iterate
for it=1:itmax
% Update velocities and positions
    v(1:N,1:D)=w(it)*v(1:N,1:D)+c1*rand*...
    (pbest(1:N,1:D)-x(1:N,1:D))+c2*...
    rand*(repmat(gbest,N,1)-x(1:N,1:D));
    x(1:N,1:D)=x(1:N,1:D)+v(1:N,1:D);

    % Check if variables are in limits; if is above/below
    % the limits the inLimit variable become zero
    Ms_inLimit = all( x(:,1)>=a(1,1) & x(:,1)<=b(1,1) );
    JAa_inLimit = all( x(:,2)>=a(1,2) & x(:,2)<=b(1,2) );
    alpha_inLimit = all( x(:,3)>=a(1,3) & x(:,3)<=b(1,3) );
    k_inLimit = all( x(:,4)>=a(1,4) & x(:,4)<=b(1,4) );
    c_inLimit = all( x(:,5)>=a(1,5) & x(:,5)<=b(1,5) );

    if Ms_inLimit & JAa_inLimit & alpha_inLimit & k_inLimit &...
       c_inLimit
       continue  % No limits violated
    else
        % Limits violated, mirror at boundary
        [~ ,NumParameters] = size(x);

        % Initialise error vector:
        ViolatedLimits = zeros(N,NumParameters);

        % 20 x 5 Matrix with violated (=1) values
        for numerate = 1:NumParameters % numerate = 1:5
```

```
            ViolatedLowerLimits(:,numerate) =...
            x(:,numerate)< a(:,numerate);
            ViolatedUpperLimits(:,numerate) =...
            x(:,numerate)> b(:,numerate);

            % Update JA-Parameters with mirrod parameters

            x(ViolatedUpperLimits(:,numerate),numerate)=...
            abs(b(ViolatedUpperLimits(:,numerate),numerate)-...
            (x(ViolatedUpperLimits(:,numerate),numerate)-...
            b(ViolatedUpperLimits(:,numerate),numerate)));
            x(ViolatedLowerLimits(:,numerate),numerate)=...
            abs(a(ViolatedLowerLimits(:,numerate),numerate)+...
            (a(ViolatedLowerLimits(:,numerate),numerate)-...
            x(ViolatedLowerLimits(:,numerate),numerate)));
        end
    end

    for IterParam = 1:N
        % Set JA Parameter
        Ms = x(IterParam,1);
        JAa = x(IterParam,2);
        alpha = x(IterParam,3);
        k = x(IterParam,4);
        c = x(IterParam,5);

        Ms2 = Ms;
        JAa2 = JAa;
        alpha2 = alpha;
        k2 = k;
        c2 = c;

        % Execute Simulink Model
        try
         % Save simulation data
            out = sim('T74_elec_Hys.slx');
        catch
            disp('Simulation terminated with an error.
                  Next JA-Parameter set is choosen.')
            continue
        end
```

```
        % Find gbest and pbest (in this case coincides with x)
        [fgbest,igbest] = min(Error);
        gbest = x(igbest,:);
        pbest = x; fpbest = Error;
    end

    % Find gbest and pbest
    [minf,iminf] = min(Error);
    if minf<= fgbest
        fgbest=minf; gbest=x(iminf,:);
    end
    inewpb=find(Error<=fpbest);
    pbest(inewpb,:)=x(inewpb,:); fpbest(inewpb)=Error(inewpb);
end % end loop on iterations

[gbest,fgbest];
```